Fall 1973

NEUTRON MEASUREMENTS IN SPACE WITH OGO-VI SATELLITE

SHADRACH OKECHUKWU IFEDILI

INFORMATION TO USERS

This dissertation was produced from a microfilm copy of the original document. While the most advanced technological means to photograph and reproduce this document have been used, the quality is heavily dependent upon the quality of the original submitted.

The following explanation of techniques is provided to help you understand markings or patterns which may appear on this reproduction.

1. The sign or "target" for pages apparently lacking from the document photographed is "Missing Page(s)". If it was possible to obtain the missing page(s) or section, they are spliced into the film along with adjacent pages. This may have necessitated cutting thru an image and duplicating adjacent pages to insure you complete continuity.

2. When an image on the film is obliterated with a large round black mark, it is an indication that the photographer suspected that the copy may have moved during exposure and thus cause a blurred image. You will find a good image of the page in the adjacent frame.

3. When a map, drawing or chart, etc., was part of the material being photographed the photographer followed a definite method in "sectioning" the material. It is customary to begin photoing at the upper left hand corner of a large sheet and to continue photoing from left to right in equal sections with a small overlap. If necessary, sectioning is continued again — beginning below the first row and continuing on until complete.

4. The majority of users indicate that the textual content is of greatest value, however, a somewhat higher quality reproduction could be made from "photographs" if essential to the understanding of the dissertation. Silver prints of "photographs" may be ordered at additional charge by writing the Order Department, giving the catalog number, title, author and specific pages you wish reproduced.

University Microfilms

300 North Zeeb Road
Ann Arbor, Michigan 48106

A Xerox Education Company

NEUTRON MEASUREMENTS IN SPACE WITH OGO-VI

by

SHADRACH OKECHUKWU IFEDILI

A THESIS

Submitted to the University of New Hampshire

In Partial Fulfillment of

The Requirements for the Degree of

Doctor of Philosophy

Department of Physics

October , 1972

This thesis has been examined and approved.

Thesis director, John A. Lockwood, Prof. of Physics

William R. Webber, Prof. of Physics

Robert E. Houston, Jr., Prof. of Physics

Roger L. Arnoldy, Assoc. Prof. of Physics

Richard L. Kaufmann, Assoc. Prof. of Physics

DEC. 18, 1973
Date

ACKNOWLEDGEMENTS

The author wishes to express his deep gratitude to Dr. John Lockwood for his guidance, suggestions and support throughout the thesis work. I am also very grateful to Dr. Robert Jenkins for his invaluable assistance at the initial phases of the research. Thanks go to Dr. H. Razdan and Dr. Edward Chupp for some very useful discussions, and to Dr. William Webber and Dr. A.J. Masley for the Pioneer 8 and the OGO-VI charged particle data, respectively. Technical assistance is acknowledged from the staffs of the University of New Hampshire Space Science Center, the Oak Ridge National Laboratories and the TRW Systems, Inc. The author also wishes to thank all the members of his thesis committee for their valuable comments.

This research was supported by the National Aeronautics and Space Administration under contract NAS5-9313 and grant NGR-002-088.

TABLE OF CONTENTS

LIST OF TABLES

LIST OF ILLUSTRATIONS

ABSTRACT

NEUTRON MEASUREMENTS IN SPACE WITH OGO-VI

by

SHADRACH OKECHUKWU IFEDILI

An experiment has been performed with a neutron detector on the OGO-VI satellite to search for solar neutrons, to measure the solar proton albedo neutron flux, and to determine the flux, latitude dependence, angular distribution, energy spectrum and the solar modulation of the cosmic-ray albedo neutrons. The upper limit on the quiet-time solar neutron flux from 1-20 MeV has been measured to be less than 1.8×10^{-3} n/cm^2-sec at the 95% confidence level. This result was deduced from the neutron detector measurements of the "day-night" effect near the equator at low altitudes for the period from June 7, 1969 to December 23, 1969. We have also placed limits, $< 5 \times 10^{-2} n/cm^2$-sec in 1-20 MeV at the 95% confidence level, on neutron emission from the sun for several flares including two flares of importance 3B. The measurements are

consistent with the Lingenfelter (1969) and Lingenfelter and Ramaty (1967) models for solar neutron production during solar flares.

We have measured solar proton albedo neutron fluxes, both at high and low latitudes and for several solar proton events, which are in reasonable agreement with the predictions of Lingenfelter and Flamm (1964).

The total cosmic-ray leakage flux ($\leq$10 Mev) has been measured to be about 0.7 times the Lingenfelter (1963) flux while the latitude dependence is in good agreement with that calculated by Lingenfelter (1963). Comparison of the measured total neutron leakage flux ($\leq$10 Mev) with the measured 1-10 Mev neutron leakage flux and with the total neutron leakage flux results ($\leq$10 Mev) of the previous experiments indicated a neutron spectrum that is similar to the neutron spectrum calculated by Newkirk (1963). We measured an energy spectrum of the form $E^{-\gamma}(0.8 < \gamma < 1.0)$ in 1-10 Mev energy range for the polar region (P_c <0.3GV), which is slightly flatter than the Newkirk spectrum but which is consistent with the more recent higher energy (10-100 Mev) measurements of White et al. (1972).

The form of the angular distribution of the cosmic-ray albedo neutrons ($\leq$10 Mev) at the top of the

atmosphere was deduced from the comparison of the measured and calculated altitude dependence of the cosmic-ray albedo neutron flux. The isotropic angular distribution, $k(\nu)=1$, at geomagnetic latitudes less than 60° and the angular distribution $k(\nu)=1-0.5\cos\nu$ (ν is the angle from the zenith) in the polar region ($P_c<0.3$GV) best fit the neutron measurements.

Finally, the solar modulation of the cosmic-ray albedo neutrons has been observed. The solar cycle modulation of the albedo neutron flux ($\leq$10 MeV) was found to be similar to the 11-year variation of the integral flux of galactic cosmic-ray protons at similar geomagnetic cutoff rigidities. At low cutoff rigidities (<0.6GV) our results indicate a high depression of the low energy particles during June 7-December 23, 1969. The measured 11-yr solar modulation of the cosmic-ray albedo neutrons is in reasonable agreement with the calculations of Lingenfelter (1963). It was also observed that the cosmic-ray albedo neutron flux ($\leq$10 Mev) and the integral flux of galactic cosmic-ray protons at similar geomagnetic cutoff rigidities are similarly depressed during Forbush decreases; the lower the geomagnetic cutoff rigidity the larger the Forbush decrease effects on the cosmic-ray albedo neutrons.

CHAPTER I

INTRODUCTION

Almost all the neutrons in the earth's atmosphere are generated by interactions of the primary and secondary cosmic rays with the atmospheric nitrogen and oxygen nuclei. Some of these primary rays are galactic, others are solar "cosmic rays" which were accelerated in solar flares. There may also be some solar neutrons present. The 12-minute half-life of free neutrons precludes the possibility, however, that any except extremely energetic neutrons could reach the earth from beyond the solar system.

The neutrons produced in the atmosphere are moderated by elastic and inelastic scattering with air nuclei and are eventually captured by atmospheric nitrogen, mainly through the reaction $_{7}N^{14}(n,p)\ _{6}C^{14}$. A small fraction of the energetic neutrons leak out of the atmosphere. If they decay into a proton and an electron within the magnetosphere, the decay particles may then be trapped by the geomagnetic field to contribute to the radiation belts (Singer, 1958).

However, the neutron source function for calculating the cosmic-ray albedo neutron decay (CRAND)

contributions to the radiation belts was, until our measurements, poorly known (Chapter 2). The measured albedo neutron flux ($\leq$10 MeV) above the atmosphere was known to no better than a factor of 3-5 in magnitude and 2-3 in latitude dependence. No measurements of >10 MeV albedo neutrons have been made above the atmosphere. Most of the scanty neutron flux measurements (>10 MeV) in the atmosphere could not identify the upward moving neutrons. Furthermore, there are very large uncertainties attending the extrapolation of the neutron flux measurements, made deep in the atmosphere, to outside the atmosphere. Moreover, the angular distribution of the cosmic-ray albedo neutrons at the top of the atmosphere was not known though this is needed to calculate the contributions of decaying neutrons to the trapped radiation and to obtain the neutron leakage flux from the counting rate of a detector near the top of the atmosphere. We therefore flew an experiment to measure the flux, energy and spatial distributions of the cosmic-ray albedo neutrons in order to provide a reliable neutron source function for verifying or disproving the CRAND theory of injection and for related problems such as the radio carbon, C^{14}, dating.

The production of neutrons in the earth's atmosphere is affected by the modulation of the cosmic

radiation near the earth. The irregular interplanetary magnetic field, carried by the continuously expanding solar corona and which is affected by the 11-year sunspot cycle, sweeps away some galactic cosmic rays which consequently do not reach the earth. Though Lingenfelter (1963) calculated the effect of the 11-year modulation on the albedo neutrons, no measurement of the total albedo neutron flux has yet checked the solar cycle modulation of albedo neutrons. Some cosmic-ray particles are also screened from reaching the earth during Forbush decreases. However, the Forbush decrease effects on cosmic-ray albedo neutrons have not been measured nor any theoretical estimates made. To remedy the situation we have, in this thesis, studied the effects of solar modulation on cosmic-ray albedo neutrons.

During solar proton events large fluxes of particles usually arrive at the earth and contribute to the neutrons in the atmosphere. For example, the solar protons could interact with the polar atmosphere to produce neutrons (Lingenfelter and Flamm 1964a, b). The solar proton albedo neutron decay products may provide the anomalously large fluxes of the low-energy radiation belt protons. However, this neutron source is scarcely and poorly known (Chapter 2, 3). We have measured the solar proton albedo neutrons during several

solar proton events. The measurements will be reported and the implications discussed.

Solar neutrons could also be among the particles arriving at the earth during solar proton events. That neutrons and gamma rays are emitted from the sun during solar flares was first suggested by Bierman et al. (1951). This suggestion was supported by the theoretical calculations by Hess (1962), Lingenfelter et al. (1965) and Lingenfelter and Ramaty (1967), which produced estimates of solar neutrons measurable at 1A.U. and which demonstrated that the only significant source of solar neutrons is from protons accelerated and slowed down in the solar atmosphere during solar flares. Lingenfelter et al. (1965) also calculated the time-averaged solar neutron flux above 10 MeV over the last solar cycle (1954-1965) at 1A.U. to be about 3×10^{-3} neutrons/cm^2-sec with a peak intensity at 20-60 MeV; for a P_0=125Mv the maximum energy is 40 MeV with the corresponding flux $\sim 2 \times 10^{-5}$ neutrons/cm^2-sec. However, the existence of a detectable solar neutron flux, during solar flares or during relatively quiet periods, has not yet been confirmed experimentally (Chapter 3.3).

Since solar neutrons, unlike the solar charged particles, are not affected by the solar and inter-planetary magnetic fields, the detection of solar neutrons

could elucidate the high energy processes occuring in the solar atmosphere. It could also contribute to the understanding of solar abundances. For example, any measured flux of solar neutrons could be used to evaluate some parameters of the accelerating, trapping, storage and release of solar cosmic rays such as the time dependence of and the time scale for the acceleration, the size and location of the acceleration region, the nuclear interaction time, the position in the solar atmosphere where interactions occured and the total energy released. We could also use the measured solar neutrons as a source function to verify or disprove the solar neutron decay theory of injection (Chapter 3.2). Even a lower upper limit to the solar neutron flux would furnish more constraints on the solar flare models. Moreover, if we measure the quiet-time solar neutrons, we could suggest that nuclear reactions which produce protons are continuously taking place in the solar atmosphere. Furthermore, a comparison of the solar neutron and proton fluxes as well as their relative delay in arrival at the earth could provide some information about the interplanetary medium.

In this thesis the results of a search for solar neutrons will first be reported. Secondly, the measurements of the solar proton albedo neutrons

will be presented. Finally, the flux, spatial and energy distributions as well as the solar modulation of the cosmic-ray albedo neutrons will be determined and compared with the previous theoretical and experimental results if any. The neutron data were acquired by a neutron detector flown on the OGO-VI satellite.

CHAPTER II

ATMOSPHERIC NEUTRONS

2.1 The Birth, Life-History and Fate of Atmospheric Neutrons

The cosmic rays, which are energetic nuclear particles arriving from outside the earth's atmosphere, interact with air nuclei generating atmospheric neutrons by two mechanisms depending on the energy of the incident cosmic rays. If the kinetic energy of the incident particle is roughly equal to or greater than the average interaction energy between nucleons in oxygen and nitrogen (about 10 MeV or more), the incident particle interacts with only a single nucleon or with a small number of nucleons. This knock-on process thus produces many fast nucleons with energies greater than 10 MeV traveling in about the same direction as the initial cosmic-ray particle. These knock-on neutrons can be scattered to lower energies by air nuclei. In the other mechanism, the evaporation process, the incident cosmic ray energy raises the target's nuclear "temperature" to a value of about 1 MeV per nucleon. As neutron emission is the most probable de-excitation reaction when nitrogen and

oxygen are excited to energies above about 8 MeV by cosmic rays (Hess et al., 1961), the cooling process expels evaporation neutrons with roughly a Maxwellian energy distribution which has a peak at about 1 MeV. Lingenfelter (1963) deduced an energy spectrum for the evaporation spectrum to be $N(E)dE \alpha E \exp(-E/\theta)dE$ where $N(E)$ is the number of neutrons per second produced in the energy interval E to E+dE and θ is the nuclear "temperature." He chose a value of 1 MeV for θ to agree with the neutron spectrum of neutrons evaporated from Carbon, excited by 190 MeV protons (Gross, 1956) and to agree with the nuclear-evaporation calculations of LeCouteur (1952). Simpson (1951) showed that about 90% of the cosmic ray neutrons were produced by evaporation stars.

The atmospheric neutrons suffer elastic and inelastic scattering with air nuclei and may be lost by high energy inelastic collisions ; or by low energy nuclear absorption mainly $N^{14}(n,p)C^{14}$ producing C^{14} for radiocarbon dating in archaeology and by the reaction $N^{14}(n,T)C^{12}$ producing tritium for tritium studies in glaciology; or by absorption by the solid earth. The only high energy neutrons that escape the atmosphere are those from cosmic rays striking the atmosphere tangentially since knock-on neutrons continue in about the same direction as the primary cosmic rays. But low energy neutrons (<10 MeV) are

emitted essentially isotropically. Neutrons with energies less than 2/3 ev will not have the necessary escape velocity so they are trapped by the gravitational field to decay near the earth. High energy neutrons move so fast that relatively few decay in the magnetosphere. In fact, only about 1% of neutrons with 1 MeV energy decay near the earth (Hess, W., 1962).

The neutrons (about 10% of all neutrons formed by interactions of cosmic rays with oxygen and nitrogen nuclei in the atmosphere) which travel outward from the earth are called albedo neutrons and may decay within the magnetosphere in the mode $n \rightarrow p + e + \bar{\nu}$ with a half-life of about 12 minutes. If these decay products are injected at pitch angles $\alpha \gtrsim \alpha_D$ where $\frac{\sin^2 \alpha_D}{B} = \frac{1}{B_{100\ km}}$ thenthe proton and/or electron may be trapped by the geomagnetic field, B, to give rise to the radiation belts (Fig. 2). The density of neutrons decaying at radius R and latitude λ is $\frac{dn}{dV}(E,R,\lambda) = \frac{1}{\gamma v_n \tau_n} J_n(E,R,\lambda)$ where v_n is the neutron's velocity, τ_n the neutron mean life and $\gamma = (1 - \frac{v^2}{c^2})^{1/2}$ (Hess, 1962). $J_n(E)$ is the albedo neutron flux corresponding to the energy, E (Fig. 1). As the proton kinetic energy and direction are nearly those of the parent neutron, the neutron decay-density

energy spectrum is also the proton source energy spectrum $S_p(E,R,\lambda)$, that is, $S_p(E,R,\lambda) = \frac{dn}{dV}(E,R,\lambda)$. Electrons are emitted essentially isotropically with the β decay spectrum having a maximum at about 300 KeV and no electrons with $E_e \gtrsim 780$ KeV. Since the electron's kinetic energy is roughly the mass difference of the neutron and proton, the electron's energy is not changed by the neutron's kinetic energy. Therefore, the electron source strength S_e from neutron decay is the sum of all neutron decay events. Hence

$$S_e(R,\lambda) = \int \frac{dn}{dV}(E,R,\lambda)dE = \int \frac{1}{\gamma v_n \tau_n} J_n(E,R,\lambda)dE$$

2.2 Cosmic-ray Albedo Neutrons

The energy, latitude and altitude distributions of the galactic cosmic-ray atmospheric neutrons have been calculated. Hess, Canfield and Lingenfelter (1961) first calculated the neutron albedo spectrum at 44°N using a multigroup diffusion theory with a decreasing exponential dependence, $\exp(-x/155\ \text{gm-cm}^2)$, of the neutron source normalized by the atmospheric neutron measurements of Hess, Patterson, Wallace and Chupp (1959). Lingenfelter (1963) revised this calculation and deduced the energy, latitude and altitude

distributions of the neutron albedo for solar minimum and solar maximum (Fig. 1). For the altitude and latitude dependence of the neutron source Lingenfelter used the altitude dependence of star production measurements of Lord (1951), and the altitude and latitude dependence of the equilibrium neutron flux measured by Simpson (1951), Simpson and Fagot (1953), Meyer and Simpson (1955), Rose et al. (1956) and Soberman (1956). The dependence of neutron production with solar activity cycle was obtained from the measurements of the cosmic ray intensities by Neher (1959), Lockwood (1960), Anderson (1961) and Neher and Anderson (1962), as well as the satellite measurements of the latitude variation of the primary cosmic-ray intensity by Albert et al. (1962). Since the diffusion approximation to the Boltzmann transport equation assumes that the neutron flux is not highly anisotropic, the Hess and Lingenfelter calculations only apply to neutrons with energies less than 10 MeV. Newkirk (1963), with a slightly different approach, calculated the neutron flux in the atmosphere at 57°N using the S_n approximation to the transport theory developed by Carlson (Carlson 1955,58,59; Carlson and Bell, 1958) which was based on difference equation techniques. The angular distribution for the source neutrons was derived from the nitrogen cloud chamber

experiments of Miyake et al. (1957) and the altitude distribution for star formation of Lord (1951). The calculation was also normalized by the atmospheric neutron measurements of Smith et al. (1961). The neutron intensity deduced by Newkirk was in good agreement with the result of Lingenfelter. However, the Newkirk energy spectrum is flatter than the Lingenfelter spectrum in the 1-10 MeV range. Since Lingenfelter's results include the changes with solar activity at all latitudes, they are extensively used as a basis of comparison for experimental measurements of the albedo neutrons and for calculating the trapped proton intensities.

The cosmic ray albedo neutron flux predicted by these theories and used to evaluate the decaying albedo contributions to the radiation belts has been checked by various leakage flux measurements. The low energy neutron experiments which measure neutron fluxes with energy $E \lesssim 1$ MeV directly, detect neutrons by the exothermic nuclear reactions:

(i) $Li^6(n,\alpha)T + 4.78$ MeV

(ii) $He^3(n,p)T + 0.76$ MeV

(iii) $B^{10}(n,\alpha)Li^7 + 0.48$ MeV$(\gamma) + 2.30$ MeV

The charged particle products of these reactions are

then detected by their ionization loss. The He^3 reaction has the best resolution due to its lowest Q value; the reaction cross section is not only the largest but it is a smoothly varying function of the neutron energy; and it has no excited states which could produce uncertainty in the available energy. Since proportional counters filled with helium and a quenching gas can be operated at high pressures at reasonable potentials, efficiencies of the order of 70% are readily achieved with the He^3 reaction. To increase the detection efficiency, impinging higher energy neutrons are moderated by elastic collisions with the hydrogeneous moderator surrounding the neutron detector (which could be a proportional counter, a scintillator, or a solid state detector) to energies acceptable to the slow-neutron counter. Bame et al. (1963) in a series of rocket flights used the $Li^6(n,T)$ He^4 reaction in Li^6I scintillation counters with different thicknesses of polyethylene moderator surrounding the scintillator to extract the different ranges of neutron energy. They observed a spectral shape for the albedo neutron flux which agreed with the calculation of Hess, Canfield and Lingenfelter (1961) in the energy range from thermal to 10 MeV. The absolute neutron fluxes measured between 8° and

44° geomagnetic latitude agreed with the calculation of Lingenfelter (1963). However, the background of γ-rays and charged particles introduced a 30% error. Furthermore, there was no discrimination in the experiment against neutrons produced by the cosmic rays impinging on the detector assembly. An estimate of this effect was later made and the count rates reduced by 20%.

Williams and Bostrom (1964) used an array of solid state detectors coated with B^{10} placed inside a large polyethylene moderator. This system was flown on a Traac Satellite. They measured fluxes that were less than the values calculated by Hess et al. (1961) and 5-10 times larger than the values of Lingenfelter (1963). Boella et al. (1963, 1965) on several balloon flights suppressed background counts due to γ-rays and charged particles by taking the differences in the counting rates of two Boron plastic scintillators (containing different isotopic compositions of Boron) encased in polyethylene moderators. By minimizing the surrounding material the local production was reduced to 20% of the counting rate. The latitude variation observed was in agreement with Lingenfelter's curve up to 42°N. The neutron flux was half of the expected

value at high latitudes. Albert et al. (1962) used a plastic scintillating moderator around a $B^{10}F_3$ counter and took anticoincidences between the scintillator and the slow-neutron counter to eliminate locally produced neutrons. The albedo results obtained were contaminated by very many locally produced neutrons due to too short a blanking time for the neutron counter.

Trainor and Lockwood (1963) on a Agena Satellite experiment used a bank of proportional counters around a BF_3 - filled proportional counter. The entire array of counters was encased in a cylindrical paraffin moderator. The charged particle counters were used to turn off the neutron detector any time that charged particles entered the system. This discriminated against locally produced neutrons by charged particles. The results agreed with Lingenfelter's fluxes near the equator but were much less near the poles. Lockwood and Friling (1968) made several rocket flights with a He^3 proportional counter encased in a polyethylene moderator. The moderator and neutron detector were surrounded by a ring of charged particle counters. The fluxes observed agreed with the Lingenfelter calculations for latitudes $< 50^{\circ}$, but were 60% of the Lingenfelter calculations at latitudes greater

than 60°. On a series of balloon flights with a BF_3 proportional counter surrounded by polyethylene moderator Greenhill et al. (1965) measured neutron fluxes agreeing with the Lingenfelter calculations at high latitudes but measured a smaller flux near the equator. It appears that they underestimated the production effects in the detector which could reduce the measured flux by 20%.

These slow-neutron counter systems have very low efficiency for fast-neutron detection, i.e. for neutrons with energies between 1 MeV and 20 MeV. Local production effects are very much increased by the moderator material. Most important, knowledge of the neutron spectrum is required to deduce the flux from the observed counting rates. These disadvantages are obviated by the recent use of fast-neutron detectors consisting of hydrogeneous scintillators that detect neutrons by the proton-recoils. The organic scintillator is usually surrounded by an inorganic plastic scintillator. Anticoincidences are then taken between the outer and inner scintillators to subtract the charged particle background. The neutrons are assumed to make no interactions in the outer scintillator. Because certain scintillator materials have pulse shapes which depend on the

ionization loss rate, pulse-shape discrimination techniques can be used to separate the neutrons from the gamma rays both of which will pass through the plastic shield without interacting. By analyzing the pulse height distributions of the recoil proton spectrum one can determine the neutron energy spectrum. Haymes (1964) made balloon flights at latitude 41.5°N. He detected neutrons through the proton-recoil mechanism in the organic liquid scintillator NE213 surrounded by a plastic shield to reject charged particles. Gamma rays were rejected by means of pulse-shape discrimination. The measured flux agreed with the Lingenfelter and Newkirk calculations but was less than the Hess (1961) flux. The differential neutron energy spectrum was $E^{-1.3\pm0.1}$ in 1-14 MeV range in reasonable agreement with the results of Hess et al. (1961). This can be compared with the Lingenfelter spectrum of $E^{-1.6}$ in 1-10 MeV range. Mendell and Korff (1963) obtained the energy spectrum $E^{-1.16\pm0.20}$ in the 1-10 MeV range by using the proton recoil in liquid NE213 encased in plastic phosphor NE102 to reject charged particles. They also used the pulse-shape discrimination technique to reject gamma rays. Holt, Mendell and Korff (1966) measured the fast-

neutron flux using a recoil proton detector in which a combination of phoswiching and pulse-shape discrimination was used to separate neutrons from charged particles and gamma rays. The energy spectrum deduced was $E^{-1.05\pm0.15}$ in the 1-10 MeV range. The measured fluxes agreed with the Lingenfelter calculations at all latitudes. In balloon flights at geomagnetic latitude 42°N St.Onge and Lockwood (1968) flew an NE213 liquid scintillator surrounded by a plastic scintillator which also enclosed the photomultiplier and electronics to further minimize local production. The improved pulse-shape discriminating scheme consisted of a high-resolution two-parameter multiple-particle (e,p,α) pulse-shape discriminator with a two parameter logarithmic pulse-height analyzer and display scheme. A wider energy range, 3 to 20 MeV, was also included. The provisional differential energy spectrum obtained was $\sim E^{-2.0}$ from 3-20 MeV.

These methods are extremely difficult to extend to higher energies (E_n>20 MeV) since the interaction cross sections decrease rapidly with increasing neutron energy. For example, in the organic scintillator the neutron cross section for production of a charged particle in Carbon at about 80 MeV is about three times the (n-p) elastic scattering cross section.

Therefore, other methods are used to detect high energy neutrons. Neutrons of a few MeV induce fission in heavy nuclei such as Th, U, Pu, etc. while high energy neutrons induce fission in relatively light elements such as Bi, Au, Hg, etc. The fission fragments are then detected by their ionization loss. Hess et al. (1959) first studied neutrons of energy greater than 50 MeV by using two multiple-plate ionization chambers, with and without Bi^{209} respectively, at aircraft altitudes. The ionization chambers were surrounded by Geiger counters to monitor charged particle induced fission. Such fission counters are insensitive to gamma rays. However, the neutron efficiency was very small; the efficiency at 200 MeV was $\sim$2%. The statistical precision was extremely poor due to the low counting rates ($\sim$5 hr^{-1}); and the detector was insufficiently calibrated at high energies. Nuclear emulsion could also be used to detect the neutrons. The recoil proton from the (n,p) reaction with the hydrogen nucleus in the emulsion is recorded in the emulsion. The system is insensitive to γ-rays but it is extremely difficult to pick out the recoil-proton events since there are also events where a single charged particle is emitted as a result of nuclear excitation of a nonhydrogeneous nucleus in the

emulsion. The neutrons could also be measured using the proton recoil telescope. In this system the elastic collision of the incident neutron with the hydrogeneous producer is detected with two or more charged particle detectors in coincidence. Zyche (1968) and Daniel et al. (1967) used this system to study solar neutrons. The measurements of high-energy neutrons by the proton recoil telescope and the directional detectors (mainly used to study solar neutrons) will be discussed in Chapters 3.3 and 8.3.

2.3 Solar Proton Albedo Neutrons (SPAN)

During solar flares large fluxes of high-energy protons are emitted from the Sun. Since the protons usually have energies only up to some hundred MeV they are restricted to the polar region of the earth by the terrestrial magnetic field. Neutrons can be generated when the solar protons interact with the polar atmosphere. The decay products of these solar proton-produced neutrons could populate the radiation belt.

Lingenfelter and Flamm (1964 a,b) calculated the distribution of neutrons generated in the atmosphere by solar protons. They obtained the neutron production rate in the atmosphere as a function of

altitude, latitude, and time by using the Freier and Webber (1963) differential energy spectrum of solar protons $\frac{dJ}{dP} \left(\frac{dJ}{dP}\right)_o \left(\frac{dJ}{dP}\right)_o e^{-P/P_o}$ where P is the rigidity of protons, P_o is the characteristic rigidity. These calculations were based on the measured evaporation neutron production cross-sections in Nitrogen at 18 to 32 MeV (Milburn, 1956) and at 2.2 BeV (Frieman and Rowland, 1955), the cross-sections interpolated from the measurements on Aluminum and Carbon at 90, 190, and 340 MeV (Crandall and Millburn, 1953; Gross, 1956) and the Monte Carlo calculations (Metropolis et al., 1958) which gave the Cascade neutron production. The excitation function in air was taken to be 0.96 times the excitation function for nitrogen since 0.8 was assumed to be the ratio of the neutron yields in Nitrogen and Oxygen. This neutron source function was then used to calculate the equilibrium neutron flux (as a function of energy and altitude), and angular distribution of leakage neutrons < 10 MeV by using the multigroup diffusion code ZOOM (Stuart et al., 1958) and IBM 7090 with the code FLANG (Fries, 1961) respectively. Figure 3 shows the equilibrium neutron energy spectra at different altitudes for zero geomagnetic cutoff (1964b). Figure 4 is the calculated neutron leakage for different cutoff rigidities as a function of characteristic rigidity P_o(1964b).

The Lingenfelter and Flamm (1964b) flux seems to agree with the unmoderated balloon-borne $Li^6(n,\alpha)H^3$ detector measurements of Smith et al. (1962). The neutron measurements were made at Bemidji, Minnesota ($\lambda = 57^\circ N$) a few hours after the peak of the proton event following the July 19, 1961 solar flare. However, the cutoff rigidity was unknown at the time of the flight and could introduce a factor of 5 uncertainty in the interpretation of the measurements. Chupp et al. (1967), using a moderated BF_3 counter in a rocket flight at low latitude during the Nov. 15, 1960 solar-flare event, observed a neutron flux 10-15 times the prediction of Lingenfelter and Flamm. Taking into account the production of neutrons by solar alpha particles and a lowering of the cutoff rigidity by 20% they reduced the discrepancy to a factor of 2-2.5. However, since they used different detector systems for the two flights (Anton BF_3proportional counter moderated by epoxy and Reuter-Stokes BF_3 counters moderated with polyethylene for the first and second flights respectively) the background production effects could be different for the flights. Lockwood and Friling (1968), using a rocket-borne moderated He^3 detector, measured a 40% increase in the neutron intensity above 180 km during the July 7, 1967 Solar-particle event

compared with the quiet time intensity above 45 km during a flight on August 24, 1966. With a crude flux and energy spectrum for the solar particles they obtained a Lingenfelter and Flamm leakage flux which was in reasonable agreement with the measured leakage flux increase. Greenhill et al. (1970) used a polyethylene moderated BF_3 (96% B^{10}) proportional counter in a balloon flight from Wilkes on September 3, 1966. Solar-proton flares occurred at 1522UT August 28 and at 0538UT on September 2, 1966. Using the known solar proton flux and spectrum they obtained a solar proton albedo neutron increase in good agreement with the Lingenfelter and Flamm (1964b) leakage flux. Despite the conflicting and sparse results most of the above measurements were made within the atmosphere with no provision to distinguish between the upward and downward moving neutrons; and hence the fraction of neutrons leaking out of the atmosphere was extremely uncertain. Neutrons measured in space are leakage neutrons and can, therefore, be directly compared with the calculated Lingenfelter and Flamm (1964) leakage neutrons.

2.4 Atmospheric Neutron Decay Contribution to the Radiation Belts

The flux and energy spectrum of the radiation

belt protons resulting from neutron decay have been obtained using the continuity equation in energy space

$$\frac{\partial N_p(E)}{\partial t} = S_p(E) - \frac{d}{dE}\left(N_p(E)\frac{dE}{dt}\right) - \rho\,\sigma\,N_p(E)V = 0$$

where $N_p(E)$ is the trapped proton density, $S_p(E)$ is the proton-source energy spectrum, ρ is the mean atmospheric density along the particle's trajectory, σ the non-elastic proton interaction cross section for the atmospheric constituents, V is the proton velocity. Singer (1958), Hess (1959), Freden and White (1960,62) solved this equation for the steady state situation and assumed that the probability of injection for each decay proton was constant. Singer also used the albedo neutron source spectrum from interactions of protons in nuclear emulsions and energy loss due to atomic collisions with the residual atmosphere. The proton spectrum was flat in the energy range from 5 to 300 MeV. Hess used his measured atmospheric neutron source spectrum and the same atmospheric loss mechanism to get leakage neutron flux from which he obtained a trapped proton differential spectrum $E_p^{-1.30}$. The spectrum agreed with Freden and White results (1959) between 90 and 200 MeV but was less steep above 200 MeV. Freden and White (1960), Lenchek and Singer (1963), steepened the calculated spectrum above 100 MeV by further adding a loss term due to

nuclear interactions. Since some knowledge of the angular distribution of the albedo neutron as a function of neutron energy is required to calculate the proton-injection coefficients, Lenchek and Singer (1963) used an isotropic distribution for less than 50 MeV neutrons. Above 50 MeV they used a neutron-free cone with half angle, ϕ, centered on the zenith ($\phi = \frac{300}{P}$, P is neutron momentum) such that outside this cone the neutron intensity was assumed uniform with zenith angle down to the horizon. The calculated and observed spectra agreed at L $\sim$ 1.30, B $\sim$ 0.200 from 30 to 300 MeV. The experimental data showed a minimum at 20 MeV which could be due to large non-elastic (absorption) cross sections for neutrons in nitrogen and oxygen at this energy producing an albedo neutron spectrum which is different from the poorly known albedo neutron spectrum used in the calculations (Fig. 5). The flatter calculated spectrum above 200 MeV could be due to (a) a steeper neutron source spectrum than was used in the calculations, (b) a lowering of the injection efficiency since at these energies the neutron angular distribution is more pancake-shaped than at lower energy, (c) other loss mechanisms such as the adiabatic invariant breakdown. The breakdown of the first adiabatic invariant occurs because at a given L there is a critical energy beyond

which protons will not be stably trapped due to appreciable non-uniformities in the magnetic field along the particles' orbits (Lenchek and Singer, 1963; Dragt, 1965). Theory and experiment show that the larger the B along a field line or the larger the L, the smaller the critical energy (Dragt, 1965; Freden et al. 1965). The inward radial diffusion of lower energy charged particles could violate the third adiabatic invariant. However, Dragt et al. (1966) using various albedo neutron angular and spatial distributions found that the injection coefficients are very sensitive to the neutron spatial distribution only. Haerendel (1964) obtained injection coefficients numerically and, including losses due to charge-exchange and the effects of the breakdown of the magnetic moment and flux invariants, produced a trapped proton spectrum roughly agreeing with the measured apectrum (Fig. 6).

The experimental and calculated absolute flux distributions (Fig. 7 and 8) are in reasonable agreement at the equator though the spatial shape is different. At low altitude (high B) the calculated flux is lower than the observed flux by a factor of 50 at L=1.4 . In doing the calculation Dragt et al. (1966) used the Lingenfelter (1963) calculated neutron source and the averaged atmospheric densities of Cornwall et al. (1965).

while Hess and Killeen (1966) used the Harris and Priester (1962, 1965) model atmosphere. Hess and Killeen concluded that the CRAND source provided the trapped protons near the equator while a slow pitch-angle diffusion process could drive particles down the field lines to provide the preponderant off-equator proton fluxes. Dragt et al. maintained that the equatorial agreement was uncertain since the atmospheric densities at these altitudes were poorly known. The preponderance of protons at low altitudes could be due to scattering down field lines from lower B, possibly by hydromagnetic waves.

Macy et al. (1970) compared the observed 55 MeV proton intensities at 440 km (L=1.4) from 1961-1969 with a theoretical proton intensity variation (solid line) calculated with a constant source and the solar cycle variation in atmospheric densities (Fig. 9). The increase at low altitude due to starfish detonation in 1962 (Filz and Holeman, 1965) and the calculated atmospheric losses (dashed curve) for the starfish protons are also shown. The agreement between the theory and experiment is consistent with the CRAND theory since the CRAND source varies by $\sim$12% over a solar cycle compared with the $\sim$300% solar cycle variations in atmospheric densities.

Though CRAND predicts an isotropic angular distribution of trapped electrons for $\alpha > \alpha_D$, experiment shows that the pitch-angle distribution has a maximum near $\alpha_o = 90^\circ$ (Hess et al. 1961). CRAND explains inner-zone electrons with $E_e \sim 400$ keV but cannot explain low energy ($E_e \sim 50$ keV) inner zone electrons nor all outer zone electrons of any energy for even a relativistic consideration of albedo neutron β decay cannot supply the large flux of outer-zone electrons with $E_e \geq 780$ keV (Nakada, 1963).

The CRAND source seems too weak to supply the large low energy ($\leq$ 10 MeV) proton intensities found at L >1.6 by Naugle and Kniffen (1961), Fillius and McIlwain 1964, Bostrom et al., 1965, Freden et al. 1965, Gabbe and Brown, 1966 and Fillius, 1966 (Fig. 10). It was suggested that solar proton albedo neutron decay, SPAND, could produce these low energy trapped protons (Naugle and Kniffen, 1961; Armstrong, 1961; Lenchek and Singer, 1962; Lenchek, 1962). The solar proton albedo neutrons are produced by the interactions of solar flare protons with the polar atmosphere. This was a very appealing possibility since the incident solar proton spectra are softer than the galactic cosmic-ray spectrum and could therefore produce the steeper low energy trapped protons; and the non-existence

of the anomalous spectrum at L < 1.6 could be due to the impossibility of observing the polar cap solar proton-produced neutrons at these low L values. Detailed calculations of the trapped proton flux by Hess and Killeen (1966) (using the Lingenfelter et al. (1965) solar proton rigidity spectrum and the zenith angular distribution $f(\phi) = \cos \phi(1+\frac{2}{3} \cos \phi)$) and by Dragt et al. (1966) (using the Lingenfelter and Flamm (1964) solar proton albedo neutron flux and a sec ϕ zenith angle dependence) indicate that SPAND is inadequate to provide the observed fluxes.

2.5 Summary

The calculated albedo neutron flux and spectra above the atmosphere (Hess et al., 1961; Lingenfelter, 1963; Newkirk 1963) are different by a factor of 3 in magnitude and a factor of 2 in latitude dependence. The measured albedo neutron flux ($\lesssim$ 10 MeV) above the atmosphere is known to no better than a factor of 3-5 in magnitude and 2-3 in latitude dependence. No measurements of >10 MeV albedo neutrons have been made above the atmosphere. It is therefore difficult to quantitively compare the CRAND prediction with the measured proton intensities, spatial and spectral distributions since the CRAND source is at best poorly known.

The angular distribution of cosmic-ray neutron leakage flux at the top of the atmosphere is needed to calculate the contribution of decaying neutrons to the trapped radiation (Lenchek and Singer, 1963; Haerendel, 1964; Dragt et al., 1966; Hess and Killeen, 1966) and to obtain the neutron leakage flux from the counting rate of a detector near the top of the atmosphere. Hess et al. (1961) evaluated the angular distribution of the leakage neutrons and found an almost isotropic distribution for neutrons of energy <10 MeV but there was a strong energy dependence for the angular distribution at energies >10 MeV due to the presence of some knock-on neutrons. They derived an angular distribution (for <10 MeV neutrons) $f(\nu) = 1+1.41 \cos \nu$, where ν is the angle from the vertical. Hess and Killeen (1966) and Dragt et al. (1966) used a distribution $f(\nu) \alpha \cos \nu$ and $f(\nu) = \sec \nu$ respectively to predict the CRAND contribution to the trapped radiation. Moreover, Haymes (1964) and Holt et al. (1966) assumed an isotropic angular distribution to derive the leakage fluxes from measurements of the 1-10 MeV neutron counting rate near the top of the atmosphere. However, the angular distribution of the leakage neutrons is not known.

Though SPAND appears to be inadequate to provide the large fluxes of the anomalous low-energy radiation belt

protons, the neutron source used to obtain the injection coefficients (Hess and Killeen, 1966; Dragt et al., 1966) is poorly and scarcely known.

Solar modulation of cosmic rays near the Earth should be reflected in the neutron production in the atmosphere. Though Lingenfelter (1963) calculated the effect of the 11-yr modulation on the albedo neutrons, no measurement of the total albedo neutron flux has yet checked the solar modulation of albedo neutrons. The effect of the Forbush decrease on cosmic-ray albedo neutrons has not been measured nor any theoretical estimates made.

CHAPTER III

SOLAR NEUTRONS

3.1 The Sun and Solar Activity

The Sun is one of about 10^{11} stars in our galaxy. Since the Sun is the star nearest to us with the consequent colossal effect on our environment and yet a star of average luminosity (4×10^{33} ergs/sec) and surface brightness, we could use it as a model of the other stable, normal stars. Indeed we could use the observations of the sun as a starting point for some calculations for elucidating the nature of stellar structure. For example, we could begin to understand the origin of galactic cosmic rays and the universal elemental abundance. In fact, according to Morisson (1961), the cosmic ray spectrum can be divided into three energy regions. The first region contains particles with energy up to 10-100 BeV and could have been produced in the atmospheres of the sun and other sun-like or special type stars. The second region comprises particles with energy 10^2 to 10^9 BeV and could have been accelerated to these energies by the Fermi statistical acceleration mechanism in the envelopes of Supernova. The last region contains the energetic particles, 10^9-10^{10} BeV energy,

possibly from intergalactic space having been accelerated to these energies by similar processes taking place in other galaxies from which they have escaped.

The visible sun, radius 7×10^5km ($1R_o$) and temperature 5770°K, has a continuously expanding atmosphere which extends to more than $10R_o$. Above the photosphere (the visible surface) is the chromosphere which extends for about 2×10^4km where the solar corona begins. The gases in the lowest 500 km of the chromosphere, the reversing layer, selectively absorb the photospheric continuum radiation to give most of the dark lines of the solar spectrum. The reversing layer has a temperature of about 4700°K, the lowest temperature of all the solar plasma. The temperature then rises to about 7000°K at about 1500 km up in the quiet chromosphere and to 2×10^6K at the solar corona. The high coronal temperature is comparable to the temperature, $\sim 1.5 \times 10^7$°K, of the solar core. Almost all the sun's energy, which is generated in the solar core ($\lesssim 0.25R_o$) from the fusion of hydrogen nuclei to form helium nuclei ($4H^1 \rightarrow He^4$), is released into space by the relatively thin photosphere ($\sim$500km). The convection zone, whose bottom layer is at $0.86R_o$ and the top layer is the photosphere, converts a small amount of the energy from the core into mechanical energy. This mechanical

energy and the large density decrease (a factor of 10^{-4}) across the chromosphere result in the very high temperatures of the sun's outer atmosphere. From the heated corona particles and radiations escape into interplanetary space.

Dark markings on the sun, which are made up of a dark center (the umbra) and a border region (the penumbra), are called sunspots. They appear dark since they are cooler than the surrounding photosphere. The Wolf relative sunspot number, $R = K(10g + f)$, indicates the number of spots visible on the solar surface. f is the number of individual spots, g the number of groups, and the factor K ($\tilde{\sim}1$) is assigned to an individual observer and/or his equipment to reduce the individual sunspot number to a consistent scale. R is less than 10 at solar minimum and R is greater than 100 at solar maximum (Brandt, 1970).

Solar flares normally take place near sunspot groups, the number of flares per unit time depending on the 11-year solar cycle. Solar flares are the occasional sharp brightenings of small portions of the visible solar disc. They are classified into various importance categories on the basis of their area and brilliance seen in H_α, as shown in Table 3.1. Each importance figure in the table is followed by F, N or B (Faint,

TABLE 3.1

IMPORTANCE	AREA, TEN THOUSANDTHS OF SOLAR DISC	AREA, HELIOGRAPHIC, DEG^2	CHARACTERISTIC ANGULAR SIZE, ARC SEC	MEAN DURATION, HOURS
S	<2	<2.1	<0.4	<0.3
1	2-5	2.1-5.1	0.4-0.6	0.3-0.5
2	5-12	5.1-12.4	0.6-1.0	1
3	12-24	12.4-24.7	1.0-1.4	3
4	>24	>24.7	>1.4	3

Normal, Brilliant) which is assigned by the observer for the maximum brilliance. The occurrence of flares is inversely proportional to their importance. Furthermore, the average incidence in terms of the number of flares per day, of importance 1 or greater, is roughly R/25. Since R$\sim$200 at solar maximum and$\sim$0 at solar minimum we could expect eight or nine flares per day at the peak of the current maximum but less than one per day at the minimum in 1975. A solar flare is normally observed in the red light of H_α line (λ=6563Å). During solar flares the H_α intensity increases above the quiet time H_α intensity which is $\sim 2 \times 10^7$ ergs cm^{-2} Å^{-1}Sec^{-1}. In this regard, a flare may be regarded as an optical manifestation of an explosion in the solar chromosphere. In fact, the annihilation of the strong sunspot fields

(>3000 gauss) as a result of an instability could be the cause of solar flares (Wentzel, 1964; DeJager, 1967).

In solar flares radio spectra are detected. They are classified into types II, III, IV and V depending on their position in the radio frequency spectrum. It seems that type I radio noise bursts are not associated with solar flares (Swarup et al., 1960). Types II and III are plasma oscillations due to a disturbance travelling outward through the solar atmosphere. Types IV and V are polarized and appear to be due to synchrotron radiation. They are very well correlated with the emission of high energy particles, solar cosmic rays. According to DeJager (1967), the radio and X-ray waves are produced by the energetic electrons. The interaction of these electrons with the solar atmosphere and/or the magnetic field gives rise to the synchrotron and brehmstrahlung radiation.

The energetic charged particles from the sun were first recorded by Forbush (1946) from the increases in the ionization in sea level ion-chambers. McCracken et al. (1967) pointed out that 80% of flares of importance >2B produced detectable solar charged particles. They also suggested that solar energetic particles may be always associated with solar flares and that there could be a continuous emission of these particles from the sun.

However, the probability of observing the solar flare particles at the earth is greatest when the flare originates in the sun's northwestern quadrant. For example, of the 30 major solar cosmic ray events in 1956-61, 22 were from flares in the sun's western hemisphere and 8 from the eastern (Malitson and Webber, 1963).

3.2 Solar Neutron Production and Decay Injection

We do not understand the processes responsible for the acceleration, trapping, storage and release of solar cosmic rays. Since the charged particles interact with the solar and interplanetary fields we cannot understand the processes by studying these particles; we can only learn about the interplanetary characteristics (McCracken, 1962). However, the energetic charged particles (mainly protons) could, while being accelerated or slowed down, interact with the solar atmosphere generating neutrons, gamma rays and secondary charged particles. The neutral radiations are not affected by the solar and interplanetary magnetic fields. Therefore, any measured flux of solar neutrons could be used to evaluate the size and location of the acceleration region, the time dependence of and the time scale for the acceleration, the nuclear interaction time, the position in the solar atmosphere where interactions occurred and the total energy released.

Even an upper limit on the solar neutron flux could furnish some constraints on the solar flare models.

Charged particles are not observed in some solar flares. If we measure solar neutrons from these events, we can conclude that sometimes the accelerated charged particles might not be energetic enough to escape the sun and yet could produce neutrons during the interaction with the solar atmosphere. Measurement of any quiet-time solar neutrons would suggest that nuclear reactions which produce protons are continuously taking place in the solar atmosphere.

To explain the sea level neutron monitor increase at the November 19, 1949 solar flare event Bierman et al. (1951) first suggested that neutron and gamma rays might be emitted from the sun during solar flares. Hess (1962), Chupp (1964), Lingenfelter et al. (1965), Lingenfelter and Ramaty (1967), and Lingenfelter (1969) have made theoretical estimates of solar neutrons measurable at 1 A.U. The flux and energy spectrum of solar neutrons will depend on the elemental abundance in the solar atmosphere, the spectrum and charge composition of solar particle radiation and the cross-sections for producing neutrons. Lingenfelter et al. (1965), and Lingenfelter and Ramaty (1967) used the model first suggested by Hess (1962). In this model the charged particles are

accelerated in the solar atmosphere. Those which escape the sun are seen at the earth if there is good magnetic coupling between the sun and the earth. Some of the accelerated charged particles travel inwards to be stopped in the photosphere. They assumed that the solar spectrum of particles leaving the flare region was the same as that measured near the earth, which Freier and Webber (1963) expressed as an exponential rigidity spectrum $J = J_o^{-P/P_o}$, P is the particle rigidity, P_o the characteristic rigidity. The particle rigidity $P = \frac{A}{Ze}(E^2+2EMc^2)^{1/2}$ where A is the mass number, Ze the total charge of the nucleus, Mc^2 the proton rest mass energy, E the kinetic energy per nucleon. They also used the abundance of the elements in the solar atmosphere for the abundance of the elements in the acceleration and trapping regions. The extensive calculations of Lingenfelter and Ramaty (1967) produced the flux, energy spectrum and time dependence of the secondary radiations as a function of the depth of material traversed by the accelerated charged particles that escaped, and the number of charged particles that are trapped in the sun. They normalized the yields to 1 proton greater than 30 MeV. By comparing the calculated and observed ${}_1D^2$, ${}_1T^3$ and ${}_2He^3$ isotope to proton ratios

they estimated that the charged particles traversed depths $\sim$ 1-5gm/cm^2 in the acceleration region. With these depths they then determined the yields of the other secondaries for some particular flares.

Thus Lingenfelter and Ramaty (1967) calculated the expected solar neutrons for different characteristic rigidities, P_o, during the acceleration and slowing down phases. They showed that energetic neutrons (>10MeV) are produced principally by the break-up of Helium by protons (Table 3.2). Some neutrons decay in flight and some do not even leave the sun due to their energy or the depth in the solar atmosphere at which they were produced. The resulting neutron energy spectrum at 1A.U., Fig. 11, is therefore very different from that at production. Lingenfelter and Ramaty (1967) applied their calculations to the November 12, 1960 flare and found that the calculated solar neutron flux was two to three orders of magnitude larger than the cosmic-ray produced neutron flux at the equator.

The suggestion that the energy of the optical emission in solar flares could be from the ionization losses of accelerated particles in the solar chromosphere was first made by Gordon (1954). Since the accelerated particles could also generate secondary neutrons and gamma rays when they interact with the solar atmosphere, Lingenfelter (1969) estimated the expected neutron and

TABLE 3.2

THE PRINCIPAL NEUTRON PRODUCING REACTIONS IN THE SOLAR ATMOSPHERE (LINGENFELTER AND RAMATY, 1967)

Reaction	Threshold Energy (MeV/nucleon)
$H^1(P,n\pi+)H^1$	292.3
$He^4(P,pn)He^3$	25.9
$He^4(P,2Pn)H^2$	32.8
$He^4(P,2P2n)H^1$	35.6
$C^{12}(P,n...$	19.8
$N^{14}(P,n...$	6.3
$O^{16}(P,pn...$	16.5
$Ne^{20}(P,pn...$	17.7

gamma ray fluxes at the earth per unit power dissipated by ionization losses of the accelerated solar particles as a function of the characteristic rigidity, P_o (Fig. 12). Comparing the available upper limit neutron and gamma ray fluxes with the fluxes predicted by his calculations, Lingenfelter (1969) concluded that the observations were consistent with the suggested model. However, he pointed out that more sensitive measurements of the solar neutron and gamma ray fluxes were needed to test his model.

Solar neutrons could decay in flight. The low-energy protons measured outside the magnetopause could be from the decay of solar neutrons. If, on the other hand, solar neutrons decay near the earth, the decay products could then be injected into the earth's radiation belts. Lingenfelter et al. (1965a,b) suggested that protons resulting from the decay of high-energy solar neutrons could be an important source for populating the radiation belts. Claflin and White (1970), using the Lingenfelter et al.(1965a,b) solar-cycle-averaged solar flare neutron flux at the earth and the Monte Carlo method of Dragt et al. (1966) to calculate the coefficient for injecting protons into the earth's radiation belt by solar neutron decay, found that the solar neutron decay (SND) injection exceeded CRAND

injection at L greater than about 2 and E = 30 MeV. These calculations, however, did not include the possible losses from pitch-angle diffusion and radial diffusion at higher energies and higher L values. Furthermore, there are no positive measurements of solar neutrons at the earth. Therefore, the calculations only stress the solar neutron decay injection ability.

3.3 The Search For Solar Neutrons

There are two general types of detectors for measuring solar neutrons: directional and omnidirectional detectors. Directional detectors are alternately pointed towards and away from the sun. The source is, therefore, uniquely identified; the minimum omnidirectional background atmospheric neutron flux provides a lower threshold for the discrete sources because the solar neutron flux is unidirectional. (n,p) elastic scattering is usually utilized. The neutron could scatter once in each of two large plastic scintillators (White, 1968). The energy of the incident neutron is assumed to be the sum of the recoil proton energy (measured) and the scattered neutron energy (calculated from the time of flight of the scattered neutron between the two hydrocarbon scintillators). Though it is very difficult to distinguish between elastic and inelastic reactions in the hydrocarbon,

White assumed elastic scattering in the first scintillator for the energy and direction determinations. To overcome this difficulty the neutron could be scattered twice in two spark chambers interleaved with plastic scintillator and polyethylene producer, the energy being determined from the path lengths of the recoil protons (Pinkau, 1966). However, the cross-sections of directional detectors decrease with increasing neutron energy. To obtain high efficiency, we must use an extremely large area for the detectors. This results in a very heavy and complicated detector.

The omnidirectional detectors described in Chapter 2.2 indicate the definite advantages of the He^3 proportional counter. However, in trying to achieve a low minimum detectable flux, great care must be taken in interpreting the measurements made with gamma-ray sensitive detectors such as the proton recoil detectors. The contribution of gamma-ray sources can no longer be neglected. The detector must detect neutrons selectively.

Solar neutrons have not yet been unambiguously measured. Haymes (1964) studied the diurnal effect on the 1-14 MeV energy neutron flux by using the proton recoil detector. With the atmospheric neutron spectrum for the solar neutron spectrum he accounted for the day to night ratio of $1.01 \pm .02$ by a quiet-time upper

limit solar neutron flux 0.02 n/cm^{2}sec. The Vela Satellite experiment of Bame and Asbridge (1966), utilizing the polyethylene moderated He^3 neutron counters, obtained an upper limit on the diurnal variations of the counting rate 0.1 cts/sec from which they derived the upper limit solar neutron flux 0.01 n/cm^2-sec from 0.1-10Mev or 0.1n/cm^2-sec for an average energy of about 55 MeV. They observed no solar neutrons for many solar flares which included two major ones. Hess and Kaifer (1967) also observed no solar neutrons for many flares that occurred between March and May 1962. They flew a moderated BF_3 neutron counter in the OSO-1 satellite. Since they observed no diurnal variation in the neutron counting rates they set an upper limit 2×10^{-3} n/cm^2-sec (10kev-10Mev) to the quiet-time solar neutron flux.

Apparao et al. (1966) conducted a balloon borne emulsion experiment which observed proton recoils from elastic collisions of neutrons with the hydrogen in the nuclear emulsions. The ratio of the downward neutron flux to the upward neutron flux at 10 gm/cm^2 was considered too large and the excess downward flux was attributed to the solar neutron flux $(4.65 \pm 1.90) \times 10^2$ ncm^{-2}sec^{-1} in the energy range 20-160 MeV. In a later experiment with a scintillator-spark chamber detector, Daniel et al. (1967) associated the count rate increase

to solar neutrons (50-500 MeV) from a 1N flare which occurred several hours after the increase. These interpretations have been questioned by Hess and Kaifer (1967) and by Holt (1967). Hess and Kaifer (1967) were dubious about the interpretations of Apparao et al. for the following reasons: (a) it was extremely difficult to pick out only events involving hydrogen nuclei in the emulsion, (b) the assumption that the neutron travelled in the direction of the observed knock-on proton could be wrong by as much as 90°, and (c) the closeness of the down/up ratio to unity did not necessarily imply solar neutrons. Eyles et al. (1972) substantiated this criticism. By using a series of directional telescopes, they set an upper limit $30 n/m^2 sec$ on the continuous solar neutron flux in the energy range 50 to 350 MeV and also showed that in the absence of solar neutrons the down/up ratio at 10mb is 2.0 ± 0.4. Holt (1967) used Roelof's (1966) ratio of solar neutrons to decay protons at 1AU to demonstrate that a flux which is 30% of that reported by Daniel et al. would have produced decay protons detectable by OGO-A if a flat neutron spectrum and no diffusion of protons in the interplanetary magnetic field were assumed. However, the OGO-A did not observe the protons. Daniel et al. (1971) reduced their previous result by a factor of 6, with no errors or confidence

limits, to be consistent with the OGO-A results though with the questionable assumptions of a flat spectrum and no diffusion.

Kim (1967) flew two emulsion stacks which separately pointed towards and away from the sun. From the null result he derived the continuous upper limit solar neutron flux 2.8×10^{-2} neutrons/cm^2-sec in 20-100 MeV energy range. Similar results were obtained by Forrest and Chupp (1969) who derived the quiet-time upper limit solar neutron flux 2×10^{-2} n/cm^2-sec in 15-120 MeV from the difference between the day and night counting rates. The measurements were made with a balloon-borne plastic scintillator surrounded by charged particle anticoincidence shield. They also derived the upper limit solar neutron flux 4×10^{-2} n/cm^2-sec for a 1 B flare. Cortellesa et al. (1970, 1971) made balloon flights with detectors similar to those used by Forrest and Chupp (1969). By comparing the day and night results, Cortellesa et al. obtained a continuous upper limit solar neutron flux 1.2×10^{-2} n/cm^2-sec in 45-300 MeV (1970) and 5.5×10^{-3} n/cm^2-sec in 10-200 MeV (1971).

Zyche and Frye (1969) measured upper limit solar neutron fluxes 1.0×10^{-2} n/cm^2-sec (39-55 MeV) and 1.7×10^{-2} n/cm^2-sec (18-25 MeV) for two flares of importance 1.

They used a balloon-borne spark chamber which recorded the protons recoiling in the hydrocarbon radiator. Another spark chamber experiment was performed by Heidbreder et al. (1970). Using the directional detector developed by Pinkau (1966), they derived a continuous solar neutron flux limit of 1.25×10^{-3} n/cm^2-sec in the energy range 100-400 MeV.

The solar neutron measurements have been more conveniently summarized in Figure 19 (Chapter 6.1) which compares all the observations and theoretical results. Included in this comparison is the balloon experiment by Webber and Ormes (1967), which used a charge particle telescope sensitive to 60-320 MeV secondary protons. The telescope periodically pointed at the sun through 12.9 gm/cm^2 of atmosphere. They pointed out that solar neutrons interacting in the atmosphere between the sun and the detector could have produced not more than 10^{-4} protons/cm^{2}sec ster. in the energy range 60-320 MeV. It appears that the efficiency with which they derived an upper limit solar neutron spectrum was a factor of 10 too large (Alsmiller and Boughner, 1968; Forrest and Chupp, 1969). However, the upper limit spectrum is still correct to within a factor of 2 because the count rate limits set were very conservative.

No solar neutron flux has yet been unambiguously identified. Only upper limits to the solar neutron flux have been set for the impulsive and steady state emission.

However, no measurement has ever set an upper limit to the solar neutron flux for a flare of importance greater than 2B. Therefore, more measurements are needed to test the suggested measurable solar neutron flux at the earth. Positive identification of solar neutrons could elucidate the processes in the solar atmosphere and could prove or disprove the solar neutron decay theory of injection. A measured lower upper limit to the solar neutron flux would furnish more constraints on the solar flare models.

CHAPTER IV

MEASUREMENT TECHNIQUE

4.1 The Choice of a Detector

We noted in Chapter 2.2 the definite advantages of the moderated He^3 neutron counter as an omnidirectional detector of neutrons. Among the exothermic nuclear reactions for detecting neutrons the He^3 reaction has the best energy resolution due to its lowest Q value; the reaction cross section is not only the largest but it is a smoothly varying function of the neutron energy; and it has no excited states which could produce an uncertainty in the available energy. Since proportional counters filled with helium and a quenching gas can be operated at high pressures at reasonable electrical potentials, efficiencies of the order of 70% (at low energies) are readily achieved with the He^3 reaction. Neutron measurements could be extended to higher energies by surrounding the He^3 counter with a moderating material. A charged particle anti-coincidence shield could also surround both the He^3 counter and the moderating material to minimize the local production of neutrons in the moderator material by energetic charged particles. The background correction to the He^3 gated neutron

counting rate results from the local interactions of cosmic rays escaping detection in the anti-coincidence guard counters and from highly ionizing charged particles entering the unguarded ends of the He^3 counter. But, as shown in Chapter 5 and Appendix B, this correction is extremely small (<4%). Though the slow-neutron counter systems have efficiencies for fast-neutron detection lower than the omnidirectional proton recoil detectors, they are virtually insensitive to γ rays which plague the proton-recoil detectors especially when we are trying to achieve a minimum detectable neutron flux such as solar neutrons. Moreover, omni-directional detectors are simpler, more efficient and flexible than directional detectors (Chap. 3.3). Thus, the moderated He^3 neutron detector surrounded by a charged particle anti-coincidence shield seems to be an appropriate detector for measuring neutrons in space though we have to pay the price of measuring only $\leq$ 10 MeV atmospheric neutrons and $\leq$ 20 MeV solar neutrons.

4.2 Instrumentation

The neutron sensor used for the experiment has been described by Lockwood et al. (1969), Jenkins et al. (1970,71), and Ifedili (1970). The detector (Fig. 13) consists of a cylindrical proportional counter filled

with ten atmospheres of He^3 and Krypton (a quenching gas) and detects neutrons through the reaction.

$$_2He^3 + {}_0n^1 \rightarrow {}_1H^1 + {}_1H^3 + 0.76 \text{ MeV}$$

The charged particle products, proton and tritium, are then detected by their ionization loss. A discrimination level was set at 0.14 MeV to exclude all γ-rays and He^3 recoils. As the cross-section for the above reaction is an inverse function of the neutron speed, the He^3 neutron counter is surrounded by a 1" thickness of NE102 plastic scintillator to slow down the fast neutrons for more efficient detection. In slowing down, the neutrons produce recoiling protons whose ionization loss results in a light output related to the original neutron energy. Most of the neutron energy is lost within 0.5μs and is seen as a single pulse by the electronic system which has an integration time constant of several μs. The mean life of neutrons in the moderating scintillator is nearly 10μs; therefore the pulse height distribution of scintillation events followed within 25 μs by a He^3 counter event is related to the neutron energy distribution for the He^3 counter event.

The amplitude of the He^3 coincident scintillations are monitored by an RCA7151Q photomultiplier tube. The photomultiplier tube was mounted on a conical

lucite light-pipe placed at the end of the cylindrical plastic scintillator. The output of the voltage amplifier from the photomultiplier section of the sensor drives six pulse height discriminators. The lower five discriminators formed four differential channels of pulse height analysis. The pulse height determines which one of the four 25μs one-shot multivibrators is set. When a pulse from the gated neutron channel is received within 25μs it is sent to the scintillator output counter corresponding to the one-shot that was set. If there is no pulse within 25μs, the one-shot returns to zero and the gates are closed.

The gain of the analyzer is kept constant by using the upper level discriminators. To do this a light pulser, consisting of an americium doped sodium iodide crystal, was embedded in the plastic scintillator using the optical coupling material RTV615. The light pulser produces a sharply peaked symmetric (∿10%FWHM) light output distribution corresponding to alpha decay of the Am^{241} and the subsequent scintillation of the NaI crystal. The photomultiplier thus sees a light pulse distribution corresponding to events in the moderating scintillator and the light pulser events with a larger amplitude and a much higher count rate than the moderating scintillator events of similar amplitude.

The photomultiplier voltage pulses are fed into the scintillator pulse-height analyzer (PHA) and also into a two-discriminator system, E and F, which splits the light pulser distribution. The outputs E-F and F are sent into the ratemeters, then to a difference amplifier. The recoupling of the discriminator biases to the difference amplifier in such a way that a higher rate (lower rate) in E-F than F causes the biases to decrease (increase) results in equal counts in E-F and F. The allowed ratemeter output ranges cause the above condition to correspond to when the F discriminator is centered on the peak of the light pulse output distribution. The discriminators in the PHA (A,B,C,D) and the self-adjusting system (E,F) are set proportional to one another through a resistor network. Thus the self-adjusting system permits the discriminators to be set in terms of the light received by the photomultiplier tube and to be unaffected by the gain changes in the photomultiplier tube and amplifiers. Since the light pulser has an average known pulse rate of approximately 250 pulses/sec, the approximate amplitude of the voltages on the storage capacitor can be determined before hand and thus the system could not lock on a peak different from the light pulser peak.

Surrounding the scintillator is a ring of 22 proportional counters that acts as an anti-coincidence shield against charged particles in the cosmic rays that could produce local neutrons in the moderator or in any other material near the He^3 counter. These guard counters are arranged in four banks A, B, C, D. In the first mode the signals from the four banks are summed, A+B+C+D, to trigger the gate which turns off the neutron counter for 100 μs, about 10 lifetimes of the neutrons in the sensor. In the second mode the signals are put into coincidence pairs A-C and B-D, the anti-coincidence gate being produced by more energetic particles.

To check the voltage discriminator levels of the guard counter and neutron channels is an in-flight calibrator (IFC) which generates precision amplitude pulses and cycles every 100 minutes. There are sixteen steps in the IFC cycle. After being amplified by the charge sensitive preamplifiers and the voltage amplifiers the pulses are sent down a 50 ohm coaxial cable to the pulse height discriminators, first to the guard channels for two main frames, then to the neutron channel for one main frame, and back to the guard channels. The pulses are varied in amplitude from 130% to 70% of the original threshold level of the discriminators. Any change in the amplifier gain, either charge sensitive

preamplifiers or voltage amplifiers or a change in the discriminator level of the pulse height discriminator will cause a change in the pulse needed to trigger the discriminator. For the duration of the experiment, June 7 to December 23, the IFC system indicated that the discriminator levels to the guard channels 1,3,2,4, and neutron counter increased by only 0.8%, 0.8%, 1.1%, 1.1% and 0.7% respectively.

The total neutron counter output, the gated neutron output, the scintillator output, the coincidence rates A-C and B-D and the total charged-particle counting rate, A+B+C+D, are fed into the spacecraft experiment words 1,4,6,2,3 and 5 respectively (Fig. 14). The spacecraft subcommutator analog word 86 is a logarithmic counting ratemeter since very high counting rates are expected in the radiation belts. The total neutron counter, the coincidence guard counters, the gated neutron counter, the total charged particle counter and the scintillator counter have a read-out time in ms (capacity in counts) of 288 (703), 576 (703), 288 (255), 144 (2749), and 288 (3) respectively.

Figure 13 shows the components of the neutron sensor and its orientation with respect to the spacecraft and the earth. The neutron sensor, which weighs 5.7 lbs. with dimensions 12 3/8 in. long and 4 3/8 in.

diameter, is covered with a highly reflective aluminized mylar 1 mil. thick and wrapped with a light-tight adhesive tape. It is placed on the EP-5 boom seventeen feet from the main body of the satellite to minimize the contributions from local neutrons produced by the interaction of cosmic rays with the satellite.

4.3 Calibration of the Neutron Detector

The neutron sensor was calibrated by exposing it to known fluxes of neutrons from monoenergetic neutrons in the range 5 KeV to 20 MeV obtained in the reactions $Sc^{45}(p,n)Ti^{45}$, $H^3(p,n)He^3$, $H^2(d,n)He^3$ and $H^3(d,n)He^4$ using the 5.5 MeV Van der Graaf accelerator at the Oak Ridge National Laboratories. For each monoenergetic reaction the neutron energy was varied by varying the energy of the incident beam and the neutron emission angles, ϕ, with respect to the incident beam. The Atomic Energy Commission report (ORNL-2574,1959) contains tables of product particles energies and angles in the Laboratory and Center-of-mass systems as functions of input energy. Table 4.1 lists the pertinent information on the calibration of the OGO-VI neutron sensor with the monoenergetic neutrons.

For each neutron energy there were four sets of runs: OGO-VI sensor placed 1 meter and 2 meters from

TABLE 4.1

Reactions	Q Value	Target thickness	Incident beam energy range	Neutron Emission angle range, θ	Neutron energy range
Sc^{45} (p,n)Ti^{45}	(lab. threshold energy = 2.908 MeV)	1 mg/cm^2 Scandium	2.96-3.48 MeV	0°	5-570 KeV
H^3 (p,n)He^3	-0.764 MeV (lab. threshold energy = 1.019 MeV)	1 mg/cm^2 tritium	1.80-4.77 MeV	0°	1.0-4.0 MeV
H^2 (d,n)He^3	+3.266 MeV	5 mg/cm^2 deuterium	1.77-6.00 MeV	0°	5.0-9.20 MeV
H^3 (d,n)He^4	+17.586 MeV	7.5 mg/cm^2 tritium	1.0-4.1 MeV	0°-150°	12.17-20 MeV

the target, and the UNH long counter (Hanson and McKibben, 1947; Marion and Fowler, 1960; Friling, 1964) subsequently placed in the same positions as the OGO-VI neutron sensor. Using the known UNH long counter efficiency as a function of neutron energy, the neutron flux was determined. The Oak Ridge long counter was also used as a neutron flux monitor but was placed at a fixed position for all the runs; it provided a means of determining the scattered neutron flux. The detailed calculations are in Appendix C.

Figure 15 is the neutron detector efficiency for events in the He^3 counter as a function of energy for an isotropic neutron flux. Tatsuta et al. (1965) had used cylindrical paraffin-moderated BF_3 counters to obtain efficiency as a function of energy for different thicknesses of the moderator. When we interpolated his results to derive a neutron efficiency as a function of energy for an amount of hydrogen per unit length of moderator equal to that of the OGO-VI, we found that the derived curve agreed with our measurements as in Figure 15. We, therefore, extrapolated the neutron efficiency for the detector to lower energies using the measurements of Tatsuta et al.

The detector efficiency curve was further checked with neutron fluxes from Am^{241}-Li, Am^{241}-Be, and Am^{241}-Be

mock fission radioactive sources. For this calibration the source and the OGO-VI neutron detector were suspended in air at least 15 feet from the ground and nearby objects to minimize the contribution from scattered neutrons. The contribution from scattered neutrons was evaluated by varying the distance from the ground of both the sources and the detector. Using the observed variation of the monoenergetic neutron efficiency with energy, $\varepsilon(E)$, and the neutron energy distribution $N(E)$, for the Am^{241}-Be, Am^{241}-Li, and Am^{241}-mock fission neutron sources (Hansen, 1960; Geiger and Hargrove, 1964), the efficiencies expected for these radioactive sources were calculated as

$$\langle \varepsilon \rangle = \frac{\int \varepsilon(E) N(E) dE}{\int N(E) dE}$$

The measured efficiencies for the radioactive sources were plotted in Figure 15 at neutron energies corresponding to the calculated efficiencies on the monoenergetic curve. The efficiencies from radioactive sources are in good agreement with those obtained from the monoenergetic neutron measurements.

Similarly the efficiencies for the four scintillator channels (PHA1,2,3,4) are plotted in Fig. 16. The finite efficiences above 10 MeV (upper discriminator levels set below 10 MeV energy loss) are due to the

contribution from the inelastic carbon collisions to the slowing down of higher-energy neutrons in the scintillator.

Figure 17 shows the variation of the detector efficiency with the incident angle of the neutron flux. This was obtained using neutrons from the Am^{241}-Li source of energy $\langle E_n \rangle$ = 390 kev, and the reaction $H^3(d,n)He^4$ of E_n = 14 MeV. We observe that this angular variation does not depend on the energy of the incident neutron flux. The efficiency for neutrons incident parallel to the axis of symmetry of the detector, ε_{11}, is 0.4 times $\varepsilon_{\perp}$, the efficiency for neutrons incident perpendicular to this axis of symmetry. The efficiency for isotropic neutron flux, ε, obtained by using cylindrical symmetry and integrating over the detector, is 0.835 times $\varepsilon_{\perp}$. This fact was used to convert the efficiencies obtained with monoenergetic neutrons incident perpendicular to the axis of symmetry of the detector into the absolute efficiencies for isotropically incident neutron fluxes plotted in Figures 15 and 16.

CHAPTER V

DATA ANALYSIS

The mean efficiency for the albedo neutron flux was obtained by folding the neutron efficiency curve for the UNH detector (Figure 15) into the albedo neutron energy spectrum for the present level of solar activity calculated by Lingenfelter (1963) and also by Newkirk (1963), Lingenfelter and Flamm (1964), and Lingenfelter and Ramaty (1967). Suppose the differential neutron flux in neutrons /cm^2sec MeV is J(E) and the measured efficiency of the detector in counts/(n/cm^2)is $\varepsilon(E)$, then the mean efficiency for the albedo neutron flux is

$$\langle \varepsilon \rangle = \int J(E)\ \varepsilon(E)dE / \int J(E)dE$$

The mean detector efficiencies of $1.59 \pm 0.16 cm^2$, $1.30 \pm 0.13 cm^2$ and $1.08 \pm 0.11 cm^2$ were thus obtained from the Lingenfelter, Newkirk, and Lingenfelter and Flamm spectra respectively. For the Lingenfelter and Ramaty spectrum the mean efficiency for solar neutrons perpendicularly incident on the neutron detector is $0.38 cm^2$ and $0.37 cm^2$ for P_o = 60MV and P_o = 125MV respectively. The relative contributions to the neutron counting rate for the Lingenfelter and Newkirk neutron leakage spectra are also given in Table 5 where it is observed that

TABLE 5.1

Neutron Energy (ev)	Percentage of Neutron Counting Rate	
	Lingenfelter (1963) Spectrum	Newkirk (1963) Spectrum
$<10^1$	2.3	4.7
10^1-10^2	4.2	6.0
10^2-10^3	6.7	8.0
10^3-10^4	10.8	13.4
10^4-10^5	16.3	15.2
10^5-10^6	47.4	33.8
10^6-10^7	11.5	16.3
$>10^7$	0.8	2.6
Mean detector efficiency for an isotropic flux	1.59±0.16cm^2	1.30±0.13cm^2

for the Lingenfelter and Newkirk spectra the He^3 detector measures mostly neutrons that lie in the energy range 10^4 to 10^6 ev, with about 19% above 1 MeV and about 16% in the 1-10 MeV range.

With the mean efficiency the neutron flux can be obtained from the neutron counting rates measured by the neutron detector on board the Orbiting Geophysical Observatory (OGO-VI), a polar-orbiting satellite with altitudes between 400 and 1100 km. The minimum values of the charged particle counting rates for all vertical cut-off rigidity and altitude showed only a rigidity dependence with the polar and low latitude counting rates in the ratio of 4.3/1. Therefore, to minimize the contributions from local production, the neutron counting rates corresponding to charged particle rates in excess of 1.5 times the minimum values for that vertical cut-off rigidity were excluded from the analysis. Data from the regions near the Capetown and Brazilian anomalies in the geomagnetic field were also excluded from the analysis. The anomalies could lower the inner radiation belt into the higher altitude portions of the OGO-VI orbit. The data acquired during the occasional excursions of the OGO-VI satellite into the horns of the outer radiation belt were automatically removed

by the sorting program due to the high charged particle rates in this region. The gated neutron counting rates for June 7 to December 23, 1969 were then sorted according to vertical cutoff rigidity (Shea et al., 1968) and altitude into 18 vertical cutoff rigidity intervals by 7 altitude ranges. Vertical cutoff rigidity was considered to be an appropriate parameter for sorting the neutron counting rates since the neutron source function depends in a unique way upon vertical cutoff rigidity (Rossi and Olbert, 1970).

The counting rates were corrected for dead time using the relation $N'_G \pm \Delta N'_G = (N_G \pm \Delta N_G) \exp(10^{-4}n)$. Recall that the guard counters initiate pulses that turn off the gated neutron counter for 100 μs. This turn-off is such that turn-on occurs 100 μs after the last guard counter event. The turn-off time for any one guard counter event is $t_d = t$ when a second event occurs within $t < 100\mu s$ of the guard counter event; it is $t_d = 100$ μs when no such event occurs within 100 μs. The time distribution of "second events" is proportional to e^{-nt} using Poisson distribution, where n is the guard counter rate. The mean dead time per event is then

$$\bar{t}_d = \left(\int_0^{100\mu s} te^{-nt}\,dt + \int_{100\mu s}^{\infty} 100\mu s\; e^{-nt}dt\right)\Big/\int_0^{\infty} e^{-nt}dt$$

$$= \left(\left[-\left(\frac{t}{n}+\frac{1}{n^2}\right)e^{-nt}\right]_0^{100\mu s} + 100\mu s \left[-\frac{1}{n}e^{-nt}\right]_{100\mu s}^{\infty} \right)\Big/\left(-\frac{1}{n}e^{-nt}\right)_0^{\infty}$$

$$= \frac{1}{n}(1-e^{-100n}) \text{ microseconds where } n \text{ is counts/microsec.}$$

Check: If n is small, then $\frac{1}{n}\left[1-(1-100n)\right] = 100$ microsec.

Total dead time $= n\bar{t}_d = 1-e^{-10^{-4}n}$ sec.

Life time $= 1-n\bar{t}_d = e^{-10^{-4}n}$ sec.

$\therefore$ the correction factor $\dfrac{1}{e^{-10^{-4}n}} = e^{10^{-4}n}$ where n is charged particle counts/sec.

The gated neutrons were also corrected for local production and for non-neutron events. Background neutrons could result from the interactions of cosmic-ray particles with the mainbody of the spacecraft, with the other experiments on the EP5 boom which carries the neutron sensor, and with the material in the sensor (photomultipliers, moderator, electronic circuits) which surrounds the OGO-VI neutron detector. These targets were reduced to equivalent aluminum spheres of the same mass or equivalent spherical shell of aluminum of the same mass and surface area as the targets. Let the cosmic-ray flux incident on the target be ϕ(Webber, 1967), the

probability of interaction of cosmic ray particle in the target be ν (Chen et al., 1955), the evaporation neutrons produced per inelastic collision be n(E) (Dostrovsky et al., 1958; Bercovitch et al., 1960; Metropolis et al., 1958), then the background neutron rate is

$$N = \phi \nu n(E) \frac{\Omega}{4\pi} \varepsilon$$

where Ω is the solid angle subtended at the detector by the target, ε is the detector neutron efficiency.

$$\varepsilon_{11} = \begin{cases} 0.4\varepsilon_1 \text{ for a far source} \\ \varepsilon_1(1-0.6\frac{d}{D}) \text{ for a source close to the neutron detector,} \end{cases}$$

where D is the thickness of the sensor material adjacent to the detector and d is the distance from the neutron source to the detector. The non-neutron events contributing to the He^3 counting rate could be slow moving primary cosmic-ray protons, slow moving primary cosmic-ray alpha particles, primary cosmic-rays with z>2, shower particles due to protons or alpha interactions in the surrounding aluminum shell or moderator or electronics, shower particles from cosmic rays with z>2 and evaporation protons from inelastic collisions of the primary cosmic radiation in the surrounding moderator material. Any particle which loses more than about 0.14 MeV in the He^3 counter is counted. The contributions from each of these events (except for the

evaporation protons) were estimated by using the published flux of protons (McDonald and Ludwig, 1964), alpha particles (Balasubrahmanyan et al., 1965), cosmic rays with z>2 (Anand et al., 1965) and the range-energy curves (Ritson, 1961). Let the cosmic ray flux be ϕ (part/cm^2 sec), the carbon-atom density in the scintillator be ρ, the inelastic cross-section be σ(Alsmiller et al., 1967) and the number of evaporation protons per inelastic collision be n(E)dE (Alsmiller et al., 1967) then the number of evaporation protons being erroneously counted by the neutron detector is

$$\int \phi \rho \sigma \, n(E) \, dE \, dV \, \frac{d\Omega}{4\pi} \, K$$

where d Ω is the solid angle subtended at the detector by the source and

$$K = \begin{cases} 0 \text{ if proton direction or range does not intersect the } He^3 \text{ counter} \\ 1 \text{ otherwise} \end{cases}$$

This integral was evaluated using cyclindircal symmetry. The total correction applied to the He^3 counter gated-neutron counting rate was approximately 4%. The total correction to the gated neutron rates and the scintillator channels as a function of geomagnetic cut-off is shown in Figure 18. Appendix B gives the detailed calculations of the contributions from local production and non-neutron events.

We obtained the albedo neutron flux at the top of the atmosphere by reducing the observed neutron rate

between 400 and 500 km to the top of the atmosphere, 50 km, using the calculated altitude dependence expected for an isotropic neutron flux distribution at the top of the atmosphere (Chap. 8.2). The counting rate at 50 km, $N''_G(50)$, was converted to the leakage flux, using the relationship $\phi_L = \frac{0.5N''_G(50)}{\bar{\varepsilon}}$ for a 2π-isotropic neutron flux distribution, where $\bar{\varepsilon}$ is the mean efficiency (Haymes, 1964; Holt et al., 1966). Let $F(\mu)\, d\mu$ be the number of neutrons/second crossing a unit area perpendicularly, with direction cosines with respect to the vertical between μ and $\mu + d\mu$ (Hess et al., 1961). The counting rate is then given by

$$N''_G(50) = \int \varepsilon F(\mu) d\mu$$

$$= \int_0^1 \bar{\varepsilon} F_0 d_\mu \text{ for a } 2\pi \text{ -isotropic neutron flux distribution}$$

$$= \bar{\varepsilon} F_0 \text{ where } F_0 \text{ is the neutron scalar flux}$$

The neutron leakage flux is taken to be the number of neutrons crossing an area of 1 cm^2 at the top of the atmosphere. The area is taken parallel to the surface of the earth (Lingenfelter, 1963). The area presented by the 1 cm^2 to $F(\mu)$ is equal to the projection in the direction $\cos^{-1}(\mu)$, which is μ cm^2. The total leakage flux is then

$$\phi_L = \int_0^1 \mu F(\mu) d\mu = \int_0^1 F_o \mu d\mu = \frac{F_o}{2}$$

$$\therefore N''_G(50) = \bar{\varepsilon} F_o = 2 \bar{\varepsilon} \phi_L$$

$$\therefore \phi_L = \frac{0.5 N''_G(50)}{\bar{\varepsilon}}$$

CHAPTER VI

RESULTS AND DISCUSSION OF A SEARCH FOR SOLAR NEUTRONS

6.1 Neutrons from the Quiet Sun

A summary of the results discussed in this section will be published in Solar Physics, 1972. The neutron counting rates were derived from those events in the He^3 proportional counter not associated with events in the charged-particle guard counters. This is referred to as the "gated" neutron counting rate. For this analysis no correction was made for background events in the He^3 counter because differences in counting rates rather than absolute counting rates were used. In any case this background rate was only about 3% at the equator (Jenkins et al., 1970, 1971). Any contributions from locally produced neutrons in the OGO-VI spacecraft were calculated to be less than 4% (Appendix B).

The data for June 7, 1969, to December 23, 1969, inclusive were first sorted according to spacecraft location. As indicated in Chapter 5 the neutron rates corresponding to charged particle rates in excess of 1.5 times the minimum values for that rigidity were

excluded in the analyses. The gated neutron counting rates were then sorted according to vertical cutoff rigidity and altitude into 18 vertical cutoff rigidity intervals for seven different altitude ranges. The calculated cutoff rigidity values of Shea et al. (1968) were used in this sorting. Data from the regions near the Capetown and Brazilian anomalies in the geomagnetic field were excluded from the analysis. We also eliminated data for those days on which solar particle events were reported by detectors on Explorer 41, Pioneer 8 and Pioneer 9. The analysis for solar neutrons was restricted to only the equatorial regions for which the vertical cutoff rigidity at the earth's surface is $\geq$14 Gv. This restriction minimized the problems due to intensity - time variations and neutrons produced in the atmosphere at high latitudes by solar protons during any solar flare events which might not have been excluded. Finally, the neutron data were selected from altitudes less than 900 Km to remove neutron production effects by the energetic protons trapped in the inner radiation belt.

The differences between the neutron counting rates for the detector on the sun-ward side ("day") and for the detector completely eclipsed by the earth ("night") are listed in Table 6.1 for low altitudes and

TABLE 6.1

DIFFERENCES IN "DAY" AND "NIGHT" NEUTRON COUNTING RATES

Rigidity Interval (GV)	Average Geo-Mag. Lat. (0)	Altitude (KM)	Counting Rates(/Sec) Day	Night	Difference
14 - 16	7.5	400-500	0.14344±0.00094	0.14670±0.00220	-0.0033±0.0024
> 16	0	400-500	0.1200 ±0.0013	0.1178 ±0.0021	+0.0022±0.0024
14 - 16	7.5	500-600	0.1372 ±0.0013	0.1417 ±0.0029	-0.0045±0.0032
> 16	0	500-600	0.1129 ±0.0016	0.1177 ±0.0031	-0.0047±0.0035
14 - 16	7.5	600-700	0.1338 ±0.0014	0.1340 ±0.0025	-0.0002±0.0029
> 16	0	600-700	0.1102 ±0.0017	0.1104 ±0.0030	-0.0001^{5}±0.0035
14 - 16	7.5	700-800	0.1247 ±0.0016	0.1219 ±0.0021	+0.0028±0.0026
> 16	0	700-800	0.1059 ±0.0019	0.1054 ±0.0024	+0.0006±0.0031
14 - 16	7.5	800-900	0.1197 ±0.0018	0.1176 ±0.0019	+0.0021±0.0026
> 16	0	800-900	0.1012 ±0.0022	0.1003 ±0.0022	+0.0009±0.0030

high cutoff rigidities. The errors listed are statistical and are equal to the square root of the counting rate divided by the time of measurements. There are no statistically significant differences between the two counting rates. From these data the weighted average solar neutron rate $\bar{n}_s$ in the 1-20 MeV energy range is

$$\bar{n}_s = \frac{\sum_{i=1}^{N} \frac{n_i}{\sigma_i^2}}{\sum \frac{1}{\sigma_i^2}} \pm \sqrt{\frac{\sum_{i=1}^{N} \sigma_i^2}{N}} \qquad (1)$$

$$= (-1.54 \pm 9.30) \times 10^{-4}/\text{sec}$$

Therefore, the upper limit to the continuous solar neutron rate is 1.86×10^{-3}/sec at the 95% confidence level. This limit is reduced by less than 3% for a sorting into a smaller altitude interval.

The resulting upper limit continuous solar neutron flux F can be calculated from

$$F \leq \frac{1.86 \times 10^{-3}}{C\,\bar{\epsilon}} /\text{cm}^2\ \text{sec} \qquad (2)$$

C is a factor which depends upon the assumed angular distribution for the neutrons incident on the detector. The mean efficiency $\bar{\epsilon}$ in cm^2 was obtained by folding the efficiency $\epsilon(E_n)$ for neutrons incident perpendicular to the axis of symmetry of the detector into a solar neutron energy spectrum of the shape calculated by Lingenfelter and Ramaty (1967). The shape of the solar

neutron energy spectrum at earth depends upon the solar charged-particle spectrum which is given by $dJ/dP = (dJ/dP)_0 \exp(-P/P_0)$ where P is the particle rigidity and P_0 is the characteristic rigidity which varies from event to event (Freier and Webber, 1963). Differential solar neutron energy spectra for P_0 ranging from 60 to 400 MV have been presented by Lingenfelter and Ramaty (1967). If this differential neutron spectrum is taken to be of the form n(E) neutrons/cm^2 sec MeV, then the mean efficiency is given by

$$\bar{\varepsilon} = \int n(E)\varepsilon(E)dE / \int n(E)dE. \qquad (3)$$

The mean efficiencies for spectra with P_0 = 60 MV and P_0 = 125 MV are calculated to be respectively 0.38 cm^2 and 0.37 cm^2, about 20% larger than for an isotropic flux. If neutrons are incident perpendicular to the axis of symmetry, then C = 1. Therefore, at the 95% confidence level, the upper limit to the integral solar neutron flux in the energy range 1-20 MeV is 4.9×10^{-3}/cm^{2}sec for P_0 = 60 MV. The neutron energy range is defined by the low-energy shape of the solar neutron energy spectrum which decreases rapidly at lower neutron energies because the survival probability of the low energy neutrons is small.

If there are any solar neutrons, then this upper limit to the measured direct solar neutron flux

must be corrected for the atmospheric neutron leakage flux arising from the interaction of solar neutrons with the earth's atmosphere. This correction is carried out as follows. Let the total solar neutron count rate be $N = N_A + N_D$, where the subscript A refers to the contribution from atmospheric leakage and D to the contribution from solar neutrons directly incident on the detector. The calculations of Alsmiller and Boughner (1968) for the differential neutron flux (neutrons/cm^2 sec MeV) produced at various depths in the atmosphere by solar flare neutrons can be used to estimate the resulting neutron leakage flux. For these calculations the characteristic rigidity was taken to be 125MV and the integrated proton flux at the earth was 1.4×10^9 protons/cm^2 with energy greater than 30 MeV. These results can be converted to apply to a characteristic rigidity $P_o = 60$ MV using the predictions of Lingenfelter et al.(1965b). The resulting neutron flux per unit energy versus energy at different atmospheric depths has the same spectral shape, in the neutron energy range 0.5-20 MeV, as the neutron energy spectrum calculated by Hess et al. (1961) for cosmic-ray neutron production. The magnitude of the neutron flux produced in the atmosphere is of no consequence since it is directly proportional to the assumed proton

flux (Asmiller and Boughner, 1968), and hence only a constant scaling factor is needed to convert the flux to correspond to a smaller flare or to the quiet-time solar neutron flux. Then, the corresponding solar neutron fluxes (see equation 2) in the energy interval covered by the OGO-VI detector are: $F_D = N_D/\overline{\epsilon_D}$ and $F_A = N_A/\overline{2\epsilon}_A$, since C = 2 for a flux isotropic over a hemisphere. Putting $F_A = a F_D$,

$$F_D = \frac{\overline{\epsilon}_D}{2a\,\overline{\epsilon}_A + \overline{\epsilon}_D} \frac{N}{\overline{\epsilon}_D} \qquad (4)$$

Now, since the OGO-VI detector responds principally to direct solar neutrons with energies 1-20 MeV, $F_D = F_T$ $(\int^{20} J(E)dE/ \int_1^{\infty} J(E)dE) = 0.267F_T$. F_T is the total integral incident solar neutron flux with a differential energy spectrum J(E) given by Lingenfelter and Ramaty (1967) for P_o = 60 MV. The incident solar neutron flux F_T gives rise to an atmospheric neutron source F_N at small atmospheric depths, of which a fraction $r = (F_A{}^T)/F_N$ leaks out of the atmosphere. Of the total solar neutron leakage $F_A{}^T$, the OGO-VI detector responds to a flux F_A from 10 keV-10 MeV. Putting $b = F_A/F_A{}^T$, then F_A (10 keV-10 MeV) $= b\,F_A{}^T = br\,F_N = brn\,F_T = \frac{brn}{0.267} F_D = a\,F_D$. Assuming the neutron spectral shape

for the leakage flux to be the same as given by Hess et al. (1961), b = 0.94 at the geomagnetic equator for the period in the solar cycle corresponding to that for these measurements. For this spectrum r is estimated to be 5 < r < 10% (Lingenfelter, 1963). Taking the smallest value of n = 1 to yield the highest upper limit to F_D, a = 0.25. For this neutron leakage spectrum $\bar{\varepsilon}_A$ = 1.35 cm^2. Therefore, the corrected upper limit to the quiet time solar neutron flux from equation (4) is

$$F_D = 0.363 \frac{N}{\bar{\varepsilon}_D} = 1.8 \times 10^{-3} n/cm^2 \text{ sec}$$

In evaluating the solar neutron leakage flux from the atmosphere the contributions from neutrons with E_n <0.5 MeV were assumed to be given by the spectral shape of Hess et al. (1961). Actually, the spectrum of Alsmiller and Boughner (1968) is still richer in neutrons below 0.5 MeV. For the latter spectrum the upper limit is reduced by about 10%. Such an extrapolation is not included in the upper limit placed on the solar neutron flux by the OGO-VI measurements.

The upper limit to the "quiet-time" integral solar neutron flux deduced here is comparable to the value of $\leq 2 \times 10^{-3}$ cm/sec^2 in the 1-10 MeV range obtained by Hess and Kaifer (1967). Upper limits

to the solar neutron flux have also been set by Zych and Frye (1969), Kim (1967), Forrest and Chupp (1968), and Cortellessa et al. (1971), but at much higher energies from 10 to 200 MeV. For comparison with other measurements the OGO-VI result was converted to a differential flux by folding the energy dependent response function into the shape of the solar neutron energy spectrum calculated by Lingenfelter and Ramaty (1967) for a characteristic rigidity P_o = 60 MV. For characteristic rigidities greater than 60 MV the limiting fluxes will be smaller. These results are shown in Figure 19. Where only integral solar neutron intensities were measured, e.g., Hess and Kaifer (1967), the results have been converted to a differential neutron spectrum using the spectral shape presented by Lingenfelter and Ramaty (1967) and the known energy dependent response functions. At lower energies the OGO-VI result has the lowest experimental upper limit for the continuous emission of solar neutrons in the 1-20 MeV neutron energy range.

The OGO-VI solar neutron results should be compared with the recent higher energy results of Cortellessa et al. (1971), the limits set

by Heidbreder et al. (1970) and Eyles et al. (1971,72) and the earlier measurements by Webber and Ormes (1967), all of which are shown in Figure 19. In the energy range 20-350 MeV the new limits set by Cortellessa et al. (1971) and Eyles et al. (1972) are within a factor of two of the upper limits previously set, which is very consistent agreement. In the 2-20 MeV the OGO-6 solar neutron results set an order of magnitude lower upper limit than the measurements of Forrest and Chupp (1969) and Cortellessa et al. (1971) in the overlapping energy range.

The lowest measurements in Figure 19 are about comparable to the time-average intensity of the solar neutron flux from the many flares occurring during the last solar cycle 1954-1965 as calculated by Lingenfelter et al. (1965b). At 40 MeV this estimated flux was $\sim 2 \times 10^{-5}$ neutrons/cm^2 sec MeV. Since the solar activity in the present cycle (1965 to 1974) is considerably less than the preceding one, the time-average intensity should be considerably less. This time-average intensity is still more than an order of magnitude greater than the theoretical upper limit obtained by Roelof (1966) based upon the IMP-1 protons, assuming all the protons resulted from neutron decays and the protons suffered

isotropic diffusion. This suggests that the current measurements are predominately just background measurements. A comparison of the solar neutron flux to the atmospheric neutron flux supports this conclusion. At the geomagnetic equator for neutron energies $E_n > 50$ MeV both the solar and atmospheric neutron spectra have a similar energy dependence and magnitude if Lingenfelter et al. (1965) time-averaged values for solar neutrons are used. For $5 < E_n < 50$ MeV the atmospheric neutron flux is <u>two</u> orders of magnitude greater. Indeed, recent atmospheric neutron measurements by Simnett (1971) indicate a spectral shape which is relatively flat from 10 MeV to 50 MeV then decreasing as E^{-2} for $E_n > 50$ MeV. This would make it difficult to separate the two neutron sources by studies of the spectral shape at lower energies.

More meaningful upper limits on the solar neutron flux can only be determined by neutron detectors with much larger geometrical factors, better efficiency and directionality to reduce the background of atmospheric neutrons. Large detecting systems which do not separate neutron produced events from the background of gamma-ray interactions and other sources cannot provide more significant limits to the solar neutron flux unless detailed statistical analyses of the background counting

rates are made to eliminate any possible fluctuations, as done in the analysis of Forrest and Chupp (1969).

We conclude that the quiet-time solar neutron flux from 1-20 MeV cannot be greater than $1.8 \times 10^{-3} n/cm^2$ sec at the 95% confidence level. This estimate is based upon a solar charged particle spectrum with a characteristic rigidity $P_o = 60$ MV.

6.2 Neutron Emission During Solar Flares

During the operational period of the experiment from June 7 to December 23, 1969 several flares occured. No solar neutron flux was positively identified during these flares and hence only upper limits to the solar neutron flux are discussed for some of these flares. The results are compared with the Lingenfelter (1969) and Lingenfelter and Ramaty (1967) models for the solar neutron production during solar flares.

The details of the optical observations, X-ray bursts and proton emission are given in Tables 6.2, 6.3, and 6.4 respectively. Figure 20 shows the large flux of solar protons measured by Explorer 41 during the Solar proton event of November 2, 1969. These are the Solar-Geophysical data of the Environmental Science Service Administration (ESSA) Boulder, Colorado. We observe that the November 2 flare was a strong electron and proton emitter. In fact, this event reached the largest peak absorption 14.5db at 30 mHz during this solar cycle (Masley et al., 1971). We estimated the characteristic rigidity, P_o , for this event by using the solar Proton energy spectrum of McDonnell Douglas experiment on-board the OGO-VI satellite.

TABLE 6.2

OPTICAL ACTIVITY

Optical Flare(1969)	Importance	Position	Onset Time(ut)	End (ut)	Time of Max(ut)
June 13	3B	S24E69	15.49	20.00	16.33
June 15	2N -2B	S17W77	08.31	08.50	08.40
Sept 25	2N -3N	N14W14	07.00	08.53	07.24
Nov 02	3B	N22W90	10.28	11.57	11.39
Dec 19	1N -2F	N10W08	12.01	12.40	12.20

TABLE 6.3

X-RAY BURSTS

Date (1969)	Start time (ut)	0.5-3Å 10^{-5}ergscm^{-2}sec^{-1}		1-8Å 10^{-4}ergs cm^{-2}sec^{-1}			8-20Å 10^{-3}ergs cm^{-2}sec^{-1}			
		Peak flux	Peak time (ut)	Peak flux	Peak time (ut)	Quiet time HrAv flux	Peak flux	Peak time (ut)	Quiet time HrAv flux	End time
June 13	15.48	40.00	17.20	300.00	17.37	18.2	160.00	17.49	29.4	01.50
Sept 25	07.02	5.60	07.32	59.00	07.42	15.3	53.00	07.43	18.0	09.22
Nov 02	09.49	130.00	12.01	3000.00	11.00	14.2	710.00	11.08	15.6	20.06

TABLE 6.4

SOLAR PROTON EMISSION (EXPLORER 41)

Date(1969)	Solar Proton Flux (ster $cm^2 sec)^{-1}$			Peak time
	>60MeV	>30MeV	>10MeV	
Sept 25	0.2	1	15	∿11.00
Nov 02	39	257	1437	12.00-13.00
Dec 20	0.6	1.1	8.3	∿01.00

TABLE 6.5

(JUNE 13)

Time	Geomagnetic Latitude Degrees	Alti-tude km	Counting Rate cts/sec	Monthly Average cts/sec	Counting Rate Difference cts/sec
16h 40m 39s	15.1	891	0.072±0.036	0.130±0.005	-0.058±0.036
16 41 46	18.5	871	0.072±0.036	0.140±0.005	-0.068±0.036
16 43 18	23.2	842	0.199±0.060	0.175±0.006	+0.024±0.060
16 44 32	27.6	815	0.163±0.054	0.213±0.008	-0.050±0.055

Figure 21 shows the relationship between the integral proton flux, J, and the rigidity of the protons, P. From this relationship and assuming the exponential relation $J = J \exp -P/P_o$ we derived the protons' characteristic rigidity, P_o =46 Mv, the total directional intensity of solar proton near the earth, J_o =8.50x10^4 proton/cm^2 sec ster, and $\left|\frac{dJ}{dP}\right|_o = \frac{J_o}{P_o}$ = 1850 protons/cm^{2}sec ster Mv. The P_o = 46 Mv is in reasonable agreement with the value obtained from a rough estimate using the Explorer 41 proton data of Table 6.4. The characteristic rigidities P_o = 57 Mv and P_o = 148 Mv were similarly derived for the September 25 and December 19 solar flare events respectively. The intense X-ray emission coincident with the June 13 event indicates that electrons were emitted.

The data used for this study were the gated neutron counting rates for the OGO-VI detector on the sunward side of the earth. As in Chapter 6.1 no background correction was made for background events since only differences in counting rates were used; and only neutron rates corresponding to charged particle rates less than 1.5 times the minimum values for that vertical cutoff rigidity were included in the analysis. To exclude the solar proton albedo neutrons we restricted the solar neutron analysis to geomagnetic latitudes

less than 30°. The neutron data were also selected from altitudes less than 900 km to remove neutron production effects by the energetic protons trapped in the inner radiation belt.

Lingenfelter and Ramaty (1967) suggested that solar neutrons would arrive at the earth monoenergetic in time if the neutrons were emitted impulsively from the sun in a time interval which is comparable with the risetime of the optical flare ($\tilde{\sim}$100 sec). With this assumption they calculated the time-dependent solar neutron flux at 1 A.U. as a function of time for neutron production during the acceleration and slowing down phases. For example, Figure 22 is the time-dependent solar neutron flux at the earth as a function of time for neutron production during the slowing down phase. Therefore, we selected the neutron data assuming this time distribution. The gated neutron counting rates are shown in Tables 6.5 - 6.9. In column 4 the errors listed are statistical and are equal to the square root of the counting rate divided by the time of measurements. In column 5 the errors are the standard deviations. There are no statistically significant differences between the two counting rates.

The weighted average solar neutron rate $\bar{n}_S$ in the 1-20 MeV range is

TABLE 6.6 (JUNE 15)

Time	Geomagnetic Latitude Degrees	Alti-tude km	Counting Rate cts/sec	Monthly Average cts/sec	Counting Rate Difference cts/sec
09h 11m 29s	30.6	445	0.307±0.075	0.306±0.006	+0.001±0.075
09 12 25	26.8	457	0.217±0.063	0.229±0.005	-0.012±0.063
09 13 29	22.6	471	0.163±0.054	0.182±0.004	-0.019±0.054
09 14 24	19.0	484	0.163±0.054	0.179±0.004	-0.016±0.054
09 15 29	15.0	501	0.217±0.063	0.163±0.004	+0.054±0.063

TABLE 6.7 (SEPT 25)

07h 31m 40s	19.7	430	0.253±0.068	0.192±0.003	+0.061±0.068
07 32 35	15.9	421	0.127±0.048	0.170±0.003	-0.043±0.048
07 33 39	11.8	413	0.181±0.057	0.161±0.003	+0.020±0.057
07 34 35	8.2	407	0.090±0.040	0.151±0.003	-0.061±0.040
07 36 25	0.9	400	0.181±0.057	0.123±0.003	-0.058±0.057
07 39 30	-11.1	401	0.145±0.051	0.161±0.003	-0.016±0.051
07 40 25	-14.7	404	0.109±0.044	0.165±0.003	-0.056±0.044
07 41 29	-18.4	409	0.127±0.048	0.182±0.003	-0.055±0.048
07 42 25	-22.5	416	0.127±0.048	0.196±0.004	-0.069±0.048

TABLE 6.8 (NOV 02)

11h 21m 39s	26.5	772	0.109±0.044	0.200±0.010	-0.091±0.045
11 22 34	23.3	791	0.109±0.044	0.181±0.009	-0.072±0.045
11 23 29	20.1	810	0.145±0.051	0.160±0.007	-0.015±0.051
11 24 24	16.8	829	0.145±0.051	0.133±0.007	+0.012±0.051

TABLE 6.9 (DECEMBER 19)

Time	Geomagnetic Latitude Degrees	Altitude km	Counting Rate cts/sec	Monthly Average cts/sec	Counting Rate Difference cts/sec
12h 28m 31s	28.0	834	0.271±0.070	0.262±0.006	+0.009±0.070
12 29 26	24.8	816	0.217±0.063	0.197±0.005	+0.020±0.063
12 30 22	21.6	797	0.081±0.057	0.171±0.005	+0.010±0.057
12 31 17	18.4	778	0.163±0.054	0.169±0.005	-0.006±0.054
12 32 12	15.2	757	0.145±0.051	0.164±0.004	-0.019±0.051
12 33 07	11.9	740	0.253±0.068	0.160±0.004	+0.093±0.068
12 34 03	8.6	721	0.163±0.054	0.129±0.004	+0.034±0.054
12 34 58	5.3	702	0.127±0.048	0.120±0.004	+0.007±0.048
12 35 53	2.0	684	0.145±0.051	0.114±0.003	+0.031±0.051
12 36 49	- 1.3	665	0.199±0.060	0.114±0.003	+0.085±0.060
12 37 44	- 4.6	647	0.145±0.051	0.114±0.003	+0.031±0.051
12 38 48	- 8.1	629	0.163±0.054	0.142±0.003	+0.021±0.054
12 39 44	-11.9	609	0.109±0.044	0.152±0.003	-0.043±0.044
12 40 39	-15.3	592	0.217±0.063	0.167±0.005	+0.050±0.063
12 41 34	-18.7	576	0.217±0.063	0.180±0.005	+0.037±0.063
12 42 30	-22.1	560	0.181±0.057	0.188±0.005	-0.007±0.057
12 43 25	-25.5	545	0.289±0.072	0.219±0.007	+0.070±0.072
12 44 20	-28.9	531	0.253±0.068	0.275±0.007	-0.022±0.068

$$\bar{n}_s = \frac{\sum_{i=1}^{N} \frac{n_i}{\sigma_i^2}}{\sum \frac{1}{\sigma_i^2}} \pm \sqrt{\frac{\sum_{i=1}^{N} \sigma_i^2}{N}}$$

$$= + 0.017 \pm 0.014 \text{ cts/sec (December 19)}$$

$$= - 0.047 \pm 0.024 \text{ cts/sec (November 2)}$$

$$= - 0.030 \pm 0.017 \text{ cts/sec (September 25)}$$

$$= - 0.001 \pm 0.027 \text{ cts/sec (June 15)}$$

$$= - 0.049 \pm 0.025 \text{ cts/sec (June 13)}$$

Therefore, at the 95% confidence level, the upper limit to the solar neutron rate is 5.0×10^{-2} cts/sec. The corresponding upper limit solar neutron flux, at the 95% confidence level, is 0.135 n/cm^{2}sec.

The upper limit to the measured direct solar neutron flux was further corrected for the atmospheric solar neutron leakage flux arising from the interaction of solar neutrons with the earth's atmosphere following the methods of Chapter 6.1. The corrected upper limit to the solar neutron flux was thus obtained to be 5×10^{-2} n/cm^2-sec in the 1-20 MeV at the 95% confidence level.

In order to compare the upper limits to the solar neutron flux with the theoretical predictions we need sufficient information on the flux and rigidity spectra of the solar protons associated with the flare. This information is available for the November 2 event. Using the estimated characteristic rigidity, P_o , for the November 2 event we shall now compare the solar

neutron upper limit flux with the flux calculated using the Lingenfelter model (1969). In this model, the energy of the optical emission in solar flares is assumed to result from the ionization losses of the accelerated particles in the solar chromosphere. The accelerated charged particles interact with the solar atmosphere to produce neutrons and gamma rays. He estimated the expected neutron and gamma ray fluxes at the earth per unit power dissipated by ionization losses of the accelerated solar particles as a function of the characteristic rigidity, P_o. For the optical energy, $\leq 10^{29}$ erg sec^{-1}, of the 3B flare (Kiepenheuer, 1965; Lingenfelter, 1969) and for P_o = 46 Mv, the expected neutron flux at the earth is $\sim 1.5 \times 10^{-1} n/cm^2$-sec. We obtained an upper limit to the solar neutron flux of $5 \times 10^{-2} n/cm^2$-sec in the 1-20 MeV energy range. Chapter 6.1 showed that about 27% of all solar neutrons is in the 1-20 MeV energe range. Therefore, the measured upper limit total solar neutron flux is 1.9×10^{-1} n/cm^2 -sec. This means that according to the Lingenfelter model, the measured upper limit to the solar neutron flux implies that the characteristic rigidity, P_o , should be less than 60 Mv for the November 2 flare. Therefore the observations are consistent with the model. The solar neutron flux predicted by the Lingenfelter and Ramaty (1967)

calculations will also be compared with our upper limit to the solar neutron flux. Recall that $J_o \sim 8.5 \times 10^4$ protons/cm^{2}sec ster for the solar protons observed by the McDonell Douglas experiment at 1A.U. during the solar proton event of November 2, 1969. We obtained the solar neutron upper limit for this event by assuming an event duration at 1A.U. of $\sim 10^3$sec (Lingenfelter and Ramaty, 1967). Therefore the time-integrated flux of protons is $\sim 10^8$ protons/cm^2. This would imply, according to Lingenfelter and Ramaty (1967), that about 3×10^{33} protons greater than 30 MeV were released from the sun during the November 2, 1969 event. If half of the accelerated particles escaped from the sun, we observe from Figures 23 and 24 of Lingenfelter and Ramaty (1967) that a peak flux of 0.06 n/cm^2 -sec is expected from production during acceleration over a path length of 1 gm/cm^2 and a flux ~ 0.15 n/cm^2 -sec from production during the slowing down of those particles which did not escape from the sun. The total <u>peak</u> flux, ~ 0.21 n/cm^2-sec, is comparable to our measured upper limit to the total solar neutron flux, 0.19 n/cm^2-sec, for the solar proton event of November 2. However, the expected flux might have been detected by a more sensitive instrument.

We shall further compare the measured upper limit solar neutron flux with the theoretical predictions

for the September 25 and December 19 solar flare events. The characteristic rigidities for the September 25 and December 19 solar flare events were 57 Mv and 148 Mv respectively. For the optical energy, $\leq 10^{27}$ erg sec^{-1}, of the class 2 flares (Lingenfelter, 1969) and for P_0=57Mv, the expected neutron flux at the earth is $\sim 8 \times 10^{-3} n/cm^2$-sec. This means that according to the Lingenfelter model, the measured upper limit to the solar neutron flux implies that the characteristic rigidity, P_0, should be less than 110 Mv for the September 25 flare. For the optical energy, $\lesssim 10^{24}$ erg sec^{-1}, of the class 1 flare and for P_0 = 148 Mv the expected neutron flux at 1 A.U. is $\sim 6 \times 10^{-4} n/cm^2$-sec. The observations are consistent with the Lingenfelter model.

Having shown that our measurements for the November 2, September 25, and December 19 solar proton events are consistent with the Lingenfelter model (1969), we shall now use our solar neutron measurements of the June 15 and June 13 events to estimate the unknown characteristic rigidities of the solar protons accelerated during the events. For the June 15 and June 13 events we obtained an upper limit solar neutron flux $5 \times 10^{-2} n/cm^2$-sec in the 1-20 MeV energy range. This corresponds to the total solar neutron flux upper limit $1.9 \times 10^{-1} n/cm^2$-sec. For the optical energy, $\leq 10^{27}$ erg sec^{-1}, of the 2B

flare, the characteristic rigidity of the protons accelerated in the solar atmosphere during the June 15 event must be less than 110 Mv assuming the Lingenfelter model. For the optical energy, $\leq 10^{29}$ erg sec^{-1}, of the 3B flare, the characteristic rigidity of the protons accelerated in the solar atmosphere during the June 13 event must be less than 60Mv assuming the Lingenfelter model (1969).

We conclude that the 1-20 MeV solar neutron flux for the November 2, September 25, December 19, June 13 and June 15 solar flare events cannot be greater than $5 \times 10^{-2} n/cm^2$-sec at the 95% confidence level. This is the first time that an upper limit solar neutron flux has been measured for a flare of importance greater than 2B. Our measurements are not inconsistent with the Lingenfelter (1969) and Lingenfelter and Ramaty (1967) models for solar neutron production during solar flares. There could be neutrons from the sun during solar particle events. To observe the neutron flux or to set a lower upper limit to the solar neutron flux we suggest that, during large solar flares such as the November 2 flare, flights be made with neutron detectors which have much larger geometrical factors, better efficiency and directionality to reduce the

background of atmospheric neutrons. To minimize the loss of solar neutrons by decay and to provide a good time coverage, we further suggest that the detectors be carried by satellites orbiting very close to the sun. However, the detectors should be capable of eliminating the background of non-neutron sources such as gamma rays.

CHAPTER VII

RESULTS AND INTERPRETATIONS OF THE SOLAR PROTON ALBEDO NEUTRON MEASUREMENTS

7.1 Polar Studies

For the polar study of the solar proton albedo neutrons, the neutron counting rates were again derived from those events in the He^3 proportional counter not associated with events in the charged-particle guard counters. These gated neutron counting rates were limited to geomagnetic latitudes (north and south) greater than 70° since the solar protons which give rise to the solar proton albedo neutrons are restricted to the polar regions of the earth by the terrestrial magnetic field and therefore only a few solar flare events are seen at latitudes less than 70°. The neutron counting rates, corrected for dead time, were then reduced to 450 km using the observed altitude dependence (Chapter 8.2).

The details of the optical observations, the riometer absorptions, and the solar proton emissions are shown in Tables 7.1 and 7.2 for the solar flares of September 25, November 24, December 18 and December 19.

TABLE 7.1

SOLAR FLARE EVENTS

Date (1969)	Onset Time (ut)	End (ut)	Time of Maximum (ut)	Importance	Solar Region	Max Riometer Absorption db at 30mHz
Sept 25	0700	0853	0724	2N-3N	N14W14	0.7
Nov 02	1028	1157	1139	3B	N22W90	14.5
Nov 24	0913	1000	0918	2B-3N	N16W32	0.7
Dec 18	0745	0826	0725	1N-2F	N15E28	0.6
Dec 19	1201	1240	1220	1N-2F	N10W08	1.3

TABLE 7.2

SOLAR PROTON EMISSION (EXPLORER 41)

Date (1969)	Proton flux (ster cm s)$^{-1}$			Time of Peak flux (ut)
	>60Mev	>30Mev	>10Mev	
Sept 25	0.2	1	15	∿11.00
Nov 02	39	257	1437	12.00-13.00
Nov 24	0.4	0.9	3.5	∿17.00
Dec 18	0.6	1.2	1.5	∿20.00
Dec 20	0.6	1.1	8.3	∿01.00

Coincident with the proton flux enhancements recorded on Explorer 41 are transient increases in the gated neutron rates above the cosmic-ray albedo neutron rate background (Figures 23, 24, 25 and 26).

To compare our results with the Lingenfelter and Flamm (1964) calculations of the solar proton albedo neutron flux we need sufficient information about the energy spectra and charge composition of the solar particles which arrived at the earth. First, we need the information to do the background correction. As we showed in Chapter 5 and Appendix B the background correction to the He^3 gated neutron counting rate results from neutrons produced locally in the spacecraft, adjacent electronic circuitry, and moderator by energetic solar particles escaping detection in the anti-coincidence guard counters. Charged particles could enter the unguarded ends of the He^3 counter and produce pulses above the discriminator threshold. These charged particles are protons with initial energy between 100 and 125 MeV, α-particles with initial energy between 100 and 375 MeV/nucleon, $Z > 2$ particles of all energies sufficient to reach the He^3 counter, evaporation protons produced in the moderator and walls of the He^3 counter by solar particles, and shower particles produced in nuclear interactions of the solar particles

with the moderator and walls of the He^3 counter. The background corrections were calculated using the solar particle fluxes obtained by the McDonnell Douglas OGO-VI experiment, the neutron production cross sections and the resulting energy distributions of the locally produced neutrons given by Chen et al. (1955), Dostrovski et al. (1958), Jain et al. (1959), Jain (1961), Bercovitch et al. (1960), Bertini (1965), and Alsmiller et al. (1967), (the details are presented in Chapter 5 and Appendix B). The background corrections for the 25th September solar flare are given in Table 7.3.

TABLE 7.3

CORRECTIONS TO THE He^3-COUNTER GATED NEUTRON COUNTING RATE (CTS/SEC) AT THE POLES FOR THE SEPTEMBER 25, 1969 SOLAR FLARE EVENT

Locally produced neutrons	
In the spacecraft mainbody	0.0052
In the EP5 set up	0.0016
In the neighboring electronics and detector walls	0.0576
In the moderator	0.0009
Highly ionizing events in the He^3 counter	
Low-energy solar protons	0.0000
Low-energy solar α particles	0.0000
Z >2 solar cosmic rays (including showers)	0.0000
Evaporation protons from solar cosmic ray interactions	0.0004
Proton and α-initiated shower particles	0.0000
Total Correction	0.0657

Making the necessary background correction for local production and non-neutron events, we obtained 0.18 ± .05 cts/sec as the actual increase in the neutron counting rate at 450 km for the September 25 solar flare event. This corresponds to a neutron counting rate of 0.23 ± .06 cts/sec at the top of the atmosphere (50 km altitude). Therefore the solar proton neutron leakage flux is $(0.23 \pm 0.06) \times \frac{0.5}{1.08} n/cm^2$ sec$=0.11 \pm 0.03$ n/cm^2 -sec. From the McDonnell Douglas OGO-VI solar proton energy spectrum we obtained a relation between the integral proton flux, J, and the rigidity of the protons, P which agreed with the Explorer 41 proton data of table 7.2. From the relation $J = J_0 \exp(-P/P_0)$ and $\frac{dJ}{dP} = \left|\frac{dJ}{dP}\right|_0 \exp -P/P_0$, we found the characteristic rigidity of the solar protons, P_0, to be 57 Mv and the total directional intensity of solar protons near the earth, $J_0 = 60.4$ $(cm^2 sec\ ster)^{-1}$. Therefore, $\left|\frac{dJ}{dp}\right|_0 = \frac{J_0}{P_0} = 1.06$ $(cm^2 sec\ ster\ Mv)^{-1}$. For the $P_0 = 57$Mv and a cutoff rigidity $\sim$0GV, the neutron leakage flux per unit $\left|\frac{dJ}{dp}\right|_0$ is 0.08 n/cm^2-sec from the Lingenfelter and Flamm (1964) calculations as corrected by I.M. Karp. This gives a calculated solar proton albedo neutron flux, $\phi = 0.085$ n/cm^2-sec. Our measurement 0.11 ± 0.03 n/cm^2sec is, therefore, in reasonable agreement with the theoretical predictions for this particular flare.

Similarly, we studied the November 24, December 18 and December 19 solar proton events; the results are shown in Table 7.4. For these flares, however, the energy spectra and charge composition of the solar particles were not available. We, therefore, assumed the power law energy dependence, J (energy >T) = KT^{-B}, for the solar proton flux, J, measured by Explorer 41 for the >60 MeV and >30 MeV integral proton fluxes and obtained the integral and differential energy spectra for the solar protons. From the integral energy spectra of the solar protons and again assuming the relationships $J = J_o \exp^{-P/P_o}$ and $\frac{dJ}{dp} = \left|\frac{dJ}{dp}\right|_o \exp -P/P_o$, we found the P_o and J_o listed in Table 7.4. These P_o and $\left|\frac{dJ}{dp}\right|_o$ were then used to estimate the neutron leakage fluxes, at ∿0GV vertical cutoff rigidity, shown in Table 7.4. With the solar proton differential energy spectra and the methods used for the September 25 event we calculated the background corrections for local production and non-neutron events. Finally, the resulting actual neutron rate increases were used to evaluate the observed solar proton albedo neutron fluxes shown in Table 7.4. The measured solar proton albedo neutron fluxes for the November 24, December 18 and December 19 solar proton events are in reasonable agreement with the theoretical predictions for these flares.

TABLE 7.4

COMPARISON OF THE MEASURED AND PREDICTED SOLAR PROTON ALBEDO NEUTRON FLUX

Date of the Solar proton event (1969)	The Characteristic rigidity of the solar protons, P_o (MV)	Total directional intensity of the solar protons, J_c ($cm^2 sec\ ster)^{-1}$	Solar proton albedo neutron rate at 450km altitude cts/sec	Solar proton albedo neutron flux at the top of the polar atmosphere (50 km) $cm^{-2}sec^{-1}$	
				Measured	Predicted
September 25	57	60.4	0.18±0.05	0.11 ±0.03	0.085
November 24	113	6.83	0.21±0.09	0.12 ±0.05	0.02
December 18	130	6.96	0.11±0.05	0.063 ±0.028	0.030
December 19	148	5.21	0.13±0.05	0.074 ±0.029	0.035

7.2 Low-Latitude Studies

The measurement of the solar proton albedo neutrons at low latitudes is important because only the neutron decay products injected at low latitudes can contribute to the inner zone radiation belt particles. The data used for the low-latitude study were the gated neutron rates at geomagnetic latitudes (north and south) less than 45°. To minimize the contributions from local production of neutrons by charged particles interacting with the satellite assembly, the neutron counting rates corresponding to charged particle rates greater than 1.5 times the minimum values for the particular cutoff rigidity were excluded from the analysis. The rates were selected from small intervals of latitude and altitude to avoid any latitude or altitude bias in the neutron rates used for the analysis. For the time intervals involved in the analysis there was no measurable Forbush decrease which, otherwise, could produce uncertainties in the interpretations of the neutron data.

The neutron rates are displayed in Figures 27, 28, 29, 30, and 31 for the September 25, November 2, November 24, December 18, and December 19 events, respectively. Apart from the November 2 solar flare

event, there is no enhancement in the low-latitude neutron rates. Nevertheless, let us compare our measurements with the predictions of Lingenfelter and Flamm (1964). The theoretical calculations produced the neutron leakage flux at the top of the atmosphere resulting from the interactions of the polar cap protons with the polar atmosphere. Using the characteristic rigidities, P_o, and $\left(\frac{dJ}{dP}\right)_{P_o}$ which we had derived for the different flares (Chapters 6.2 and 7.1), we deduced the neutron leakage flux at the top of the atmosphere as a function of cutoff rigidity. With this flux as the source function and the geometrical calculations outlined in Chapter 8.2, we calculated the expected flux at the detector location. Except for the November 2 event, the predicted solar proton albedo neutron flux at the low-latitude regions was approximately zero which agrees with the observations.

The measured neutron counting rates for the November 2 event at $40° < |\text{Geomagnetic latitude}| < 45°$ in the altitude range 700 - 800 km are displayed in Figure 28. Apparently there is a brief enhancement in the neutron rate (greater than three standard deviations) at the time when large fluxes of polar cap protons were being detected. The Lingenfelter and Flamm source function (Figure 32) for the November 2 event yielded

a peak solar proton produced neutron leakage rate of 0.21 cts/sec at 42° Geomagnetic latitude and 750 km altitude. The sum of this calculated solar proton albedo neutron rate and the background, the November monthly average neutron rate, is within two standard deviations of the observed rate (Fig. 28).

Now, let us investigate the possibility that the brief neutron increase could be from sources other than the solar proton albedo neutrons. Solar neutron flux is readily dismissed as a source because we showed in Chapter 6.2 that the upper limit solar neutron flux for the November 2, 1969 solar flare event was 5×10^{-2} n/cm^2-sec in 1-20 MeV energy range. Local production could not have produced the neutron enhancement because the charged particle rates were about the same and the location identical for the short period of the analysis. Furthermore, a lowered cutoff rigidity for the charged particles at the time of the rate increase would decrease the actual neutron enhancement and consequently would bring our measurements and the calculations of Lingenfelter and Flamm into better agreement. But there is no reason to suppose that the cutoff rigidity was lowered. Finally, α-particles could not have made any significant neutron contributions. Using the P/α ratio measured by

the McDonell Douglas OGO-VI experiment and the neutron cross-sections in Figure 1 of Lingenfelter and Flamm (1964), we estimated the ratio of neutron production by protons and α-particles to be ∿10. In doing the rough calculation we assumed that each of the four nucleons of the alpha particle was as effective as a proton in producing neutrons in the atmosphere. Therefore, for the November 2 event, the solar α-particles made an insignificant contribution to the neutron production. We conclude that the brief neutron enhancement was presumably due to the polar cap protons.

7.3 Summary

The results of the polar studies of the polar cap neutron events (Table 7.4) indicate that the solar proton albedo neutron fluxes measured by the OGO-VI neutron detector are in reasonable agreement with the Lingenfelter and Flamm (1964) calculations as corrected by I.M. Karp. The low-latitude studies of the September 25, November 2, November 24, December 18 and December 19 solar flare events support the above conclusion. Hess and Killeen (1966) and Dragt et al. (1966) calculated the solar proton albedo neutron decay contributions to the radiation belts using the original Lingenfelter and Flamm flux. They found that solar proton albedo neutron decay was inadequate to provide the large fluxes of the anomalous

low-energy radiation belt protons. The original flux is twice the corrected Lingenfelter and Flamm flux. Though Dragt et al. (1966) used a flatter angular distribution to obtain the injection coefficients, Hess and Killeen (1966) assumed an angular distribution more peaked to the vertical than the isotropic angular distribution measured by our experiment (Chapter 8.2). We conclude, therefore, that solar proton albedo neutron decay is not an important source for the radiation belt particles unless severe limitations were imposed on the loss mechanisms used in the models for calculating the SPAND contribution to the radiation belt protons. This conclusion is based on the polar and low-latitude neutron measurements of the polar cap neutron events during June 7 - December 23, 1969.

CHAPTER VIII

RESULTS AND INTERPRETATIONS OF THE COSMIC-RAY ALBEDO NEUTRON MEASUREMENTS

8.1 The Latitude Dependence

The results of the latitude dependence of the neutron counting rate are summarized in Figures 33 and 34 for the quiet months of July and October. The months of July and October (1969) were exceptionally quiet with low solar indices and no solar proton events (ESSA). The Figures show the relationship between the neutron rates at 400-500 km altitude and the vertical cutoff rigidity/geomagnetic latitude. The neutron counting rate is a smoothly varying function of rigidity and/or geomagnetic latitude. The latitude dependence of the counting rate from the poles to the equator is 8.3 ± 0.2 for July and 8.6 ± 0.2 for October in good agreement with those predicted by Lingenfelter (1963) for this period in the solar-activity cycle. Table 8.1 shows that this ratio is essentially independent of altitude but is time dependent. We shall, however, discuss this time variation in section 4 of this Chapter.

TABLE 8.1

THE POLAR TO EQUATOR RATIO OF THE NEUTRON COUNTING RATE

Altitude (Km)	Month, 1969 July	October
450	8.3 ± 0.2	8.6 ± 0.2
550	8.2 ± 0.3	8.7 ± 0.3
650	8.3 ± 0.4	8.5 ± 0.3
750	8.4 ± 0.4	9.2 ± 0.4
850	8.2 ± 0.4	8.5 ± 0.3
1050	8.4 ± 0.3	9.0 ± 0.6

The latitude dependence of the neutron counting rate results from the latitude variation of the cosmic-ray intensity. The vertical intensity of a component of secondary cosmic rays, such as atmospheric neutrons, measured at latitude λ and depth x, $j_{\perp}(\lambda,x)$ is expressed as (Treiman, 1952)

$$j_{\perp}(\lambda,x) = \sum_{z} \int_{W_z(\lambda)}^{\infty} j_z(W_o) \; S_z(W_o, x)\,dW_o,$$

where $j_z(W_o)$ is the intensity of primary cosmic-ray particles with atomic number z and kinetic energy per nucleon W_o in dW_o; $W_z(\lambda)$ is the vertical cutoff energy; $S_z(W_o, x)$, the specific yield, indicates the number of particles at x that are produced by a primary particle of energy W_o and charge z. The vertical intensity is derived from the omnidirectional intensity J(x) using

the Gross transformation (Gross, 1933),

$$2\pi\, j_{\perp}(x) = J(x) - xJ'(x)$$

The cutoff energy results from the geomagnetic effect; the earth's magnetic field acts as a momentum or magnetic rigidity analyzer for the primary cosmic-ray particles, thus introducing a threshold rigidity at a particular zenith and azimuth. In a dipole field, for example, all primary cosmic-ray particles with arrival direction Ψ and cutoff rigidity less than

$$P(GV) = \frac{59.6 \cos^4 \lambda}{(1 + \sqrt{1+\cos^3\lambda \cos\Psi})^2}$$

are excluded from the region with latitude, λ. For particles arriving from the east, west and vertical $\Psi = \pi$, 0 and $\pi/2$ respectively. Consequently, the number of cosmic rays arriving at the top of the atmosphere progressively increases from the equator to the poles.

The total leakage flux results of the OGO-VI neutron experiment are summarized in Table 8.2. We have also summarized the recent measurements of the total neutron leakage flux ($\leq$10 MeV) in Figures 35 and 36 for July and October respectively. The fast neutron detector measurements of Haymes (1964) and of Holt et al. (1966) were first corrected to the same period in the solar-activity cycle as for OGO-VI by assuming that at any

TABLE 8.2

TOTAL LEAKAGE FLUX ($\leq$10 MEV)

Rigidity Range, GV	Geom. latitude degrees	JULY		OCTOBER	
		(Ling.)	(Newkirk)	(Ling.)	(Newkirk)
0- 0.3	80.0	0.444±.045	0.543±.055	0.469±0.047	0.573±0.058
0.3- 0.6	68.0	0.449±.046	0.549±.056	0.468±0.048	0.573±0.058
0.6- 1.0	62.5	0.426±.045	0.521±.054	0.477±0.049	0.583±0.060
1.0- 1.5	58.5	0.421±.043	0.515±.052	0.458±0.047	0.560±0.057
1.5- 2.0	55.0	0.402±.041	0.492±.050	0.427±0.043	0.522±0.053
2.0- 2.5	52.0	0.386±.039	0.472±.048	0.403±0.041	0.493±0.050
2.5- 3.0	49.5	0.354±.036	0.433±.044	0.375±0.038	0.459±0.046
3.0- 3.5	47.0	0.319±.032	0.390±.039	0.352±0.036	0.430±0.043
3.5- 4.0	45.0	0.287±.029	0.351±.036	0.318±0.032	0.389±0.039
4.0- 5.0	42.5	0.255±.026	0.312±.032	0.271±0.028	0.332±0.033
5.0- 6.0	39.5	0.213±.022	0.260±.026	0.228±0.023	0.279±0.028
6.0- 7.0	37.0	0.174±.018	0.213±.022	0.192±0.020	0.235±0.024
7.0- 8.0	35.0	0.157±.016	0.191±.019	0.168±0.017	0.206±0.021
8.0-10.0	31.5	0.130±.013	0.159±.016	0.133±0.014	0.163±0.016
10.0-12.0	26.5	0.099±.010	0.121±.012	0.100±0.010	0.122±0.012
12.0-14.0	20.0	0.071±.007	0.087±.009	0.074±0.008	0.091±0.009
12.0-16.0	7.5	0.062±.006	0.075±.008	0.063±0.006	0.077±0.008
>16	0.0	0.053±.005	0.065±.007	0.054±0.006	0.066±0.007

TABLE 8.2, Continued

Rigidity Range, GV	Geom. latitude degrees	JUNE (Newkirk)	AUGUST (Newkirk)	SEPTEMBER (Newkirk)	NOVEMBER (Newkirk)	DECEMBER (Newkirk)
0- 0.3	80.0	0.561±.057	0.556±.056	0.582±.059	0.548±.055	0.592±.060
0.3- 0.6	68.0	0.564±.057	0.549±.055	0.580±.059	0.511±.052	0.589±.060
0.6- 1.0	62.5	0.535±.055	0.558±.058	0.509±.054	0.567±.059	0.464±.051
1.0- 1.5	58.5	0.516±.052	0.531±.055	0.538±.056	0.527±.054	0.569±.059
1.5- 2.0	55.0	0.496±.050	0.501±.051	0.519±.053	0.554±.056	0.539±.055
2.0- 2.5	52.0	0.482±.049	0.463±.047	0.505±.051	0.510±.052	0.505±.051
2.5- 3.0	49.5	0.443±.045	0.439±.044	0.464±.047	0.471±.048	0.485±.049
3.0- 3.5	47.0	0.396±.040	0.400±.040	0.440±.045	0.426±.043	0.418±.042
3.5- 4.0	45.0	0.351±.036	0.358±.036	0.400±.041	0.389±.039	0.388±.040
4.0- 5.0	42.5	0.302±.031	0.310±.031	0.340±.034	0.331±.033	0.338±.034
5.0- 6.0	39.5	0.255±.026	0.253±.026	0.283±.029	0.282±.029	0.269±.027
6.0- 7.0	37.0	0.215±.022	0.212±.022	0.237±.024	0.237±.024	0.224±.023
7.0- 8.0	35.0	0.192±.020	0.190±.020	0.207±.021	0.201±.021	0.195±.021
8.0-10.0	31.5	0.157±.016	0.157±.016	0.165±.017	0.167±.017	0.162±.017
10.0-12.0	26.5	0.118±.012	0.115±.012	0.127±.013	0.124±.013	0.116±.012
12.0-14.0	20.0	0.085±.009	0.085±.009	0.092±.009	0.094±.010	0.092±.010
12.0-16.0	7.5	0.076±.008	0.074±.008	0.079±.008	0.079±.008	0.074±.008
>16	0.0	0.061±.006	0.060±.006	0.064±.007	0.063±.006	0.062±.007

latitude the change in neutron leakage flux calculated by Lingenfelter was a linear function of the cosmic-ray intensity. The 1-10 MeV neutron fluxes were also converted to a total neutron leakage flux by using the calculated fraction of 1-10 MeV neutron flux to the total neutron flux (Lingenfelter, 1963; Newkirk, 1963). The slow neutron detector measurements of Bame et al. (1963), and Boella et al. (1963, 1965), Lockwood and Friling (1968) determined the neutron flux, $\phi = N/\varepsilon$. This is the leakage flux only for the case in which all the neutrons are moving vertically upward at the top of the atmosphere. We shall show later that the true angular distribution of the leakage neutrons (<10MeV) at the top of the atmosphere is mainly isotropic. We therefore corrected their results using $\phi_L = 0.5\ N/\varepsilon$ (Chap. 5), after having corrected them for solar modulation and for altitude using the altitude dependence expected for an isotropic neutron flux distribution at the top of the atmosphere; the total neutron leakage flux measurements of the OGO-VI detector are in reasonable agreement with the other experimental results. All the experiments, both the fast and the slow neutron detector experiments, agree when the Newkirk energy spectrum is used to get the total leakage flux. There is much less agreement

when the Lingenfelter spectrum is used (Figures 37 and 38). It appears that the Lingenfelter spectrum is deficient in 1-10 MeV neutrons. Mendell and Korff (1963), Haymes (1964), Holt et al. (1966) have found an energy spectrum of 1-10 MeV neutrons similar to the Newkirk spectrum. The energy spectrum measurements of the OGO-VI experiment (Chapter 8.3) indicates a slightly flatter spectrum than the Newkirk spectrum. The total leakage flux using Newkirk's spectrum is about 0.7 times the calculated Lingenfelter and Newkirk fluxes in agreement with Miles (1964) who, using BF_3 ionization chambers, measured a neutron density in the atmosphere 0.6 times the Lingenfelter's.

8.2 The Angular Distributions as Deduced From the Altitude Dependence

8.2.1 Calculation of the Altitude Change in Counting Rate of Leakage Neutrons for Various Angular Distributions

The altitude variation of the neutron counting rate above the atmosphere is related to the angular distribution of leakage neutrons at the top of the atmosphere as follows: The counting rate of a neutron detector above the earth's atmosphere, neglecting

neutron decay, is given by

$$n = \int_{4\pi} d\vec{\Omega}\ \varepsilon(\vec{\Omega})\ \Phi_o(\vec{\Omega}) ,$$

where $\varepsilon(\vec{\Omega})$ is the efficiency of the detector (cts/ncm^{-2}) for neutrons arriving in the direction $\vec{\Omega}$ at the detector. The neutron flux, $\Phi_o(\vec{\Omega})$, in the direction $\vec{\Omega}$ at the spacecraft is the same as the neutron flux $\Phi(\vec{\Omega})$, at the top of the atmosphere if the direction $(-\vec{\Omega})$ measured from the detector intersects the top of the atmosphere. Otherwise, the flux is zero. $d\vec{\Omega}$ can be replaced by $\frac{dA \cos \nu}{r^2}$ where dA is a small horizontal area at the top of the atmosphere, ν is the angle between the vertical and $\vec{\Omega}$, and r is the distance along the direction $\vec{\Omega}$ between the top of the atmosphere and the detector. These relationships are illustrated in Figure 39 where the spacecraft is located at (R,θ_o,α_o), while the point (R_o,θ,α) is on the top of the atmosphere. The effects of gravitational trapping have been excluded since we are considering neutrons in the energy range 0.1 Kev $\leq E < 10$ Mev. The count rate is now written as

$$N = \int dA\ \varepsilon(\vec{\Omega})\ \Phi(\vec{\Omega})\ \frac{\cos(\nu)}{r^2}$$

$$= \int dA\ \varepsilon(\vec{\Omega})\ \Phi(\theta)\ k(\nu)\ \frac{\cos(\nu)}{r^2}$$

where the integration is over the top of the atmosphere visible to the detector, and $\Phi(\vec{\Omega})$ has been written as

a separable function in θ and ν.

To evaluate the above equation, $d\vec{A}$, $\vec{\Omega}$, ν and r were written in terms of height, h, above the top of the atmosphere (50km), geomagnetic colatitude θ and geomagnetic longitude α. The detailed calculations are in Appendix A.

The latitude dependence $\Phi(\theta)$ was determined from the observed latitude dependence of the neutron counting rate for altitudes 400-500 km. Since the latitude dependence of the decrease in count rate with altitude between the top of the atmosphere (50 km) and 500 km is considerably smaller than the latitude dependence, $\Phi(\theta)$, this approximation is justified. The counting rate of the detector as a function of altitude was then evaluated at various geomagnetic latitudes. To do this, we used the measured detector efficiency, $\varepsilon(\Phi)$, and various expressions for the angular distribution, $K(\nu)$, of leakage neutrons at the top of the atmosphere.

8.2.2 Deduction of the Angular Distribution from the Neutron Measurements

In the last section we evaluated the counting rate of the OGO-VI neutron detector as a function of altitude at different geomagnetic latitudes and for

different angular distributions of leakage neutrons at the top of the atmosphere. In this section we shall present the measured and calculated altitude dependence of the albedo neutron flux above the atmosphere at different latitudes. From the comparison of the measured and calculated altitude dependence we shall suggest the form of the angular distribution of albedo neutrons at the top of the atmosphere.

The neutron counting rates were derived from those events in the He^3 proportional counter not associated with events in the charged-particle guard counters. To minimize the contributions from local production, the neutron counting rates corresponding to charged particle rates less than twice the minimum values for that vertical cutoff rigidity were used for the analysis. We excluded the data from regions of the earth where the Capetown and Brazilian anomalies lowered the inner radiation belt into the higher altitude portions of the OGO=VI orbit. The data acquired during the occasional excursions of the OGO-VI satellite into the hornsof the outer radiation belt were automatically removed by the sorting program due to the high charged particle rates in this region.

If there is any error in the rigidity location or if the vertical cutoff rigidity was not an adequate

description of the geomagnetic effect on neutron intensity, that location could contribute to an error in the altitude variation of neutron intensity. However, if each location in a rigidity bin contributed equally at all altitudes, then such errors would disappear. This will be the situation when the period of analysis equals the time taken for the apogee or perigee of the satellite orbits to precess through 360°. This was approximately four months for the OGO-VI satellite. Hence, the time period selected for study was June 7 to September 30, 1969.

The results of the sorting yielded neutron counting rates at each rigidity-altitude bin. These counting rates were then corrected for locally produced neutrons and highly ionizing charged particles by the technique described in Chapter 5 and Appendix B.

Table 8.3 summarizes the results of the altitude dependence of the cosmic-ray albedo neutron flux. The table contains the percentage change in counting rate between 450 and 1050 km, $\frac{N_{450} - N_{1050}}{N_{450}} \times 100\%$, for different geomagnetic latitudes. The corresponding power law, $R^{-\beta}$, is also included (R is the distance from the center of the earth). The changes of the altitude

TABLE 8.3

THE ALTITUDE DEPENDENCE OF THE ALBEDO NEUTRON FLUX

Rigidity range(GV)	Geomagnetic latitude degrees	Neutron Rate Percentage change $\frac{N_{450}-N_{1050}}{N_{450}} \times 100\%$	Power law, $R^{-\beta}$ (R is distance from center of earth)
0- 0.3	80.0	25.3±1.1	$R^{-3.45\pm0.18}$
0.3- 0.6	68.0	26.8±1.1	$R^{-3.68\pm0.18}$
1.5- 2.0	55.0	27.6±1.4	$R^{-3.83\pm0.23}$
2.0- 2.5	52.0	28.0±1.1	$R^{-3.89\pm0.17}$
2.5- 3.0	49.5	27.3±1.0	$R^{-3.78\pm0.16}$
3.0- 3.5	47.0	25.7±1.0	$R^{-3.51\pm0.16}$
3.5- 4.0	45.0	23.1±1.1	$R^{-3.11\pm0.17}$
4.0- 5.0	42.5	24.2±1.0	$R^{-3.27\pm0.15}$
5.0- 6.0	39.5	22.4±1.1	$R^{-3.01\pm0.16}$
6.0- 7.0	37.0	20.3±1.3	$R^{-2.68\pm0.19}$
7.0- 8.0	35.0	19.4±1.4	$R^{-2.55\pm0.20}$
8.0-10.0	31.5	21.1±1.1	$R^{-2.80\pm0.17}$
10.0-12.0	26.5	18.5±1.3	$R^{-2.41\pm0.19}$
12.0-14.0	20.0	18.1±1.4	$R^{-2.36\pm0.20}$
14.0-16.0	7.5	21.0±1.4	$R^{-2.79\pm0.20}$
>16.0	0.0	20.3±1.6	$R^{-2.69\pm0.23}$

variation of the albedo neutron with latitude are attributed to the shape of the latitude variation of neutron flux and the effects of latitude mixing, since the detector sees neutrons from a wider range of latitudes as the altitude increases. Recall that the graph of the albedo neutron flux with latitude turns up at about 20°, gradually increases and starts turning again, at about 55°, to a constant value at the polar region. Therefore, at about 20° latitude the higher the altitude the higher the geomagnetic latitude included. Noting the increase of the albedo neutron flux above 20°, we expect a minimum altitude change in the counting rate at this latitude. Similarly, we expect a maximum altitude change in the counting rate at about 55°. This is exactly what was measured.

The percentage change in the counting rate as a function of geomagnetic latitude is shown in Figure 40 where the corresponding calculated changes, assuming different angular distributions of the albedo neutrons at the top of the atmosphere, are also included. It is observed that the measured values suggest an angular distribution of leakage flux at the top of the atmosphere that is mainly isotropic.

Table 8.4 gives the values of Chi-squared between the experimental values of the altitude change

TABLE 8.4

THE ALTITUDE DEPENDENCE FIT AT GEOMAGNETIC LATITUDES LESS THAN 60°

Angular Distribution	X^2(13 degrees of freedom)	Significance of fit, %
$k(\nu)=\cos\nu$	63.4	<<0.1
$k(\nu)=1+1.41\cos\nu$	13.3	40
$k(\nu)=1$(isotropic)	9.9	71
$k(\nu)=1-0.5\cos\nu$	38.0	<0.1
$k(\nu)=1-\cos\nu$	261.2	<<0.1

TABLE 8.5

COMPARISON OF THE NORMALIZED PREDICTED COUNTING RATES AND OBSERVED RATES (SEC^{-1}) AT THE POLAR REGION (P_c< 0.3GV)

Altitude (km)	Observed rates	Calculated Rates				
		$k(\nu)=\cos\nu$	$k(\nu)=1+1.41\cos\nu$	$k(\nu)=1$	$k(\nu)=1-0.5\cos\nu$	$k(\nu)=1-\cos\nu$
443.7	1.0179±0.0116	0.9952	1.0058	1.0151	1.0241	1.0477
546.5	0.9556±0.0118	0.9367	0.9406	0.9440	0.9472	0.9555
648.7	0.9063±0.0118	0.9017	0.9024	0.9030	0.9036	0.9046
749.5	0.8650±0.0118	0.8692	0.8674	0.8657	0.8641	0.8594
850.4	0.8289±0.0118	0.8387	0.8349	0.8315	0.8282	0.8190
952.6	0.7935±0.0117	0.8103	0.8048	0.8000	0.7952	0.7823
1067.7	0.7591±0.0116	0.7832	0.7764	0.7704	0.7645	0.7485
X^2(5 degrees of freedom)		13.7	6.7	2.4	1.1	9.3
Significance of fit, %		3	24	79	96	11

in the counting rates and the calculated curves of Figure 40 for geomagnetic latitudes less than 60°. The best fit is the isotropic angular distribution, $k(\nu) = 1$. The fit for the angular distribution $K(\nu) = 1+1.41\cos\nu$ is barely significant. However, the fits for the more nearly vertical angular distribution, $K(\nu) = \cos\nu$, and the flatter angular distributions, $K(\nu) = 1-0.5\cos\nu$ and $K(\nu) = 1-\cos\nu$, are in definite disagreement with the observations.

The good statistics in the polar region enabled us to compare the calculated altitude dependence directly with the measured neutron rates at different altitudes. To do this, we normalized the calculated neutron rates to the observed rates by means of a constant multiplying factor which was chosen such that the Chi-squared between the observed and the normalized expected rates was a minimum. Figure 41 compares the calculated and measured altitude dependence at the polar region (P_c <0.3GV). We have also listed,in Table 8.5, the measured and the normalized predicted neutron rates at different altitudes together with the chi-squared for the different fits using various angular distributions of the albedo neutrons at the top of the atmosphere. The best fit is the angular distribution $K(\nu) = 1-0.5\cos\nu$. The fit for the isotropic angular distribution ($K(\nu)=1$)

is significant but is much less significant than for $k(\nu) = 1-0.5\cos\nu$. The flatter angular distribution, $k(\nu) = 1-\cos\nu$, and the more vertical angular distributions, $k(\nu) = \cos\nu$ and $k(\nu) = 1.+1.41\cos\nu$, are in definite disagreement with the observations.

The variation with altitude of the scintillator neutron counting rates of the detector was also found. These rates are a measure of the neutron flux in the 1-10 MeV energy range. Because of the very low count rates and the susceptibility of the scintillator to the trapped radiation present at higher altitudes and lower latitude, only the altitude variation near the poles (P_c <0.3GV) could be investigated. The fractional change between 450 and 1050 km was found to be 25.0 ± 1.4% which is in good agreement with that observed for the He^3-counter (25.3 ± 1.1%).

The flatter angular distribution at the poles than at other latitudes could be due to the enrichment of the neutron energy spectrum preferentially in the high-energy region at high latitude. The high energy neutrons are very strongly peaked in the forward direction (pancake-shaped) and travel near the horizontal. However, they have to be degraded in energy to less than 10 MeV to be detected by the OGO-VI neutron sensor. Above 10 MeV the principal mechanism of neutron degradation is

inelastic collisions (Hess et al., 1961). Hess also estimated that 52% of the knock-on neutrons are degraded to less than 10 MeV (44% between 10 and 3.16 NeV, 6% between 3.16 and 1 MeV, 2% below 1 MeV). According to Hayakawa (1969), in an inelastic reaction,"the angular distribution of emitted particles depends on their energy rather than the energy of an incident particle; it is more peaked in the forward direction as the energies of emitted particles increase, and it also depends slightly on the size of a target nucleus, being flatter for heavier nuclei." Rosen and Stewart (1955, 1957), using a beam of 14 MeV neutrons to bombard Ta and Bi, found that the emitted low energy neutrons (0.5 to 4 MeV) have an isotropic angular distribution while the emitted higher energy neutrons (4 to 12 MeV) are strongly peaked in the forward direction in agreement with the calculations of Brown and Muirhead (1957). Furthermore, the scattering of 14.1 MeV neutrons in nitrogen by Smith (1954), 14.1 MeV neutrons in oxygen gas by Conner (1952) and 95 MeV neutrons from Carbon by DeJuren et al. (1950) showed that the angular distribution of the elastically scattered neutrons is peaked in the forward direction. Therefore, the admixture of the anisotropic higher energy neutrons degraded to below 10 MeV ($\sim$4%) with the

preponderant evaporation neutrons (~96%) may explain the flatter angular distribution in the polar region.

This enrichment of the fast neutron leakage spectrum in the polar region is in agreement with the suggestions of Boella et al. (1965). He interpreted his observed change of latitude effect with atmospheric depth as being due to more of the neutron sources being close to the top of the atmosphere at high latitudes, and anticipated a resultant enrichment of the 1-10 MeV neutrons at high latitudes.

In summary, the altitude variation of the counting rate for a detector sensitive to neutrons below 10 MeV, as a function of latitude, is indicative of an angular distribution of the flux at the top of the atmosphere that is mainly isotropic. The best fitting angular distribution is $k(\nu) = 1-0.5 \cos\nu$ at the polar region and $k(\nu) = 1$ (isotropic) at other latitudes. For these distributions the leakage flux, ϕ_L, is related to the counting rate, N, by

$$\phi_L = C \frac{N}{\bar{\varepsilon}}$$

, where $\bar{\varepsilon}$ is the mean efficiency and $c = 0.5$, 0.44 and 0.57 for the angular distributions $k(\nu) = 1$ (isotropic), $1-0.5 \cos\nu$ and $1 + 1.41 \cos\nu$, respectively.

8.3 The Energy Dependence

We re-examine our results on the energy dependence of the 1-10 MeV cosmic-ray albedo neutrons for June 7 to September 30, 1969 in the light of the very recent measurements of the neutron energy spectrum at energies of 10-100 MeV by White et al. (1972). The data used for the analysis were the He^3-counter events not gated off by the charged-particle guard counters (GN) and the rates of events in the four scintillation channels that precede GN events by less than 25 μs (PHA1, 2, 3, and 4). These data were from the time duration June 7 - September 30, 1969 and from the polar region (P_c<0.3GV) at 400-500 km altitude and the equatorial region ($P_c \geq$12GV) at 400-600 km altitude. Having corrected the neutron rates for background as in Chapter 5 and Appendix B, we reduced them to 50 km assuming the altitude dependence expected for our detector for a 2π isotropic angular distribution of leakage neutrons at the top of the atmosphere.

First, we assumed an energy spectrum of the form $AE^{-\gamma}$ which we folded into the scintillator efficiency curves to derive the expected counting rates of PHA1, 2, 3,

and 4 for various values of A and γ. The expected and observed rates were then compared in both the polar and equatorial regions by a chi-squared test to determine which values of A and γ best fitted the observations. The results are shown in Table 8.6 where the upper limit to the steepness of the energy spectrum, γ_{max}, is given at 95% confidence level. γ_{max} may be lower in the polar than in the equatorial region though this is not significant considering the large statistical errors in the equatorial region.

Secondly, the scintillator efficiencies were folded into the neutron energy spectrum calculated by Newkirk (1963), Lingenfelter (1963), Wilson et al. (1969), and Merker (1970). The expected rates in the PHA channels for each of the spectra were then normalized to the observed rates by means of a constant multiplying factor which was chosen such that chi-squared between the observed and the normalized expected rates was a minimum. The normalized rates and the observed rates were then compared. Table 8.7 shows the results for June 1969. We observe that: (a) the Lingenfelter spectral shape, $E^{-1.6}$ in 1-10 MeV, does not fit our measurements; (b) the Newkirk spectrum, $E^{-1.0}$ in 1-10 MeV, fits the measurements fairly well; (c) the Wilson et al.

TABLE 8.6

THE UPPER LIMIT TO γ (γMAX) AND 1-10 MeV NEUTRON LEAKAGE FLUX (N_{1-10} $\int_1^{10} AE^{-\gamma}dE$)

Month 1969	Polar Region		Equatorial Region	
	γmax	$N_{1-10}(cm^2sec)^{-1}$	γmax	$N_{1-10}(cm^2sec)^{-1}$
June	1.07	0.28±0.03	1.28	0.032±0.003
July	0.95	0.26	1.12	0.035
August	0.88	0.28	1.07	0.036
September	1.02	0.27	0.85	0.032

TABLE 8.7

COMPARISON OF NORMALIZED PREDICTED COUNTING RATES AND OBSERVED RATES (SEC^{-1}) FOR THE FOUR SCINTILLATOR CHANNELS PHA 1,2,3, AND 4 IN JUNE 1969

Channel	Predictions				Observations
	Newkirk, 1963	Lingenfelter, 1963	Wilson et al., 1969	Merker, 1970	
			Equatorial Region (P_c >12Gv)		
PHA1	0.0020±0.0004	0.0026±0.0005	0.0019±0.0003	0.0021±0.0004	0.0020±0.0002
PHA2	0.0026±0.0004	0.0030±0.0005	0.0025±0.0004	0.0027±0.0004	0.0022±0.0003
PHA3	0.0022±0.0002	0.0021±0.0002	0.0023±0.0002	0.0022±0.0002	0.0019±0.0002
PHA4	0.0029±0.0003	0.0020±0.0002	0.0030±0.0003	0.0027±0.0003	0.0034±0.0003
x^2 (3 deg freedom)	3.2	16.8	2.5	5.1	
Significance of fit, %	40	<0.1	45	15	
			Polar Region (P_c<0.3Gv)		
PHA1	0.017±0.003	0.024±0.004	0.016±0.003	0.019±0.003	0.015±0.001
PHA2	0.023±0.004	0.028±0.004	0.022±0.003	0.024±0.004	0.019±0.001
PHA3	0.020±0.002	0.020±0.002	0.020±0.002	0.020±0.002	0.018±0.001
PHA4	0.026±0.003	0.019±0.002	0.027±0.003	0.024±0.003	0.030±0.001
x^2 (3 deg freedom)	4.8	34.6	3.2	9.0	
Significance of fit, %	20	<0.1	35	3	

TABLE 8.8

FIT OF NEWKIRK (1963) AND WILSON ET AL. (1969) SPECTRA TO THE OBSERVED PHA COUNTING RATES FOR JUNE-SEPTEMBER 1969

Month 1969	Equatorial Region				Polar Region			
	Significance level*				Significance level*			
	Newkirk		Wilson et al.		Newkirk		Wilson et al.	
	x^2	%	x^2	%	x^2	%	x^2	%
June	3.2	40	2.5	45	4.8	20	3.2	35
July	3.6	30	2.2	55	7.9	5	5.7	15
Aug	6.0	10	5.0	20	10.1	1	7.6	5
Sept	10.1	1	7.6	5	6.4	10	4.5	20

*3 degrees of freedom.

(1969) structural spectrum is a possibly best fit to the data, although the Wilson calculation extends only to 10 MeV and the contributions to the counting rate above 10 MeV were neglected; (d) the Newkirk and Wilson spectra are slightly steeper than the observations; and (e) the Merker spectrum is much steeper than the observed spectra. However, the fit of the PHA counting rates to the Newkirk and Wilson et al. spectra is poorer for the later months (Table 8.8). In any event, the observed counting rates for all the seven months agree within the statistical fluctuations.

Thirdly, the neutron flux at 1-10 MeV was compared with the total neutron flux. Leakage fluxes in 1-10 MeV (fast neutrons) were obtained for the spectra of Newkirk (1963) and Lingenfelter (1963) by using the normalization constants which were used to fit the calculated spectra to the observed scintillator counting rates. The total leakage fluxes were obtained from the gated neutron rates of the He^3 -counter. The measured ratio of fast neutron leakage flux to total leakage flux was then compared with the ratios predicted by Lingenfelter (1963) and Newkirk (1963). For the Lingenfelter spectrum and for the month of June the predicted ratio of fast neutron leakage flux to total neutron leakage flux near the poles is 0.32 compared with the measured

ratio 0.68 ± 0.09. At the equatorial region the predicted ratio is 0.32 and the measured ratio is 0.54 ± 0.07. Therefore the Lingenfelter spectrum appears to be deficient in the 1-10 MeV energy neutrons. However, the Newkirk spectrum agrees with our measurements at the equatorial region. At the polar region there still seems to be more fast neutrons than the Newkirk spectral shape predicts, although it must be remembered that the Newkirk spectrum was originally calculated for the geomagnetic latitude, 57°N. Table 8.9 lists the ratio of the fast neutrons to the total neutrons for the months of June through September, 1969. The enrichment of the fast neutron leakage spectrum in the polar region is also observed for all the seven months and is in agreement with the results of section 2 of this Chapter. To explain the observed variation of latitude effect with atmospheric depth, it has been suggested that there is an enrichment of the neutron energy spectrum preferentially in the high energy region at high latitude due to more of the neutron sources being closer to the top of the atmosphere (Boella et al. 1965).

Finally, the measurements of the total neutron leakage flux, the neutron leakage flux at 1-10 MeV, the spectral shapes for E<1 MeV and E>10 MeV were used to check the measured values of γ in the interval 1-10 MeV.

TABLE 8.9

COMPARISON OF THE FAST NEUTRON LEAKAGE FLUX (N_{1-10}) WITH THE TOTAL LEAKAGE (N_T) USING NEWKIRK'S (1963) ENERGY SPECTRUM

Month 1969	POLAR REGION			EQUATORIAL REGION			(N_F/N_T)poles-(N_F/N_T)eq
	N_F	N_T	N_F/N_T	N_F	N_T	N_F/N_T	
June	0.30±0.02	0.56±0.06	0.54±0.07	0.034±0.003	0.076±0.0008	0.45±0.06	+0.090±0.025
July	0.29	0.55	0.54	0.039	0.077	0.51	+0.028
Aug.	0.32	0.56	0.57	0.049	0.077	0.53	+0.040
Sept.	0.30	0.58	0.51	0.039	0.079	0.50	+0.012
Predicted ratio at λ ~57°N			0.45				

87% (Newkirk spectrum) and 81% (Lingenfelter spectrum) of the counting rates of the OGO-VI He^3 detector are contributed by neutrons with energy less than 1 MeV. We normalized the Newkirk and Lingenfelter spectra for $E < 1$ MeV by the ratio of the neutron flux measured by OGO-VI to the total flux of Newkirk at 0 gm/cm^2 and of Lingenfelter at sunspot minimum and $\lambda > 80°$. At $E < 10$ kev the spectra are of the form E^{-1}. The two spectra are different only at $E > 10$ kev. At 1 MeV the differential fluxes for the normalized spectra are equal (Fig. 42). Differential spectrum for $1 < E < 10$ MeV is most probably given by $0.10\ E^{-0.80}$ or as steep as $0.13E^{-1.05}$. Any spectrum as flat as $E^{-0.48}$ does not merge with either the Lingenfelter or Newkirk spectrum for $E < 1$ MeV. For either the normalized Lingenfelter or Newkirk spectrum in Figure 42, the ratio of the leakage flux at 1-10 MeV to the total leakage flux is 0.46, in approximate agreement with the observed value.

Therefore, in the polar region the lower limit to γ is 0.8 with the most probable value $0.8 < \gamma < 1.0$ for the interval 1-10 MeV.

Our measured neutron spectrum is again shown in Figure 43 which compares most of the recent neutron spectral measurements. White et al. (1972) measured the neutron spectrum of upward moving neutrons at 40°N with a balloon-

borne directional detector. The theoretical spectra of Lingenfelter (1963), and Freden and White (1962) are taken from Figure 3 of White et al. (1972). The Lingenfelter calculations were based on neutron measurements below 10 MeV as described in Chapter 2.2, and at higher energies on measurements in airplanes by Hess et al. (1959). However, the high energy measurements by Hess et al. (1959) had a very poor statistical precision since the neutron counting rates were very low ($\sim$5 hr^{-1}). Not only was the neutron efficiency very small at high energies ($\sim$2% at 200 MeV) but the detector was insufficiently calibrated at high energies. The Freden and White (1962) theoretical spectrum is the neutron flux calculated using the measurements of the radiation belt proton spectrum and the CRAND theory of injection including ionization and nuclear collision losses of protons in the atmosphere. Eyles et al. (1971) used a balloon-borne directional telescope to measure the neutron flux indicated in Figure 43. Heidbreder et al. (1970) made balloon-flights using the directional detector developed by Pinkau (Chapter 3.3). Their measured intensity of the ten upward-moving neutron events from 100-400 MeV is plotted in Figure 43. The balloon measurements by Holt et al. (1966) and Haymes (1964), and the rocket measurements by Baird and Wilson (1966) have all

been normalized to 40°N geomagnetic latitude at solar minimum and at the top of the atmosphere. We observe that, apart from the Baird and Wilson (1966) measurements, the lower energy measurements are consistent with the OGO-VI measurement. The OGO-VI measurement is equally consistent with the higher energy measurements of White et al. (1972), Eyles et al. (1971) and Heidbreder et al. (1970). The spectral flux is 25 times the Lingenfelter's (1963) at 55 MeV. Dragt et al. (1966), and Hess and Killeen (1966) needed this factor to explain the Radiation belt protons.

We have estimated the trapped proton fluxes produced by CRAND using the OGO-VI and White et al. (1972) neutron flux measurements as the neutron decay source. To do this we normalized the results of the calculations of Dragt et al. (1966), and of Hess and Killeen (1966) so as to apply to the recently measured neutron source. The measured and calculated trapped proton fluxes are shown in Table 8.10 for different L-values and also in Figure E for L=1.5. We observe that, though CRAND may explain the high energy trapped protons, at $\lesssim$15 MeV the CRAND source is still about two orders of magnitude too small.

Incidentally, it has been suggested that diffusion may be an important source of the lower energy inner zone protons (Williams, 1972). The comparison of

TABLE 8.10

TRAPPED PROTON FLUXES PRODUCED BY CRAND

ENERGY	$\frac{B}{B_o}$	Calculated Flux+ (Hess & Killeen, 1966; Dragt et al., 1966) L=1.4	L=1.5	L=1.75	Measured Flux+ L=1.4	L=1.5	L=1.8	OBSERVER
50 MeV	1	----	$J_p=10^3$	----	----	$J_p=300$	----	Freden et al. (1965)
	1.38	----	----	$J_p=10^3$	----	----	$J_p=40$	"
	2.55	----	$J_p \sim 2$	----	----	$J_p=4$	----	"
	4.3	----	----	$J_p=4.2$	----	----	$J_p=4$	"
55 MeV	1.77	$J_p=91.6$* $J_p=13.8$**	----	----	$J_p=30$	----	----	Filz and Holeman (1965)
	1.91	$J_p=18.3$* $J_p=2.3$**	----	----	$J_p=6$	----	----	"
	2.09	$J_p=0.5$* $J_p=0.2$**	----	----	$J_p=0.5$	----	----	"
10 MeV	1	----	$J_p=400$	----	----	$J_p=4\times10^4$	----	Freden et al. (1965)
	1.38	----	----	$J_p=400$	----	----	$J_p=6\times10^4$	"
	2.55	----	$J_p<0.4$	----	----	$J_p=20$	----	"
	4.3	----	----	$J_p=0.8$	----	----	$J_p=300$	"
2 MeV	1	----	$J_\perp=3.2\times10^2$	$J_\perp=4.8\times10^2$	----	$J_\perp \sim 10^5$	$J_\perp \sim 10^6$	Fillius and McIlwain (1965)
	2	----	$J_\perp=32$	$J_\perp=160$	----	$J_\perp \sim 5000$	$J_\perp \sim 5\times10^4$	"

+Flux in units of protons/cm^{2}sec MeV

*1962 atmosphere

**Mean atmosphere

the experimentally observed proton fluxes in the inner zone with the cross-L diffusion calculations of Nakada and Mead (1965) by Freden (1969) suggests that diffusion may be an important source of the lower energy inner zone population. However, more accurate calculations should be made to verify or disprove the diffusion theory.

More neutron measurements of the 10-200 MeV albedo neutrons should be made at different latitudes to verify or disprove the CRAND theory. Measurement of the higher energy neutrons and the angular distribution of the higher energy neutrons to supplement the angular distribution of lower energy neutrons ($\leq$10 MeV) measured by our experiment should be performed and the result used as a source for some new calculations aimed at elucidating the origin of the radiation belt protons. Preferably the measurements should be done in space since the neutrons in space are leakage neutrons. The detectors could be flown in balloons but the system must be able to identify the upward moving neutrons.

Moreover, for the balloon measurements, better calculations should be done to eliminate the large uncertainties attending the extrapolation of the neutron measurements, made deep in the atmosphere, to outside the atmosphere.

8.4 Solar Modulation of Cosmic-Ray Albedo Neutrons

8.4.1 Introduction

The solar modulation of cosmic rays should be reflected in the production of neutrons in the earth's atmosphere. The solar-induced variations could result from:

(a) Particles of cosmic-ray energies emitted by the sun during large solar flares.

(b) Forbush decreases which are transient decreases of the cosmic-ray intensity and are associated with magnetic storms. When an expanding stream of fast solar plasma envelopes the earth, some of the galactic cosmic rays are scattered away; and therefore the cosmic-ray intensity within the modulating region is temporarily depressed below that in the surrounding regions. Many theories, such as the Gold's magnetic bottle model and Parker's blast-wave model, have been

advanced to explain Forbush decreases. However, none has so far succeeded in completely explaining the details of this phenomenon.

(c) The 11-year variation which is the variation in the cosmic-ray intensity that is anticorrelated with the 11-year sunspot cycle (Forbush, 1954). The cosmic-ray intensity usually lags behind the change in sunspot number by ∿9 months when solar activity is increasing and by ∿18 months when solar activity is decreasing. This hysterisis effect could be related to the time constants of the build-up and decay of the solar modulation process (Webber, 1967). For a typical cosmic-ray detector such as the neutron monitor the amplitude of the variation is ∿20-30% and is highly energy dependent, the low energy particles being more strongly affected. The diffusion-convection model with adiabatic deceleration has successfully explained the solar cycle modulation.

(d) The solar diurnal variation which is the cosmic-ray intensity variation with a period of one solar day. For cosmic rays of rigidities 1-200 BeV, the amplitude of the diurnal variation is only ∿0.5-1.0% with the direction of maximum

intensity at approximately 85° to the east of the earth-sun line on the average. This small angular anisotropy at the earth is thought to be due to the partial co-rotation of the cosmic ray gas with the sun as a result of the interaction between the cosmic-ray particles and the spiral interplanetary magnetic field.

We studied the effects of solar flare particles in Chapters 6 and 7. In this section of Chapter 8 we are principally concerned with the effects of the 11-year variation and the Forbush decreases on cosmic-ray albedo neutrons since the solar diurnal variation is too small to be seen by our detector.

8.4.2 The Solar Cycle (or 11-yr) Modulation Effects on Cosmic-Ray Albedo Neutrons

8.4.2.1 Comparison with the Lingenfelter (1963) Calculation of the 11-yr. Modulation Effect. Lingenfelter (1963) calculated the energy, latitude and altitude distributions of the neutron albedo for solar minimum and solar maximum. He derived the dependence of neutron production with solar activity cycle from the measurements of the cosmic-ray intensities by Neher (1959), Lockwood (1960), Andersen (1961), and Neher and Andersen (1962), as well as the satellite measurements of the latitude

variation of the primary cosmic-ray intensity of Albert et al. (1962).

To check the theory of Lingenfelter (1963) on the 11-year variation we must make sure that the data being used for the test are free from all variations but the 11-yr variation. There should be no measurable Forbush decrease, no polar cap neutron events, no observable solar neutrons and no neutron production effects by the radiation belt protons. The months of July and October (1969) were exceptionally quiet with low solar indices and no solar proton events (ESSA). Therefore, for the study, we used the He^3 gated neutron counting rates at 400-500 km altitude for the months of July and October and for the locations not containing the Capetown and Brazilian anomalies. The neutron counting rates were those for which the associated total charged particle rates were less than twice the minimum for that location. The neutron rates were then corrected for dead time, for locally produced neutrons and highly ionizing charged particles by the techniques described in Chapter 5 and Appendix B.

The results are shown in Figure 44 which includes the He^3 gated neutron rates for the months of July and October, 1969. Assuming that at any latitude the change in neutron leakage flux calculated by Lingenfelter was a linear function of the cosmic-ray intensity as

measured by a ground-based detector, we found the Lingenfelter fluxes for the months of July and October, 1969. We further normalized the Lingenfelter fluxes by the He^3 neutron counting rate for July. The Figure shows that our measurements are in good agreement with the Lingenfelter calculations of the 11-year solar modulation effect on cosmic-ray albedo neutrons. We suggest, therefore, that the Lingenfelter calculations be used, with greater confidence, to correct neutron fluxes for the 11-yr variation or to compare neutron fluxes measured at different times in the solar activity cycle.

8.4.2.2 Comparison with the Effects of the Solar Cycle Variation on the Protons in the Primary Cosmic-ray Radiation. The solar cycle modulation of the leakage neutron flux ($\leq$10 MeV) is shown in Figures 45 and 46. In Figure 45 we have plotted the monthly average neutron rates (OGO-VI) against the Mt.Washington neutron monitor monthly average rates. The Mt.Washington neutron monitor (P_c=1.25GV) is at 828 gm/cm^2 altitude. The regression curve (4-5GV) is similar in shape to a curve of Webber (1967) which showed the modulation at the earth of the integral flux of protons of rigidity greater than 4.5 GV as a function of Mt.Washington neutron monitor monthly average rates. However, at low vertical cutoff rigidities

(0-0.3GV, 0.3-0.6GV) the plots of the OGO-VI neutron rates against the Mt.Washington neutron monitor rates indicate a high depression of the low energy particles (figure 46). Fig. 46 also contains a plot of the Pioneer 8 monthly average rates against the Mt.Washington neutron monitor monthly average rates. We observe that at this low geomagnetic cutoff the solar cycle variation of the neutron flux ($\leq$10 MeV) is similar to the modulation of the integral flux of galactic cosmic-ray protons of rigidity greater than 0.4GV. The Pioneer 8 telescope responds to protons with Ep > 60 MeV or rigidity $\gtrsim$0.4GV.

Lockwood et al. (1972) observed a similar depression of the low energy particles at the same period in the solar-activity cycle. He plotted the monthly average counting rates of the Pioneer 8 cosmic-ray telescope against the Mt. Washington neutron monitor rates for 1968-1971. He found that there was a transition of the 11-yr modulation onto a completely different regression curve and that this transition was directly related to the June 8 (1969) Forbush decrease and its recovery. From this time up to August 1971 the low energy particles were still very much depressed relative to 1968.

We conclude, therefore, that the 11-year variation

of the albedo neutron flux ($\leq$10 MeV) is similar to the solar cycle modulation of the integral flux of galactic cosmic-ray protons at similar geomagnetic cutoff rigidities. However, it appears that the low energy particles were extremely depressed relative to the high energy particles during June 7 - December 23, 1969.

8.4.3 The Forbush Decrease Effects on Cosmic-ray Albedo Neutrons

The effects of Forbush decreases on the primary cosmic rays have been measured but no theory has succeeded in completely explaining the details of this phenomenon. However, the Forbush decrease effects on cosmic-ray albedo neutrons have not been measured nor any theoretical estimates made. Our data for this analysis were the He^3 gated neutron rate for which the total charged particle rates were not greater than 1.5 times the normal rates for the particular cutoff rigidity. We used the altitude range 400-500 km to ensure that we removed the neutron production effects by the radiation belt protons. The regions of the Brazilian and Capetown anomalies were excluded from the analysis. However, the results are limited by statistics. For example, Figure 47 is the plot of the latitude dependence of the September Forbush decrease compared with the neutron monthly average rate for September. Though the neutron rates during

the Forbush decrease seem lower than the monthly rates the large statistical errors vitiate any quantitative comparison.

However, a series of two successive Forbush decreases (as recorded by a ground-based neutron monitor) occured in November, 1969. It began on November 21 attaining its maximum depression on about December 5. The combined Forbush decreases totalled 6% in amplitude for the Mt.Washington neutron monitor and 15% for the Pioneer 8 cosmic-ray telescope (Figure 48). We have plotted the latitude dependence of the OGO-VI neutron daily average rates during this Forbush decrease in Figure 49 where we have also included the OGO-VI neutron monthly average rates for November and December, 1969. The OGO-VI neutron rates are depressed by 16% in the polar region ($P_c < 0.3$GV). This depression is consistent with the 15% decrease in the Pioneer 8 telescope rates. We conclude that cosmic-ray albedo neutron flux ($\leq$10 MeV) and the integral flux of galactic cosmic-ray protons, at similar geomagnetic cutoff rigidities, are similarly depressed during Forbush decreases. We also explain (a) the smaller Forbush decrease amplitude for the Mt.Washington neutron minitor and (b) the fact that the higher the geomagnetic latitude the larger the Forbush decrease amplitude to be as a result of the greater

effect of the phenomenon on the lower energy particles.

However, the results of Chapter 7 and the short duration of the Forbush decrease indicate that the observed Forbush decrease effects on cosmic-ray albedo neutrons do not significantly decrease the CRAND source of charged particles in the radiation belt.

CHAPTER IX

SUMMARY OF THE CONCLUSIONS

The search for solar neutrons near solar maximum, reported in this thesis, imposes the restriction that the quiet-time solar neutron flux from 1-20 MeV cannot be greater than 1.8×10^{-3} n/cm^2-sec at the 95% confidence level. The resulting solar neutron differential spectrum is an order of magnitude lower than the previous measurements in the overlapping energy range. We have also placed limits on neutron emission from the sun for several flares including two flares of importance 3B. The upper limit solar neutron flux, 5×10^{-2} n/cm^2-sec in 1-20 MeV energy range at the 95% confidence level, which we set for the solar proton event of November 2 (1969) and the solar flare event of June 13 (1969) is the first measured upper limit for solar neutrons emitted during a flare of importance greater than 2B. The event of November 2, 1969 reached the largest peak absorption, 14.5db at 30mH$_z$ during this solar cycle (Masley et al., 1971). The measured upper limit to the solar neutron flux is consistent with the Lingenfelter (1969), and Lingenfelter and Ramaty (1967) models for solar neutron production during solar flares. To observe

the solar neutron flux or to set a lower upper limit to the solar neutron flux we suggest that, during large solar flares such as the November 2 (1969) flare, flights be made with neutron detectors which have much larger geometrical factors, better efficiency and directionality to reduce the background of atmospheric neutrons. To minimize the loss of solar neutrons by decay and to provide a good time coverage we further suggest that the detectors be carried by satellites orbiting closer to the sun. However, the detectors should be capable of eliminating the background of non-neutron sources such as gamma rays.

The solar proton albedo neutrons were also studied at high and low latitudes for the solar proton events of September 25, November 2, November 24, December 18 and December 19, 1969. In the polar region we measured solar proton albedo neutron fluxes which were in reasonable agreement with the predictions of Lingenfelter and Flamm (1964). The low latitude studies, which included the November 2 solar proton event of importance 3B, substantiated this agreement. We conclude that SPAND is inadequate to provide the anomalously large fluxes of the low-energy protons observed at $L > 1.6$ in the inner radiation belt unless severe limitations are imposed on the loss mechanisms used

in the models for calculating the SPAND contribution to the radiation belt protons.

Finally, the flux, latitude dependence, angular distribution, energy spectrum and the solar modulation of the cosmic-ray albedo neutrons ($\leq$10 MeV) were measured. The neutron leakage flux obtained by the OGO-VI experiment agrees with the results of the other neutron albedo experiments ($\leq$10 MeV) if the Newkirk energy spectrum and the same angular distribution of albedo neutrons for the different experiments are used to obtain the total leakage flux. The measured neutron flux was about 0.7 times the Lingenfelter (1963) flux in agreement with Miles (1964) who, using BF_3 ionization chambers, measured a neutron density in the atmosphere 0.6 times the Lingenfelter's. The latitude dependence was in reasonable agreement with that calculated by Lingenfelter (1963).

We have, by an indirect method, measured for the first time the angular distribution of the albedo neutrons ($\leq$10 MeV) at the top of the atmosphere. The isotropic angular distribution, $k(\nu) = 1$, of the albedo neutrons at the top of the atmosphere best fits our neutron measurements at geomagnetic latitudes less than 60°. However, the angular distribution $k(\nu) = 1-0.5 \cos \nu$ is the best fit in the polar region ($P_c<0.3$ GV). The isotropic angular distribution gives a significant

fit even in the polar region. The slightly flatter angular distribution in the polar region is attributed to the enrichment of the neutron energy spectrum preferentially in the high energy region at high latitude. We suggest that similar experiments be performed to determine the angular distribution of leakage neutrons with energy greater than 10 MeV since the angular distribution of the albedo neutrons is needed to calculate the coefficient for injecting the CRAND products into the radiation belt.

We measured the energy spectrum of the form $E^{-\gamma}(0.8 < \gamma < 1.0)$ in 1-10 MeV energy range, which is consistent with the more recent higher energy (10-100 MeV) measurements of White et al. (1972) at 40°N geomagnetic latitude. The White et al. (1972) flux is about a factor of 25 higher than the Lingenfelter value at 55 MeV. The calculations by Dragt et al. (1966) and by Hess and Killeen (1966) needed approximately this spectral flux to explain the measurements of the trapped proton fluxes by Filz and Holeman (1965). More neutron measurements of the 10-200 MeV albedo neutrons should be performed at different latitudes to verify or disprove the CRAND theory. Preferably the neutron measurements should be done in space since the neutrons in space are leakage neutrons. The detectors could be flown

on balloons but the system must be able to identify the upward moving neutrons. However, for the balloon measurements, better calculations should be done to eliminate the large uncertainties attending the extrapolation of the neutron measurements, made deep in the atmosphere, to outside the atmosphere.

The solar modulation of the cosmic-ray albedo neutrons was also observed. We found that the solar cycle modulation of the albedo neutron flux ($\leq$10 MeV) is similar to the 11-year variation of the integral flux of galactic cosmic-ray protons at similar geomagnetic cutoff rigidities. The regression curve between the OGO-VI neutron rates at low geomagnetic cutoff rigidities (0-0.6GV) and the Mt.Washington neutron monitor rates indicated a high depression of the low energy particles during June 7 - December 23, 1969. We also found, for the first time, that the total leakage neutron flux ($\leq$10 MeV) and the integral flux of galactic cosmic-ray protons at similar geomagnetic cutoff rigidities are similarly depressed during Forbush decreases. The measured 11-yr solar modulation of the cosmic-ray albedo neutrons is in reasonable agreement with the calculations of Lingenfelter (1963). This is the first test of the Lingenfelter (1963) thecry on the 11-yr solar modulation of the cosmic-ray albedo neutrons. We suggest that the

Lingenfelter calculations be used, with more confidence, to correct the neutron flux for solar-cycle modulation and to compare neutron measurements made at different times in the solar activity cycle.

BIBLIOGRAPHY

Albernhe, F., and R. Talon, Ann. Geophys. 25, 99, 1969.

Albert, R.D., C. Gilbert and W. N. Hess, J. Geophys. Res. 67, 3537, 1962.

Alsmiller, R.G. and R.T. Boughner, J. Geophys, Res., 73, 4935, 1968.

Alsmiller, R.G., M. Leimdorfic and J. Bavish ORNL-4046, 1967.

Anand, K.C., S. Biswas, P.J. Lavakare, S. Ramadurai and N. Sreenivasan, Proc. Int. Conf. Cosmic Rays, Lond., 396, 1965.

Apparao, M.V.K., R.R. Daniel, B. Vijayalakshmi and V.L. Bhatt, J. Geophys. Res. 71, 1781, 1966.

Armstrong, A.H., F.B. Harrison, H.H. Heckman and L. Rosen, J. Geophys. Res. 66, 351, 1961.

Baird, G.A., and B.G. Wilson, Can. J. Phys. 44, 2131, 1966.

Balasubrahmanyan, V.K., E. Boldt and R.A.R. Palmeira NASA publication S-611-65-249, 1965.

Bame, S.J., J.P. Conner, F.B. Brumley, R.L. Hostetler and A.C. Green, J. Geophys. Res. 68, 1221, 1963.

Bame, S.J. and J.R. Asbridge, J. Geophys. Res., 71, 4605, 1966.

Bercovitch, M., H. Carmichael, G.C. Hanna and E.P. Hincks, Phys. Rev. 119, 412, 1960.

Bertini, H.W., ORNL-TN-1225, ORNL, 1965.

Bierman, L.V., O. Haxel and A. Schlüter, Z. Naturforschg., 6a, 47, 1951.

Boella, G., G.D. Antoni, G. Dilworth, A. Giannelli, E. Rocca, L. Scarsi and D. Shapiro, Nuovo Cimento 29, 103, 1963.

Boella, G., G.D. Antoni, C. Dilworth, L. Scarsi, G. Pizzi and M. Tagliabue, Nuovo Cimento 27, 1232, 1965.

Boella, G., G.D. Antoni, C. Dilworth, M. Panetti, L. Scarsi and D.S. Intriligator, J. Geophys. Res. 70, 1019, 1965.

Bostrom, C.O., A.J. Zmuda and G.F. Pieper, J. Geophys. Res. 70, 2035, 1965.

Brandt, J.C., Introd. to the Solar Wind, pp.47-48, W.H. Freeman and Co., San Francisco, 1970.

Brown, G. and H. Muirhead, Phil. Mag. 2, 473, 1957.

Carlson, B.G., LA1891, Los Alamos Sc. Lab., Los Alamos, New Mexico, 28, 1955.

Carlson, G.B., LAMS2201, Los Alamos Sci. Lab., Los Alamos, New Mexico, 62, 1958.

Carlson, G.B. and G.I. Bell Proc. Intern. Conf. Peaceful Uses At. Energy 2nd, Geneva, 1958.

Carlson, G.B. LA2260, Los Alamos, Sci. Lab., Los Alamos, New Mexico, 30, 1959.

Chen, F.F., C.P. Leavitt and A.M. Shapiro, Phys Rev. 99, 857, 1955.

Chupp, E.L., Proc. AAS-NASA Symposium on Phys. of Solar Flares (ed. W.N. Hess) p.445, 1964.

Chupp, E.L., W.N. Hess, and C. Curry, J. Geophys. Res. 72, 3809, 1967.

Claflin, E.S., and R.S. White, J. Geophys. Res. 75, 1257, 1970.

Conner, J.P., Phys. Rev. 89, 712, 1953.

Cornwall, J.M., A.R. Sims and R.S. White, J. Geophys. Res. 70, 3099, 1965.

Cortellessa, P., P.D. Benedetto and C. Paizis, Solar Phys. 14, 427, 1970; 20, 474, 1971.

Daniel, R.R., G. Joseph, P.J. Lavakare and R. Sundemajan, Nature, 213, 21, 1967.

Daniel, R.R., G.S. Gokhale, G. Joseph and P.J. Lavakare, J. Geophys. Res. 76, 3152, 1971.

DeJager, C., Space Research VII, p.785, North-Holland Pub. Co., Amsterdam, 1967.

DeJuren, J. and N. Knable, Phys. Rev. 77, 606, 1950.

Dostrovsky, I., P. Rabinowitz and R. Biuins, Phys. Rev. 111, 1659, 1958.

Dragt, A.J., Rev. Geophys. 3, 255, 1965.

Dragt, A.J., M.M. Austin and R.S. White, J. Geophys. Res. 71, 1293, 1966.

Eyles, C.J., A.D. Linney and G.K. Rochester, Proc. XII Int. Cosmic Ray Conf., Hobart, Tasmania, 1971, SOL-12.

Eyles, K.J., A.D. Linney and G.K. Rochester, Solar Physics, 24, 483, 1972.

Fillius, R.W. and C.E. McIlwain, Phys. Rev. letters, 12, 609, 1964.

Fillius, R.W., J. Geophys. Res. 71, 97, 1966.

Filz, R.C. and E. Holeman, J. Geophys. Res. 70, 5807, 1965.

Forbush, S.E., Phys. Rev. 70, 771, 1946.

Forest, D.J. and E.L. Chupp, Solar Physics, 6, 339, 1969.

Fowler, J.L., C.H. Johnson and J.R. Risser, Phys. Rev. 91, 441, 1953.

Freden, S.C. and R.S. White, Phys. Rev. letters 3, 9, 1959.

Freden, S.C. and R.S. White, J. Geophys. Res. 65, 1377, 1960.

Freden, S.C., J.B. Blake, and G.A. Paulikas, J. Geophys. Res. 70, 3113,1965.

Freier, P.S. and N.R. Webber, J. Geophys. Res. 68, 1605, 1963.

Friling, L.A., Unpublished M.S. thesis, Univ. of New Hamp., 1964.

Gabbe, J.D. and W.L. Brown, Radiation Trapped in the Earth's Magnetic Field, p.165, (ed.E.M. McCormac) D. Riedel Pub. Co., Dordrecht, Holland.

Geiger, K.W. and C.K. Hargrove, Nucl. Phys. 53, 204-208, 1964.

Greenhill, J.G., J. Phillips, K.B. Fenton, A.G. Fenton and M. Bowthorpe, Proc. Int. Conf. Cosmic Rays, Lond. 1, 538, 1965.

Greenhill, J.G., K.G. Fenton and A.G. Fenton, J. Geophys. Res. 75, 4595, 1970.

Gross, B., Z. Physik 83, 214, 1933.

Gross, E., Lawrence Radiation Lab. Rept. UCRL-330, Feb. 29, 1956.

Haerendel, G., Fortschritte der Physik 12, 271, 1964.

Hanson, A.O., Fast Neutron Physics 1, 3-48 edited by J.B. Marion and J.L. Fowler, Interscience, New York, 1960.

Hanson, A.O. and J.L. McKibben, Phys. Rev. 72, 673, 1947.

Harris, I. and W. Priester, J. Geophys. Res. 67, 4585, 1962.

Harris I. and W. Priester Cospar Int. Ref. Atmos., Part 3, North Holland Pub. Co., Amsterdam, 1965.

Hayakawa, S., Cosmic Ray Physics, p.183, John Wiley & Sons, 1969.

Haymes, R.C., J. Geophys. Res., 69, 841, 1964.

Haymes, R.C., J. Geophys. Res., 69, 841, 853, 1964.

Heidbreder, E., K. Pinkau, C. Reppin and V. Schonfelder, J. Geophys. Res. 75, 6347, 1970.

Hess, W.N., H.W. Patterson, R. Wallace and E.L. Chupp, Phys. Rev. 116, 445, 1959.

Hess, W.N., Phys. Rev. letters 3, 11, 1959.

Hess, W.N. and A.J. Starnes, Phys. Rev. letters 5, 48, 1960.

Hess, W.N., E.H. Canfield and R.E. Lingenfelter, J. Geophys. Res. 66, 665, 1961.

Hess, W.N., J. Killeen, C.Y. Fan, P. Meyer and J.A. Simpson, J. Geophys. Res. 66, 2313, 1961.

Hess, W.N., Proc. 5th Intern. Seminar on Cosmic Rays, La Paz, Bolivia, 17-27 July 1962.

Hess, W.N., Space Sc. Rev. 1, 278, 1962.

Hess, W.N. and J. Killeen, J. Geophys. Res. 71, 2799, 1966.

Hess, W.N. and R.C. Kaifer, Solar Physics, 2, 202, 1967.

Hess, W.N., The Radiation Belt and Magnetosphere, p.71, Blaisdell Pub. Co., 1968.

Holt, S.S., R.B. Mendell and S.A. Korff, J. Geophys. Res. 71, 5109, 1966.

Holt, S.S., J. Geophys. Res. 72, 3507, 1967.

Ifedili, S.O., M.S. thesis, Univ. of New Hampshire, 1970.

Jain, P.L., E. Lohrmann and M.W. Teacher, Phys. Rev. 115, 643, 1959.

Jain, P.L., Phys. Rev., 122, 1890, 1961.

Jenkins, R.W., J.A. Lockwood, S.O. Ifedili and E.L. Chupp, J. Geophys. Res. 75, 4197, 1970.

Jenkins, R.W., S.O. Ifedili, J.A. Lockwood and H. Razdan, J. Geophys. Res. 76, 7470, 1971.

Kiepenheuer, K.O., The Solar Spectrum, p.240 (ed. C. de Jager) D. Riedel, Dordrecht, Holland, 1965.

Kim, C.Y., Can. J. Phys. 46, S753, 1968.

Kim, C.Y., Can. J. Phys. 48, 2155, 1970.

LeCouteur, K.J., Proc. Phys. Soc. Lond., A, 65, 718, 1952.

Lenchek, A.M. and S.F. Singer, Planetary Space Sci. 11, 1151, 1963.

Lingenfelter, R.E., Rev. Geophys. 1, 35, 1963.

Lingenfelter, R.E., J. Geophys. Res. 68, 5633, 1963.

Lingenfelter, R.E., and E.J. Flamm, Science 144, 292, 1964.

Lingenfelter, R.E., and E.J. Flamm, J. Geophys. Res. 69, 2199, 1964.

Lingenfelter, R.E., E.J. Flamm, E.H. Canfield and S. Kellman, J. Geophys. Res. 70, 4077, 1965; 70, 4087, 1965.

Lingenfelter, R.E. and R. Ramaty, High Energy Nuclear Reactions in Astrophysics, p.99 (ed.B.S.P. Shen) W.A. Benjamin Inc., N.Y., 1967.

Lingenfelter, R.E., Solar Physics, 8, 341, 1969.

Lockwood, J.A., J. Geophys. Res. 65, 19, 1960.

Lockwood, J.A., and L.A. Friling, J. Geophys. Res. 73, 6649, 1968.

Lockwood, J.A., E.L. Chupp, and R.W. Jenkins, I.E.E.E. Trans. GeoScience Electronics, GE-7, 88, 1969.

Lockwood, J.A., J.A. Lezniak and W.R. Webber, J. Geophys. Res. 77, 4839, 1972.

Lord, J.J., Phys. Rev. 81, 901, 1951.

Macy, W.W., R.S. White, R.C. Filz and E. Holeman, J. Geophys Res. 75, 4322, 1970.

Malitson, H.H. and W.R. Webber, Solar Proton Manual, NASA Technical Report, TRR-169, 1, 1963.

Marion, J.B. and J.L. Fowler, Fast Neutron Physics 1, 362-371 Interscience Publishers Inc., New York, 1960.

Martin J.P., L. Witten and L. Katz, J. Geophys. Res. 68, 2613, 1963.

Masley, A.J., I.W. McDonough and P.R. Satterblom, Antartic J. United States 5, 172, 1971.

Masley, A.J. and P.R. Satterblom, Proc. XII Int. Cosmic Ray Conf., Hobart, Tasmania, 1971, SOL-33.

McCracken, K.G., J. Geophys. Res. 67, 447, 1962

McCracken, K.G., U.R. Rao and R.P. Bukata, J. Geophys. Res. 72, 4293, 1967.

McDonald, F. B. and G.H. Ludwig, Phys. Rev. letters 13, 783, 1964.

Mendell, R.B. and S.A. Korff, J. Geophys. Res. 68, 5487, 1963.

Merker, M., Ph.D. thesis, New York University, N.Y., 1970.

Merker, M., E.S. Light, R.B. Mendell and S.A. Korff, Acta Phys. Acad. Sci. Hung., 29-2, 739, 1970.

Metropolis, N., R. Bivins, M. Storm, J. M. Miller, G. Friedlander and A. Turkevich, Phys. Rev. 110, 1, 185 and 204, 1958.

Meyer, P. and J.A. Simpson, Phys Rev. 99, 1511, 1955.

Miles, R.F., J. Geophys. Res. 69, 1277, 1964.

Miyake, S., K. Hinotani and K. Nunogaki, J. Phys. Soc. Japan 12, 113, 1957.

Miyake, S., K. Hinotani, I. Katsumata and T. Kaneko, J. Phys. Soc. Japan 12, 845, 1957.

Morrison, P., Encyclopedia of Physics 46/I, p.1., Springer-Verlag, Berlin, 1961.

Nakada, M.P., J. Geophys. Res. 68, 47, 1963.

Naugle, J.E. and D.A. Kniffen, Phys Rev. letters 7, 3, 1961.

Neher, H.V., Nature 184, 423, 1959.

Neher, N.V. and H.R. Anderson, J. Gkophys. Res. 67, 1309, 1962.

Newkirk, L.L., J. Geophys. Res. 68, 1825, 1963.

Pinkau, K., Z. Naturforschg., 219, 2100, 1966.

Preszler, A.M., G.M. Simnett and R.S. White, Phys. Rev. letters 28, 982, 1972.

Ritson, D.M., Techniques of High Energy Physics pp.526-529, 1961.

Roelof, E.C., J. Geophys. Res., 71, 1305, 1966.

Rose, D.C., K.B. Fenton, J. Katzman and J.A. Simpson, Can. J. Phys. 34, 968, 1956.

Rosen, L. and L. Stewart, Phys. Rev. 99, 1052, 1955.

Rosen, L. and L. Stewart, Phys. Rev. 107, 824, 1957.

Rossi, B. and S. Olbert, Introd. to the Phys. of Space, p.115, McGraw-Hill Book Co., N.Y., 1970.

Shea, M.A., D.F. Smart and K.G. McCracken, J. Geophys. Res. 70, 4117, 1965.

Shea, M.A., D.F. Smart and J.R. McCall, Can. J. Phys. 46, S1098, 1968.

Simnett, G., Trans. Am. Geophys, 52, 892, 1971.

Simpson, J.A., Phys Rev. 83, 1175, 1951.

Simpson, J.A., and W.C. Fagot, Phys. Rev. 90, 1068, 1953.

Singer, S.F., Phys. Rev. letters 1, 181, 1958.

Singer, S.F., Phys. Rev. letters 1, 171, 1958.

Smith, J.R., Phys. Rev. 95, 730, 1954.

Smith, R.V., L.F. Chase, W.L. Imhof, J.B. Reagan and M. Walt, ARL-TDR-62-2, 6751 St, Aeronautical Research Lab., Holloman AFB, New Mexico, 1961.

Soberman, R.K., Phys. Rev. 102, 1399, 1956.

St. Onge, R.N., and J.A. Lockwood, Am. Phys.Soc. Bull. 14, 500, 1969.

Tatsuta, H., K. Katoh and Y. Yoshida, Japan J. Appl. Phys. 4, 321, 1965.

Trainor, J.H. and J.A. Lockwood, Trans. Am. Geophys. Union 44, 73, 1963.

Treiman, S.B., Phys. Rev. 86, 917, 1952.

Webber, W.R., Handbuch der Physik 46-2, 197, 1967.

Webber, W.R. and J.F. Ormes, J. Geophys. Res. 72, 3387, 1967.

Wentzel, D.G., Proc. of AAS-NASA Sym. on the Phys. of Solar Flares, (ed. W.N. Hess), NASA SP-50, p.397, 1964.

White, R.S., Trans. Bull. Am. Phys. Soc. 13, 714, 1968.

White, R.S., S. Moon, A.M. Presler and G.M. Simnett, 15th Plenary Meeting COSPAR, 10-24 May 1972, Madrid, Spain.

Williams, D.J. and C.O. Bostrom, J. Geophys. Res. 69, 377, 1964.

Wilson, J.N., J.J. Lambiotti and T. Foelsche, J. Geophys. Res. 74, 6494, 1969.

APPENDIX A

CALCULATION OF THE ALTITUDE VARIATION OF THE NEUTRON COUNTING RATE

A calculation was performed to determine the altitude variation expected for the OGO-VI neutron detector, assuming several different angular distributions of albedo neutrons at the top of the atmosphere. The counting rate of a neutron detector above the earth's atmosphere is given by

$$N = \int_{4\pi} d\vec{\Omega}\, \epsilon(\vec{\Omega})\, \Phi_0(\vec{\Omega}),$$

where $\epsilon(\vec{\Omega})$ is the efficiency of the detector (counts/neutron cm^{-2}) for neutrons arriving in the direction $\vec{\Omega}$, and $\Phi_0(\vec{\Omega})$ is the neutron flux in the direction $\vec{\Omega}$ at the detector (neutrons/cm^2sec ster). The neutron flux $\Phi_0(\vec{\Omega})$ in the direction $(\vec{\Omega})$ at the spacecraft is the same as the neutron flux $\Phi(\vec{\Omega})$ at the top of the atmosphere if the direction $(-\vec{\Omega})$ measured from the detector intersects the top of the atmosphere, and is zero otherwise. $\vec{\Omega}$ can be replaced by $\frac{dA \cos \nu}{r^2}$ where dA (shaded area in figure 39) is a small horizontal area at the top of the atmosphere, ν is the angle between the vertical and $\vec{\Omega}$, and r is the distance (along the direction $\vec{\Omega}$) from the small horizontal dA at

the point (R_o, θ, α) on the earth surface to the spacecraft located at (R, θ_o, α_o). Define $\Phi(\theta)k(\nu)$ (neutrons/cm^2-sterad-sec.) as the angular neutron flux distribution at the top of the atmosphere. $\Phi(\theta)$ is the Lingenfelter leakage flux in neutron/cm^2 sec as a function of latitude. $k(\nu)$ is a constant for an isotropic flux distribution. The neutron counting rate, neglecting neutron decay, is then

$$\int_{\substack{\text{total} \\ \text{visible surface}}} \frac{dA}{r^2} \cos\nu \; \varepsilon(\phi) \; \Phi(\theta) \; k(\nu)$$

where $\varepsilon(\phi)$ is the measured detection efficiency (counts/neutron/cm^2). The effects of gravitational trapping have been excluded since we are considering neutrons in the energy range, 0.1 kev$\leq$E<10 Mev. The direction cosines of the line joining the center of the earth to (θ_o, α_o) are $\cos\alpha_o\sin\theta_o$, $\sin\alpha_o\sin\theta_o$ and $\cos\theta_o$; and for the line joining the center of the earth to (θ, α) the direction cosines are $\cos\alpha\sin\theta$, $\sin\alpha\sin\theta$, $\cos\theta$. Let the angle between these two lines be δ. Then

$$\cos\delta = \cos\alpha_o\sin\theta_o\cos\alpha\sin\theta + \sin\alpha_o\sin\theta_o\sin\alpha\sin\theta + \cos\theta_o\cos\theta$$

$$\therefore \cos\delta = \cos(\alpha_o - \alpha)\sin\theta_o\sin\theta + \cos\theta_o\cos\theta$$

$$\therefore \delta = \cos^{-1}\left[\cos(\alpha_o - \alpha)\sin\theta_o\sin\theta + \cos\theta_o\cos\theta\right]$$

$$dA = R_o^2 \sin\theta \, d\theta \, d\alpha$$

$$r^2 = R^2 + R_o^2 - 2RR_o\cos\delta$$

$$\frac{R_o}{\sin\beta} = \frac{r}{\sin\delta}$$

$$\therefore \beta = \sin^{-1}\frac{R_o\sin\delta}{r}$$

$$\therefore \nu = \beta + \delta = \delta + \sin^{-1}\frac{R_o\sin\delta}{r}$$

The limits of the colatitude, θ, are $\theta_o \pm \cos^{-1}\frac{R_o}{R_o + h}$

The limits of the longitude, α, are obtained by finding the value of α given by the values of $\delta = \cos^{-1}\frac{R_o}{R_o+h}$ for a particular value of θ.

$$\text{Cos } \delta_{max} = \text{Cos}(\alpha_o-\alpha)\ \text{Sin}\theta_o\text{Sin}\theta + \text{Cos}\theta_o\text{cos}\theta$$

$$= \frac{R_o}{R_o+h} \text{ where } R = R_o+h$$

$$\therefore \cos(\alpha_o-\alpha) = \frac{\frac{R_o}{R_o+h} - \text{cos}\theta_o\text{cos}\theta}{\text{sin}\theta_o\text{sin}\theta}$$

$$\therefore \alpha_o-\alpha = \pm\ \text{Cos}^{-1}\left(\frac{\frac{R_o}{R_o+h} - \text{Cos}\theta_o\text{Cos}\theta}{\text{sin}\theta_o\text{sin}\theta}\right)$$

$$\therefore \quad \alpha = \alpha_o \pm \text{Cos}^{-1}\left(\frac{\frac{R_o}{R_o+h} - \text{Cos}\theta_o\text{Cos}\theta}{\text{Sin}\theta_o\text{Sin}\theta}\right)$$

A point on the earth's surface is

$$\bar{S} = R_o\text{Sin}\theta\text{Cos}\alpha\hat{i} + R_o\text{Sin}\theta\text{Sin}\alpha\hat{j} + R_o\text{Cos}\theta\ \hat{K}$$

$$\frac{\partial\bar{S}}{\partial\theta} = R_o\text{Cos}\theta\text{Cos}\alpha\hat{i} + R_o\text{Cos}\theta\text{Sin}\alpha\hat{j} - R_o\text{Sin}\theta\ \hat{K}$$

$\therefore$ the unit vector, $\vec{y}'$, parallel to the line of longitude at (R,θ_o,α_o) is $\vec{y}' = \frac{R_o\text{Cos}\theta_o\text{Cos}\alpha_o\hat{i} + R_o\text{Cos}\theta_o\text{Sin}\alpha_o\hat{j} - R_o\text{Sin}\theta_o\hat{K}}{[(R_o\text{Cos}\theta_o\text{Cos}\alpha_o)^2+(R_o\text{Cos}\theta_o\text{Sin}\alpha_o)^2+(R_o\text{Sin}\theta_o)^2]^{1/2}}$

$$= \text{Cos}\theta_o\text{Cos}\alpha_o\hat{i} + \text{cos}\theta_o\text{sin}\alpha_o\hat{j} - \text{Sin}\theta_o\hat{K}$$

$$\frac{\partial\bar{S}}{\partial\alpha} = -R_o\text{Sin}\theta\text{Sin}\alpha\hat{i} + R_o\text{Sin}\theta\text{Cos}\alpha\ \hat{j}$$

$\therefore$ the unit vector, $\vec{x}'$, parallel to the latitude at (R,θ_o,α_o) is

$$\vec{x}' = \frac{-R_o\text{Sin}\theta_o\text{Sin}\alpha_o\hat{i} + R_o\text{Sin}\theta_o\text{Cos}\alpha_o\ \hat{j}}{[(R_o\text{Sin}\theta_o\text{Sin}\alpha_o)^2+\ (R_o\text{Sin}\theta_o\text{Cos}\alpha_o)^2]^{1/2}}$$

$$= -\text{Sin}\alpha_o\hat{i} + \text{Cos}\alpha_o\hat{j}$$

Let the vector along the spacecraft, $\vec{r}$ (which is in the $\vec{x}'$, y' plane), make an angle of γ_o with $\vec{y}'$.

Then $\vec{r} = (\cos\gamma_o)\vec{y}' + (\sin\gamma_o)\vec{x}'$

$= (\cos\gamma_o)[\cos\theta_o\cos\alpha_o\hat{i} + \cos\theta_o\sin\alpha_o\hat{j} - \sin\theta_o\hat{K}]$

$+ (\sin\gamma_o)[-\sin\alpha_o\hat{i} + \cos\alpha_o\hat{j}]$

The direction cosines of $\vec{r}$ are

$$\frac{R\sin\theta_o\cos\alpha_o - R_o\sin\theta\cos\alpha}{r}$$

$$\frac{R\sin\theta_o\sin\alpha_o - R_o\sin\theta\sin\alpha}{r} \text{ and } \frac{R\cos\theta_o - R_o\cos\theta}{r}$$

where $r = [R^2 + R_o^2 - 2RR_o\cos\delta]^{1/2}$

$\therefore \sin\phi = \cos(\frac{\pi}{2} - \phi) = \frac{\vec{r}\cdot\vec{\gamma}}{|\vec{r}|\ |\vec{\gamma}|}$

$$= \frac{R\sin\theta_o\cos\alpha_o - R_o\sin\theta\cos\alpha}{r}(\cos\gamma_o\cos\theta_o\cos\alpha_o - \sin\gamma_o\sin\alpha_o)$$

$$+ \frac{R\sin\theta_o\sin\alpha_o - R_o\sin\theta\sin\alpha}{r}(\cos\gamma_o\cos\theta_o\sin\alpha_o + \sin\gamma_o\cos\alpha_o)$$

$$- \frac{R\cos\theta_o - R_o\cos\theta}{r}(\cos\gamma_o\sin\theta_o)$$

Therefore, the total counting rate at a height h and coordinates $(R_o+h,\ \theta_o,\ \alpha_o)$ is

$$N = \int_{\theta_1}^{\theta_2} d\theta \int_{\alpha_1(\theta)}^{\alpha_2(\theta)} d\alpha\ \frac{R_o^2\sin\theta}{r^2}\,\varepsilon(\phi)\,\cos(\nu)\,\Phi(\theta)\,K(\nu)$$

where $\theta_1 = \theta_o - \cos^{-1}\left(\frac{R_o}{R_o+h}\right)$

$$\theta_2 = \theta_o + \cos^{-1}\left(\frac{R_o}{R_o+h}\right)$$

$$\alpha_1(\theta) = \alpha_o - \cos^{-1}\left[\frac{\frac{R_o}{R_o+h} - \cos\theta_o\cos\theta}{\sin\theta_o\sin\theta}\right]$$

$$\alpha_2(\theta) = \alpha_o + \cos^{-1}\left[\frac{\frac{R_o}{R_o+h} - \cos\theta_o\cos\theta}{\sin\theta_o\sin\theta}\right]$$

$$r^2 = (R_o+h)^2 + R_o^2 - 2(R_o+h)R_o\cos\delta$$

$$\delta = \cos^{-1}\left[\cos(\alpha_o-\alpha)\,\sin\theta_o\sin\theta + \cos\theta_o\cos\theta\right]$$

$$\phi = \sin^{-1}\left[\frac{(R_o+h)\sin\theta_o\cos\alpha_o - R_o\sin\theta\cos\alpha}{\gamma}(\cos\gamma_o\cos\theta_o\cos\alpha_o - \sin\gamma_o\sin\alpha_o)\right.$$

$$+ \frac{(R_o+h)\sin\theta_o\sin\alpha_o - R_o\sin\theta\sin\alpha}{\gamma}(\cos\gamma_o\cos\theta_o\sin\alpha_o + \sin\gamma_o\cos\alpha_o)$$

$$\left. - \frac{(R_o+h)\cos\theta_o - R_o\cos\theta}{\gamma}(\cos\gamma_o\sin\theta_o)\right]$$

$\epsilon(\phi)$ is the measured efficiency as a function of ϕ

$$\nu = \delta + \sin^{-1}\left(\frac{R_o\sin\delta}{\gamma}\right)$$

$\phi(\theta)$ is specified and different values of $k(\nu)$ are used.

The integral was evaluated by the IBM 360 computer.

Program for calculating the altitude dependence of the neutron counting rate.

```
0001              DIMENSION H(30),FUNCNU(20),PHI(61),EFI(37),ETA(31)
0002              RAD=57.29578
0003              READ(5,10)NOH,IFUNC,IPRIN
0004         10   FORMAT(I2,2I1)
0005              READ(5,31)(PHI(I),I=1,30)
0006         31   FORMAT(16F5.3)
0007              DO100I=31,60
0008              II=61-I
0009         100  PHI(I)=PHI(II)
0010              PHI(61)=PHI(60)
0011              READ(5,40)(EFI(I),I=1,36)
0012           40 FORMAT(16F5.3)
0013              EFI(37)=EFI(36)
0014              READ(5,20)DALPHA,ALFDEL,ETADEL,RO,(H(I),I=1,NOH)
0015           20 FORMAT(3F3.0,12F5.0)
0016              READ(5,30)(FUNCNU(I),I=1,20)
0017           30 FORMAT(20A4)
0018           o01 READ(5,41,END=600)DTHETA,CGAMMA
0019           41 FORMAT(2F3.0)
0020              TO=DTHETA/RAD
0021              AO=DALPHA/RAD
0022              GO=DGAMMA/RAD
0023              DELALF=ALFDEL/RAD
0024              DELETA=ETADEL/RAD
                  C*************************************************************
                  C START LOOP TO DO SEVERAL VALUES OF H
                  C*************************************************************
0025              DO 200 J=1,NOH
0026              WRITE(6,9)
0027            9 FORMAT(1H1,'NEUTRON COUNTING RATE ESTIMATE OVER HEIGHT AND ',
                 1'LATITUDE',//,10X,'N THETA'       THETA',1X)
0028              RARG=RO/(RO+H(J))
0029              R2=(RO+H(J))**2+RO*RO
0030              RR2=2.*RO*(RO+H(J))
0031              SINTO=SIN(TO)
0032              COSTO=COS(TO)
0033              SINAO=SIN(AO)
0034              COSAO=COS(AO)
0035              SINGO=SIN(GO)
0036              COSGO=CCS(GO)
0037              THETA1=TO-ARCOS(RARG)
0038              THETA2=TO+ARCOS(RARG)
0039              IF(THETA1.LT.0.0)THETA1=0.0
0040              FLUX=0.0
0041              II=0
0042              T=THETA1
                  C*************************************************************
                  C CONVERT THETA TO DEGREES TO GET VALUE OF PHI THETA
```

```
      C*************************************************************
0043    110 VALETA=T*RAD
0044        I=VALETA/3.0+1.
0045        PHIETA=PHI(I)
0046        ENETA=0.0
      C*************************************************************
      C CALCULATION OF ALPHA1 AND ALPHA2
      C*************************************************************
0047        IF(SIN(TO)*SIN(T))301,302,301
0048    302 AARG=-.99999
0049        GO TO 188
0050    301 AARG=(RARG-COS(TO)*COS(T))/(SIN(TO)*SIN(T))
0051    303 IF(AARG.LT.(-.99999))AARG=-.99999
0052        IF(AARG.GT.(.99999))AARG=.99999
0053    188 ANGCOS=ARCOS(AARG)
0054        A1=AO-ANGCOS
0055        A2=AO+ANGCOS
0056        A=A1
      C*************************************************************
      C CALCULATION OF SMALL N THETA  BEGINS
      C*************************************************************
0057        SINT=SIN(T)
0058        COST=COS(T)
0059        CSDEL1=SINTO*SINT
0060        CSDEL2=COSTO*COST
0061        IF(IFUNC)130,120,130
0062    120 SUBF1=COSGO*COSTO*COSAO-SINGO*SINAO
0063        SUBF2=COSGO*COSTO*SINAO+SINGO*COSAO
0064        SUBF3=COSGO*SINTO
0065    130 COSDEL=COS(AO-A)*CSDEL1+CSDEL2
0066        R=SQRT(R2-RR2*COSDEL)
0067        IF(COSDEL.LT.(-.99999))COSDEL=-.99999
0068        IF(COSDEL.GT.(.99999))COSDEL=.99999
0069    183 DELTA=ARCOS(COSDEL)
0070        XX=RC*SIN(DELTA)/R
0071        IF(IFUNC)140,150,140
0072    140 IF(XX-1)141,141,142
0073    142 XX=1
0074    141 IF(XX+1)143,144,144
0075    143 XX=0-1
0076    144 FI=ARSIN(XX)
0077        GO TO 160
0078    150 FI=((RO+H(J))*SINTO*COSAO-RO*SINT*COS(A))*SUBF1/R
           2+((RO+H(J))*SINTO*SINAO-RC*SINT*SIN(A))*SUBF2/R
           3-((RO+H(J))*COSTO-RO*COST)*SUBF3/R
0079        IF(FI.LT.(-.99999))FI=-.99999
0080        IF(FI.GT.(.99999))FI=.99999
0081    154 FI=ARSIN(FI)
```

```
C*************************************************************
C CHANGE THETA TO DEGREES  TO GET VALUE OF FUNCTION FROM TABLE
C*************************************************************
0082      160 FIDEG=FI*RAD
0083          I=(FIDEG+90.0)/5.0+1.0
0084          VALFI=EFI(I)
C*************************************************************
C CALCULATION OF K NU
C*************************************************************
0085      164 FNU=DELTA+ARSIN(XX)
C*************************************************************
C*************************************************************
0086          CHANU=1.0
C         CHANU=COS(FNU)
C*************************************************************
C*************************************************************
C CALCULATION OF F ALPHA
C*************************************************************
0087          FUNALF=RO*RO*SINT/(R*R)*VALFI*COS(FNU)*PHIETA*CHANU
0088          IF(II-50)770,771,770
0089      771 WRITE(6,71)FUNALF,FNU,T,A,A1,A2
0090       71 FORMAT(1X,'FUNALF ',F17.12,2X,'FNU ',F12.9,'T,A,A1,A2 ',4F12.9)
0091      770 II=II+1
0092          ENETA=ENETA+FUNALF*DELALF
0093          A=A+DELALF
0094          IF(A-A2)130,170,170
0095      170 IF(IPRIN)190,180,190
0096      180 WRITE(6,50)ENETA,VALETA
0097       50 FORMAT(10X,F6.2,F14.2)
0098      190 FLUX=FLUX+ENETA*DELETA
0099          T=T+DELETA
0100          IF(T-THETA2)110,200,200
0101      200 WRITE(6,60)H(J),OTHETA,ALPHA,OGAMMA,(FUNCNU(I),I=1,20),FLUX
0102       60 FORMAT(1HO,'H IN KILOMETERS  ',F5.0,'THETAO ',F6.2,'DEGREES',
             1/,1X,'ALPHAO  ',F4.0,'DEGREES',/,1X,'GAMMAO  ',F4.0,'DEGREES',/,
             21X,20A4,//,1X,'FLUX ',F11.7)
0103          GO TO 601
0104      600 ETA(1)=0.0
0105          DO 210 I=2,31
0106      210 ETA(I)=(I-1)*3
0107          WRITE(6,70)(ETA(I),PHI(I),I=1,31)
0108       70 FORMAT(1HO,10X,'THETA          PHI THETA ',/,(10X,F6.2,F20.3))
0109          CALL EXIT
0110          END
```

Program for obtaining the total leakage flux using different theoretical spectra.

```
01              DIMENSION ALTXN(126),XN(126),JJ(126),DXNALT(126),GN50(18),FLUX(18)
               2,ALT(18),GNALT(18),DGNALT(18),CN50(18),CN450(18),CN950(18),
               3DFLUX(18)
02        1     FORMAT(T11,I3,T4,F7.2,T29,F8.6/T29,F8.6)
03              DO2 I=1,126
04        2     READ(5,1)JJ(I),ALTXN(I),XN(I),DXNALT(I)
05              DO6 I=1,126
06              IF(ALTXN(I)-400.)6,13,13
07        13    IF(ALTXN(I)-500.)3,6,6
08        3     J=JJ(I)
09        5     GNALT(J)=XN(I)
10              ALT(J)=ALTXN(I)
11              DGNALT(J)=DXNALT(I)
12        6     CONTINUE
13              DO4 J=1,18
14        7     FORMAT(I2,3F9.6)
15        4     READ(5,7)J,CN50(J),CN450(J),CN950(J)
16        8     READ(5,9,END=500)EFF,DEFF,CONST
17              WRITE(6,10)EFF,DEFF,CONST
18        9     FORMAT(2F4.2,F7.5)
19        10    FORMAT(1H1,'EFF= ',2F4.2,5X,'LEAKAGE FLUX= ',F7.5,'*GN(50)/EFF',/)
20              DO11 J=1,18
21              GN50(J)=GNALT(J)*CN50(J)/(CN450(J)+(ALT(J)-450.)*(CN950(J)-CN450(J
               2))/500.)
22              FLUX(J)=CONST*GN50(J)/EFF
23              DFLUX(J)=FLUX(J)*SQRT((DGNALT(J)/GNALT(J))**2+(DEFF/EFF)**2)
24        11    WRITE(6,12)J,GN50(J),FLUX(J),DFLUX(J)
25        12    FORMAT(1X,'RIGIDITY= ',I3,1X,'COUNT RATE(50)= ',F9.6,1X,'LEAKAGE F
               2LUX(50)= ',F9.6,'+-',F9.6/)
26              GO TO 8
27        500   CALL EXIT
28              END
```

Program for fitting AE^{γ} to PHA(scintillator) data

```
0001        101   FORMAT(F5.4)
0002        102   FORMAT(F4.3)
0003        103   FORMAT(8F8.6)
0004        104   FORMAT(F8.6,3F4.2)
0005        201   FORMAT(1H1,'    A    ',2X,'    G    ',8F10.6,4X,'NEUTRONS',2X,'CHI2',
                  2/)
0006        202   FORMAT(F7.5,2X,F4.2,2X,8F10.6,2X,F9.6,2X,F9.6)
0007              DIMENSION EFF(4,97),DEFF(4),EX(4),DEX(4),EC(4),DEC(4),X(97)
0008              DO 2 I=1,4
0009              DO 1 J=1,97
0010              READ(5,101)EFF(I,J)
0011              EFF(I,J)=EFF(I,J)/0.50
0012        1     EFF(I,J)=0.835*EFF(I,J)
0013        2     READ(5,102)DEFF(I)
0014              READ(5,103)EX(1),DEX(1),EX(2),DEX(2),EX(3),DEX(3),EX(4),DEX(4)
0015        7     WRITE(6,201)EX(1),DEX(1),EX(2),DEX(2),EX(3),DEX(3),EX(4),DEX(4)
0016              READ(5,104,END=500)A,GSTART,GEND,GSTEP
0017              G=GSTART
0018        6     CHISQR=0.0
0019              EN=0.0
0020              DO 3 J=1,97
0021              E=0.6+0.2*J
0022              X(J)=A*0.2/(E**G)
0023        3     EN=EN+X(J)
0024              DO 5 I = 1,4
0025              EC(I)=0.0
0026              DO 4 J=1,97
0027        4     EC(I)=EC(I)+EFF(I,J)*X(J)
0028              DEC(I)=EC(I)*DEFF(I)
0029        5     CHISQR=CHISQR+(EC(I)-EX(I))*(EC(I)-EX(I))/(DEC(I)*DEC(I)+
                  2DEX(I)*DEX(I))
0030              EN=A*(1.0-10.**(1.-G))/(G-1.00001)
0031              WRITE(6,202)A,G,EC(1),DEC(1),EC(2),DEC(2),EC(3),DEC(3),EC(4),
                  2DEC(4),EN,CHISQR
0032              G=G+GSTEP
0033              IF(G-GEND)6,6,7
0034        500   CALL EXIT
0035              END
```

Program for fitting different theoretical spectra to the 1-10 MeV neutron rates.

```
001         101   FORMAT(3X,F7.2,I3,I7,8X,F8.6,6X,4F9.7,/,3X,F7.2,I3,I7,8X,F8.6,6X,
                  24F9.7)
002         102   FORMAT(I3)
003         103   FORMAT(2I3)
004         104   FORMAT(I2,3F9.6)
005         105   FORMAT(3A4,F6.4,8F7.6)
006         106   FORMAT(' CARDS MISSORTED')
007         107   FORMAT(1H1,'COUNT RATES AND LEAKAGE FLUXES AT 50 KM FOR ALTITUDE-R
                  2IGIDITY BINS*')
008         108   FORMAT(70X,6(2I4,2X))
009         109    FORMAT(/,30X,'GATED NEUTRONS      PHA1       PHA2       PHA3       P
                  2HA4',/)
010         110   FORMAT(' OBSERVED COUNT RATES',10X,F13.6,4F10.6,'  COUNTS/SECOND')
011         111   FORMAT(' STANDARD DEVIATIONS',11X,F13.6,4F10.6)
012         112   FORMAT(//,1X,3A4,' SPECTRAL SHAPE* FITTED RATES  ',4F10.6,/,
                  2' STANDARD DEVIATIONS',24X,4F10.6,/)
013         113   FORMAT(' CHI-SQUARED BETWEEN FITTED AND OBSERVED RATES = ',F10.4,/
                  2,' 1-10 MEV LEAKAGE FLUX = ',F10.6,' &/- ',F10.6,' /CM2/SEC')
014                DIMENSION PPHA(4),DPPHA(4),ALT(7,18),NTIME(7,18),DATA(5,7,18),
                  2DDATA(5,7,18),NNALT(126),NNRIG(126),X50(18),X450(18),X950(18),
                  3ISPEC(10,3),DATAV(5),DDATAV(5),CALC(10,4),DCALC(10,4),FLUX(10),
                  4CALL(10,4),DCALL(10,4)
015         1      DO 6 N=1,126
016                READ(5,101)AALT1,NNRIG1,NNTIME,GGN,(PPHA(I),I=1,4),AALT2,NNRIG2,
                  2NN,DGGN,(DPPHA(I),I=1,4)
017                IF(AALT1-AALT2)2,3,2
018         3      IF(NNRIG1-NNRIG2)2,4,2
019         4      IF(NN-9999999)2,5,2
020         5      NALT=AALT1/100-3
021                IF(NALT.GT.7)NALT=7
022                IF(NALT)6,6,7
023         7      NRIG=NNRIG1
024                ALT(NALT,NRIG)=AALT1
025                NTIME(NALT,NRIG)=NNTIME
026                DATA(1,NALT,NRIG)=GGN
027                DDATA(1,NALT,NRIG)=DGGN
028                DO 8 I=1,4
029                II=I+1
030                DATA(II,NALT,NRIG)=PPHA(I)
031         8      DDATA(II,NALT,NRIG)=DPPHA(I)
032         6      CONTINUE
033                DO 11 J=1,18
034         11     READ(5,104)NRIG,X50(NRIG),X450(NRIG),X950(NRIG)
035                DO 12 J=1,2
036         12     READ(5,105)(ISPEC(J,K),K=1,3),FLUX(J),((CALC(J,K),DCALC(J,K)),K=1,
                  24)
037         9      DO 18 J=1,126
038                NNALT(J)=0
```

```
      18    NNRIG(J)=0
            READ(5,102,END=500)NBIN
            DO 10 J=1,NBIN
      10    READ(5,103)NNALT(J),NNRIG(J)
            TIMTOT=0.
            ALTAV=0.
            X50AV=0.
            X450AV=0.
            X950AV=0.
            DO 14 I=1,5
            DATAV(I)=0.
      14    DDATAV(I)=0.
            DO 13 J=1,NBIN
            NALT=NNALT(J)
            NRIG=NNRIG(J)
            TIMTOT=TIMTOT+NTIME(NALT,NRIG)
            ALTAV=ALTAV+ALT(NALT,NRIG)*NTIME(NALT,NRIG)
            X50AV=X50AV+X50(NRIG)*NTIME(NALT,NRIG)
            X450AV=X450AV+X450(NRIG)*NTIME(NALT,NRIG)
            X950AV=X950AV+X950(NRIG)*NTIME(NALT,NRIG)
            DO 15 I=1,5
            DATAV(I)=DATAV(I)+DATA(I,NALT,NRIG)*NTIME(NALT,NRIG)
      15    DDATAV(I)=DDATAV(I)+(DDATA(I,NALT,NRIG)*NTIME(NALT,NRIG))**2
      13    CONTINUE
            ALTAV=ALTAV/TIMTOT
            X50AV=X50AV/TIMTOT
            X450AV=X450AV/TIMTOT
            X950AV=X950AV/TIMTOT
            DO 16 I=1,5
            DATAV(I)=DATAV(I)/TIMTOT
      16    DDATAV(I)=SQRT(DDATAV(I))/TIMTOT
            FACTOR=X50AV/(X450AV+(X950AV-X450AV)*(ALTAV-450)/500)
            DO 17 I=1,5
            DATAV(I)=DATAV(I)*FACTOR
      17    DDATAV(I)=DDATAV(I)*FACTOR
            WRITE(6,107)
            WRITE(6,108)((NNALT(K),NNRIG(K)),K=1,NBIN)
      20    WRITE(6,109)
            WRITE(6,110)(DATAV(I),I=1,5)
            WRITE(6,111)(DDATAV(I),I=1,5)
            DO 21 J=1,2
            A1=DATAV(4)/CALC(J,3)
      25    TOP=0.
            BOTTOM=0.
            DO 22 I=1,4
            II=I+1
            FACTOR=(CALC(J,I)*(DDATAV(II))**2+A1*DATAV(II)*(DCALC(J,I))**2)/(
           2A1*A1*(DCALC(J,I))**2+DDATAV(II)**2)
```

```
86                TOP=TOP+DATAV(II)*FACTOR
87          22    BOTTOM=BOTTOM+CALC(J,I)*FACTOR
88                A2=TOP/BOTTOM
89                IF(ABS(A1-A2)-.00001*A1)23,23,24
90          24    A1=A2
91                GO TO 25
92          23    SUM1=0.
93                SUM2=0.
94                CHI2=0.
95                DO 26 I=1,4
96                II=I+1
97                CALL(J,I)=CALC(J,I)*A2
98                DCALL(J,I)=DCALC(J,I)*A2
99                SUM1=SUM1+DDATAV(II)**2
00                SUM2=SUM2+DATAV(II)
01          26    CHI2=CHI2+((CALL(J,I)-DATAV(II))**2)/(DCALL(J,I)**2+DDATAV(II)**2
02                XEAK=0.5*A2*FLUX(J)/.835
03                DLEAK=XEAK*SQRT(.074**2+SUM1/(SUM2**2))
04                WRITE(6,112)(ISPEC(J,K),K=1,3),(CALL(J,I),I=1,4),(DCALL(J,I),I=1,
                  2)
05          21    WRITE(6,113)CHI2,XEAK,DLEAK
06                GO TO 9
07          2     WRITE(6,106)
08          500   CALL EXIT
09                END
```

APPENDIX B

Background Correction of the He^3 Counter Rate

The corrections to the He^3 gated counting rate necessary before using it to determine the leakage neutron fluxes arise from the following types of events.

a. Neutrons produced locally in the spacecraft, adjacent electronic circuitry, and moderator by cosmic rays escaping detection in the anti-coincidence guard counts;

b. Charged particles entering the unguarded ends of the He^3 counter which by their high ionization loss in the He^3 counter produced voltage pulses above discriminator threshold. The following particle events fall into this classification:

   1. Cosmic-ray protons with original energy between 100 and 125 Mev;
   2. Cosmic-ray alphas with original energy between 100 and 375 Mev/nucleon;
   3. Cosmic-ray L, M, and H nuclei, of all energies sufficient to reach the He^3 counter;
   4. Evaporation protons produced in the moderator and walls of the He^3 counter by cosmic rays, and
   5. Shower particles produced in nuclear interactions of the cosmic rays with the moderator and walls of the He^3 counter.

Corrections to the He^3 counter-gated counting rate were evaluated for these sources with the cosmic-ray fluxes given by Webber (1967) corrected to the present time in the solar activity cycle by using the Mt. Washington neutron monitor intensity. The cosmic-ray cutoff rigidities (P_c) were evaluated from the tables given by Shea et al. (1968). The neutron production cross sections and resulting energy distributions of the locally produced neutrons were taken from Chen et al. (1955), Dostrovsky et al. (1958), Jain et al. (1959 and 1961), Bercovitch et al. (1960), Bertini (1965), and Alsmiller et al. (1967). The geometry used for these calculations is shown in Figure B1.

Partial corrections calculated for the polar region at 750 km altitude are listed in Table A. The total correction as a function of geomagnetic cutoff is plotted in Figure 18.

Background Correction of the Scintillator Rates

A scintillator output pulse will occur for several of the types of He^3 counter background events listed in section 1. Since, however, the uppermost discrimination level on the scintillator corresponds to a 10 Mev proton energy loss, the geometry involved excludes a large fraction of the background because the events correspond to more than

TABLE A

CORRECTIONS TO THE He^3 COUNTER GATED COUNTING RATE (GN) AT 750 KM ALTITUDE FOR $P_c \leq 0.3$ GV

A. LOCALLY PRODUCED NEUTRONS		
A) IN THE SPACECRAFT	.002	COUNTS/SECOND
B) IN THE NEIGHBORING ELECTRONICS AND DETECTOR WALLS	.014	
C) IN THE MODERATOR	.002	
B. HIGHLY IONIZING EVENTS IN THE He^3 COUNTER		
A) LOW ENERGY COSMIC RAY PROTONS	.005	
B) LOW ENERGY COSMIC RAY ALPHAS	.010	
C) $Z \geq 3$ COSMIC RAYS (INCLUDING SHOWERS)	.008	
D) EVAPORATION PROTONS FROM COSMIC-RAY INTERACTIONS	.001	
E) PROTON AND ALPHA-INITIATED SHOWER PARTICLES	.000	
TOTAL CORRECTION	.042	COUNTS/SECOND
(ESTIMATED UNCERTAINTY ±30%)		

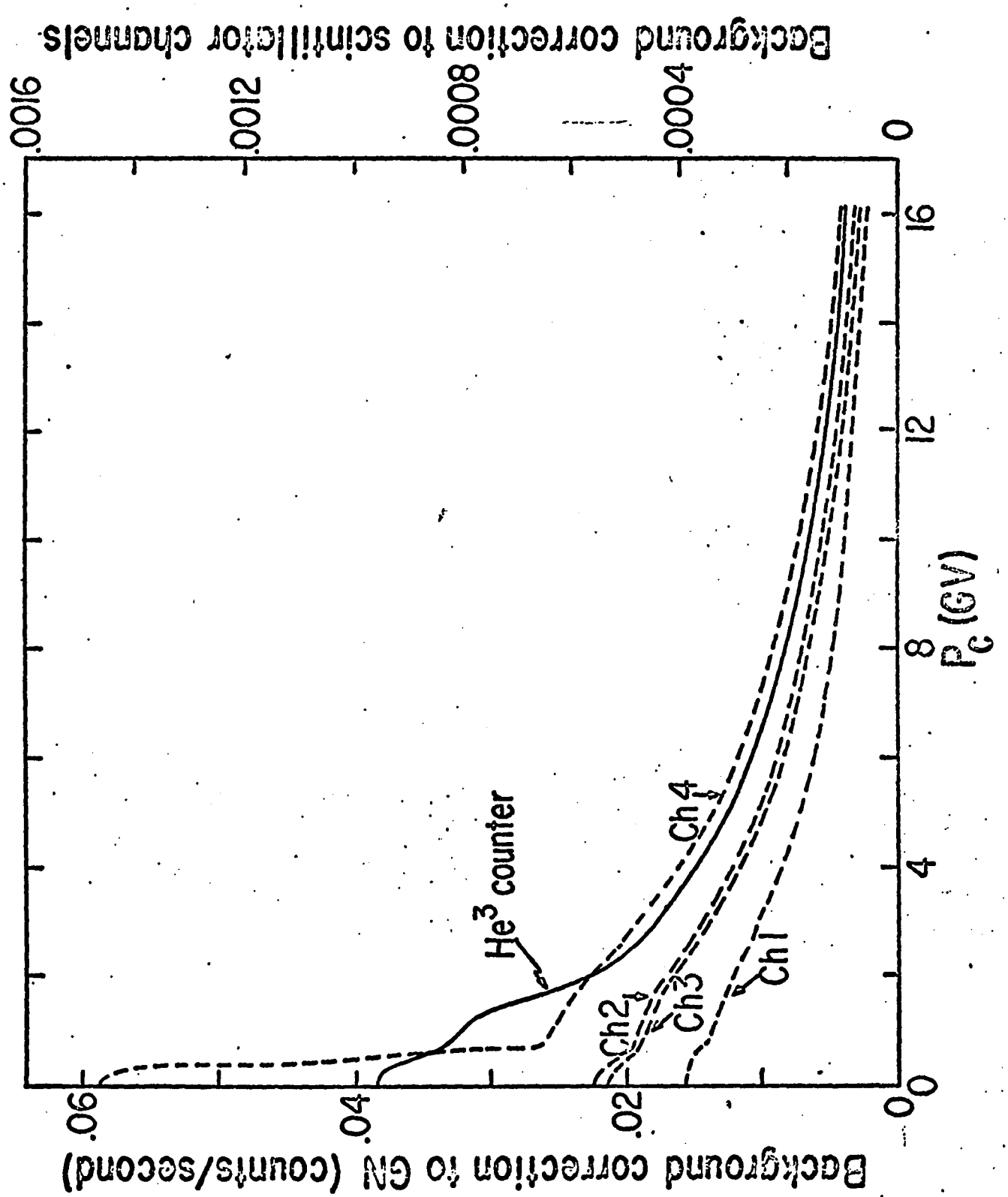
Background correction to GN (counts/second)
.06
.04
.02
0
0
4
8
12
16
P_c (GV)
He^3 counter
Ch4
Ch2
Ch3
Ch1
Background correction to scintillator channels
.0016
.0012
.0008
.0004
0

FIGURE 18

a 10 Mev proton energy in the scintillator. Only a small fraction of the cosmic-ray protons counted by the He^3 detector as GN events have a sufficiently small scintillator light output to be counted as PHA events. The contribution from particles with $Z > 2$ is negligible. On the other hand, the locally produced neutrons having energies between 1 and 15 Mev can contribute to the PHA events.

The contribution to the counting rates PHA 1, 2, 3, and 4 of the scintillator from locally produced neutrons was determined by assuming an evaporation energy spectrum. The spectrum of Alsmiller et al. (1967) for evaporation neutrons produced by 400 Mev protons incident on aluminum was assumed. Then the relative contributions (f_{GN}, f_i,) of these neutrons to the counting rates GN and PHA 1, 2, 3, and 4 were evaluated from the measured efficiency curves. The absolute contribution of locally produced neutrons to the PHA 1, 2, 3, and 4 rates was then determined by putting $R_i = \frac{f_i}{f_{GN}} R_{GN}$, where R_{GN} is the absolute contribution of background to the gated neutron rate calculated in the previous section.

The low energy proton contributions to the PHA counting rates were deduced by noting the relative increases in GN and PHA 1, 2, 3, and 4 rates that occurred in the South Atlantic anomaly, where large fluxes of protons are known to be present. From these relative increases, and the normal contribution of low energy protons to GN calculated in the previous section, the normal contribution of low

TABLE B

Background Contributions to the Counting Rate of the Scintillator PHA Channels for the Polar Region

	PHA 1	PHA 2	PHA 3	PHA 4
LOCALLY PRODUCED NEUTRONS	3.6%	3.8%	3.7%	3.0%
LOW ENERGY PROTONS	0.2%	0.5%	0.6%	3.5%
TOTAL	3.8%	4.3%	4.3%	6.5%

energy protons to PHA 1, 2, 3, and 4 rates were evaluated. Table B lists the background corrections to the scintillator as percentages of the normal counting rate for the polar region. The corrections are less than 7% at all latitudes.

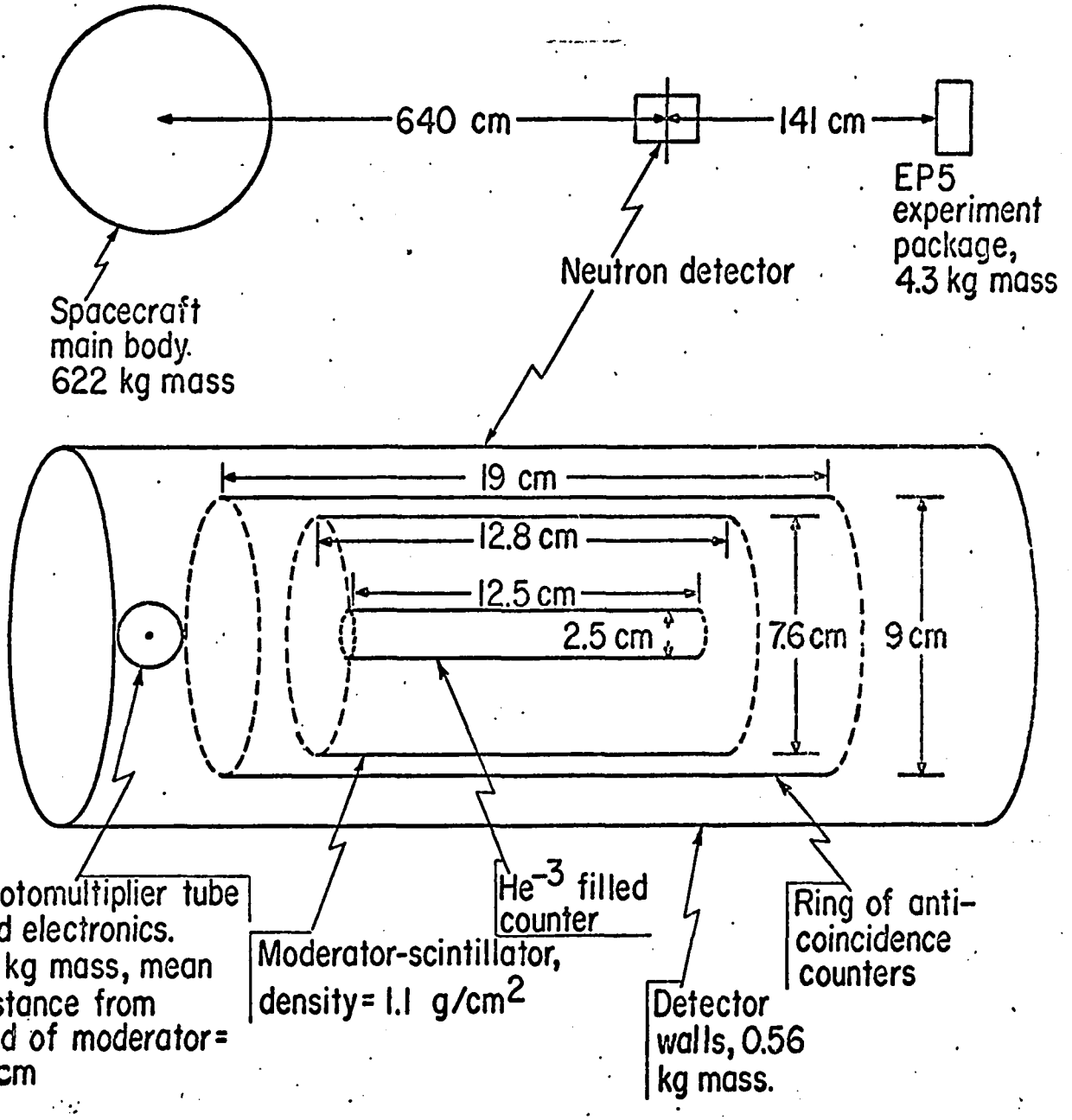
640 cm
141 cm
EP5
experiment
package,
4.3 kg mass
Neutron detector
Spacecraft
main body.
622 kg mass
19 cm
12.8 cm
12.5 cm
2.5 cm
7.6 cm
9 cm
Photomultiplier tube
and electronics.
1.5 kg mass, mean
distance from
end of moderator=
6 cm
Moderator-scintillator,
density= 1.1 g/cm2
He-3 filled
counter
Detector
walls, 0.56
kg mass.
Ring of anti-
coincidence
counters

FIGURE B1

APPENDIX C

In this appendix we shall discuss the calculation used in calibrating the OGO-VI neutron detector with the monoenergetic neutron sources from the Oak Ridge Van der Graaf Accelerator. Let $n(i)$, $N_{LC}(i)$, $N_{GN}(i)$ be the Oak Ridge Long Counter, UNH long counter, OGO-VI gated neutron counts for run i. Let $R(i)$ be the distance of the UNH long counter or OGO-VI sensor from the target for run i. $D_{LC}(i)$ (or $D_{GN}(i)$) is the counts in the UNH long counter (or OGO-VI gated neutron counter) due to neutrons coming directly from the target for run i. $S_{LC}(i)$ (or $S_{GN}(i)$) is the counts in the UNH long counter (or OGO-VI gated neutron counter) due to neutrons scattered from the material surrounding the target or sensor for run i.

$S(i) = S_o\, n(i)$ since independent of distance $R(i)$

$D(i) = D_o \frac{n(i)}{R^2(i)}$ since the direct flux varies as $1/R^2$

$N(i) = S(i) + D(i)$

Put i = 1 when OGO-VI sensor is 1 meter from target

i = 2 when OGO-VI sensor is 2 meters from target

i = 3 when UNH long counter is 1 meter from target

i = 4 when UNH long counter is 2 meters from target

For the OGO-VI sensor,

$N(1) = S(1) + D(1)$

$N(2) = S(2) + D(2)$

But $S(2) = S_o n(2) = S(1) \frac{n(2)}{n(1)}$

$$\text{and } D(2) = D_o \frac{n(2)}{R^2(2)} = D(1) \frac{n(2)}{n(1)} \frac{R^2(1)}{R^2(2)}$$

$$\therefore N(2) = S(1)\frac{n(2)}{n(1)} + D(1) \frac{n(2)}{n(1)} \frac{R^2(1)}{R^2(2)}$$

$$S(1) = N(2)\frac{n(1)}{n(2)} - D(1) \frac{R^2(1)}{R^2(2)}$$

$$N(1) = N(2)\frac{n(1)}{n(2)} - D(1) \frac{R^2(1)}{R^2(2)} + D(1)$$

$$\therefore D(1)_{GN} = \frac{N(1)_{GN} - N(2)_{GN} \frac{n(1)}{n(2)}}{1 - \frac{R^2(1)}{R^2(2)}}$$

$$\text{and } S(1)_{GN} = N(1)_{GN} - D(1)_{GN}$$

For the UNH long counter, we similarly have

$$D(3)_{Lc} = \frac{N(3)_{LC} - N(4)_{LC} \frac{n(3)}{n(4)}}{1 - \frac{R^2(3)}{R^2(4)}}$$

$$\text{and } S(3)_{LC} = N(3)_{LC} - D(3)_{LC}$$

Using the known UNH long counter efficiency, $\epsilon_{LC}(E)$, we obtain the direct neutron flux for run 3,

$$\phi(3) = D(3)_{LC}/\epsilon(E)_{LC}$$

For run 1, the direct flux becomes

$$\phi(1) = \phi(3) \frac{R^2(3)}{R^2(1)} \frac{n(1)}{n(3)}$$

$$\text{i.e. } \phi(1) = \frac{D(3)_{LC}}{\epsilon(E)_{LC}} \frac{R^2(3)}{R^2(1)} \frac{n(1)}{n(3)}$$

The OGO-VI neutron detector efficiency is then

$$\epsilon(E)_{GN} = \frac{D(1)_{GN}}{\phi(1)}$$

$$\text{where } D(1)_{GN} = \frac{N(1)_{GN} - N(2)_{GN} \frac{n(1)}{n(2)}}{1 - \frac{R^2(1)}{R^2(2)}}$$

$$\text{and} \quad \phi(1) = \frac{\frac{D(3)}{LC}}{\frac{\epsilon(E)}{LC}} \frac{R^2(3)}{R^2(1)} \frac{n(1)}{n(3)}$$

$$\text{where } \frac{D(3)}{LC} = \frac{\frac{N(3)}{LC} - \frac{N(4)}{LC}\frac{n(3)}{n(4)}}{1 - \frac{R^2(3)}{R^2(4)}}$$

APPENDIX D

NORTH-SOUTH ASYMMETRY OF THE SOLAR PROTON ALBEDO NEUTRON FLUX (DEC. 19, 1969)

In Chapter 7.1 we discussed the studies of the polar cap neutron events including the December 19 (1969) solar proton event. The December 19 flare was a very interesting event as can be seen in figures D1-D3 which indicate that during the December 19 polar cap neutron event (a) the neutron counting rates ($\leq$10 MeV) in the north polar cap appeared larger than the rates in the south polar cap, (b) the total charged particle rates ($E_p \geq 15$ Mev; $E_e \geq 1.5$ MeV) in the north polar cap were larger than the rates in the south polar cap, and (c) the neutron rates in the north polar cap during the "day" (detector on the sunward side) and "night" (detector completely eclipsed by the earth) appeared to be equal.

There was no north-south asymmetry in the polar neutron counting rates during the December 18 (1969) polar cap neutron event, figure D4.

The December 18 event was a flare from the North-East quadrant of the solar disc. Some of the solar charged particles might have diffused towards

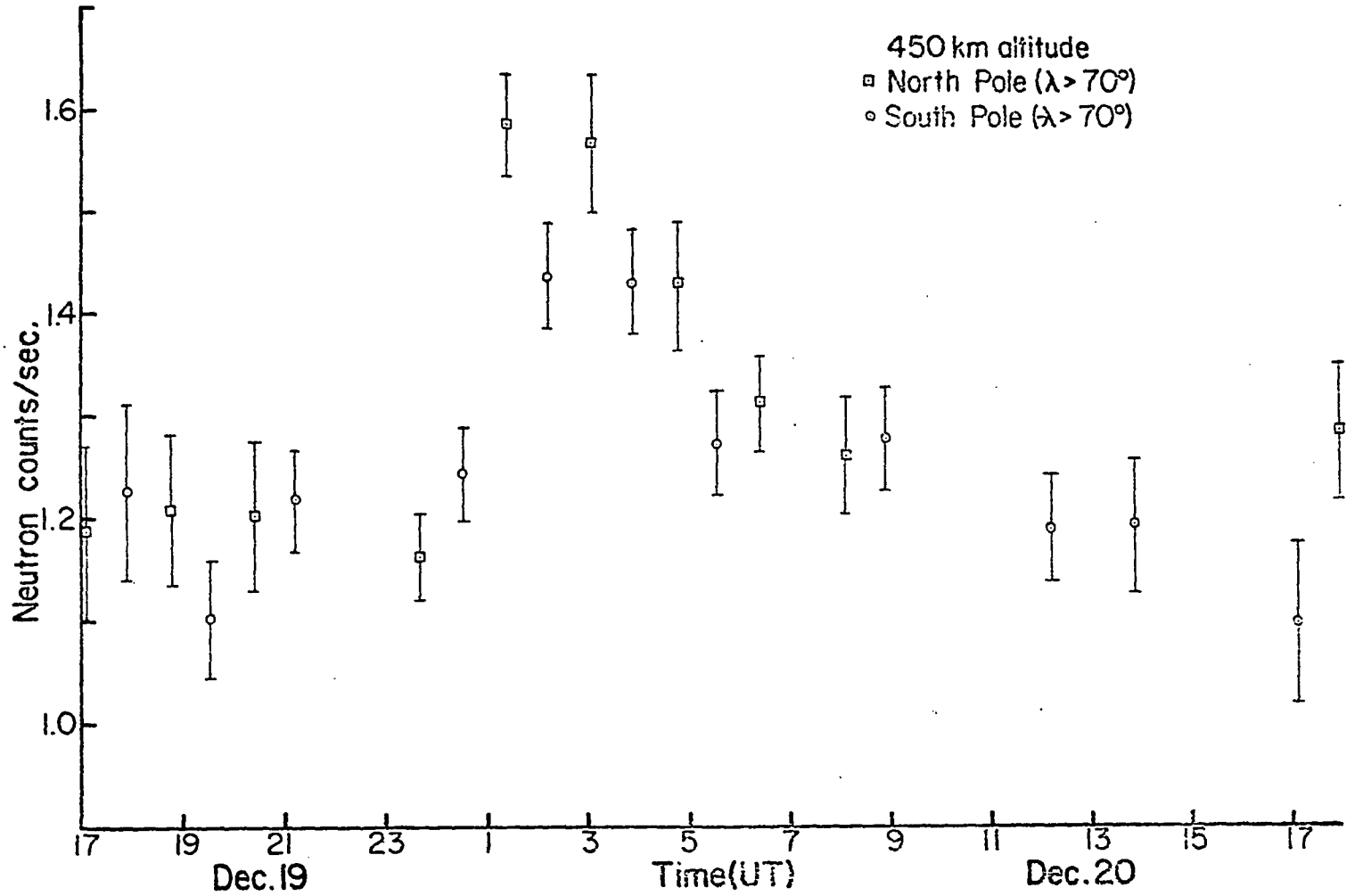
450 km altitude
North Pole (λ > 70°)
South Pole (-λ > 70°)
Neutron counts/sec.
1.6
1.4
1.2
1.0
17
19
21
23
1
3
5
7
9
11
13
15
17
Dec.19
Time(UT)
Dec.20

Figure D1

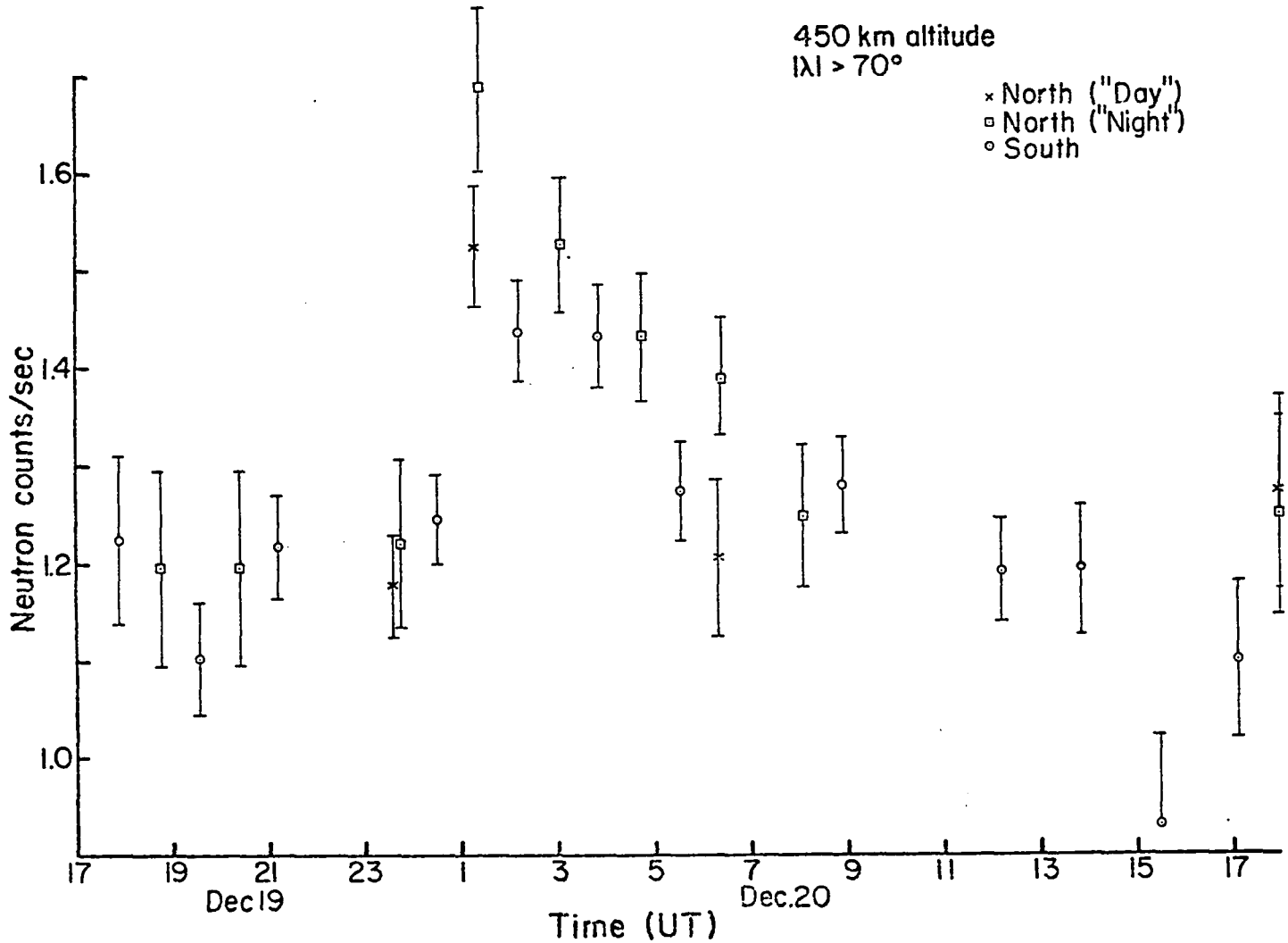
450 km altitude
|λ| > 70°
× North ("Day")
□ North ("Night")
○ South
Neutron counts/sec
1.6
1.4
1.2
1.0
17
19
21
23
1
3
5
7
9
11
13
15
17
Dec19
Dec.20
Time (UT)

Figure D2

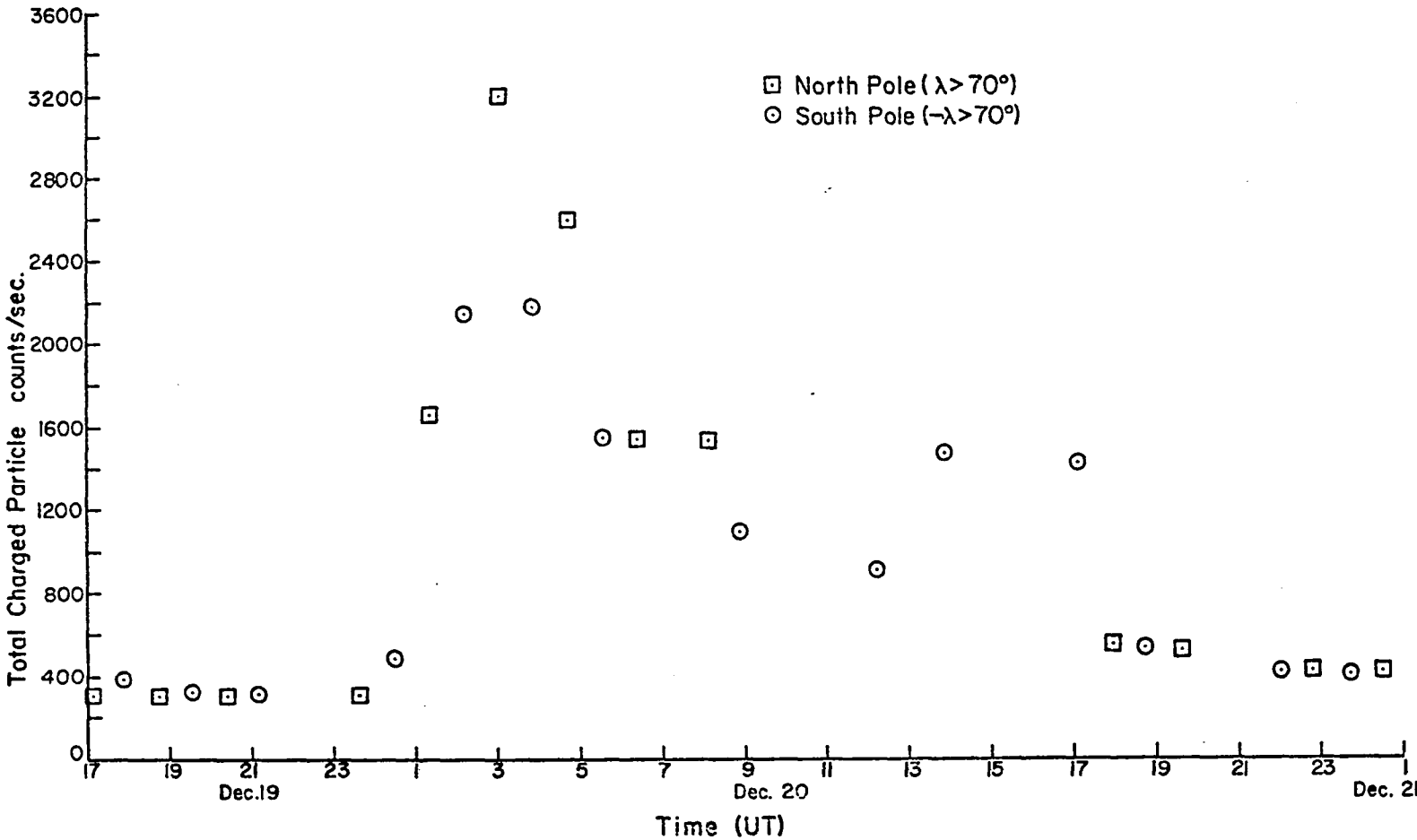
North Pole (λ>70°)
South Pole (¬λ>70°)
Total Charged Particle counts/sec.
3600
3200
2800
2400
2000
1600
1200
800
400
0
17
19
21
23
1
3
5
7
9
11
13
15
17
19
21
23
1
Dec.19
Dec. 20
Dec. 21
Time (UT)

Figure D3

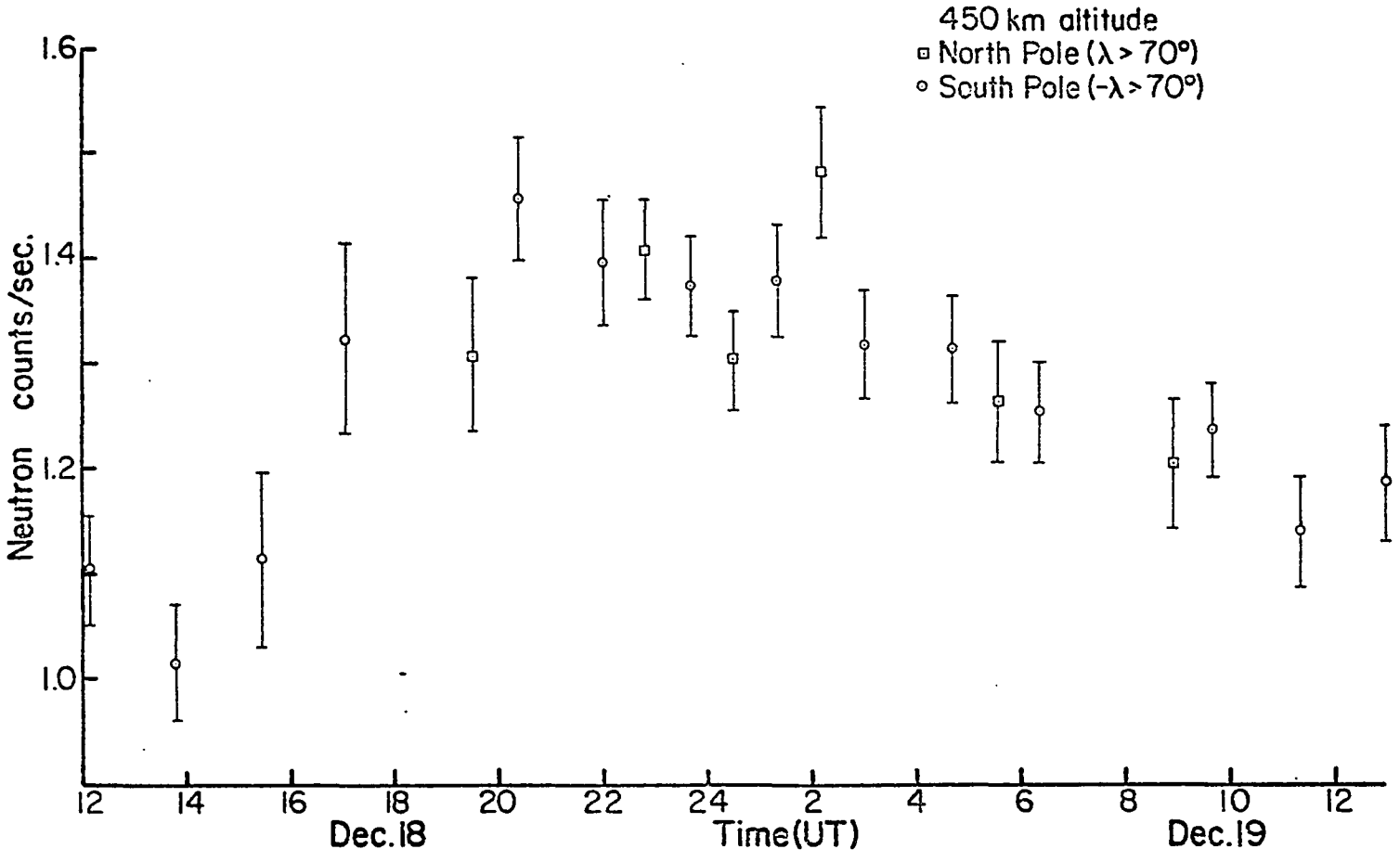
450 km altitude
North Pole (λ > 70°)
South Pole (-λ > 70°)
Neutron counts/sec.
1.6
1.4
1.2
1.0
12
14
16
18
20
22
24
2
4
6
8
10
12
Dec.18
Time(UT)
Dec.19

Figure D4

the sun's western hemisphere, resulting in an isotropized solar beam incident on the earth. We also note that during December 18-20 the sun continuously illuminated the south polar cap and that the December 19 event was a flare from the North-West quadrant of the solar disc. If the fluxes or spectra of the solar charged particles arriving at the earth were different at the north and south polar caps during the December 19 solar proton event, then there could be a North-South asymmetry of the solar proton albedo neutron flux. We suggest that the solar charged particle beams be checked for North-South asymmetry. The North-South asymmetry of the solar charged particles could be consistent with the interconnection of the spiral interplanetary magnetic field lines to the polar (earth) magnetic field lines and with anisotropy in the interplanetary beam.

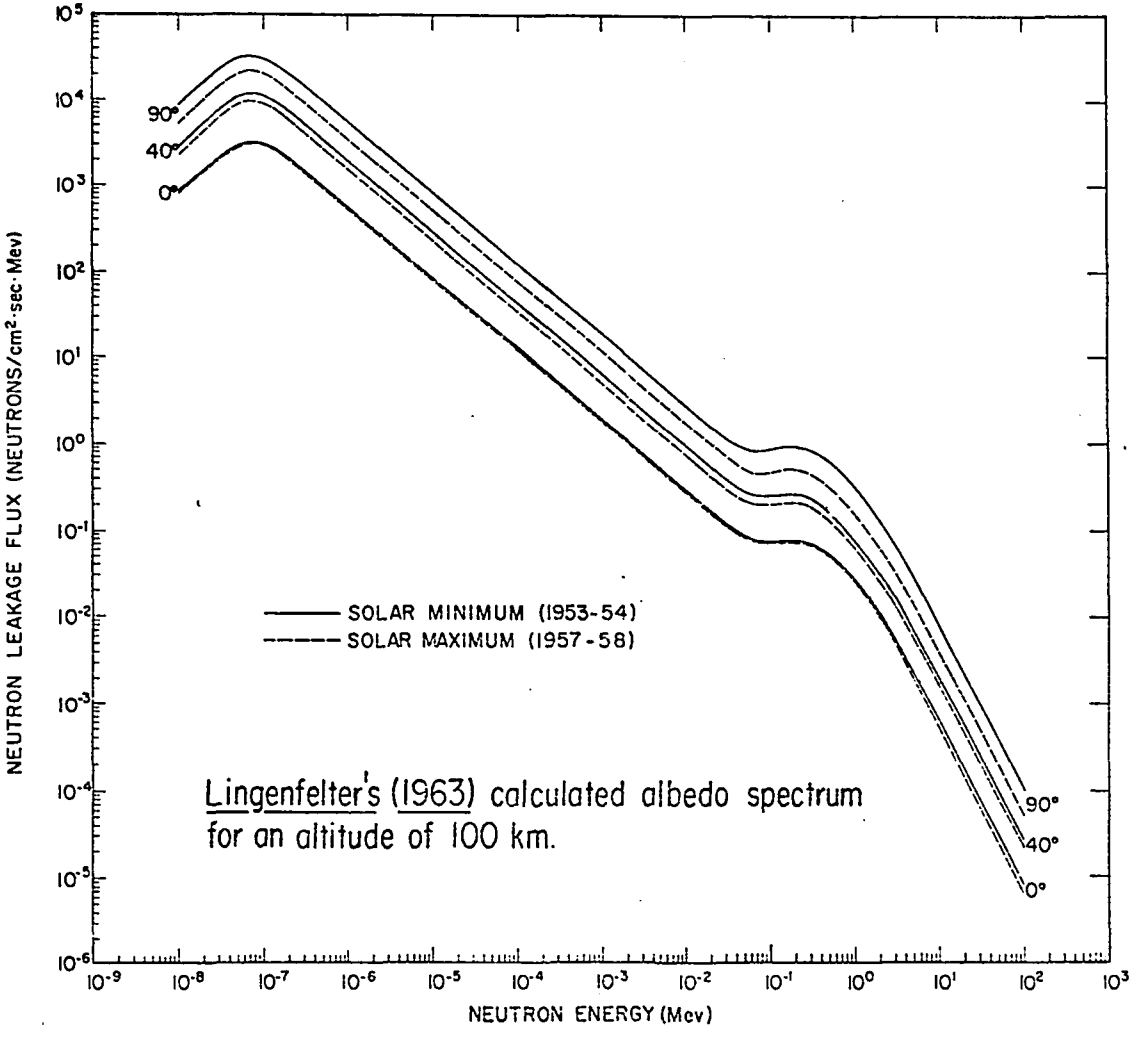
NEUTRON LEAKAGE FLUX (NEUTRONS/cm²·sec·Mev)
NEUTRON ENERGY (Mev)
90°
40°
0°
SOLAR MINIMUM (1953-54)
SOLAR MAXIMUM (1957-58)
Lingenfelter's (1963) calculated albedo spectrum for an altitude of 100 km.

Figure 1

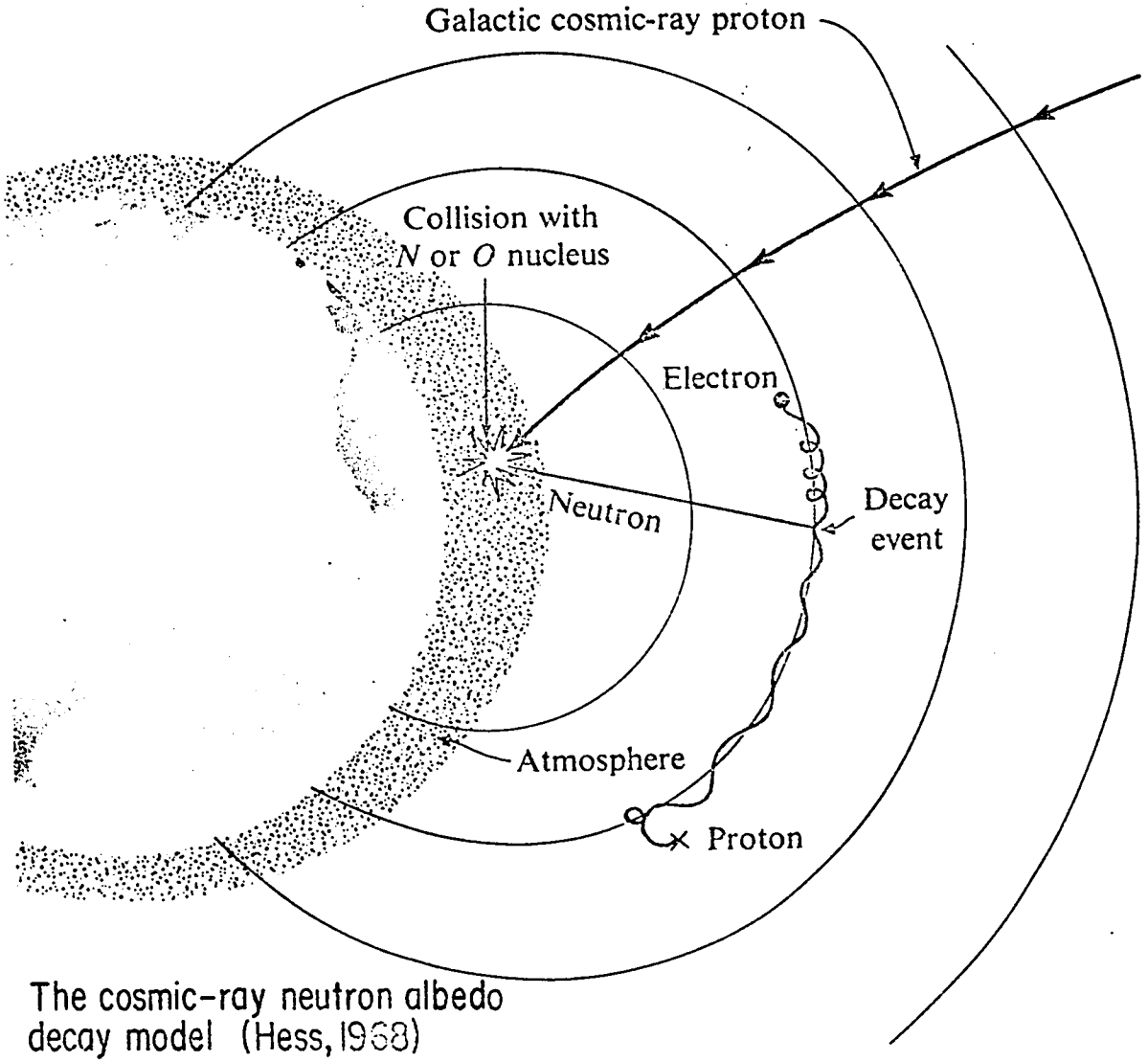

The cosmic-ray neutron albedo decay model (Hess, 1968)

Figure 2

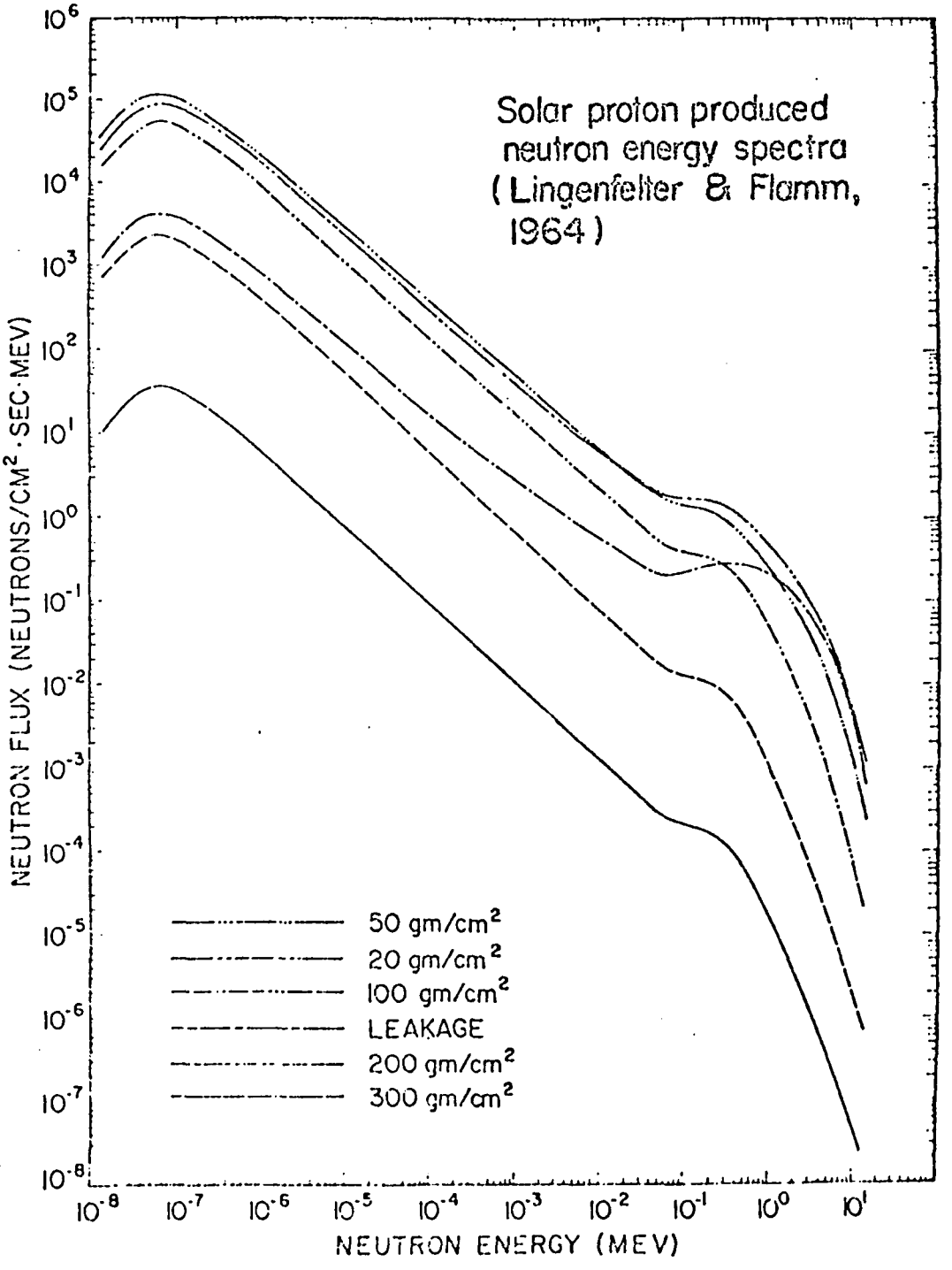
Solar proton produced
neutron energy spectra
(Lingenfelter & Flamm,
1964)
NEUTRON FLUX (NEUTRONS/CM² · SEC · MEV)
NEUTRON ENERGY (MEV)
50 gm/cm²
20 gm/cm²
100 gm/cm²
LEAKAGE
200 gm/cm²
300 gm/cm²

Figure 3

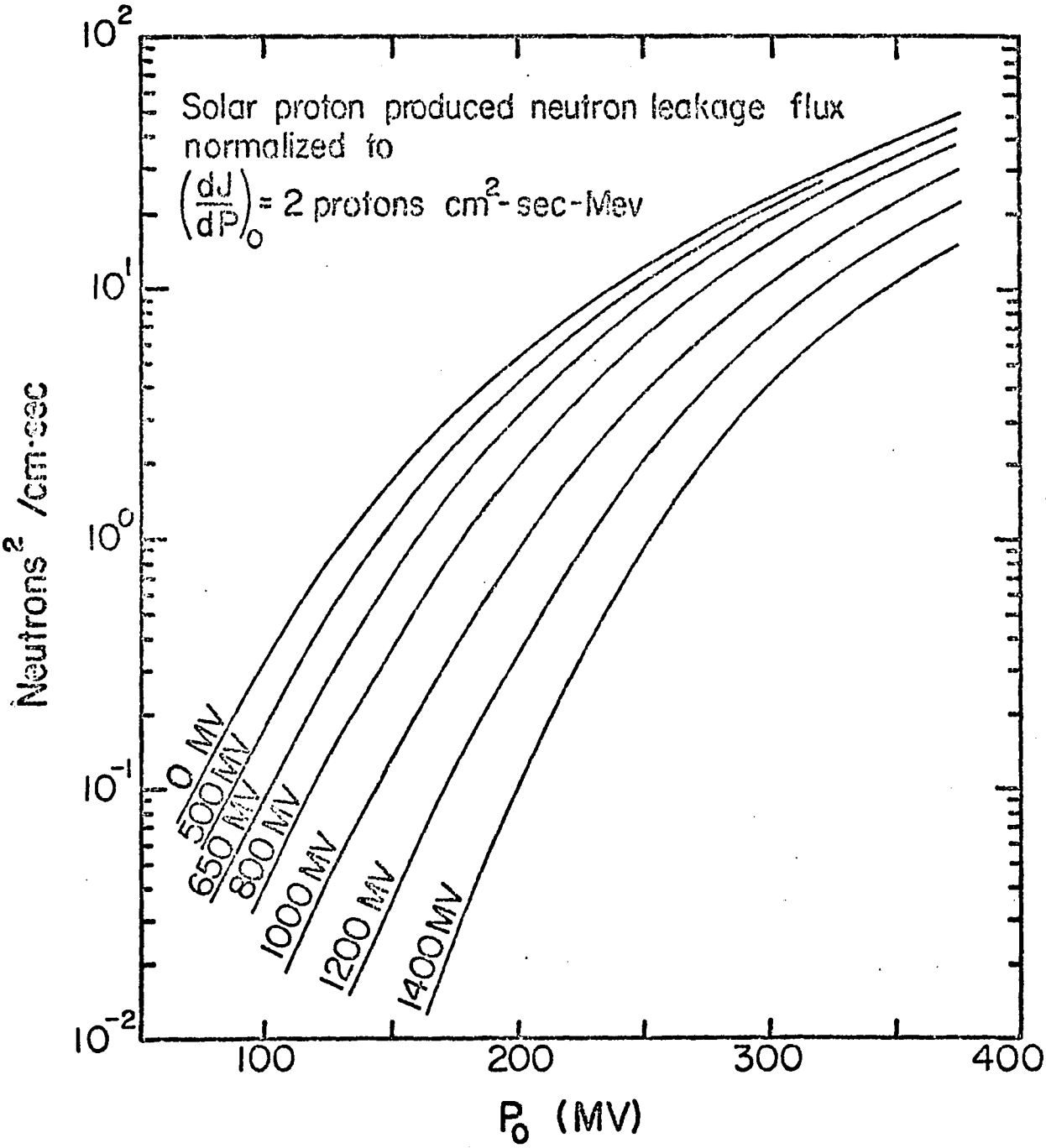
Solar proton produced neutron leakage flux
normalized to
$\left(\frac{dJ}{dP}\right)_0$ = 2 protons cm^2-sec-Mev
Neutrons^2 /cm-sec
10^2
10^1
10^0
10^{-1}
10^{-2}
0 MV
500 MV
650 MV
800 MV
1000 MV
1200 MV
1400 MV
100
200
300
400
P_0 (MV)

Figure 4

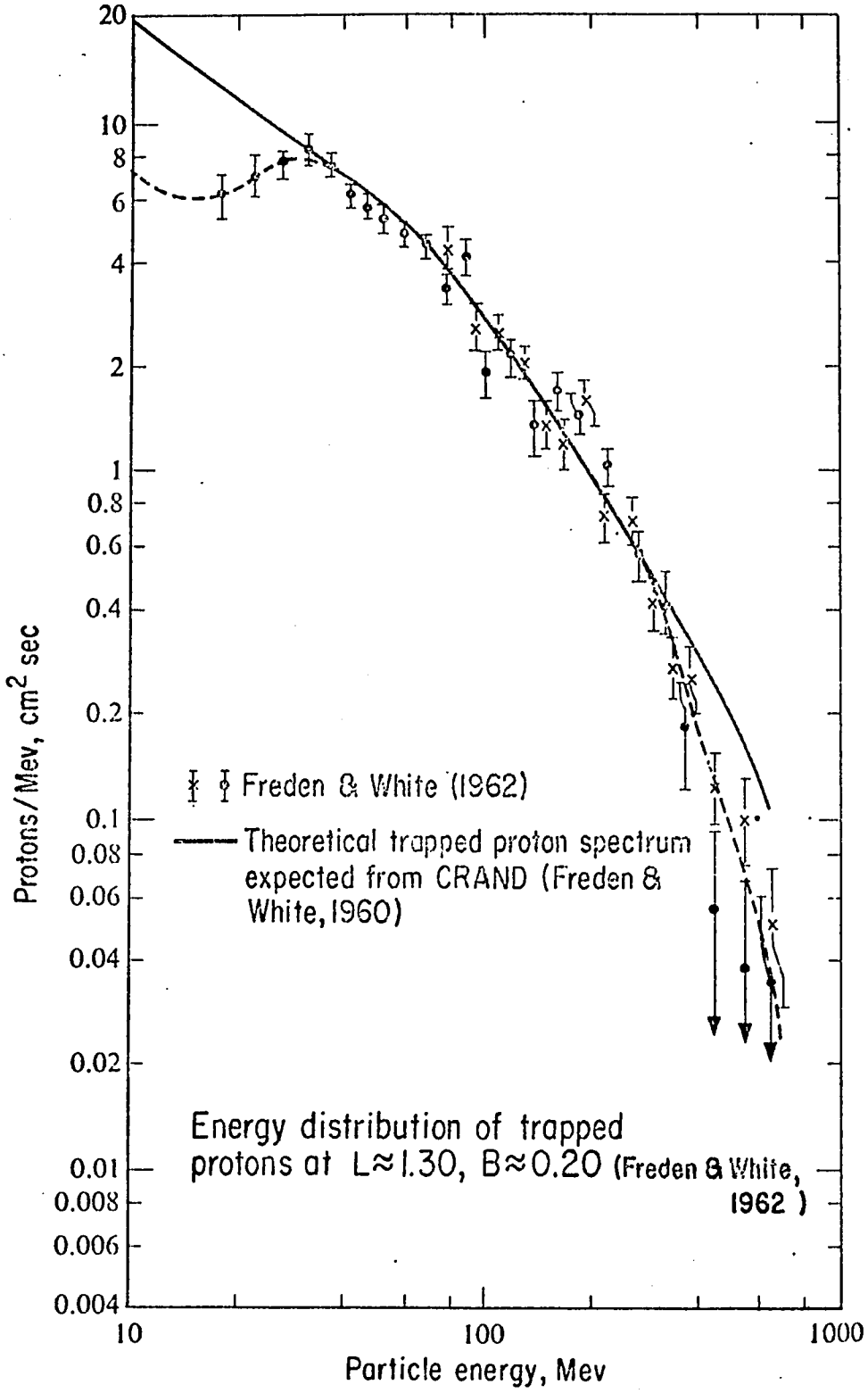
20
10
8
6
4
2
1
0.8
0.6
0.4
0.2
0.1
0.08
0.06
0.04
0.02
0.01
0.008
0.006
0.004
Protons/Mev, cm² sec
Freden & White (1962)
Theoretical trapped proton spectrum expected from CRAND (Freden & White, 1960)
Energy distribution of trapped protons at L≈1.30, B≈0.20 (Freden & White, 1962)
10
100
1000
Particle energy, Mev

Figure 5

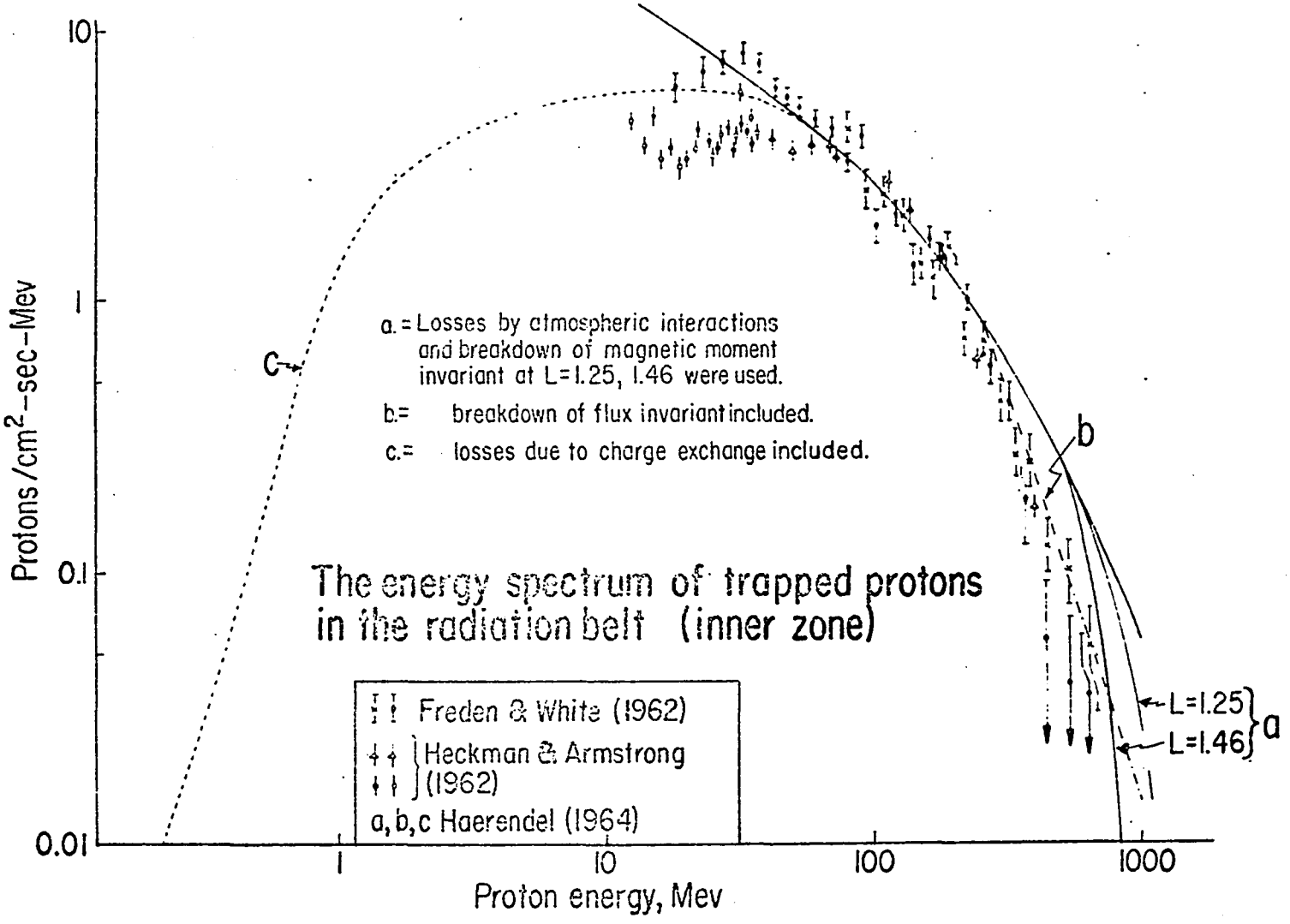
10
1
0.1
0.01
Protons /cm²-sec-Mev
a. = Losses by atmospheric interactions and breakdown of magnetic moment invariant at L=1.25, 1.46 were used.
b.= breakdown of flux invariant included.
c.= losses due to charge exchange included.
The energy spectrum of trapped protons in the radiation belt (inner zone)
Freden & White (1962)
Heckman & Armstrong (1962)
a, b, c Haerendel (1964)
c
b
L=1.25
L=1.46
a
1
10
100
1000
Proton energy, Mev

Figure 6

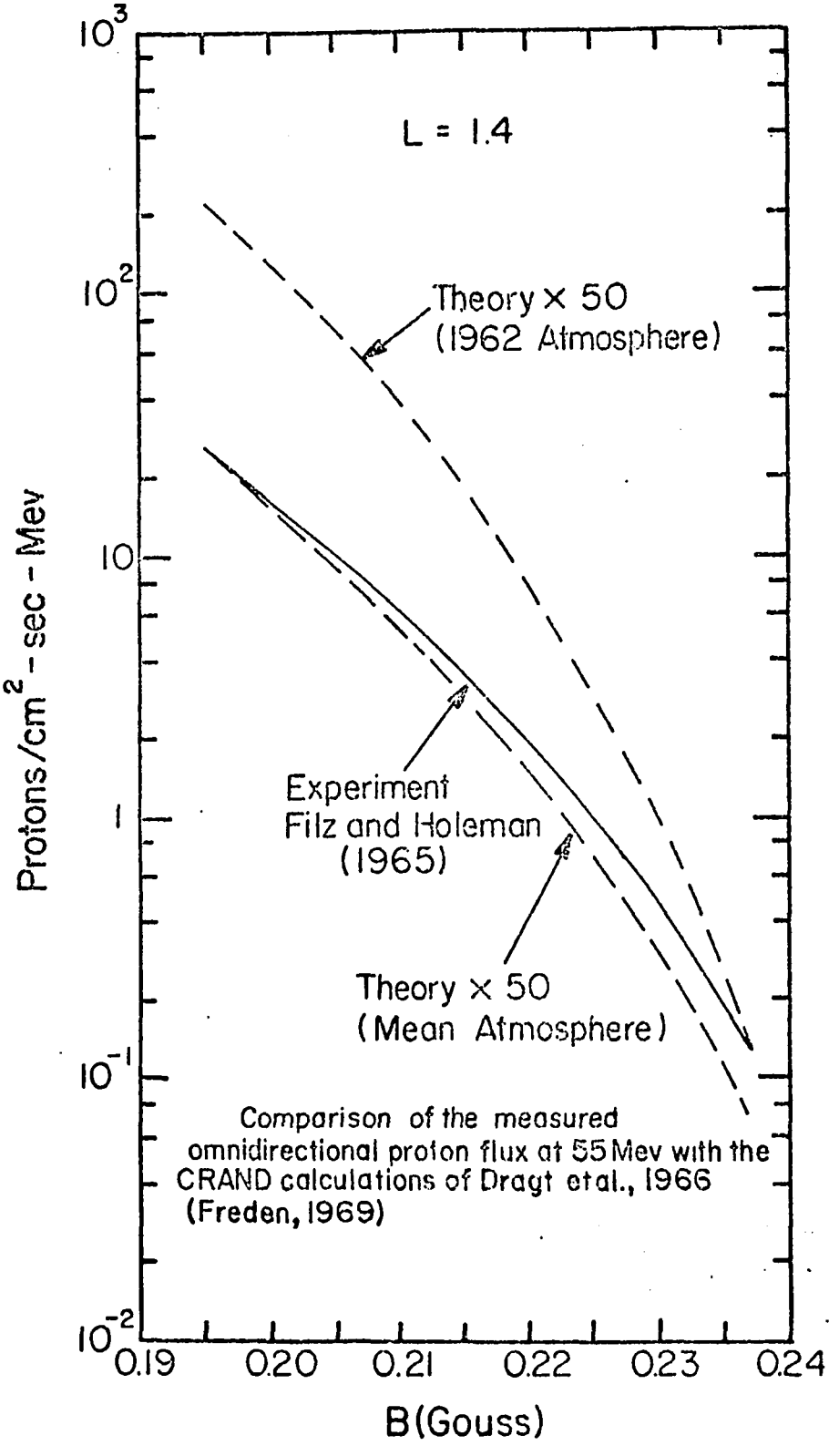
L = 1.4
Theory × 50
(1962 Atmosphere)
Experiment
Filz and Holeman
(1965)
Theory × 50
(Mean Atmosphere)
Comparison of the measured
omnidirectional proton flux at 55 Mev with the
CRAND calculations of Dragt et al., 1966
(Freden, 1969)
Protons/cm² - sec - Mev
B(Gouss)
10³
10²
10
1
10⁻¹
10⁻²
0.19
0.20
0.21
0.22
0.23
0.24

Figure 7

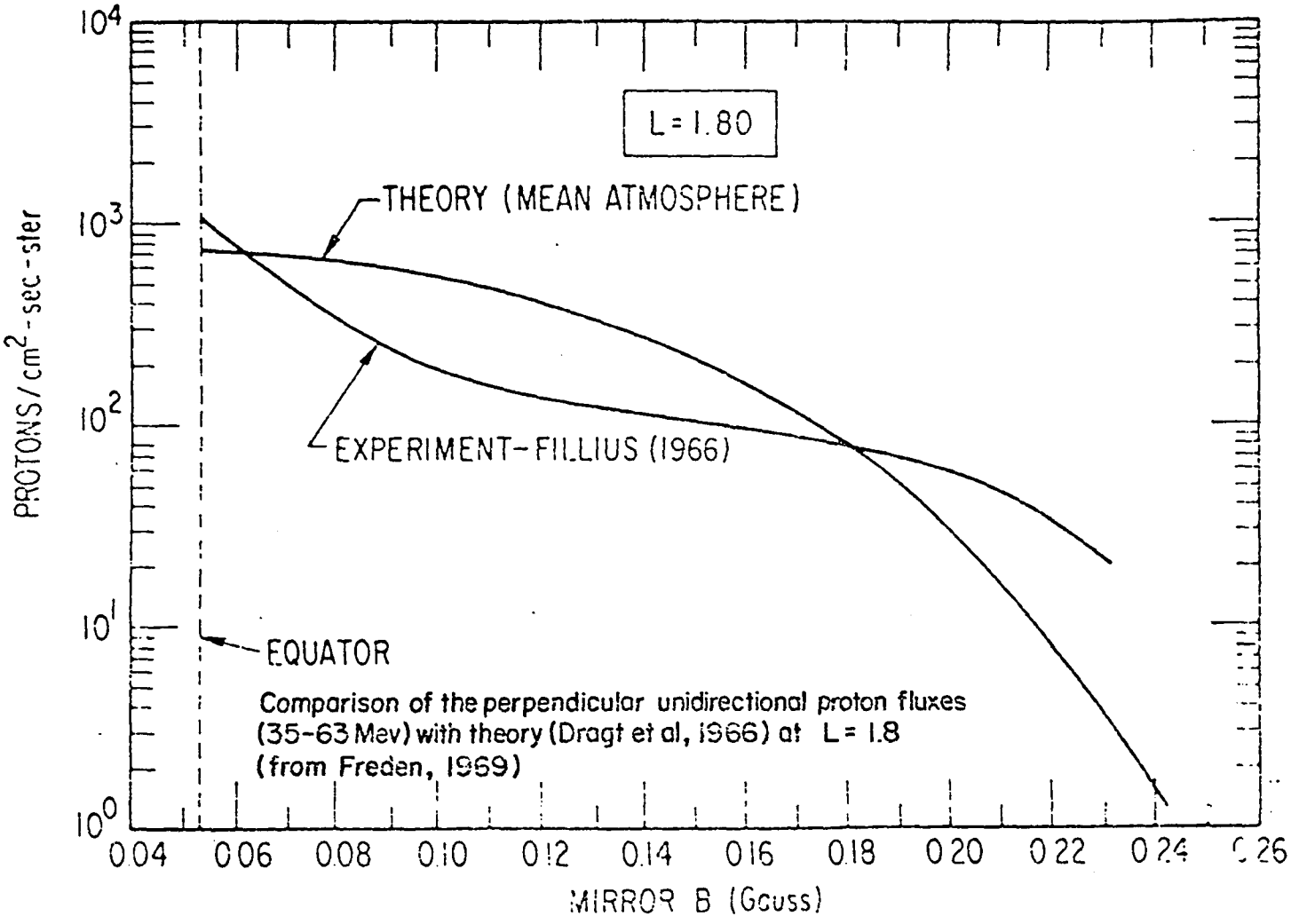
L = 1.80
THEORY (MEAN ATMOSPHERE)
EXPERIMENT-FILLIUS (1966)
EQUATOR
Comparison of the perpendicular unidirectional proton fluxes
(35-63 Mev) with theory (Dragt et al, 1966) at L = 1.8
(from Freden, 1969)
PROTONS/cm^2-sec-ster
10^4
10^3
10^2
10^1
10^0
0.04
0.06
0.08
0.10
0.12
0.14
0.16
0.18
0.20
0.22
0.24
0.26
MIRROR B (Gauss)

Figure 8

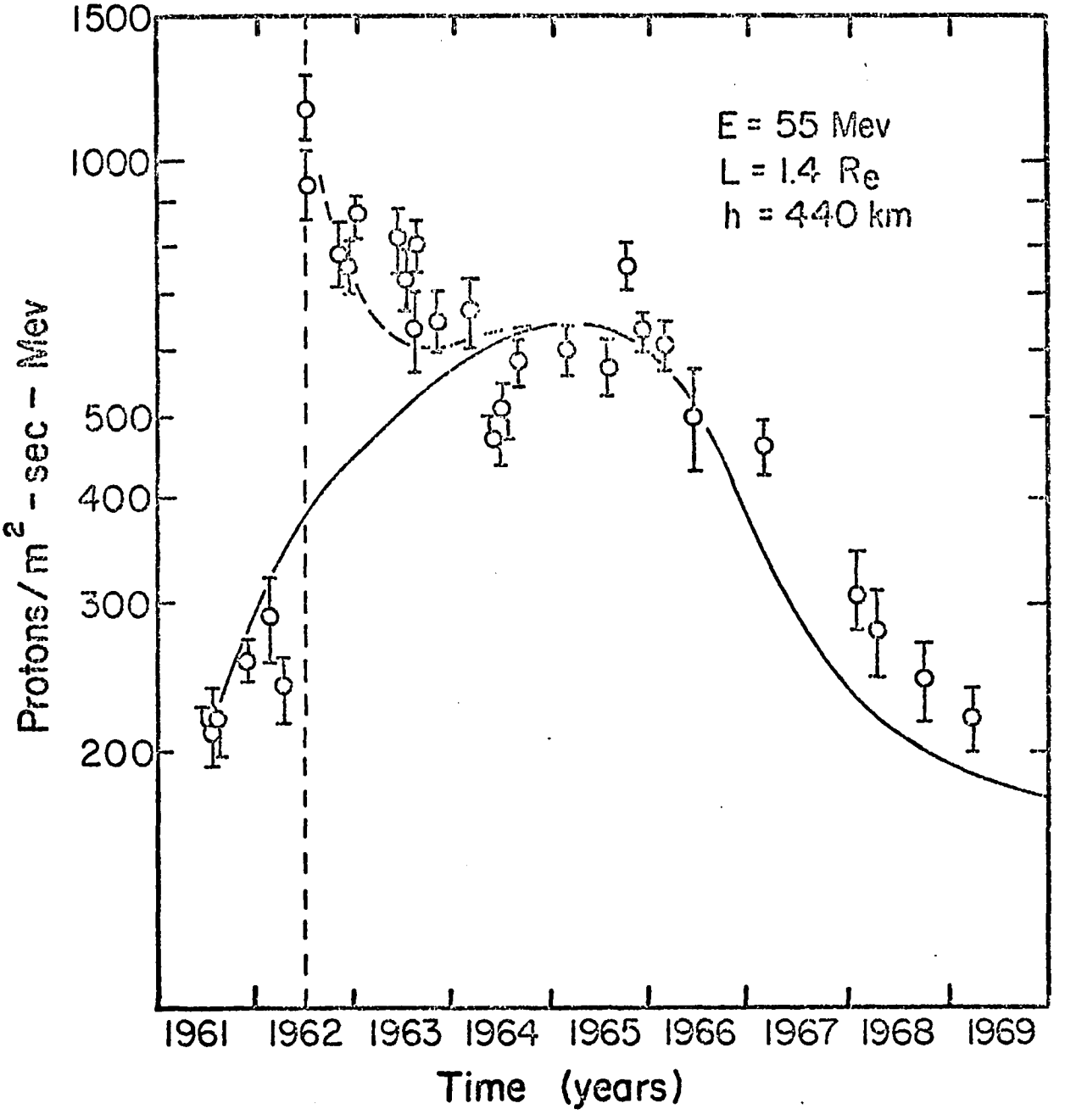
E = 55 Mev
L = 1.4 Re
h = 440 km
Protons/m² - sec - Mev
1500
1000
500
400
300
200
1961
1962
1963
1964
1965
1966
1967
1968
1969
Time (years)

Figure 9

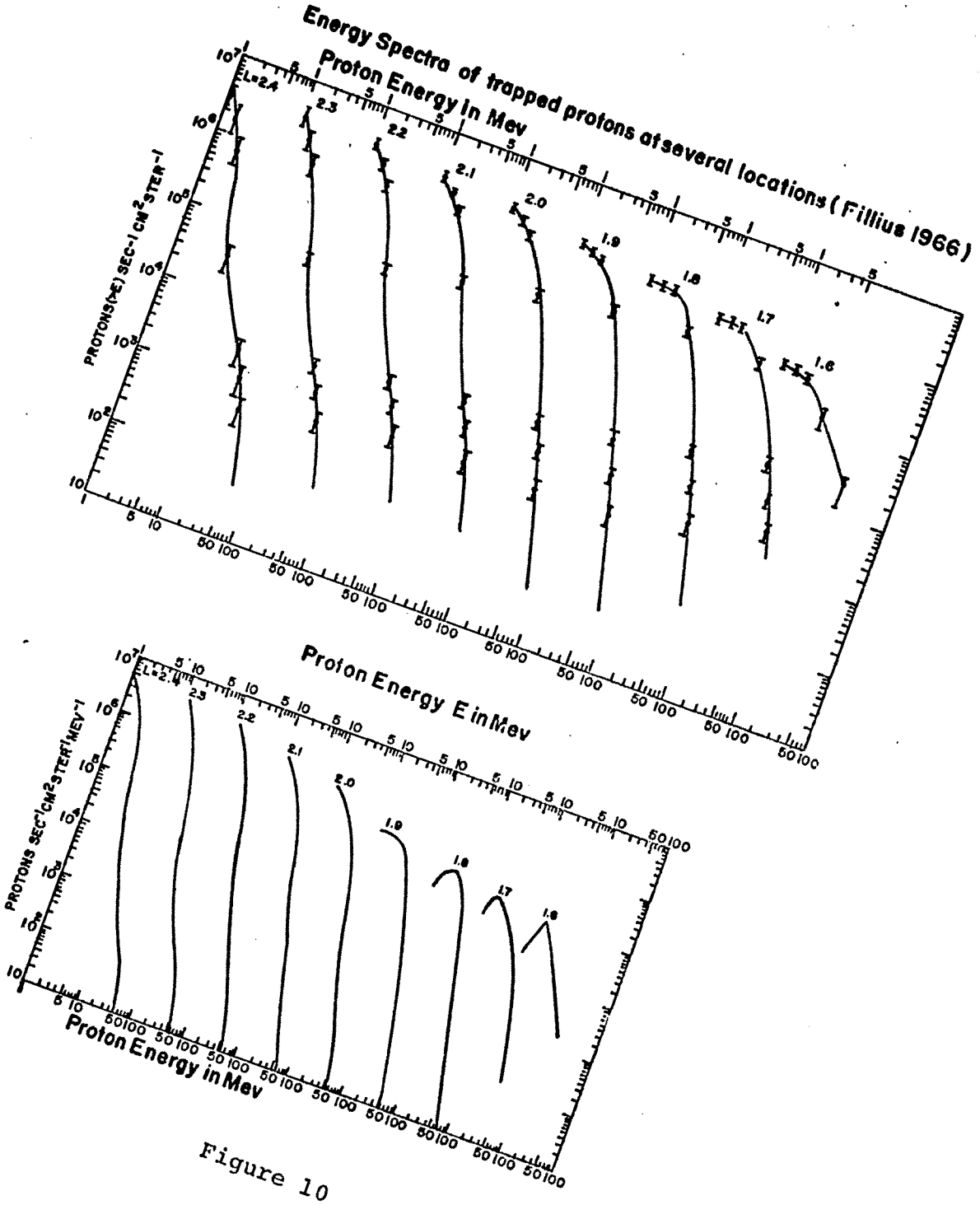
Energy Spectra of trapped protons at several locations (Fillius 1966)
Proton Energy in Mev
PROTONS(>E) SEC-1 CM-2 STER-1
EL=2.4
2.3
2.2
2.1
2.0
1.9
1.8
1.7
1.6
Proton Energy E in Mev
PROTONS SEC-1 CM-2 STER-1 MEV-1
Proton Energy in Mev

Figure 10

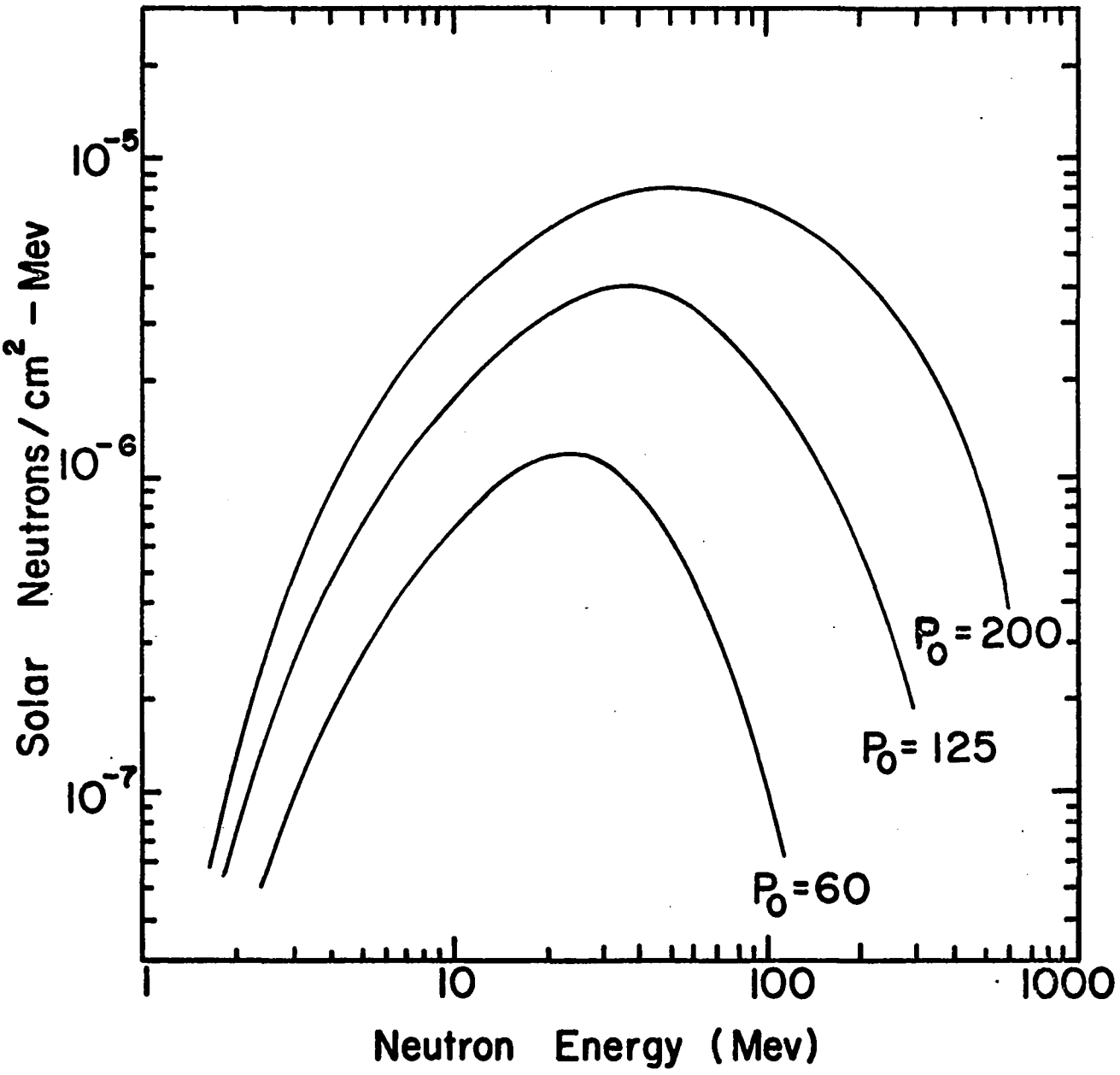
Solar Neutrons / cm² - Mev
10⁻⁵
10⁻⁶
10⁻⁷
P₀ = 200
P₀ = 125
P₀ = 60
1
10
100
1000
Neutron Energy (Mev)

Figure 11

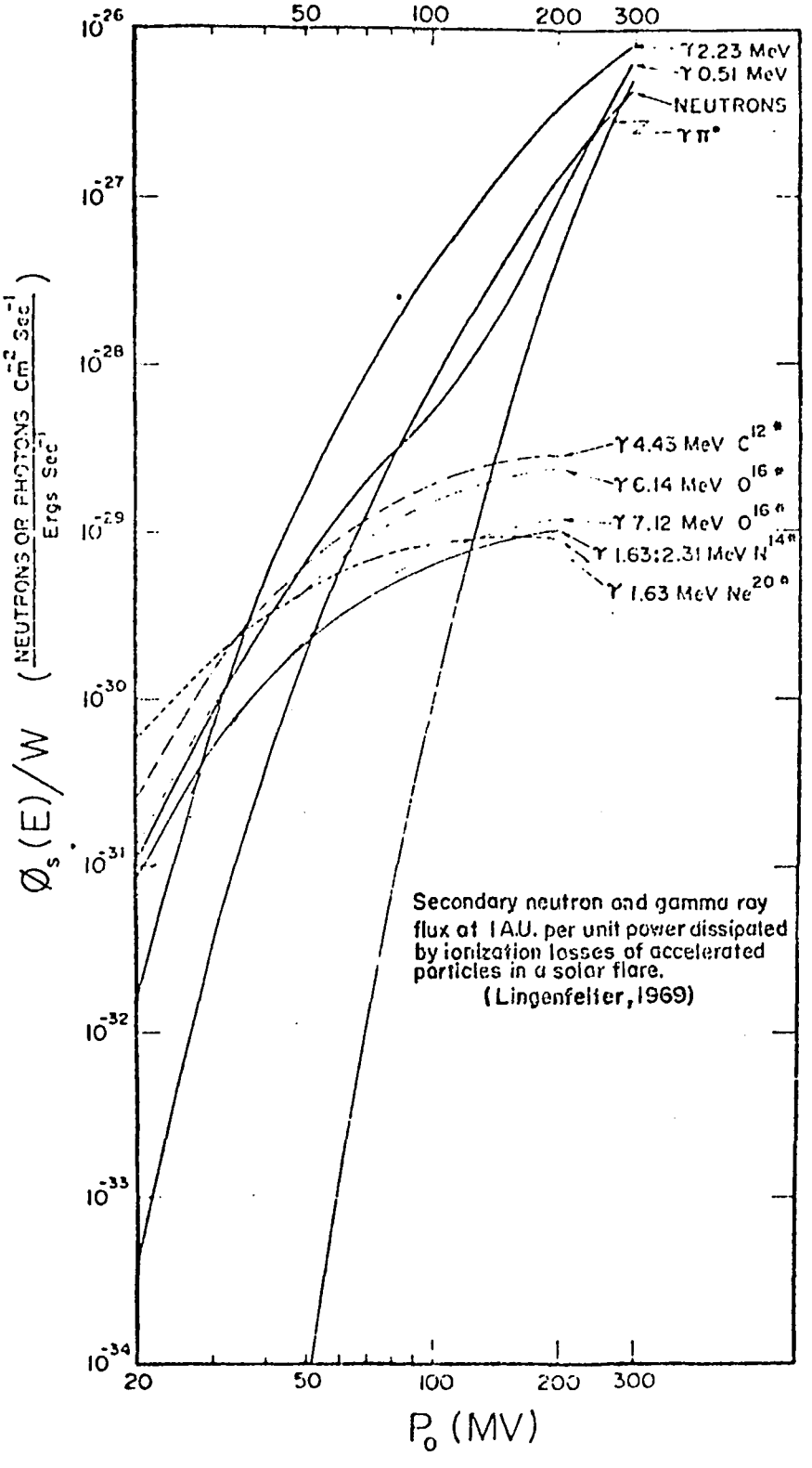
50
100
200
300
10^{-26}
10^{-27}
10^{-28}
10^{-29}
10^{-30}
10^{-31}
10^{-32}
10^{-33}
10^{-34}
20
50
100
200
300
P_o (MV)
$\phi_s(E)/W$ ($\frac{\text{NEUTRONS OR PHOTONS } Cm^{-2} Sec^{-1}}{\text{Ergs } Sec^{-1}}$)
γ 2.23 MeV
γ 0.51 MeV
NEUTRONS
γ π°
γ 4.43 MeV C^{12*}
γ 6.14 MeV O^{16*}
γ 7.12 MeV O^{16*}
γ 1.63;2.31 MeV N^{14*}
γ 1.63 MeV Ne^{20*}
Secondary neutron and gamma ray flux at 1 A.U. per unit power dissipated by ionization losses of accelerated particles in a solar flare.
(Lingenfelter, 1969)

Figure 12

The neutron sensor (components and orientation)

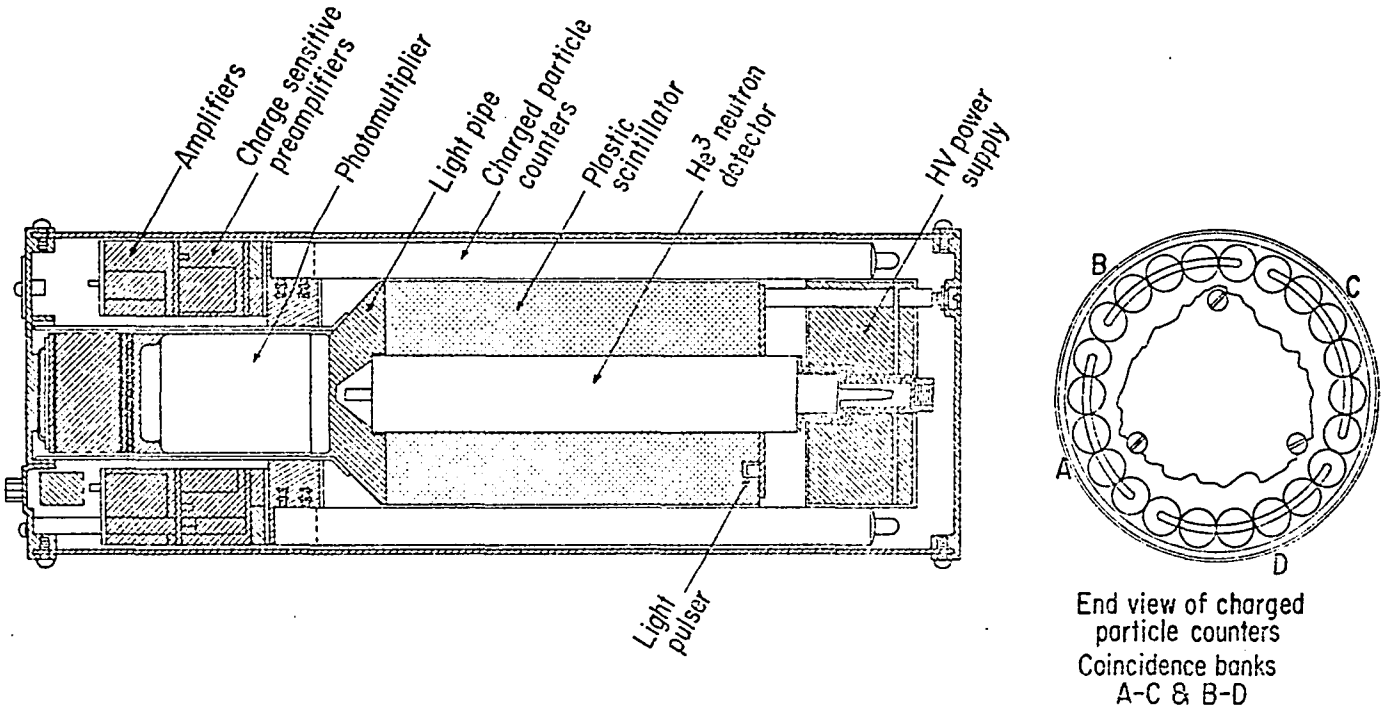

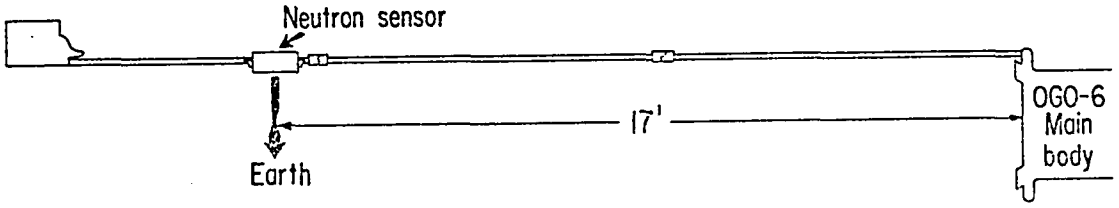

Figure 13

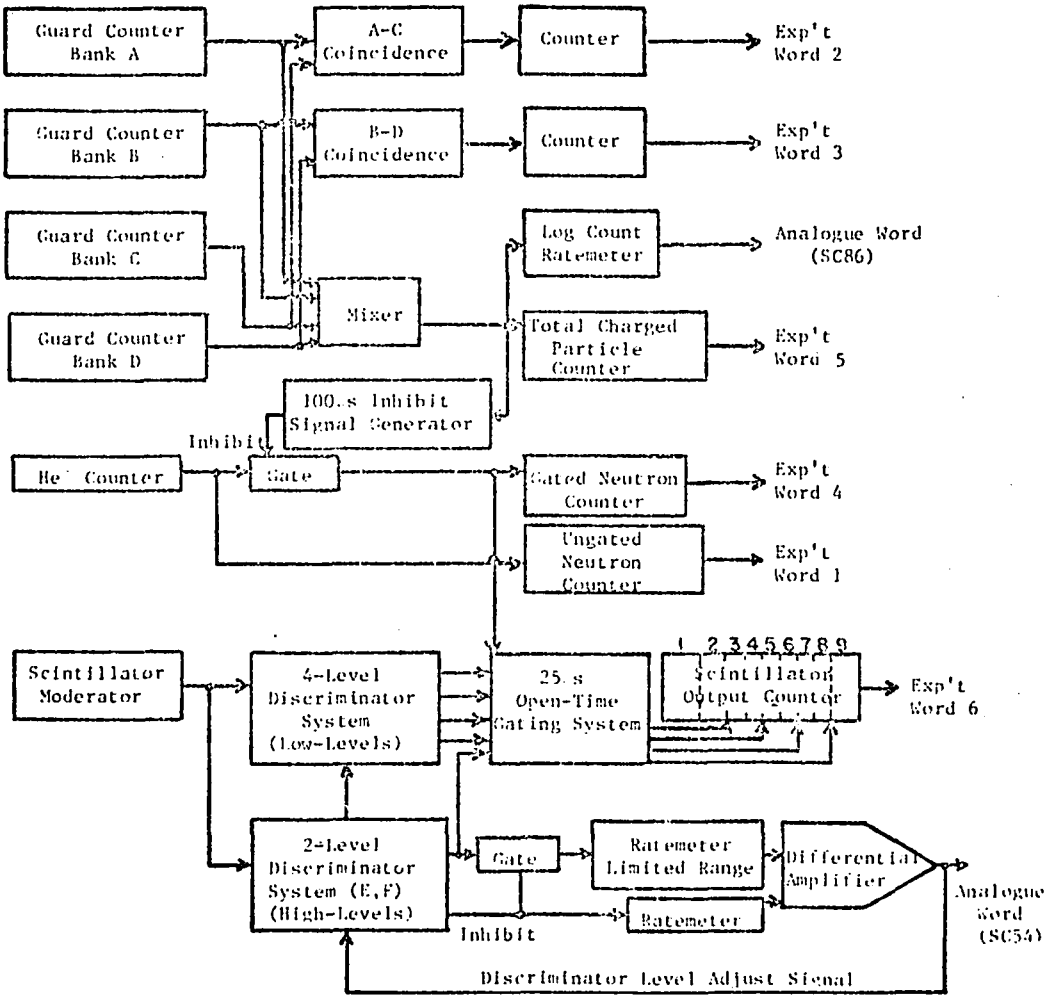

-BLOCK DIAGRAM OF ELECTRONICS SYSTEM-

Figure 14

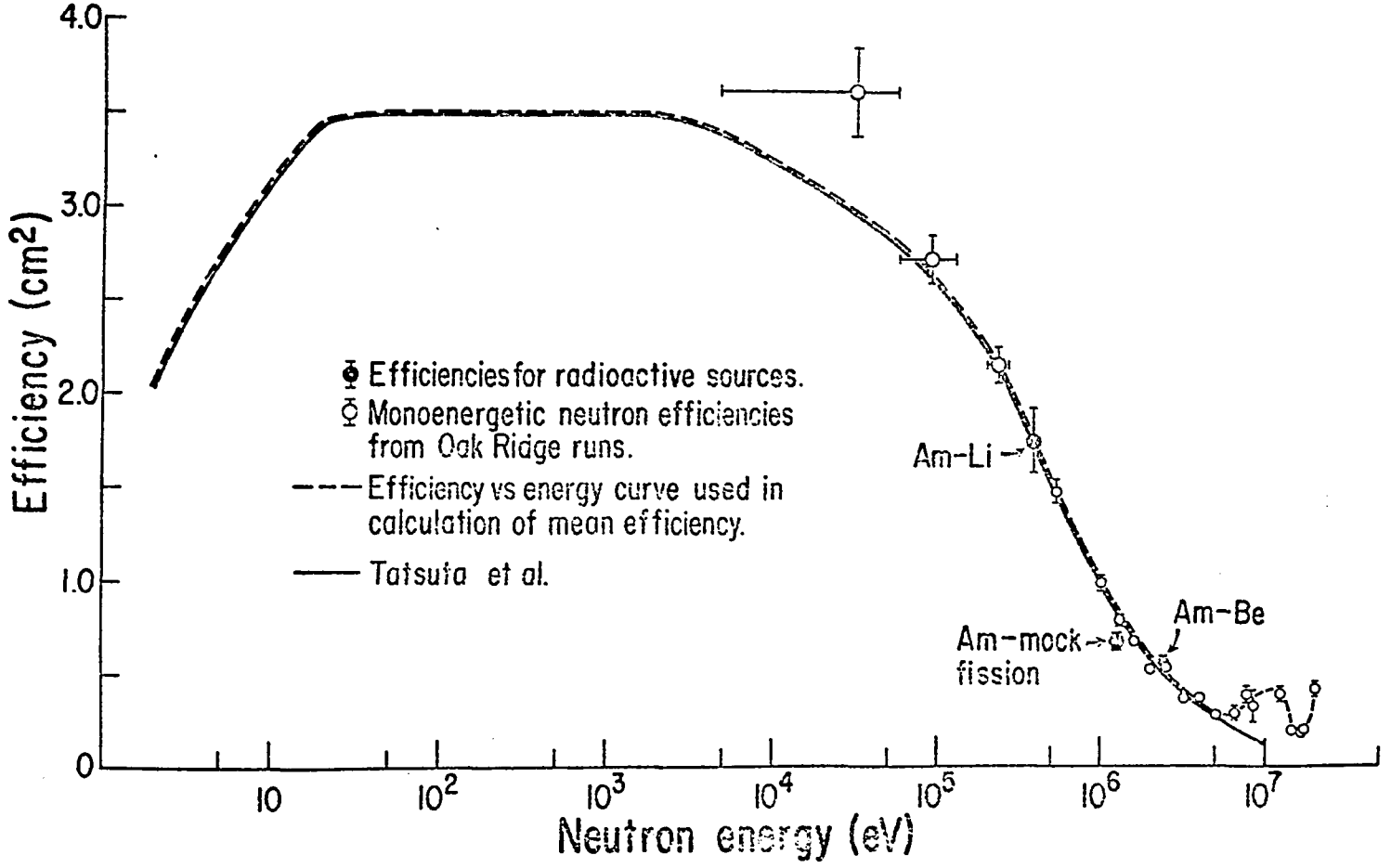

Energy dependence of the neutron detector efficiency

Figure 15

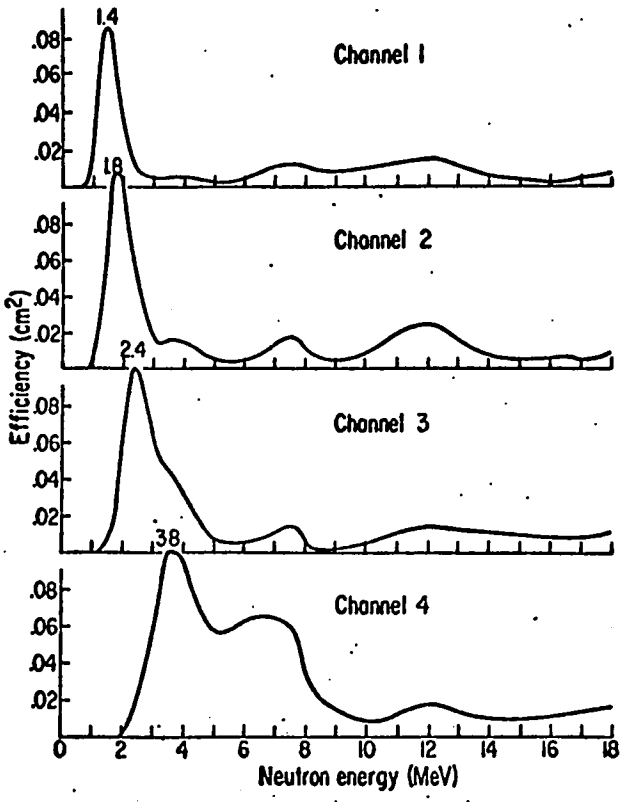
1.4
Channel 1
1.8
Channel 2
2.4
Channel 3
3.8
Channel 4
.08
.06
.04
.02
Efficiency (cm²)
0
2
4
6
8
10
12
14
16
18
Neutron energy (MeV)

FIGURE 16

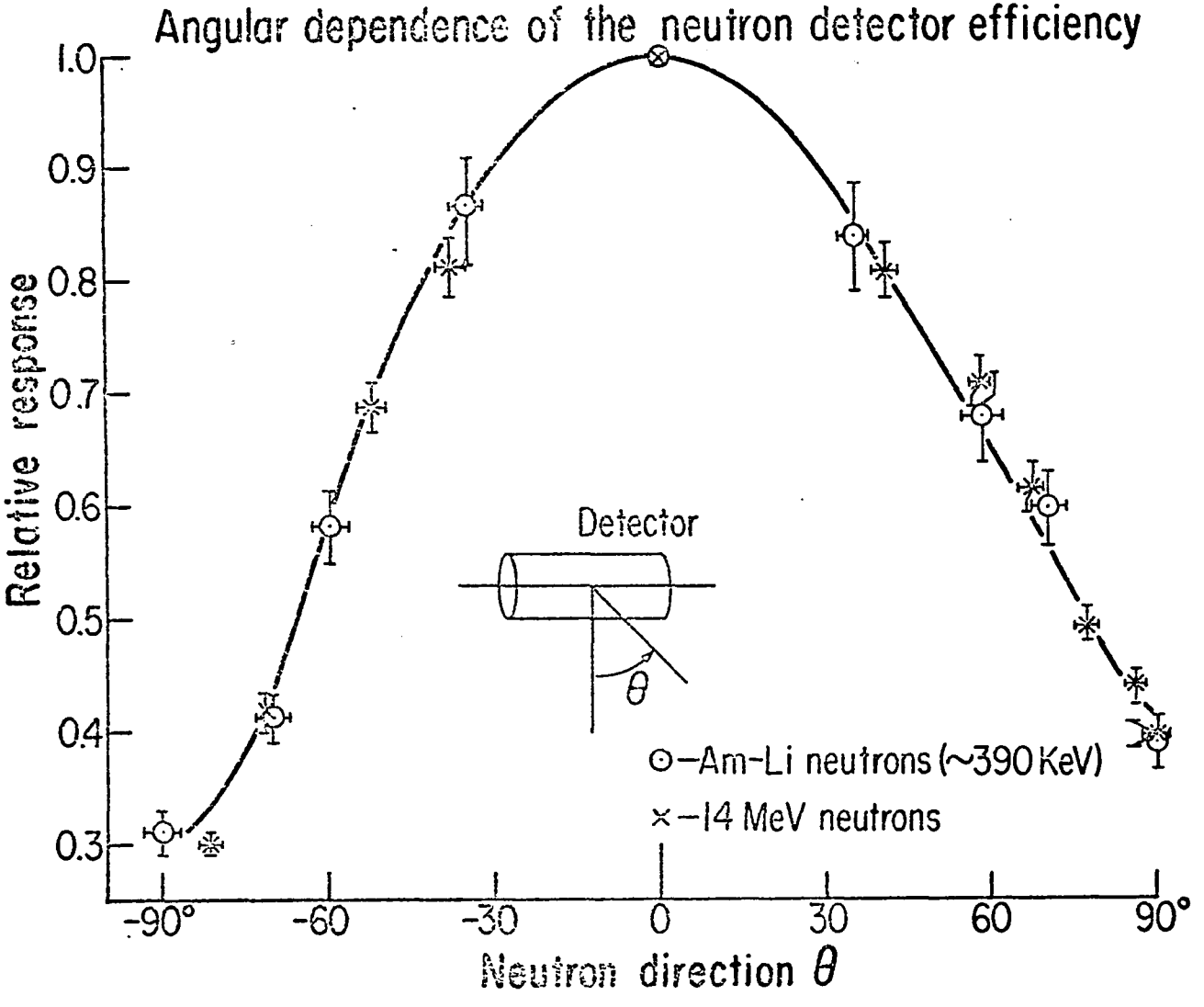
Angular dependence of the neutron detector efficiency
Relative response
1.0
0.9
0.8
0.7
0.6
0.5
0.4
0.3
Detector
θ
⊙—Am-Li neutrons (~390 KeV)
×—14 MeV neutrons
-90°
-60
-30
0
30
60
90°
Neutron direction θ

Figure 17

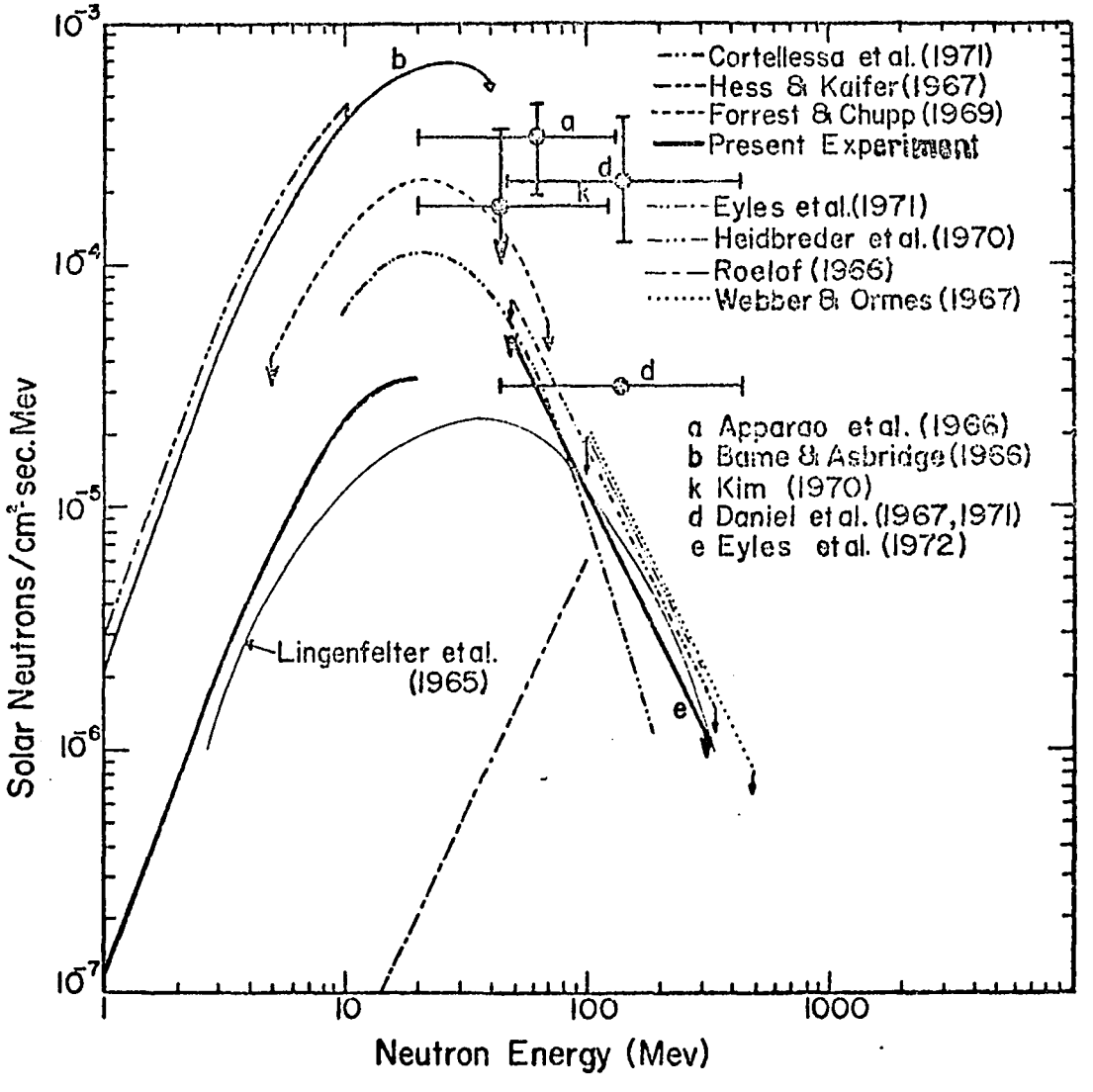
Solar Neutrons/cm²-sec.Mev
Neutron Energy (Mev)
10⁻³
10⁻⁴
10⁻⁵
10⁻⁶
10⁻⁷
1
10
100
1000
b
a
d
k
d
e
Lingenfelter et al. (1965)
Cortellessa et al. (1971)
Hess & Kaifer (1967)
Forrest & Chupp (1969)
Present Experiment
Eyles et al. (1971)
Heidbreder et al. (1970)
Roelof (1966)
Webber & Ormes (1967)
a Apparao et al. (1966)
b Bame & Asbridge (1966)
k Kim (1970)
d Daniel et al. (1967, 1971)
e Eyles et al. (1972)

Figure 19

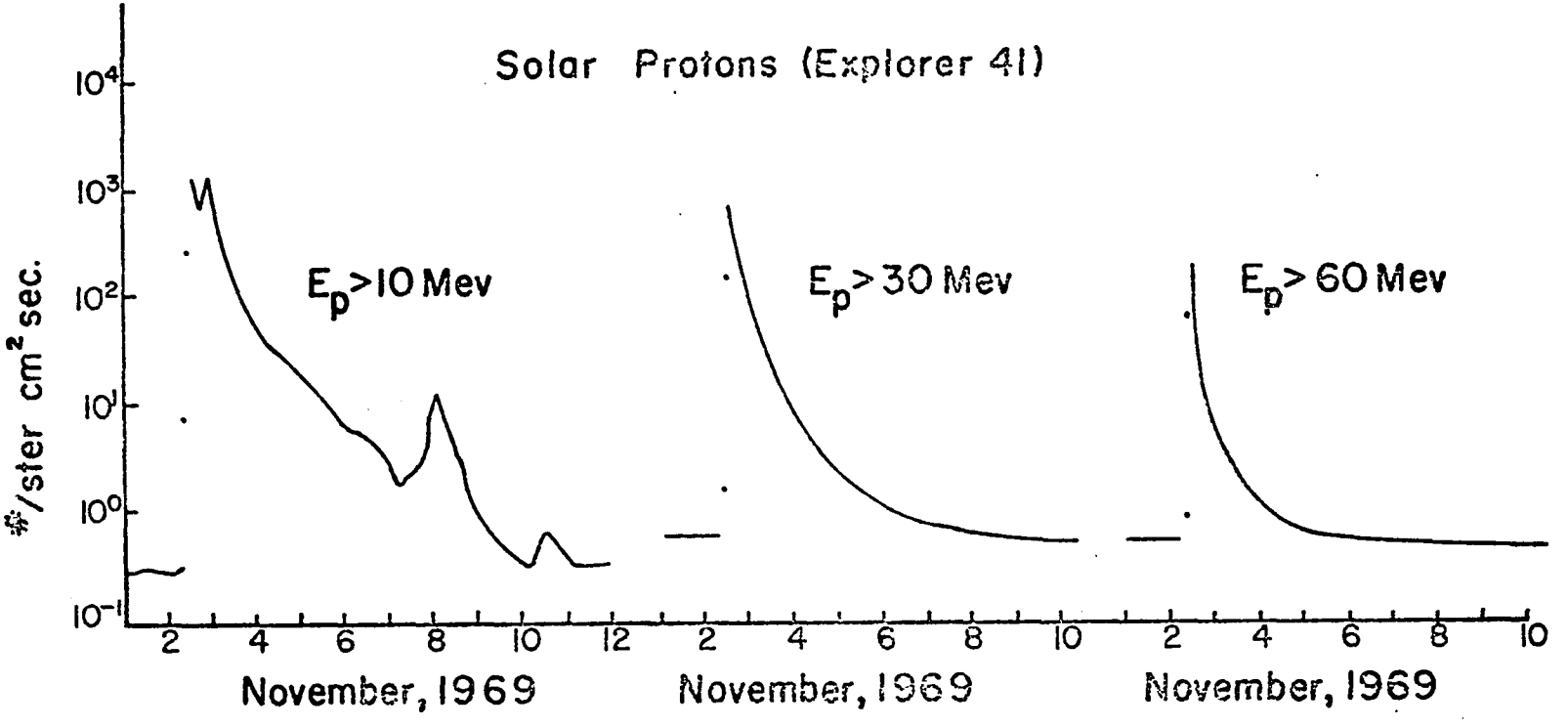
Solar Protons (Explorer 41)
#/ster cm² sec.
10⁴
10³
10²
10¹
10⁰
10⁻¹
Ep>10 Mev
Ep>30 Mev
Ep>60 Mev
2 4 6 8 10 12
2 4 6 8 10
2 4 6 8 10
November, 1969
November, 1969
November, 1969

Figure 20

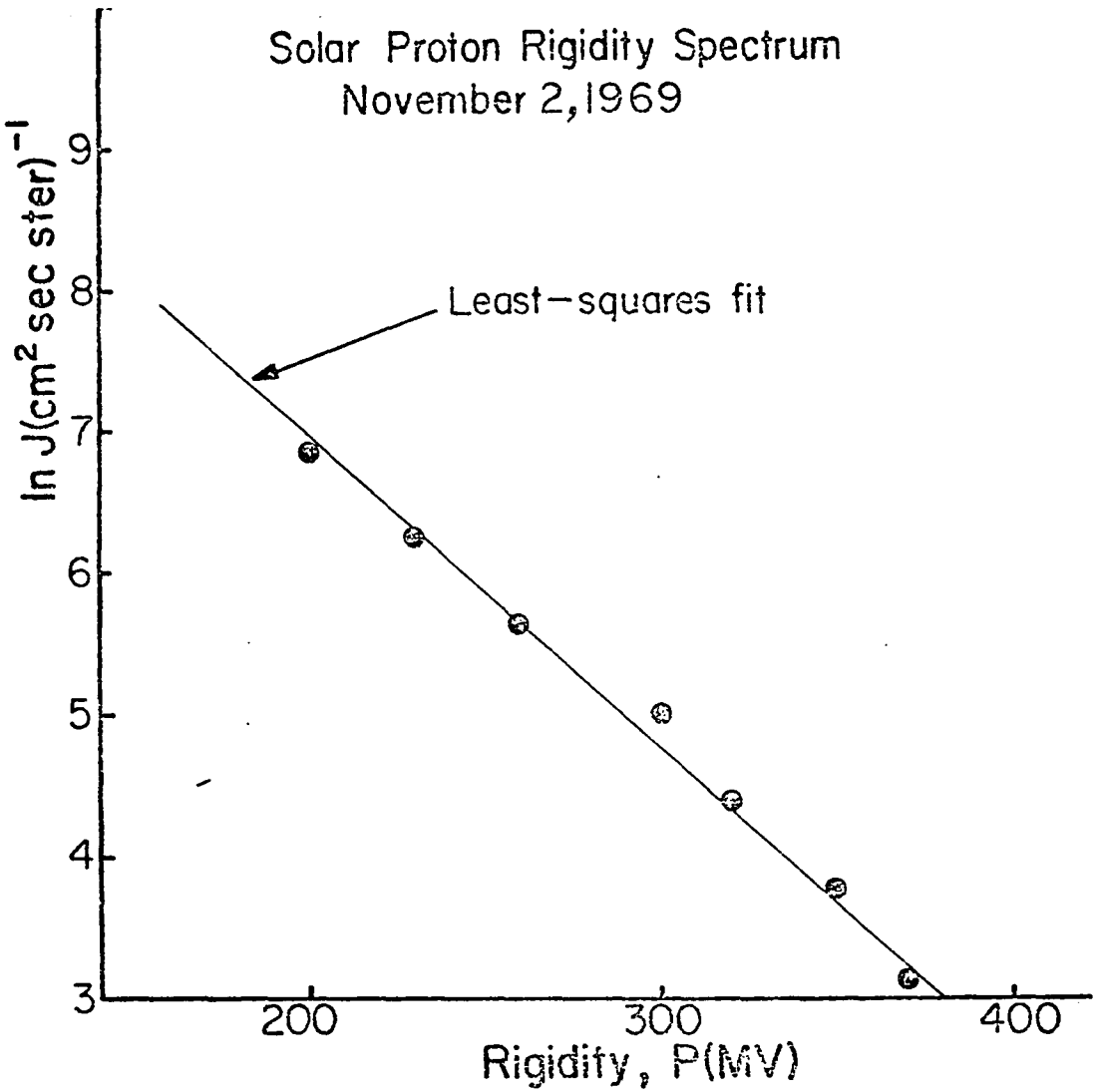
Solar Proton Rigidity Spectrum
November 2,1969
Least-squares fit
ln J(cm² sec ster)⁻¹
9
8
7
6
5
4
3
200
300
400
Rigidity, P(MV)

Figure 21

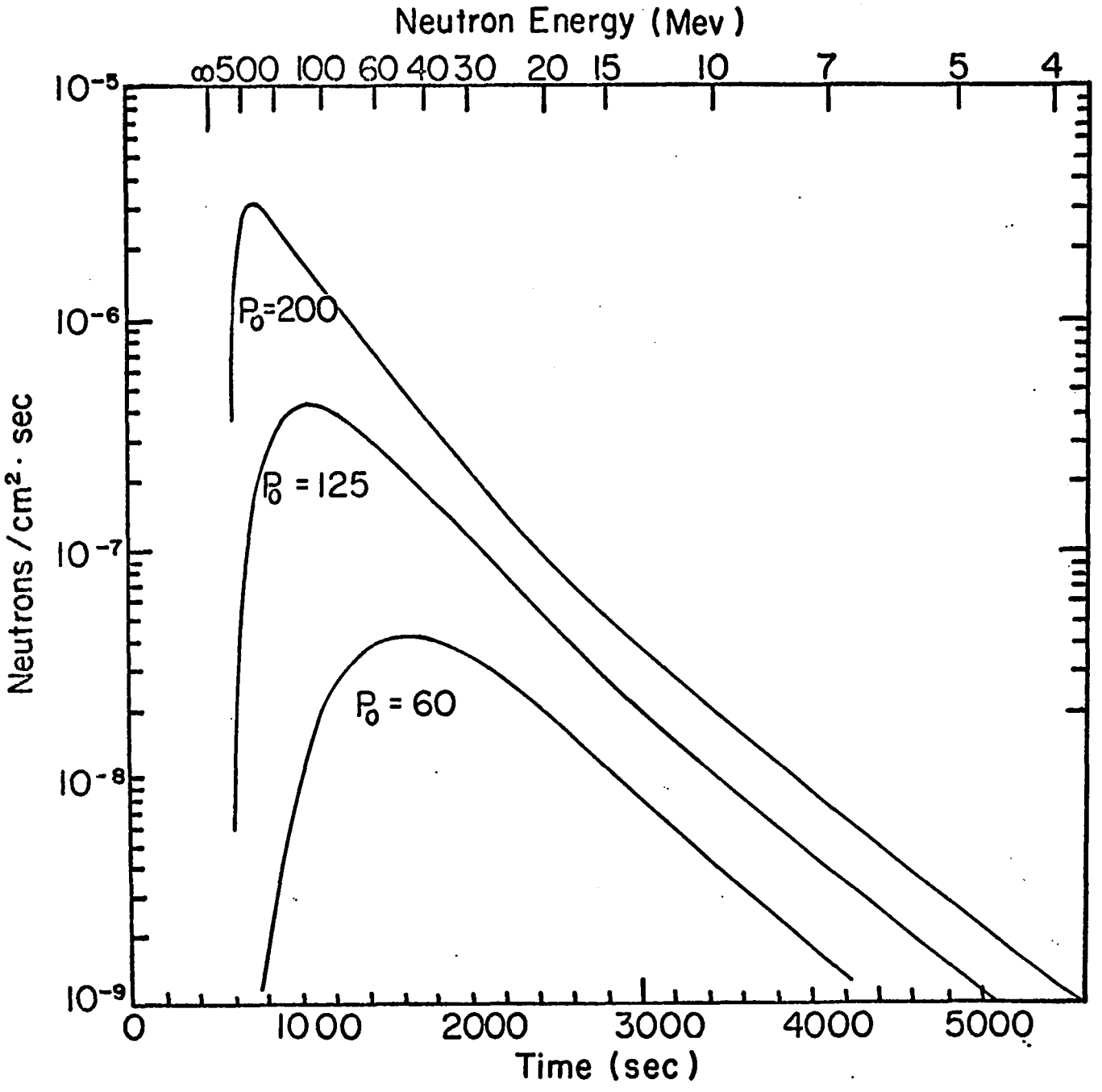
Neutron Energy (Mev)
∞ 500 100 60 40 30 20 15 10 7 5 4
10^{-5}
10^{-6}
10^{-7}
10^{-8}
10^{-9}
Neutrons / cm² · sec
P_0=200
P_0 = 125
P_0 = 60
0
1000
2000
3000
4000
5000
Time (sec)

Figure 22

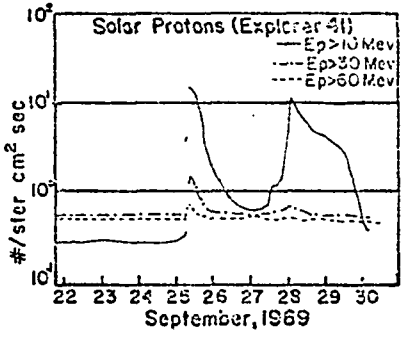

450 km altitude
$|\lambda| > 70°$
— monthly average rate (Sept)

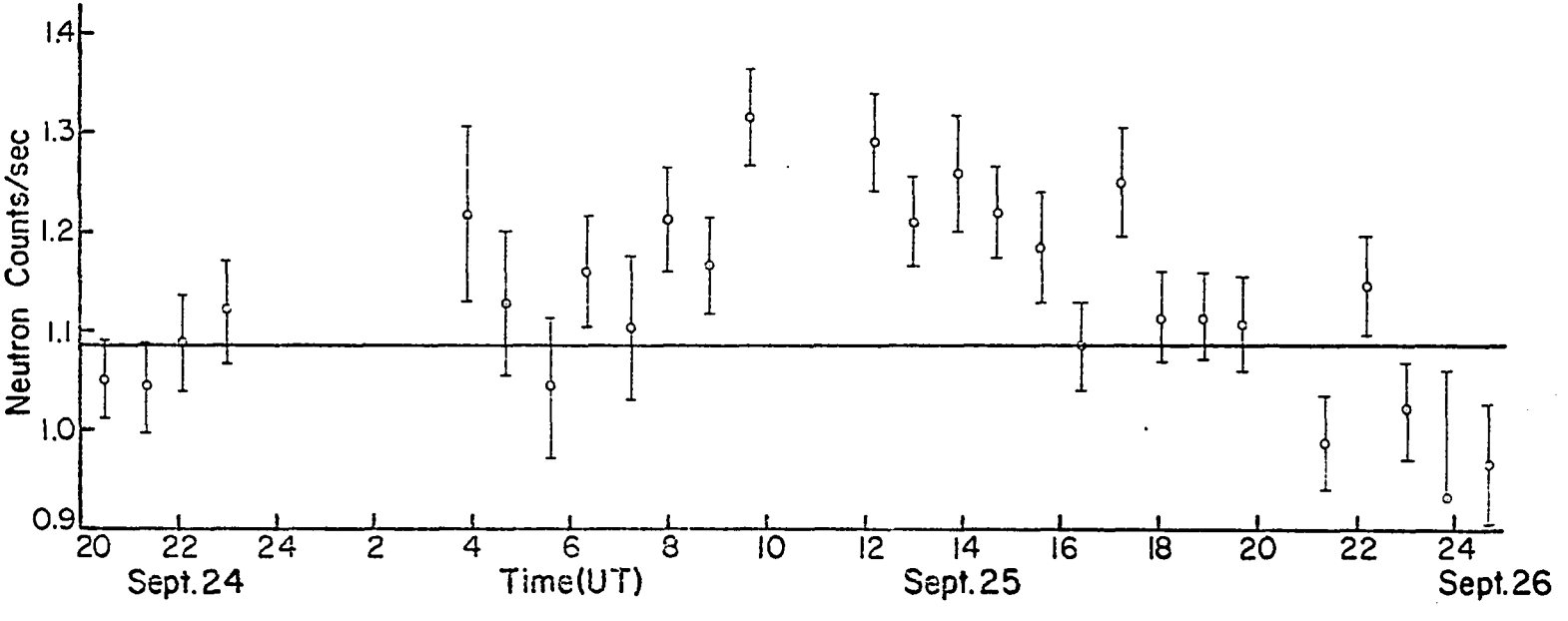

Figure 23

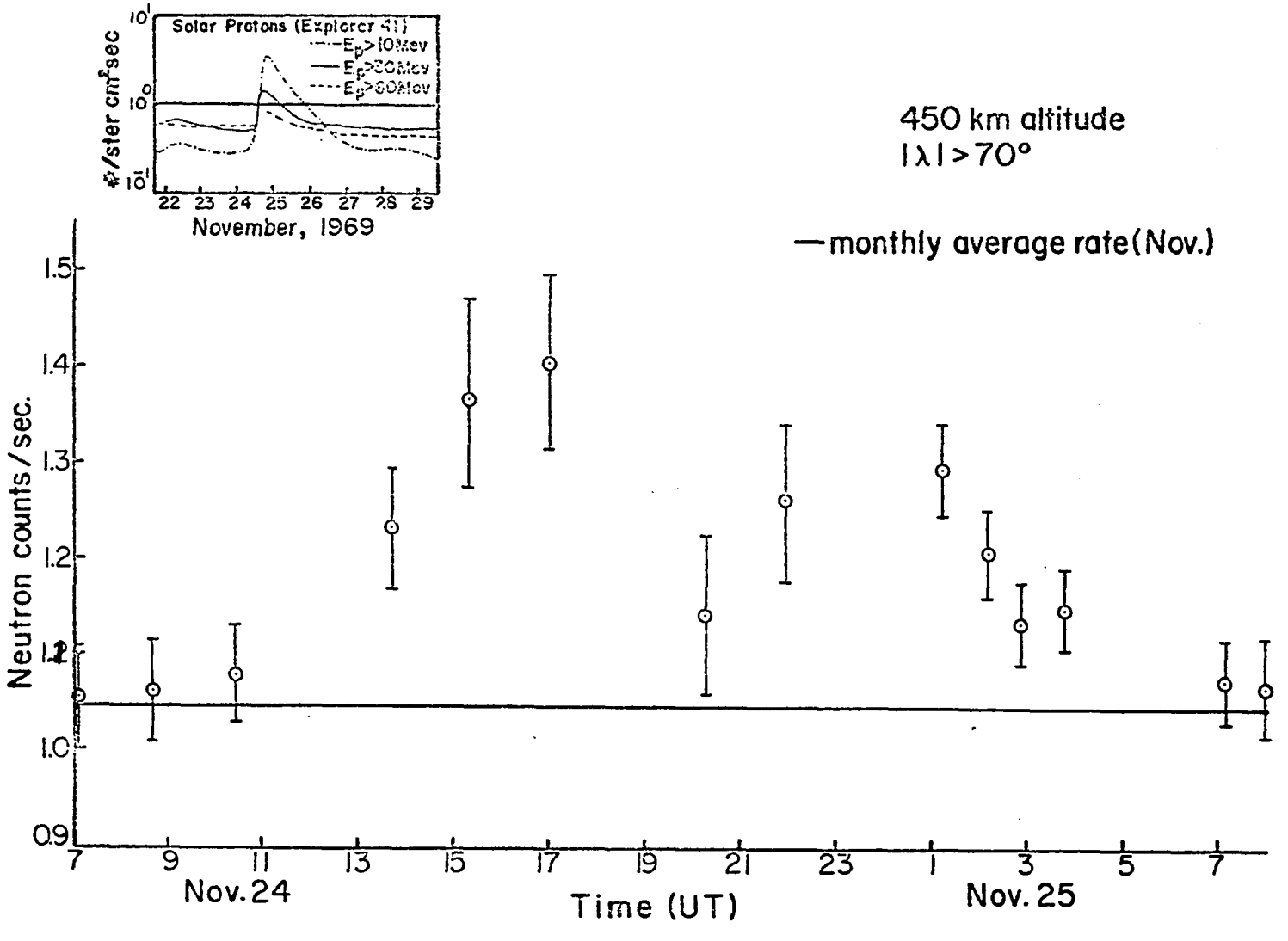
Solar Protons (Explorer 41)
E_p>10Mev
E_p>30Mev
E_p>60Mev
#/ster cm²sec
November, 1969
450 km altitude
|λ|>70°
—monthly average rate(Nov.)
Neutron counts/sec.
Nov.24
Time (UT)
Nov.25

Figure 24

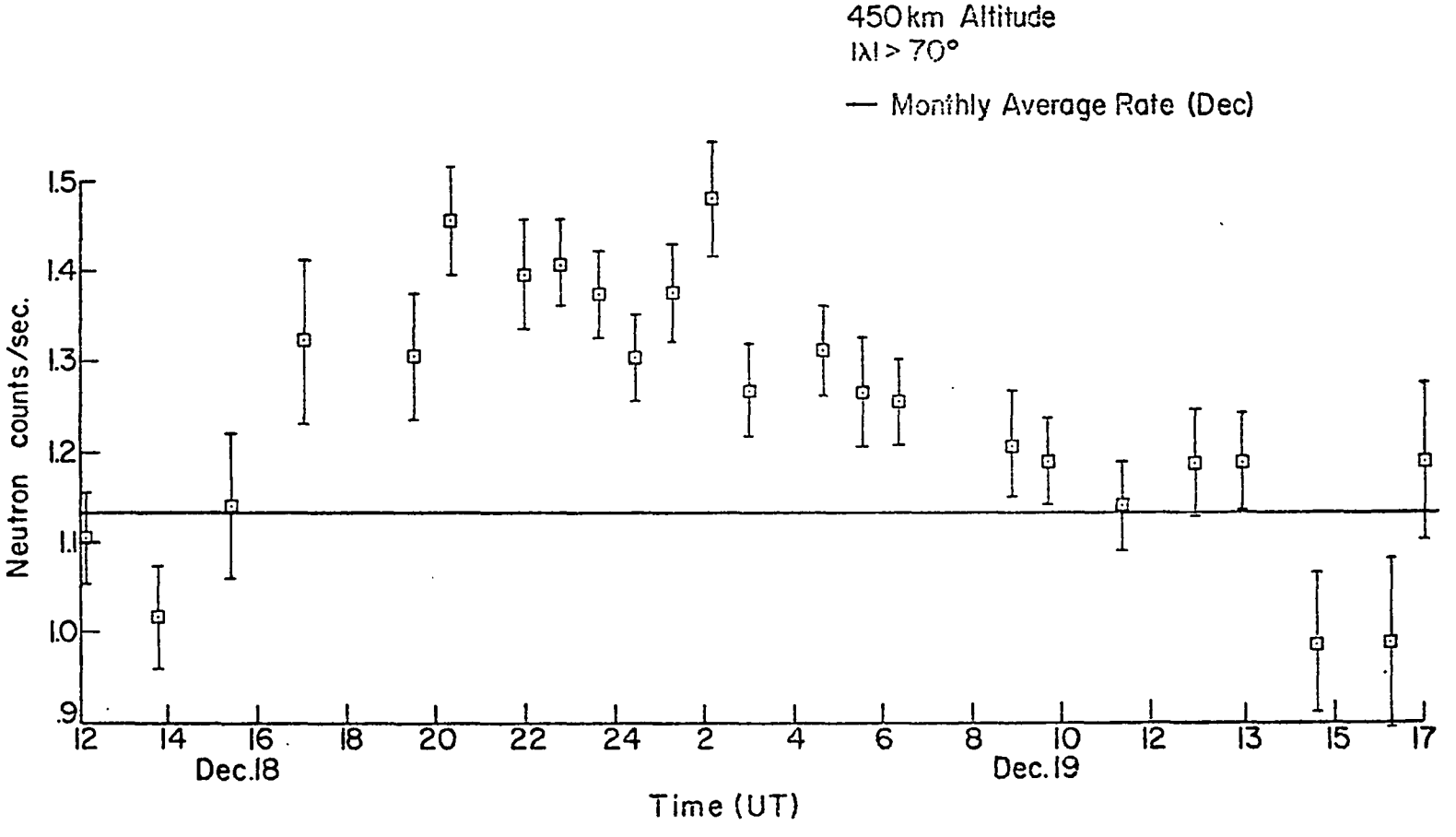
450km Altitude
|λ| > 70°
— Monthly Average Rate (Dec)
Neutron counts/sec.
1.5
1.4
1.3
1.2
1.1
1.0
.9
12
14
16
18
20
22
24
2
4
6
8
10
12
13
15
17
Dec.18
Dec.19
Time (UT)

Figure 25

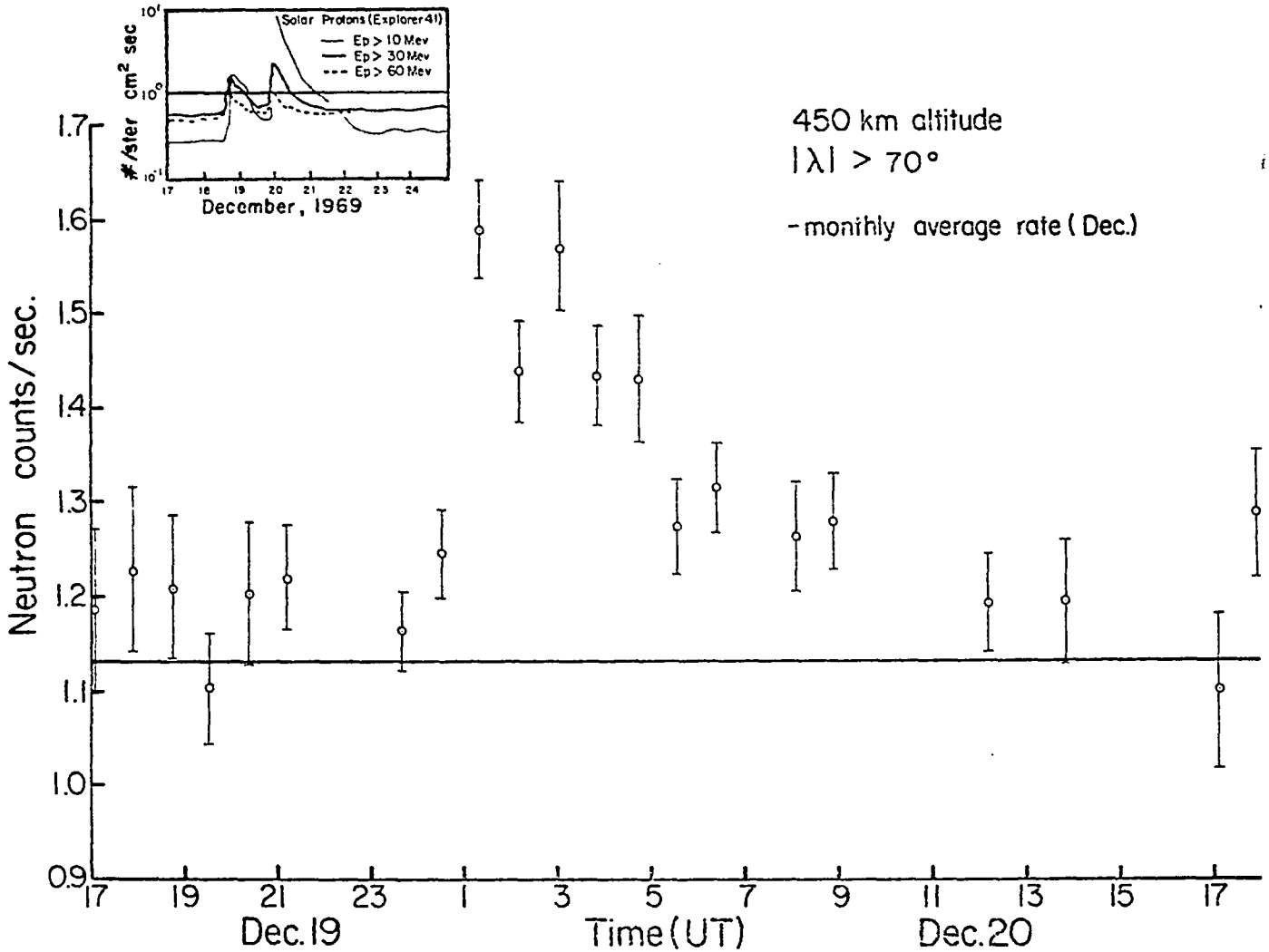
Solar Protons (Explorer 41)
Ep > 10 Mev
Ep > 30 Mev
Ep > 60 Mev
#/ster cm² sec
December, 1969
450 km altitude
|λ| > 70°
- monthly average rate (Dec.)
Neutron counts/sec.
1.7
1.6
1.5
1.4
1.3
1.2
1.1
1.0
0.9
17 19 21 23 1 3 5 7 9 11 13 15 17
Dec. 19
Time (UT)
Dec. 20

Figure 26

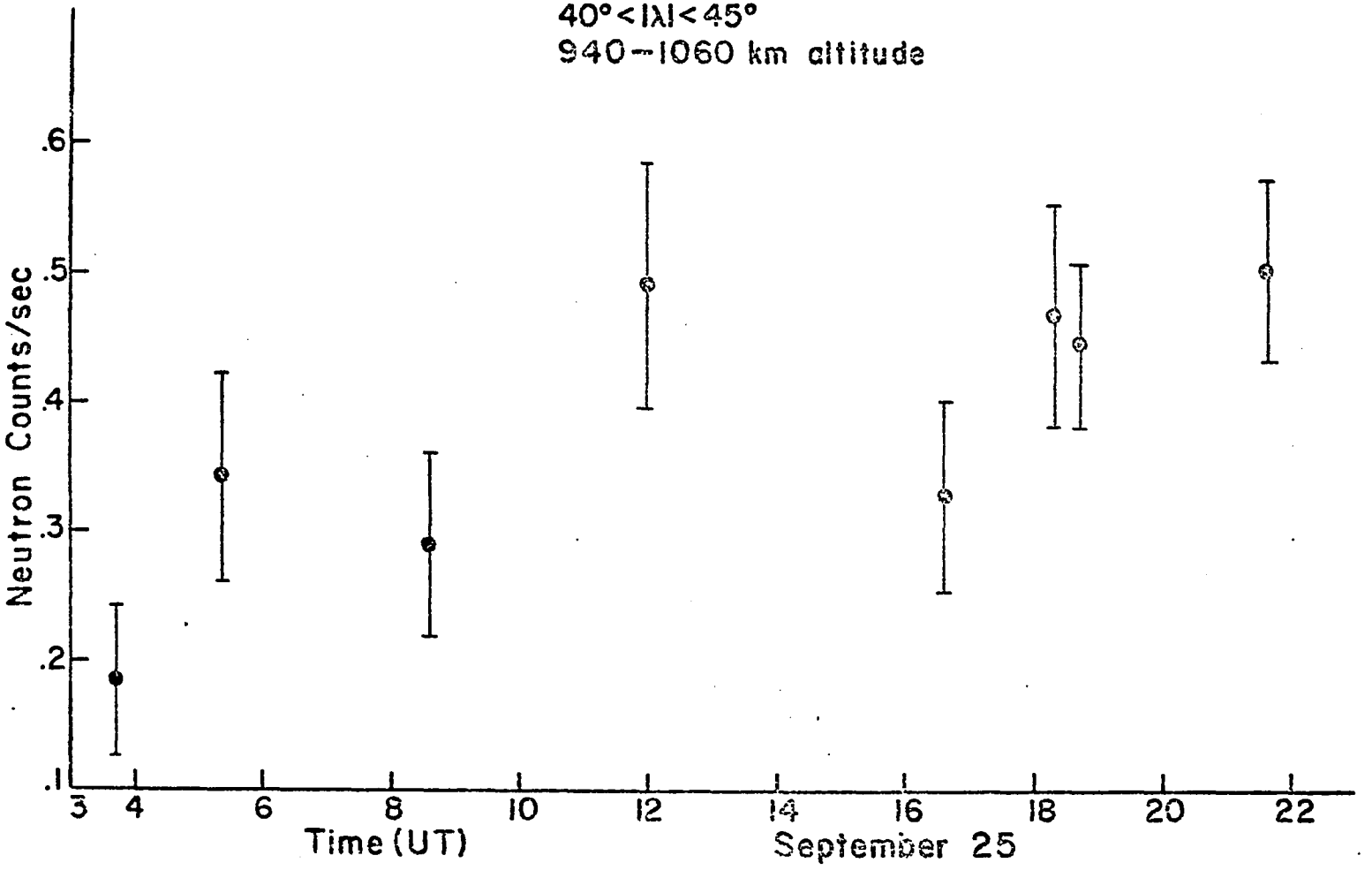
40°<|λ|<45°
940-1060 km altitude
Neutron Counts/sec
.6
.5
.4
.3
.2
.1
3
4
6
8
10
12
14
16
18
20
22
Time (UT)
September 25

Figure 27a

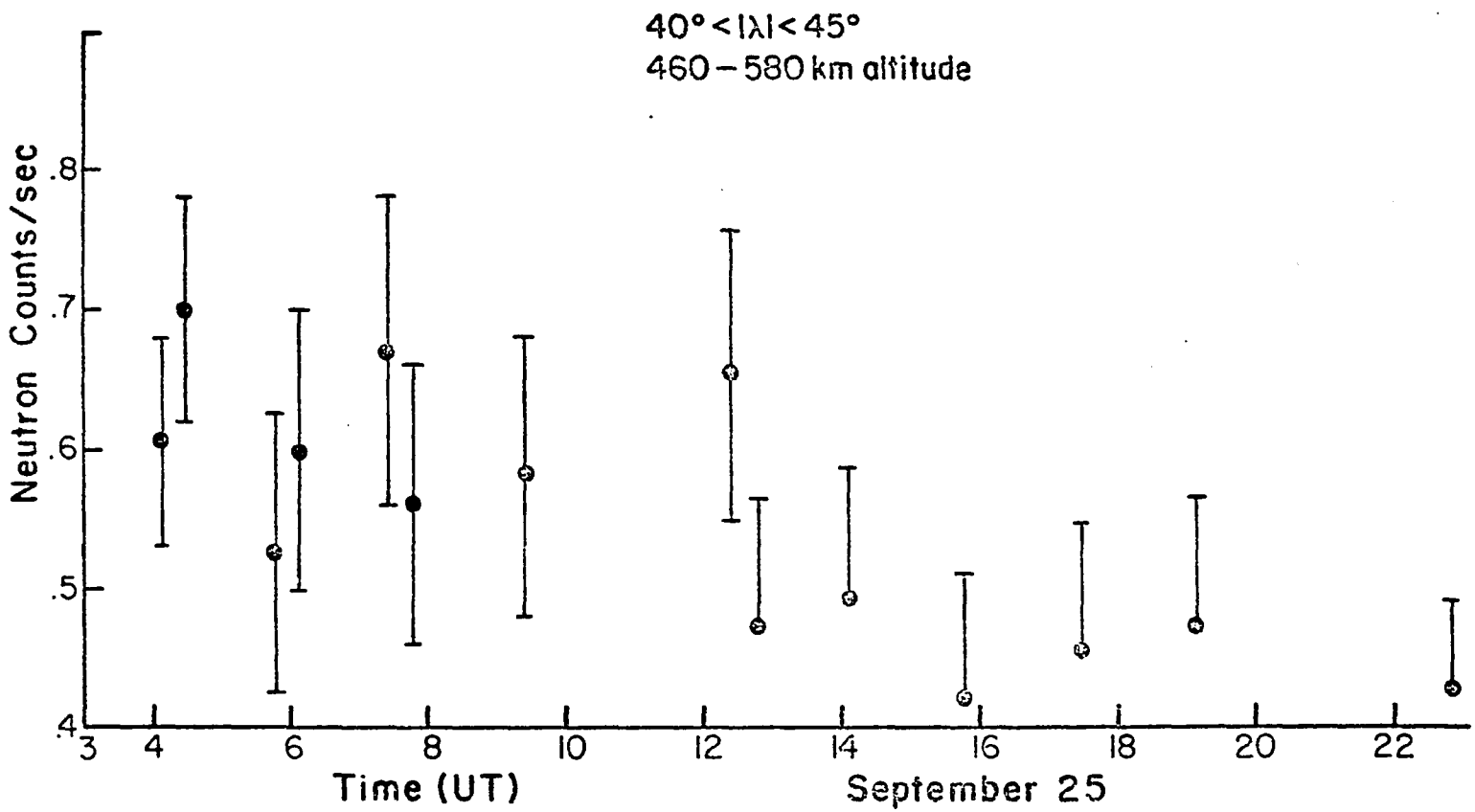
40° < |λ| < 45°
460 – 580 km altitude
Neutron Counts/sec
.8
.7
.6
.5
.4
3
4
6
8
10
12
14
16
18
20
22
Time (UT)
September 25

Figure 27b

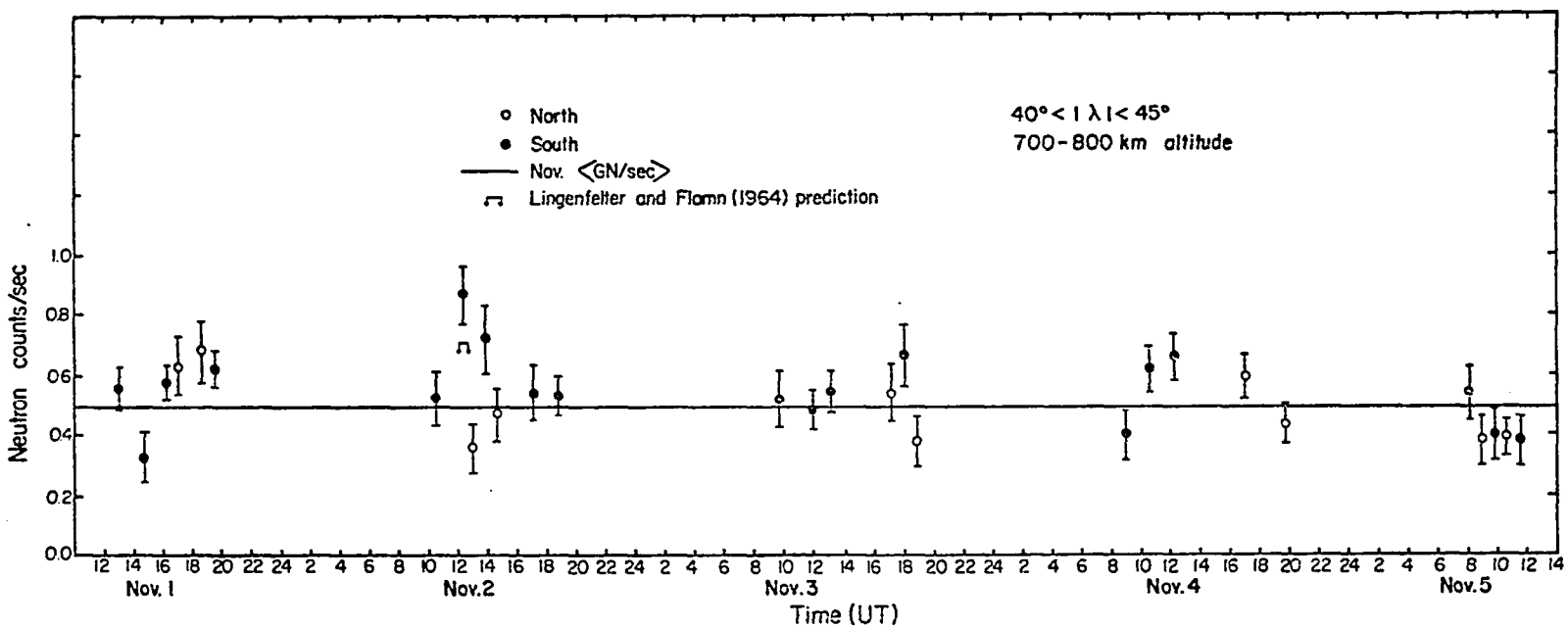
North
South
Nov. ⟨GN/sec⟩
Lingenfelter and Flamn (1964) prediction
40° < | λ | < 45°
700 - 800 km altitude
Neutron counts/sec
0.0
0.2
0.4
0.6
0.8
1.0
12 14 16 18 20 22 24 2 4 6 8 10 12 14 16 18 20 22 24 2 4 6 8 10 12 14 16 18 20 22 24 2 4 6 8 10 12 14 16 18 20 22 24 2 4 6 8 10 12 14
Nov. 1
Nov. 2
Nov. 3
Nov. 4
Nov. 5
Time (UT)

Figure 28

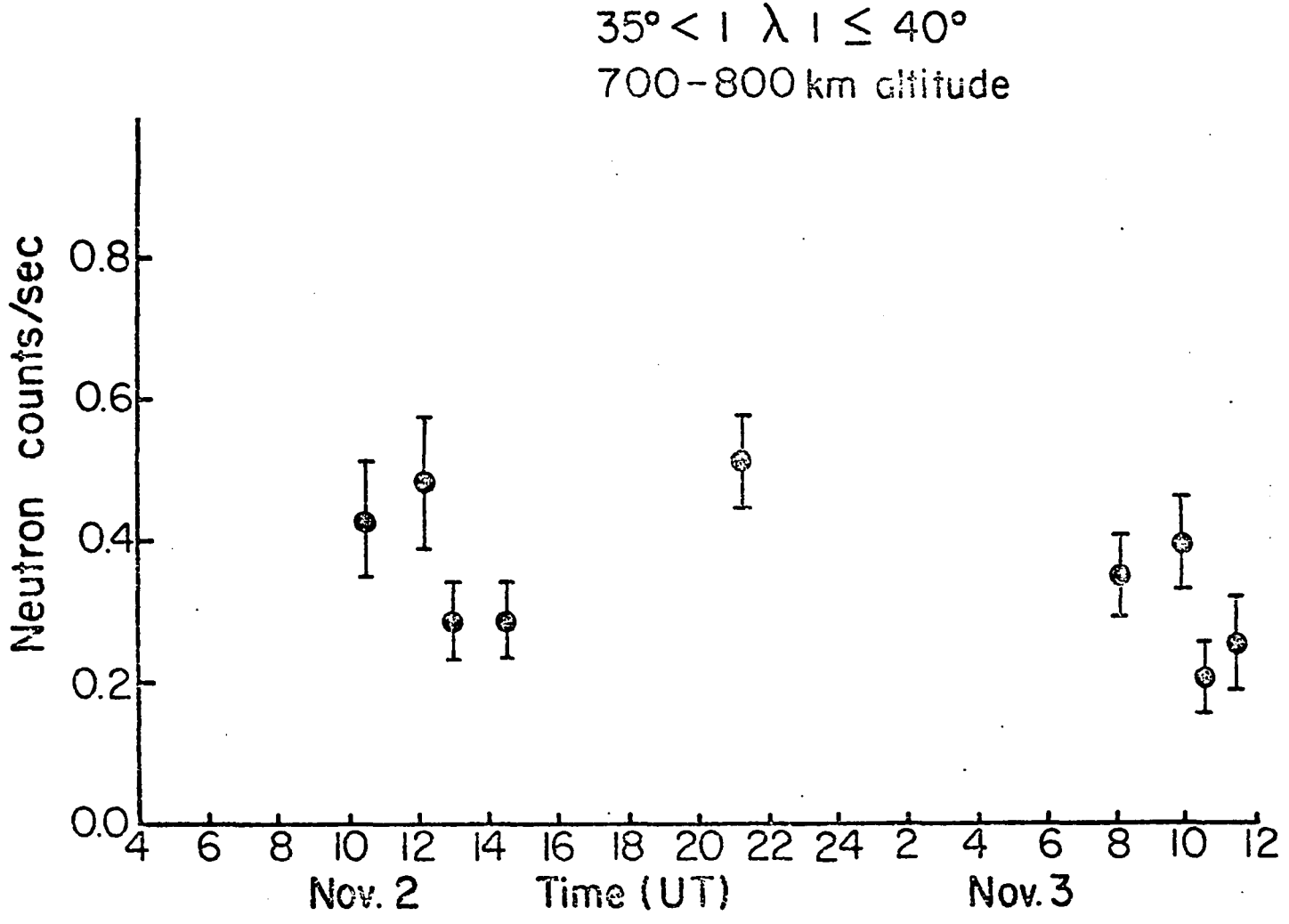
35° < | λ | ≤ 40°
700-800 km altitude
Neutron counts/sec
0.0
0.2
0.4
0.6
0.8
4 6 8 10 12 14 16 18 20 22 24 2 4 6 8 10 12
Nov. 2
Time (UT)
Nov. 3

Figure 23b

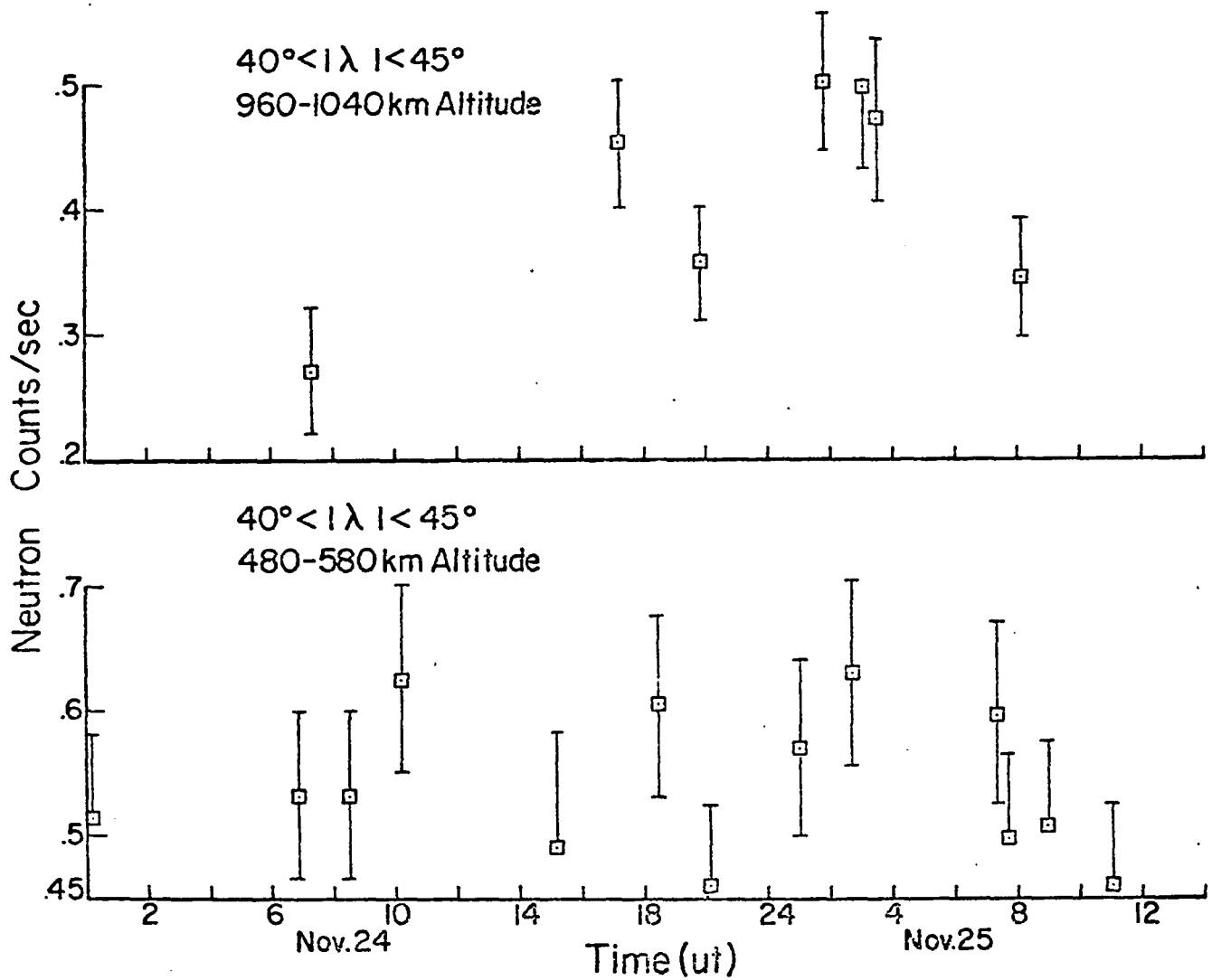
40°<|λ|<45°
960-1040km Altitude
40°<|λ|<45°
480-580km Altitude
Neutron Counts/sec
.5
.4
.3
.2
.7
.6
.5
.45
2
6
10
14
18
24
4
8
12
Nov.24
Nov.25
Time (ut)

Figure 29a

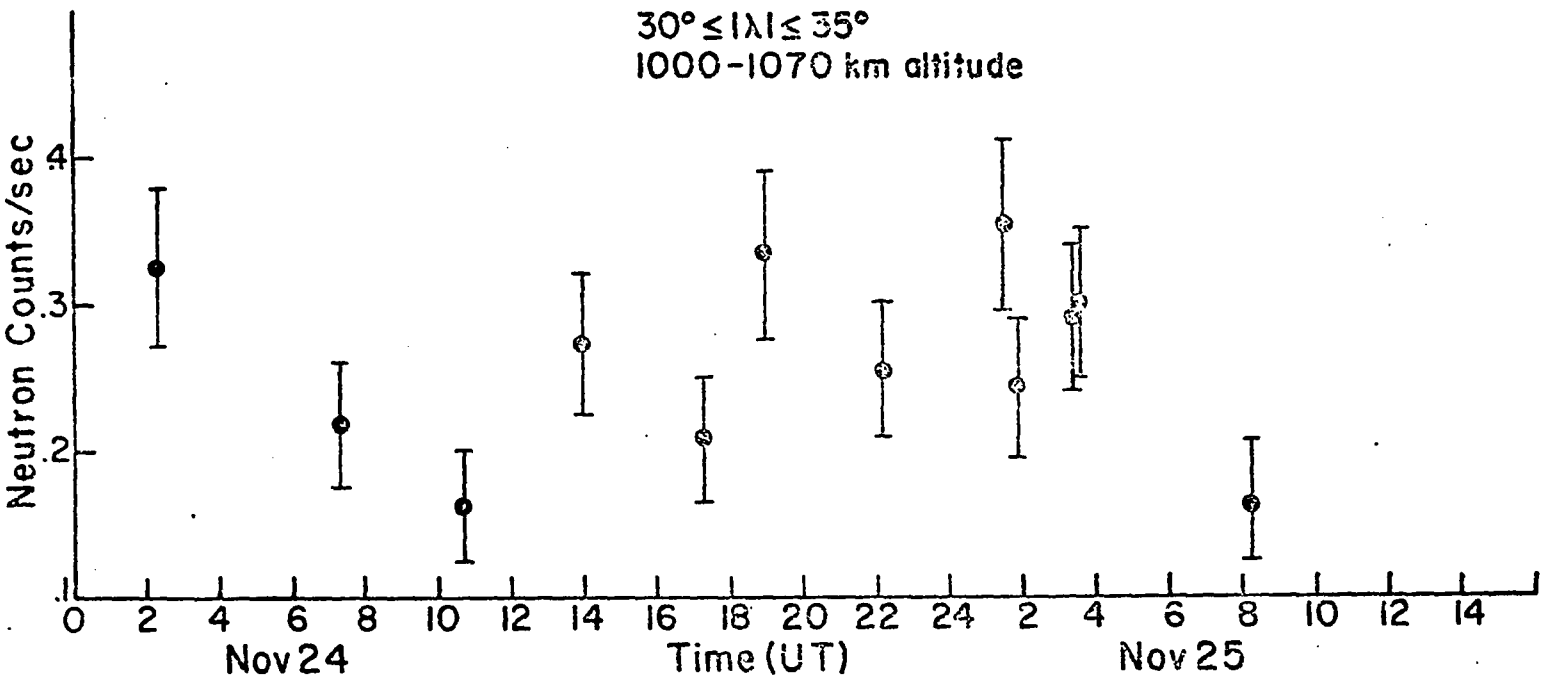
30° ≤ |λ| ≤ 35°
1000-1070 km altitude
Neutron Counts/sec
.1
.2
.3
.4
0 2 4 6 8 10 12 14 16 18 20 22 24 2 4 6 8 10 12 14
Nov 24
Time (UT)
Nov 25

Figure 29b

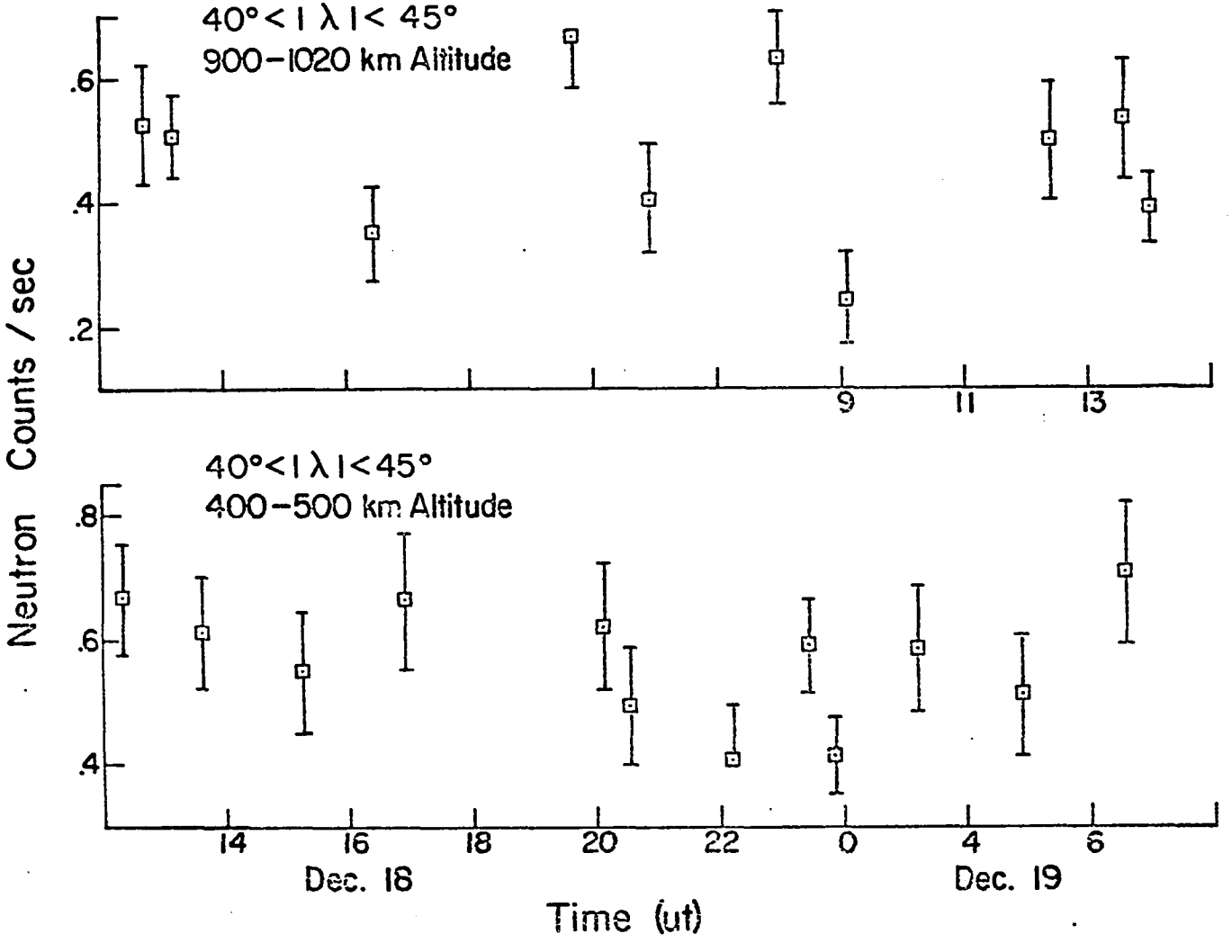
40°<|λ|< 45°
900–1020 km Altitude
.6
.4
.2
9
11
13
40°<|λ|<45°
400–500 km Altitude
.8
.6
.4
14
16
18
20
22
0
4
6
Dec. 18
Dec. 19
Neutron Counts / sec
Time (ut)

Figure 30

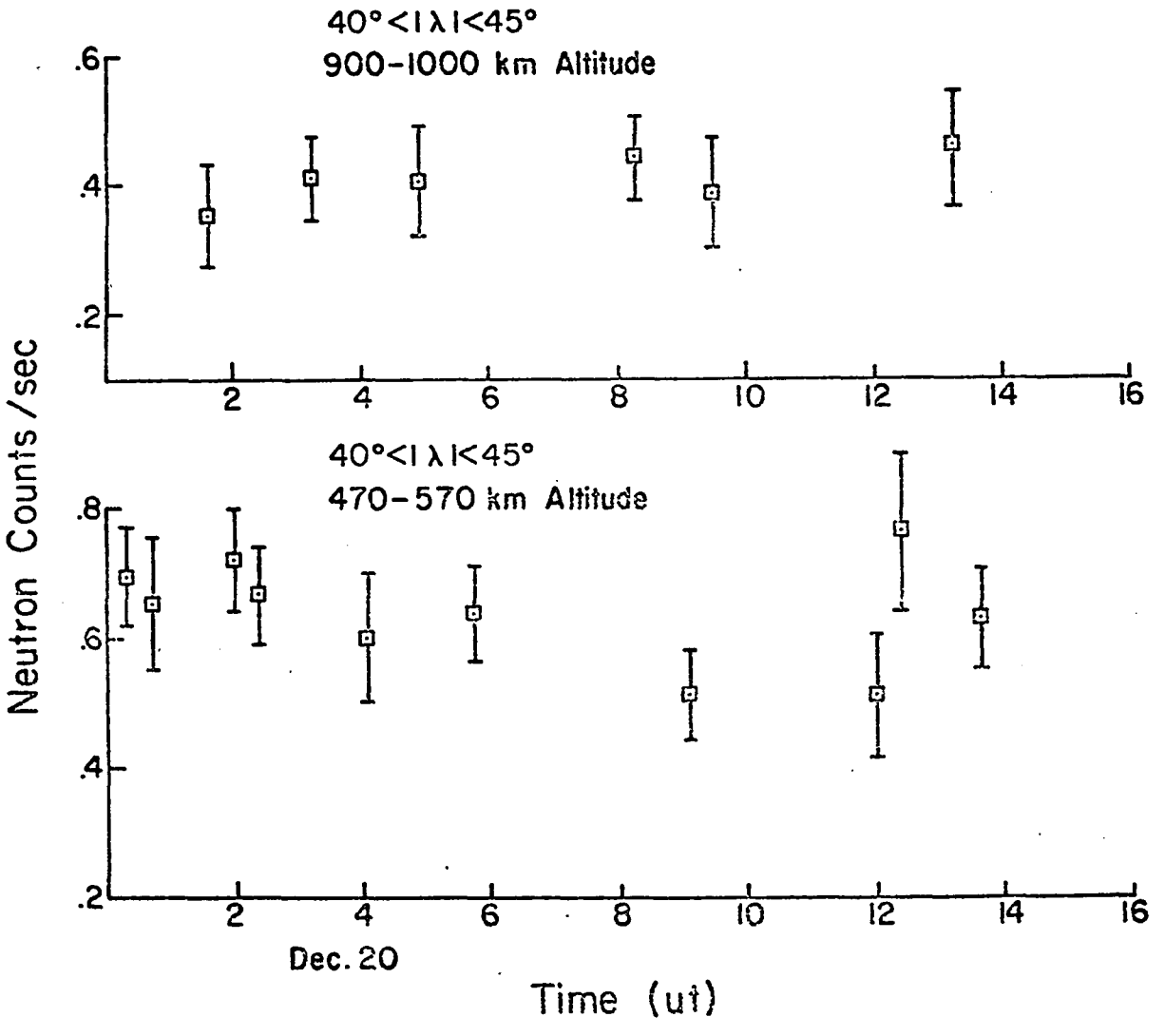
40°<|λ|<45°
900-1000 km Altitude
40°<|λ|<45°
470-570 km Altitude
Neutron Counts/sec
.6
.4
.2
.8
.6
.4
.2
2
4
6
8
10
12
14
16
Dec. 20
Time (ut)

Figure 31

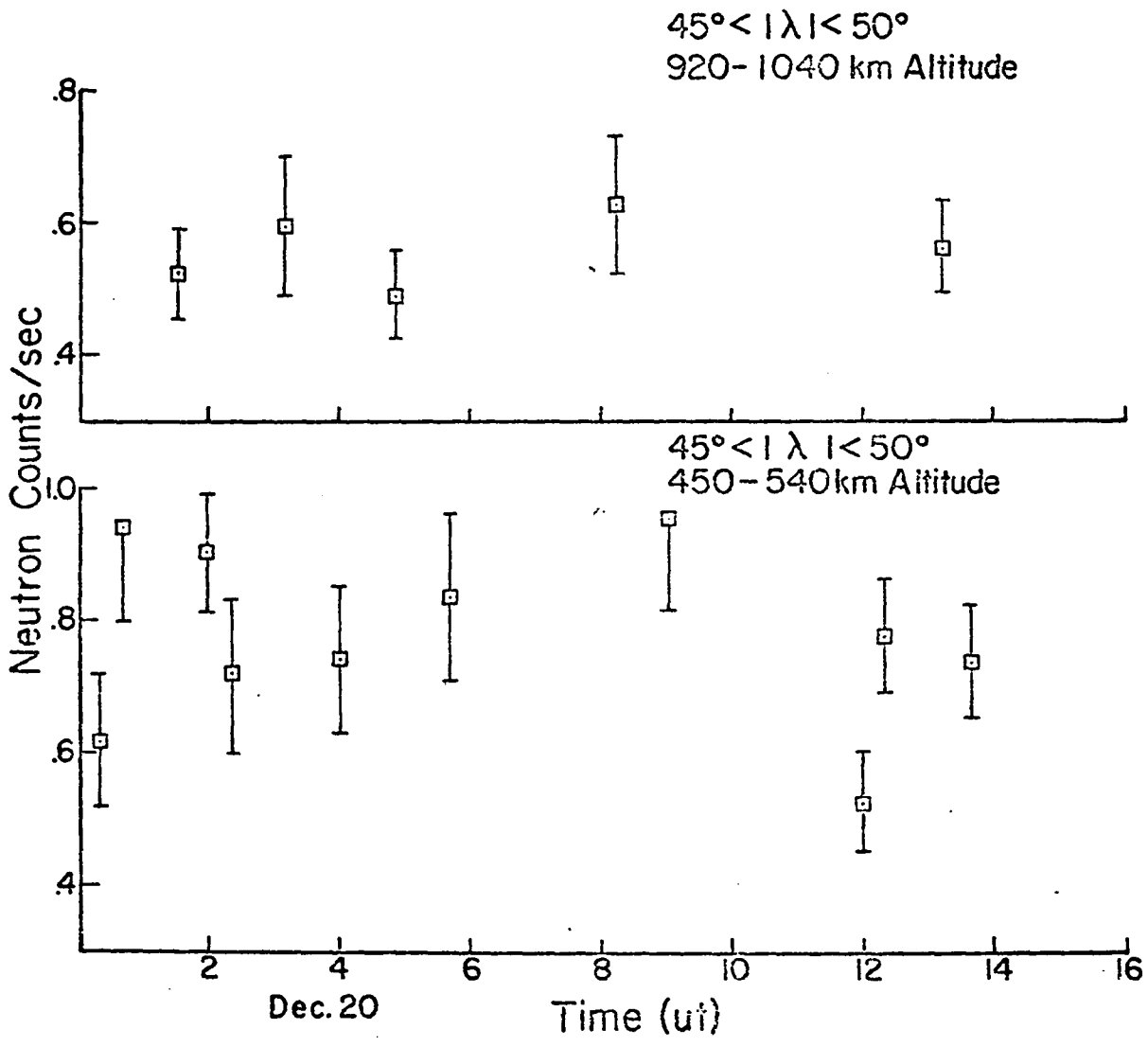
45°< |λ| < 50°
920-1040 km Altitude
45°< |λ| < 50°
450-540km Altitude
Neutron Counts/sec
.8
.6
.4
1.0
.8
.6
.4
2
4
6
8
10
12
14
16
Dec. 20
Time (ut)

Figure 31b

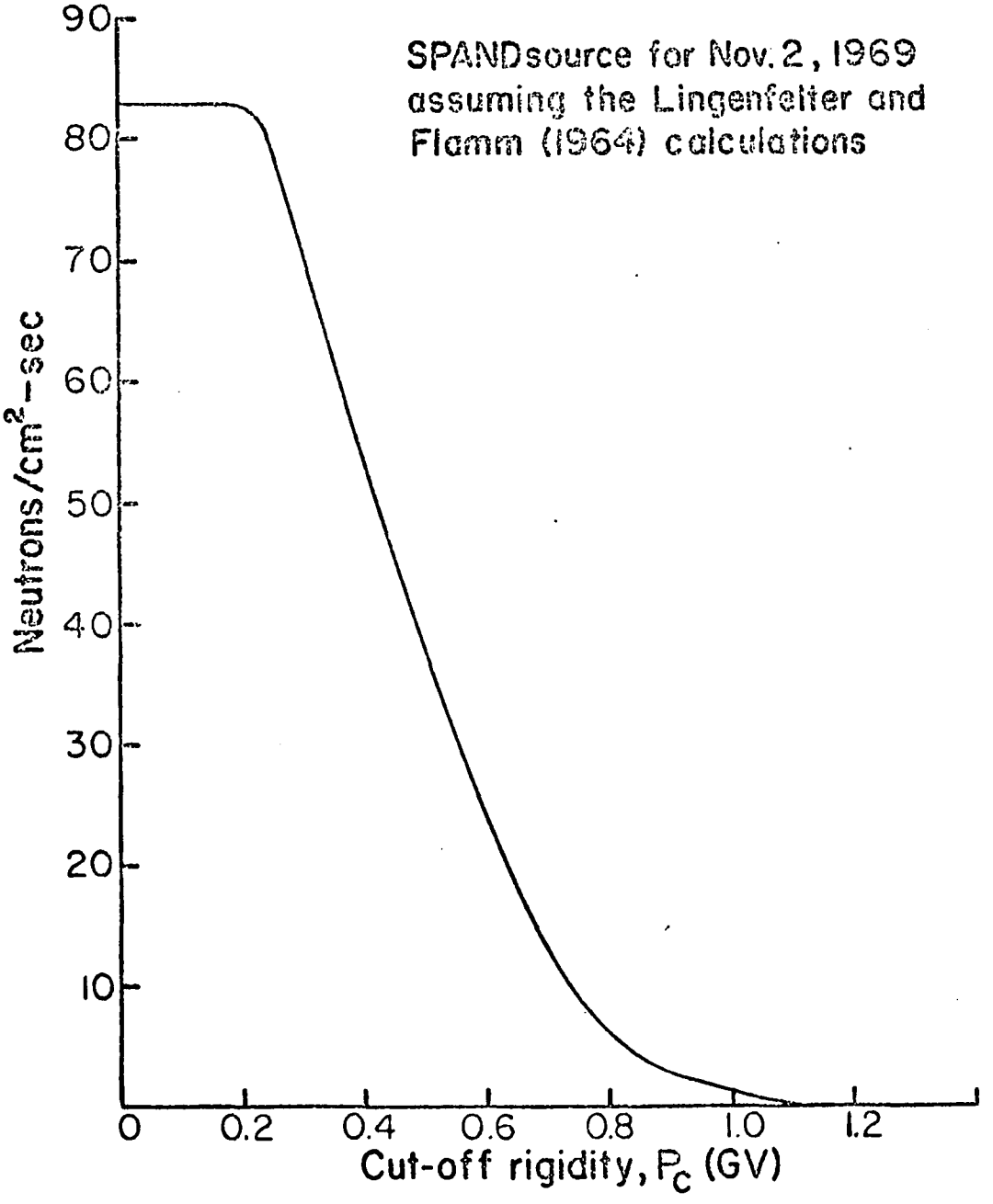
SPAND source for Nov. 2, 1969
assuming the Lingenfelter and
Flamm (1964) calculations
Neutrons/cm²-sec
90
80
70
60
50
40
30
20
10
0
0.2
0.4
0.6
0.8
1.0
1.2
Cut-off rigidity, Pc (GV)

Figure 32

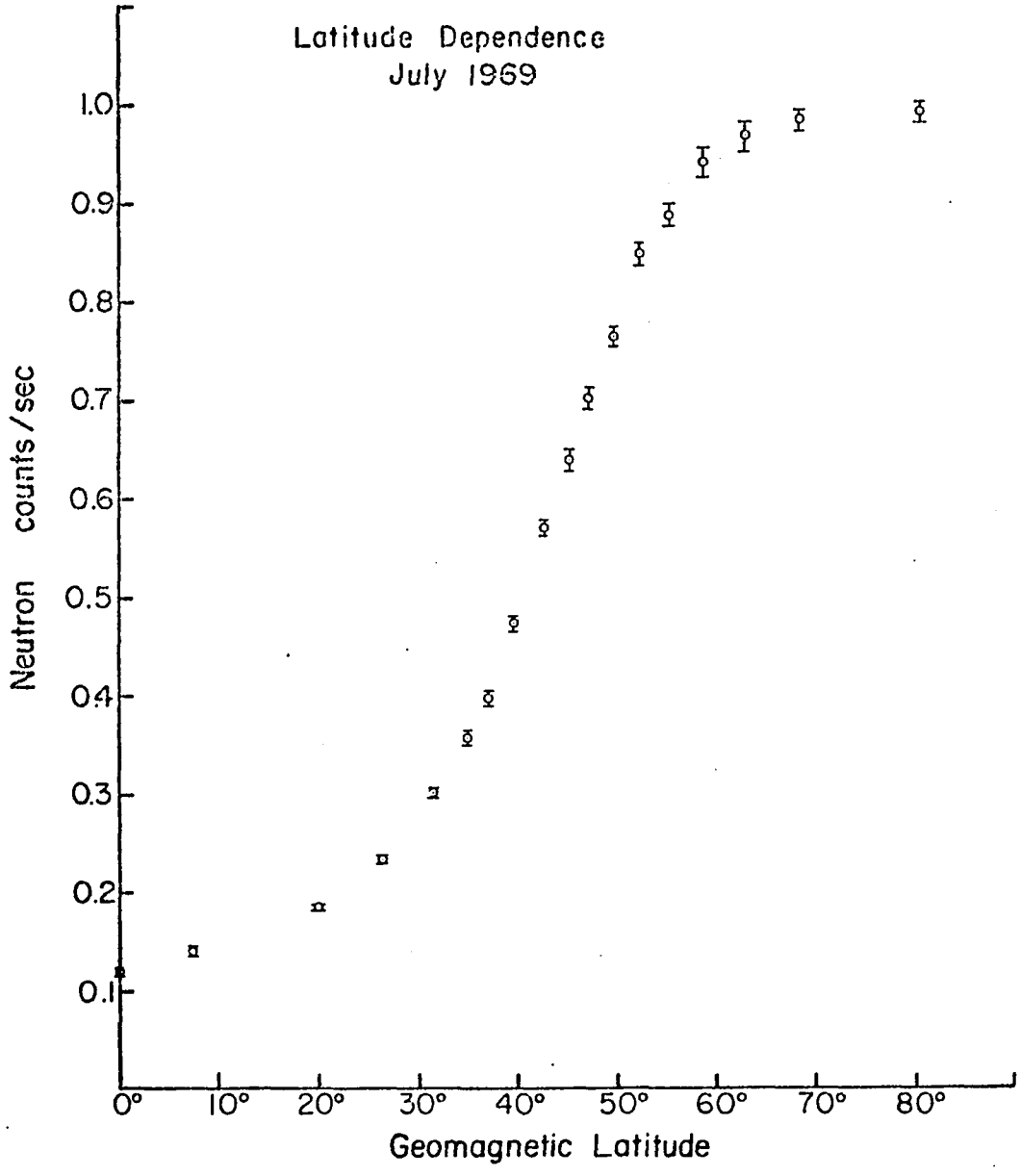
Latitude Dependence
July 1969
Neutron counts/sec
1.0
0.9
0.8
0.7
0.6
0.5
0.4
0.3
0.2
0.1
0°
10°
20°
30°
40°
50°
60°
70°
80°
Geomagnetic Latitude

Figure 33a

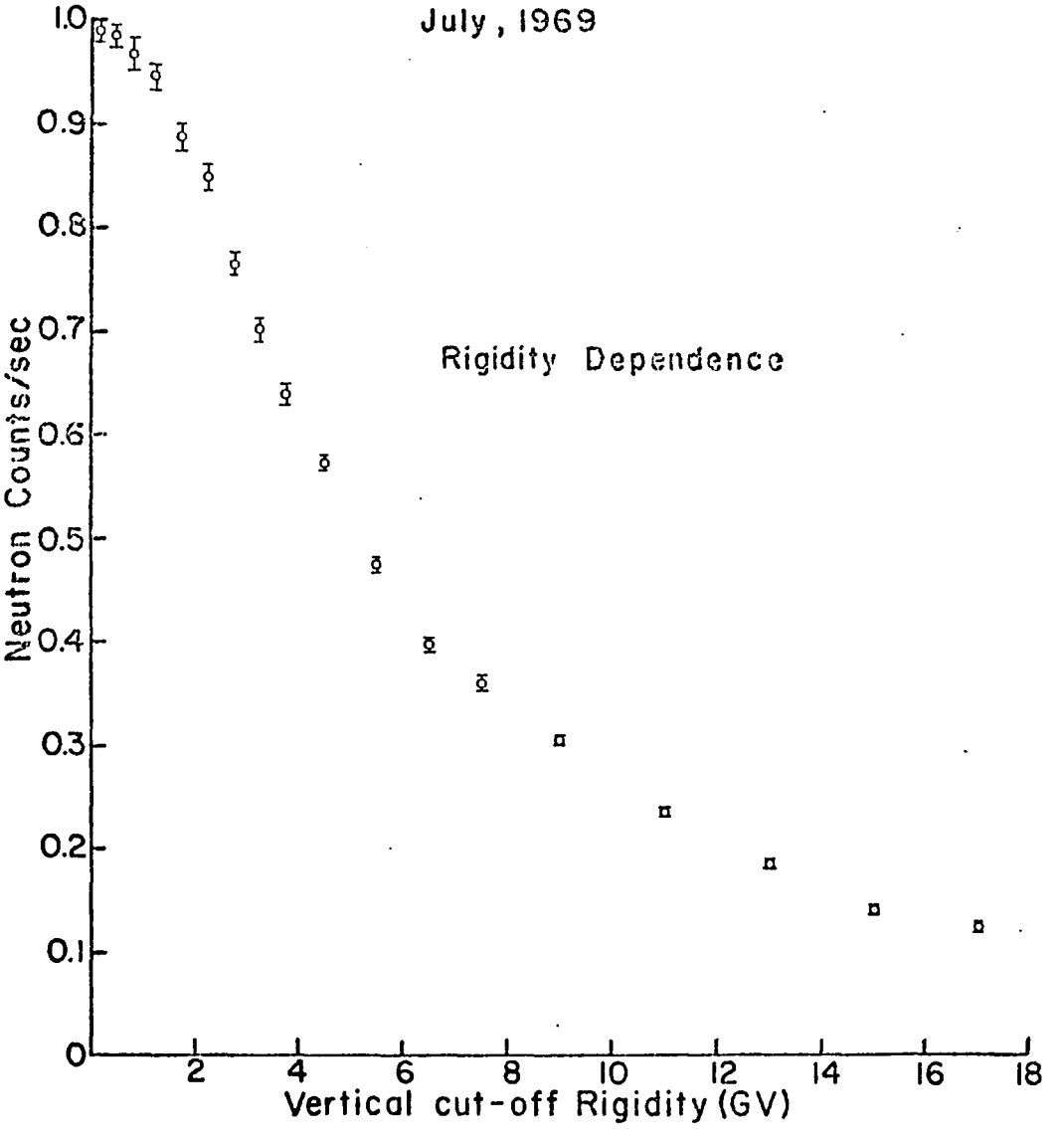
July, 1969
Rigidity Dependence
Neutron Counts/sec
Vertical cut-off Rigidity (GV)
1.0
0.9
0.8
0.7
0.6
0.5
0.4
0.3
0.2
0.1
0
2
4
6
8
10
12
14
16
18

Figure 33b

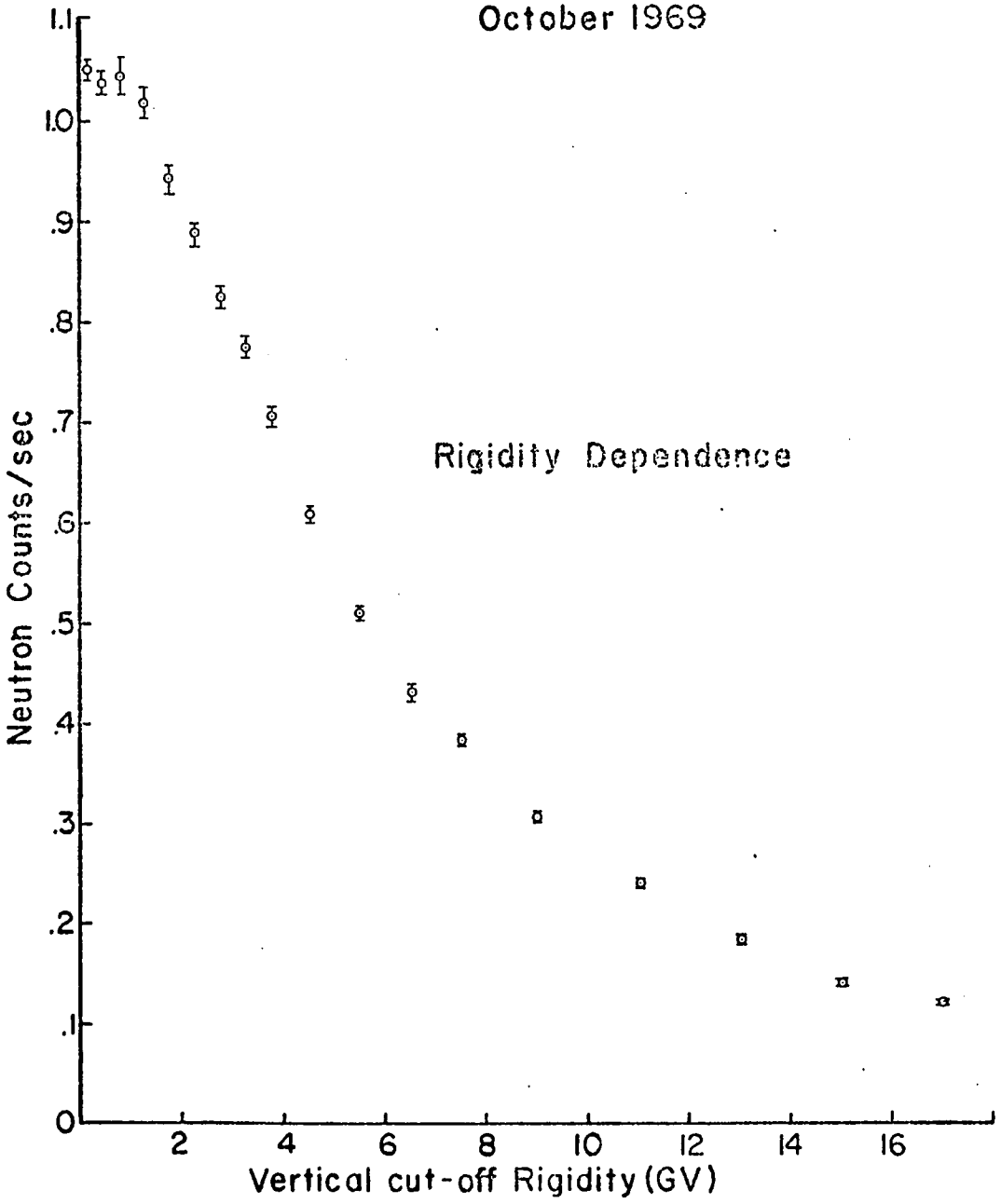
October 1969
Rigidity Dependence
Neutron Counts/sec
Vertical cut-off Rigidity (GV)
1.1
1.0
.9
.8
.7
.6
.5
.4
.3
.2
.1
0
2
4
6
8
10
12
14
16

Figure 34

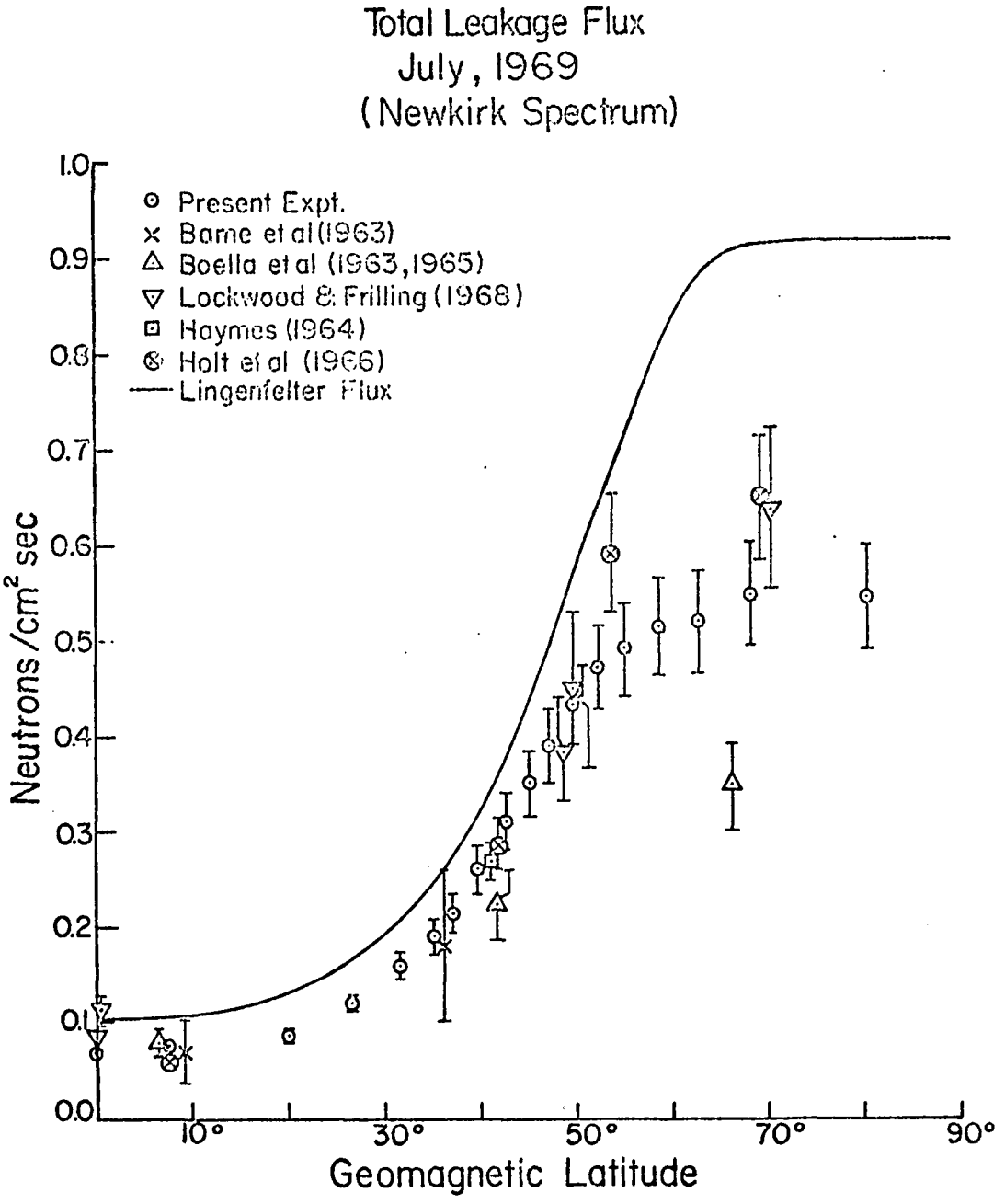
Total Leakage Flux
July, 1969
(Newkirk Spectrum)
Present Expt.
Bame et al (1963)
Boella et al (1963, 1965)
Lockwood & Frilling (1968)
Haymes (1964)
Holt et al (1966)
Lingenfelter Flux
Neutrons /cm² sec
1.0
0.9
0.8
0.7
0.6
0.5
0.4
0.3
0.2
0.1
0.0
10°
30°
50°
70°
90°
Geomagnetic Latitude

Figure 35

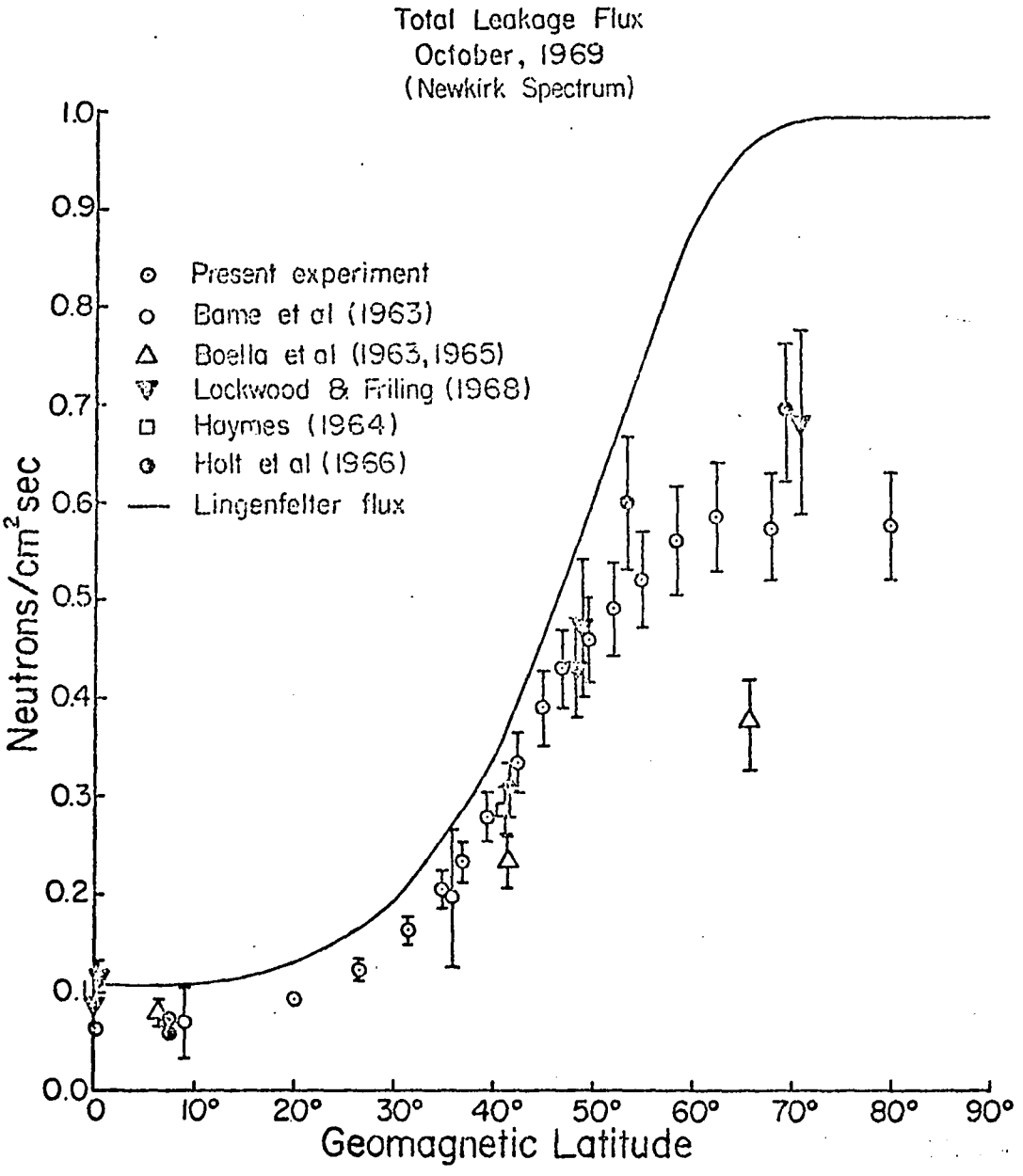
Total Leakage Flux
October, 1969
(Newkirk Spectrum)
Present experiment
Bame et al (1963)
Boella et al (1963, 1965)
Lockwood & Friling (1968)
Haymes (1964)
Holt et al (1966)
Lingenfelter flux
Neutrons/cm²sec
1.0
0.9
0.8
0.7
0.6
0.5
0.4
0.3
0.2
0.1
0.0
0
10°
20°
30°
40°
50°
60°
70°
80°
90°
Geomagnetic Latitude

Figure 36

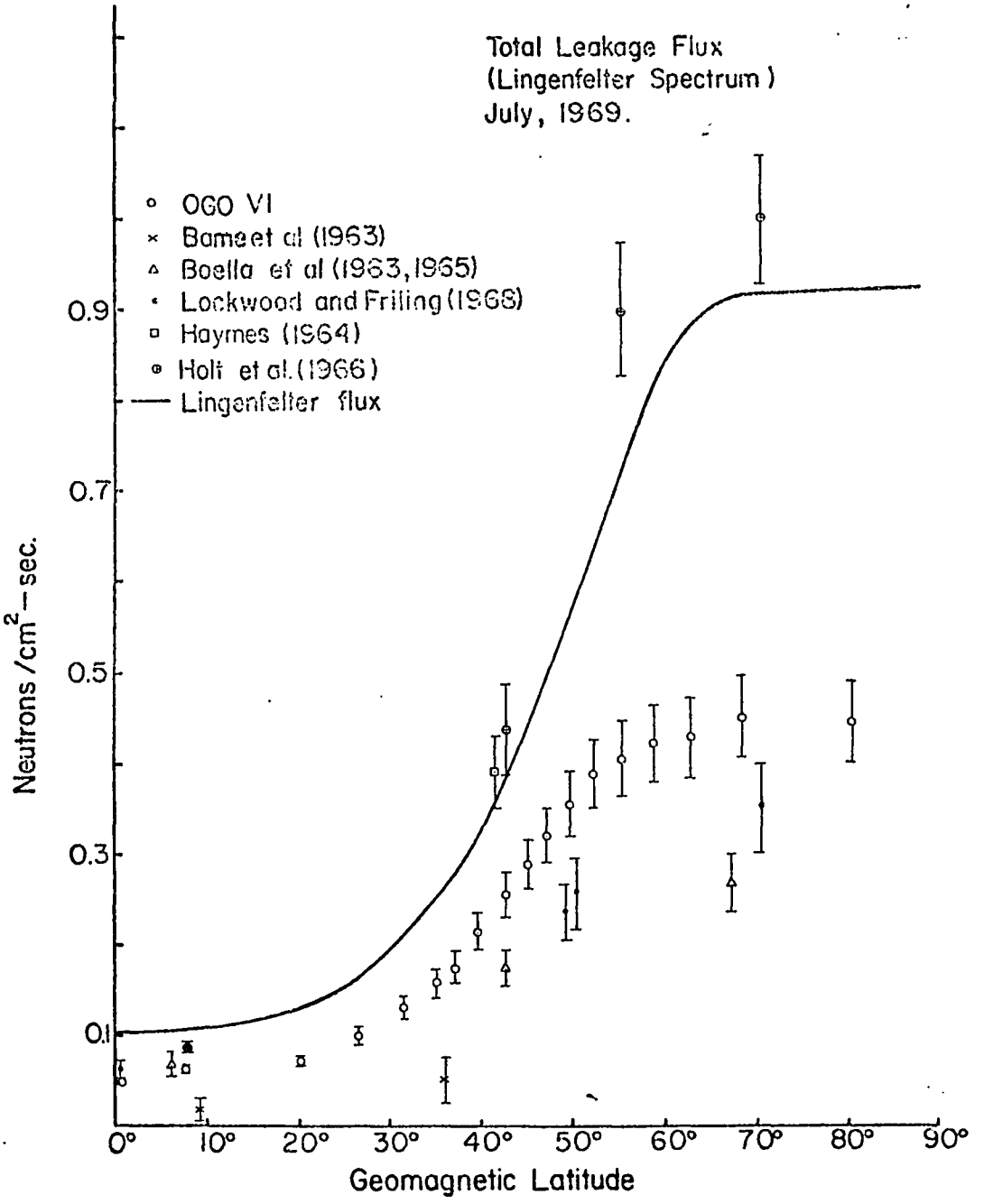
Total Leakage Flux
(Lingenfelter Spectrum)
July, 1969.
OGO VI
Bame et al (1963)
Boella et al (1963, 1965)
Lockwood and Friling (1968)
Haymes (1964)
Holt et al. (1966)
Lingenfelter flux
Neutrons /cm^2 – sec.
0.9
0.7
0.5
0.3
0.1
0°
10°
20°
30°
40°
50°
60°
70°
80°
90°
Geomagnetic Latitude

Figure 37

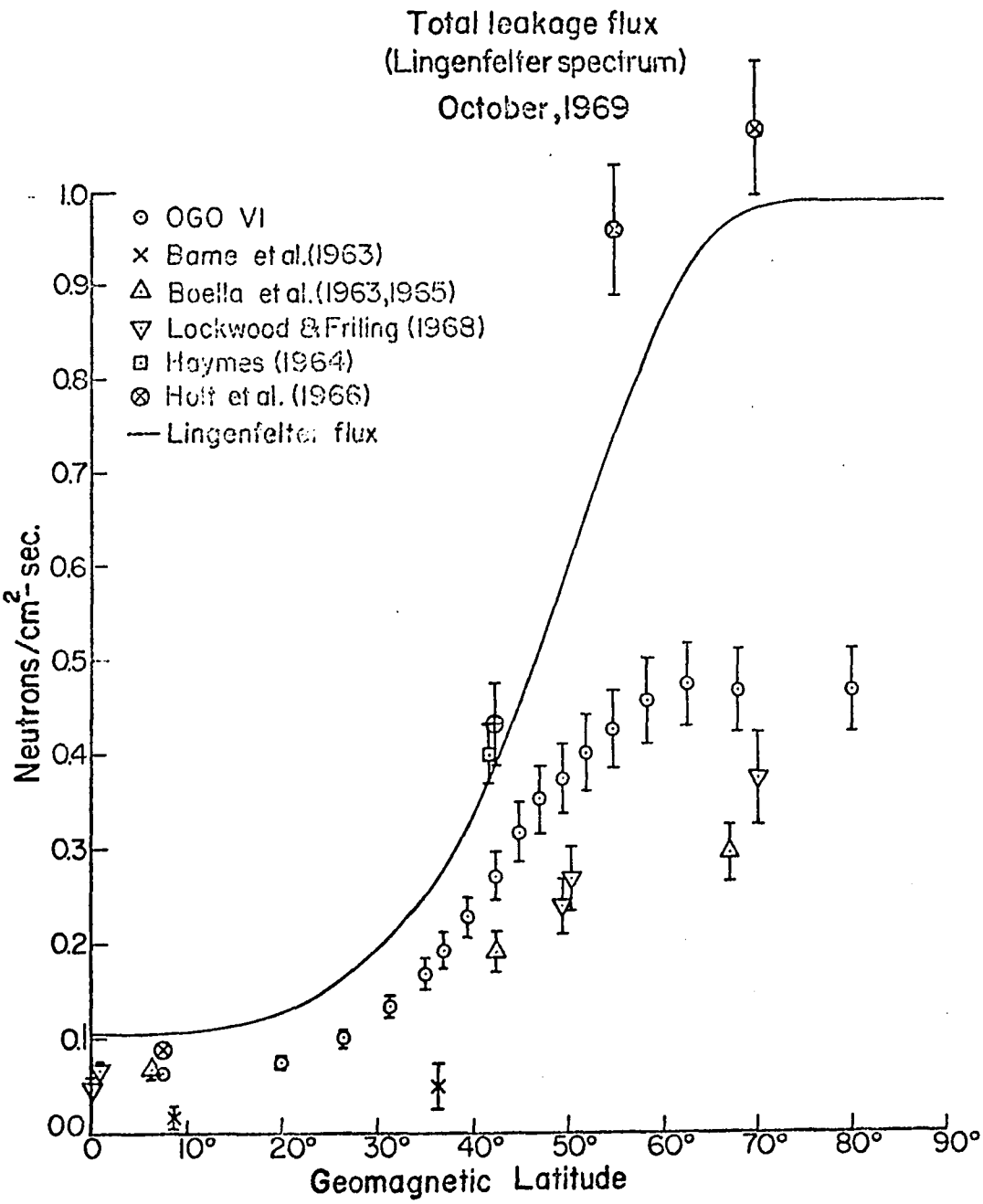
Total leakage flux
(Lingenfelter spectrum)
October, 1969
OGO VI
Bame et al.(1963)
Boella et al.(1963,1965)
Lockwood & Friling (1968)
Haymes (1964)
Holt et al. (1966)
Lingenfelter flux
Neutrons/cm²-sec.
1.0
0.9
0.8
0.7
0.6
0.5
0.4
0.3
0.2
0.1
00
0
10°
20°
30°
40°
50°
60°
70°
80°
90°
Geomagnetic Latitude

Figure 38

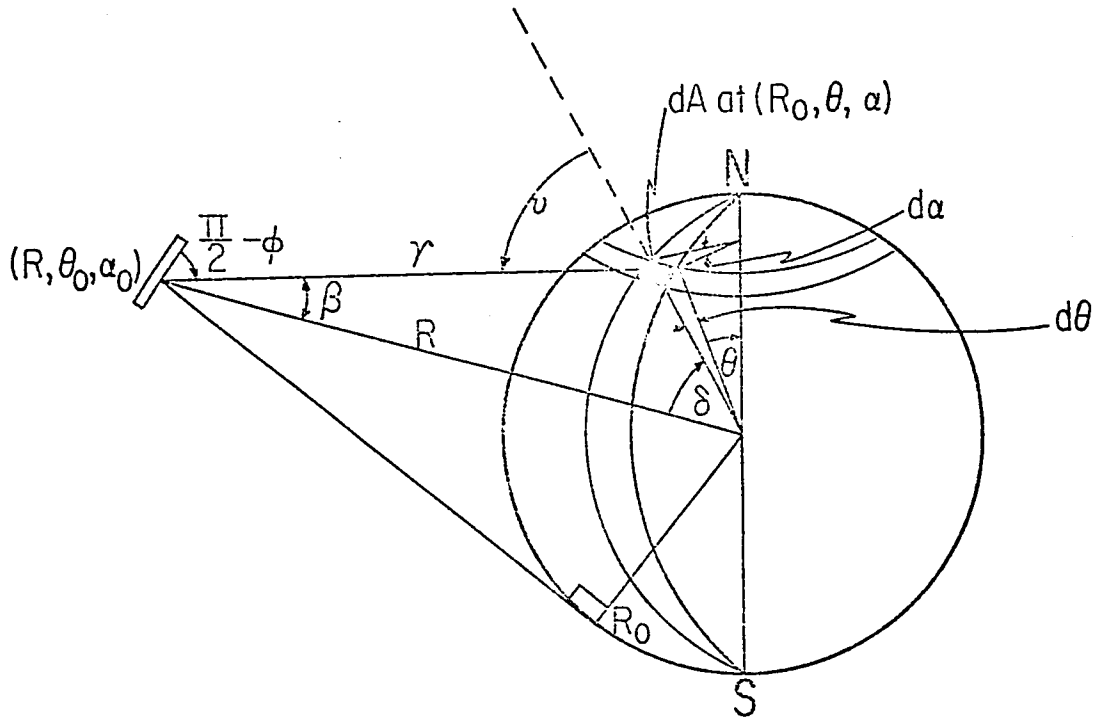

The geometry of the altitude variation of the neutron counting rate.

Figure 39

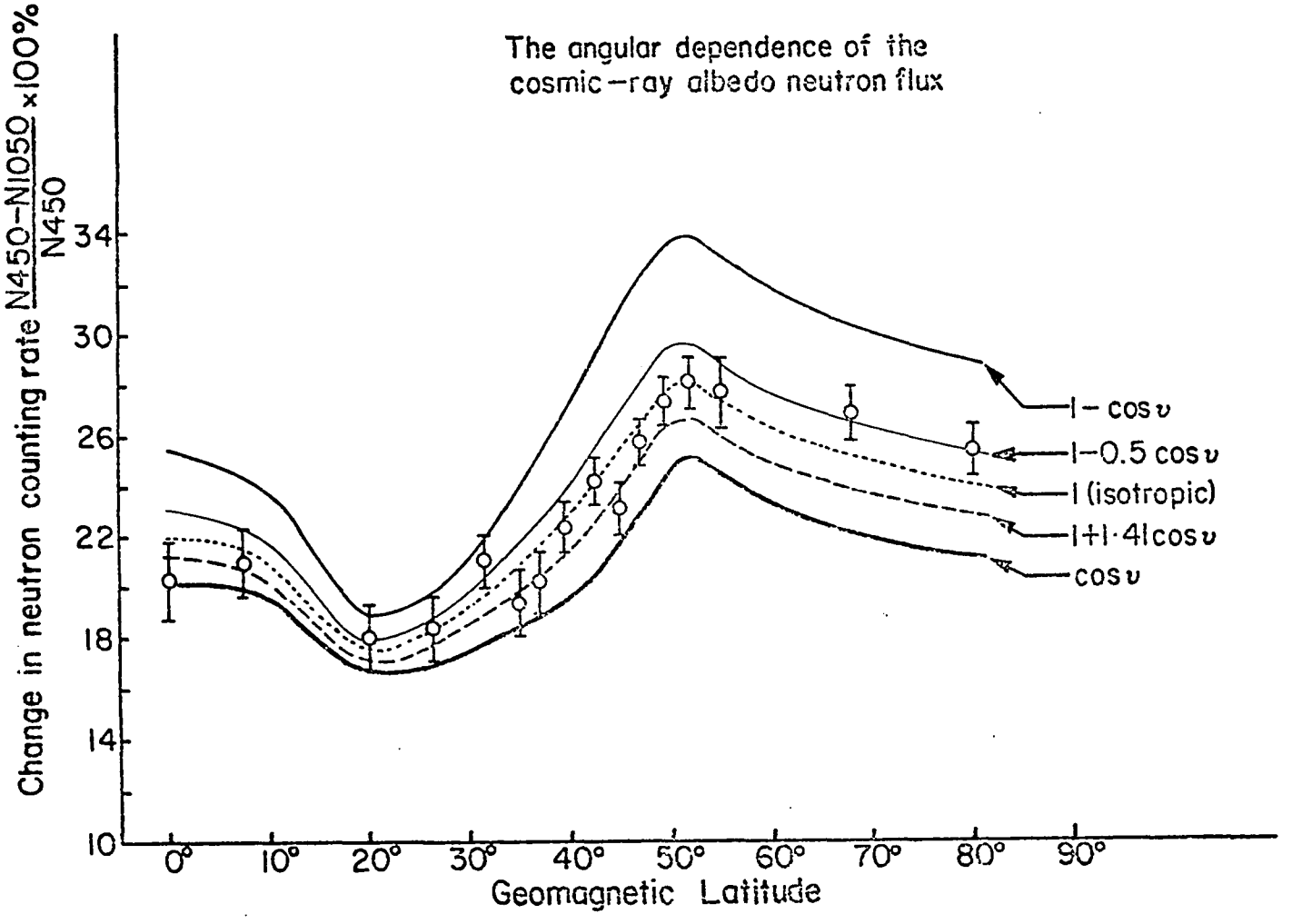
The angular dependence of the
cosmic-ray albedo neutron flux
Change in neutron counting rate (N450−N1050)/N450 ×100%
34
30
26
22
18
14
10
0°
10°
20°
30°
40°
50°
60°
70°
80°
90°
Geomagnetic Latitude
1 − cos υ
1−0.5 cos υ
1 (isotropic)
1+1·41cos υ
cos υ

Figure 40

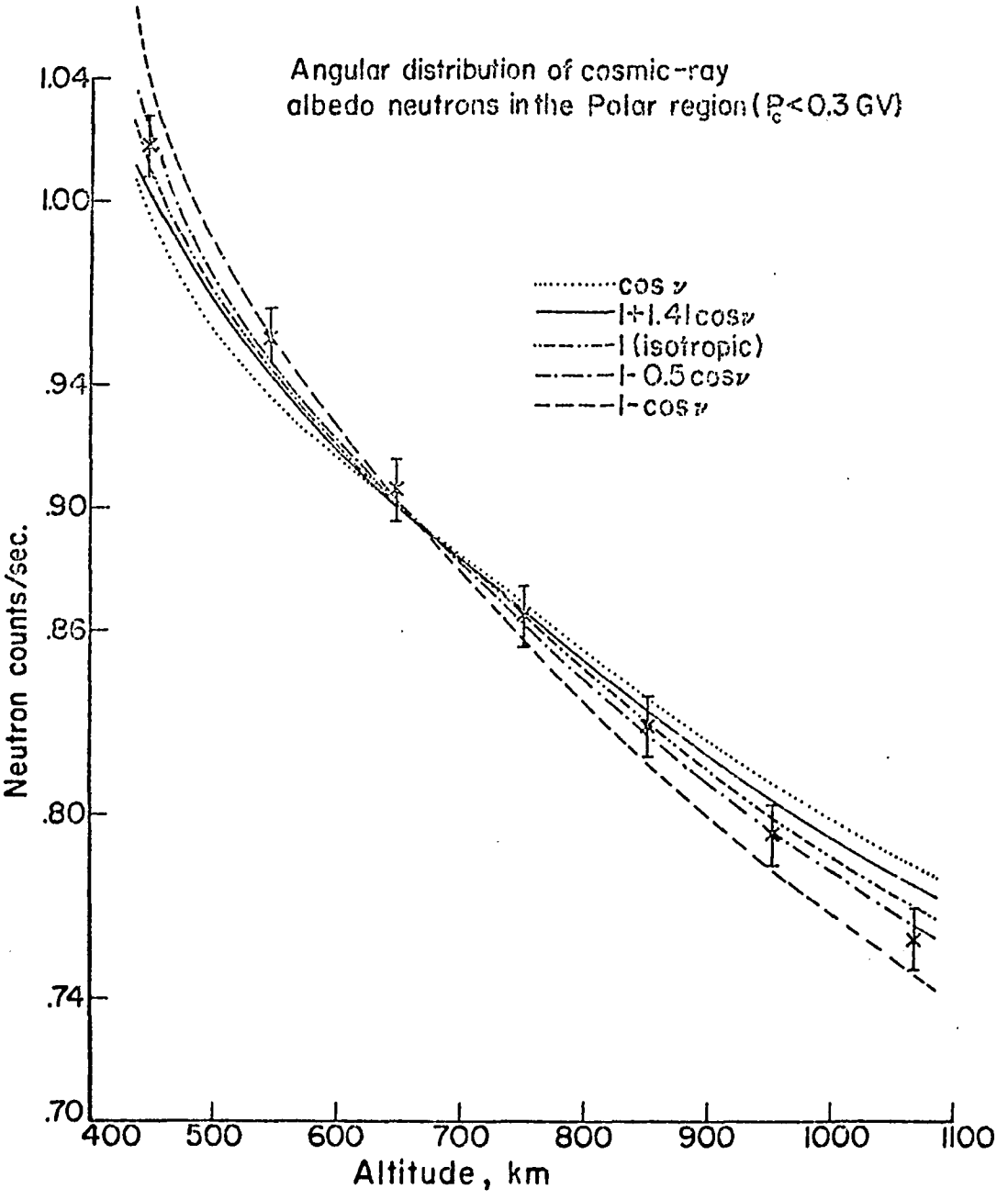
Angular distribution of cosmic-ray
albedo neutrons in the Polar region (R_c<0.3 GV)
cos ν
1+1.4 cos ν
1 (isotropic)
1- 0.5 cos ν
1- cos ν
Neutron counts/sec.
1.04
1.00
.94
.90
.86
.80
.74
.70
400
500
600
700
800
900
1000
1100
Altitude, km

Figure 41

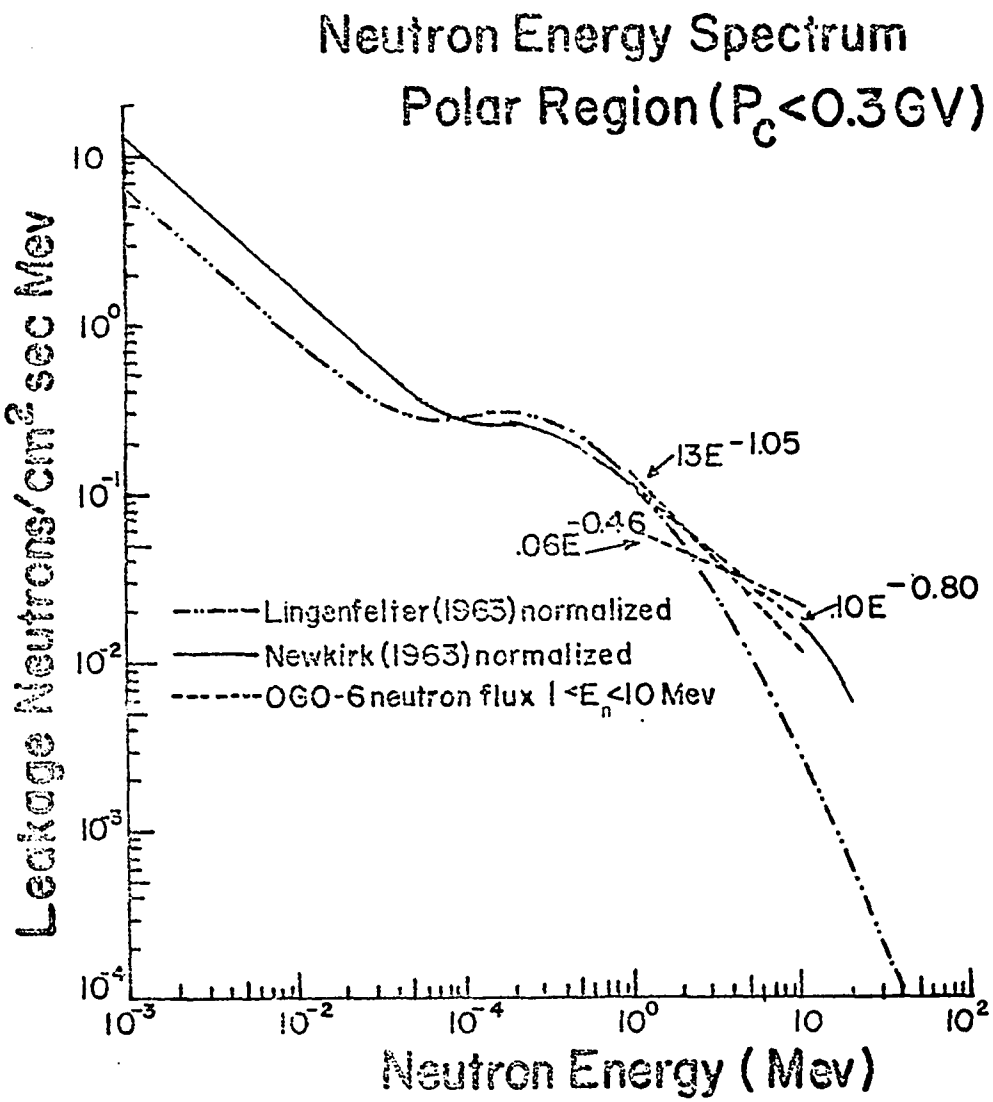
Neutron Energy Spectrum
Polar Region (P_c<0.3GV)
Leakage Neutrons/cm² sec Mev
Neutron Energy (Mev)
13E^-1.05
.06E^-0.46
.10E^-0.80
Lingenfelter (1963) normalized
Newkirk (1963) normalized
OGO-6 neutron flux 1<E_n<10 Mev

Figure 42

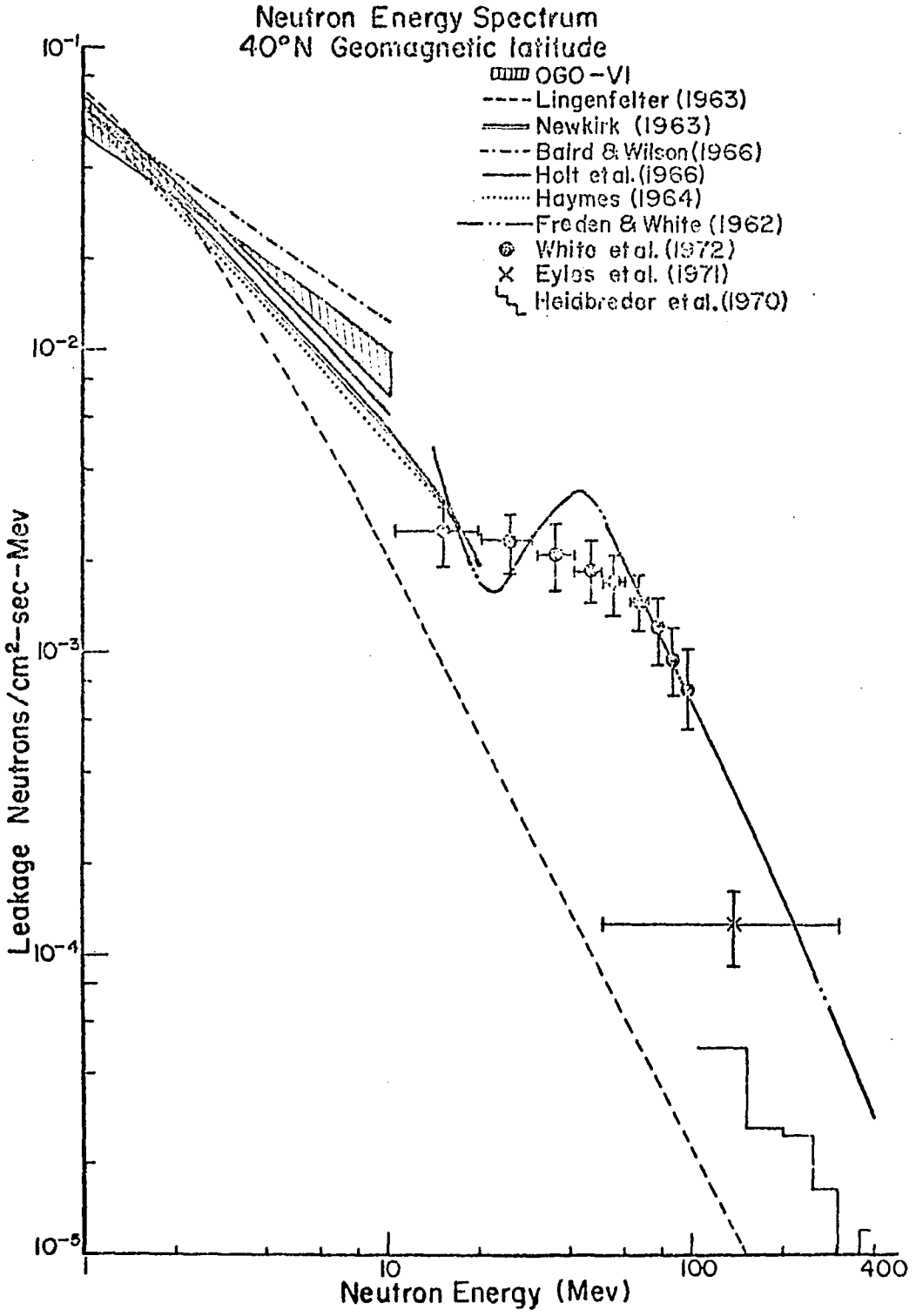
Neutron Energy Spectrum
40°N Geomagnetic latitude
OGO-VI
Lingenfelter (1963)
Newkirk (1963)
Baird & Wilson (1966)
Holt et al. (1966)
Haymes (1964)
Freden & White (1962)
White et al. (1972)
Eyles et al. (1971)
Heidbreder et al. (1970)
Leakage Neutrons/cm²-sec-Mev
10⁻¹
10⁻²
10⁻³
10⁻⁴
10⁻⁵
1
10
100
400
Neutron Energy (Mev)

Figure 43

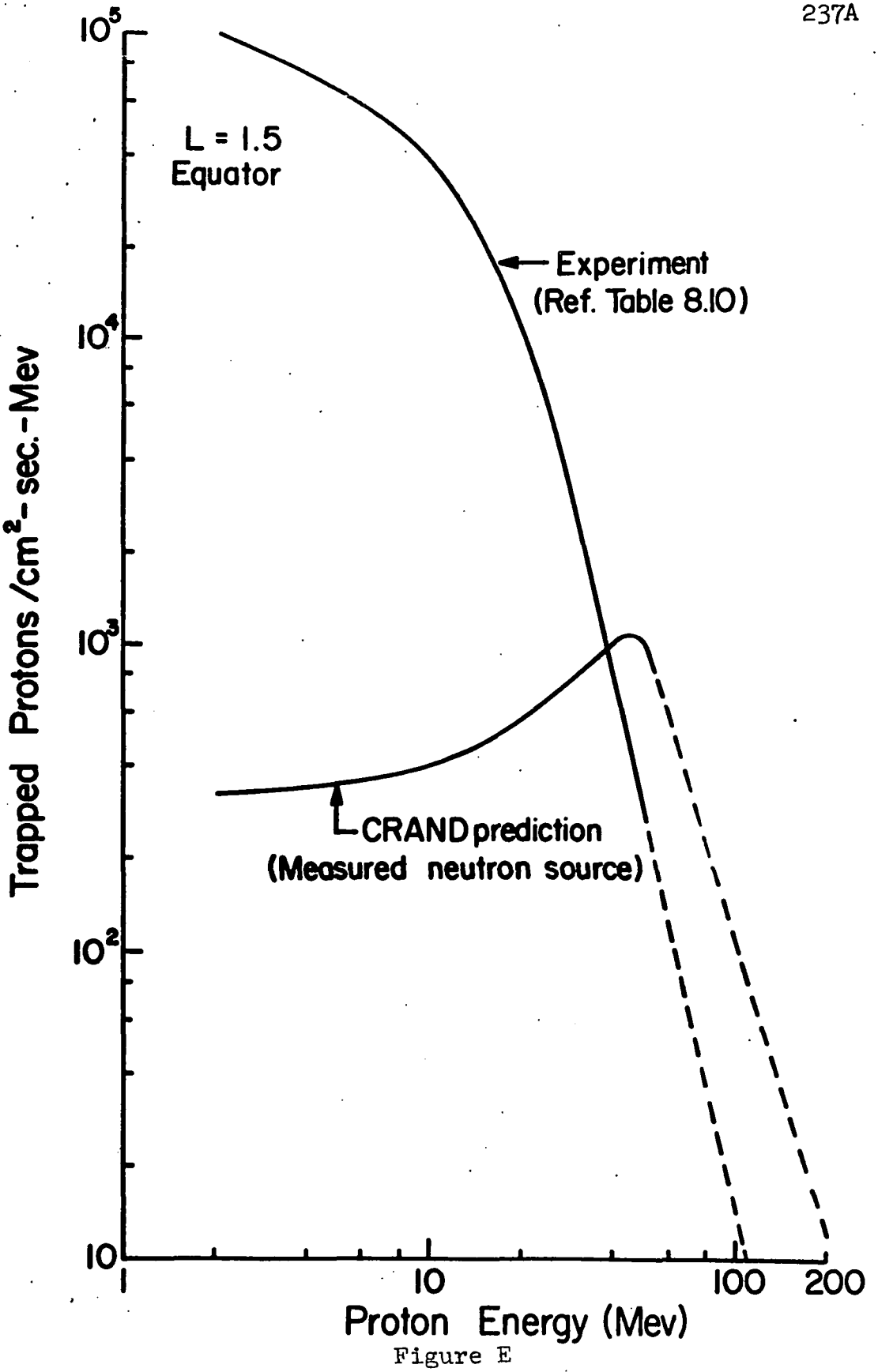
10^5
10^4
10^3
10^2
10
L = 1.5
Equator
Experiment
(Ref. Table 8.10)
CRAND prediction
(Measured neutron source)
Trapped Protons /cm²- sec.- Mev
10
100
200
Proton Energy (Mev)

Figure E

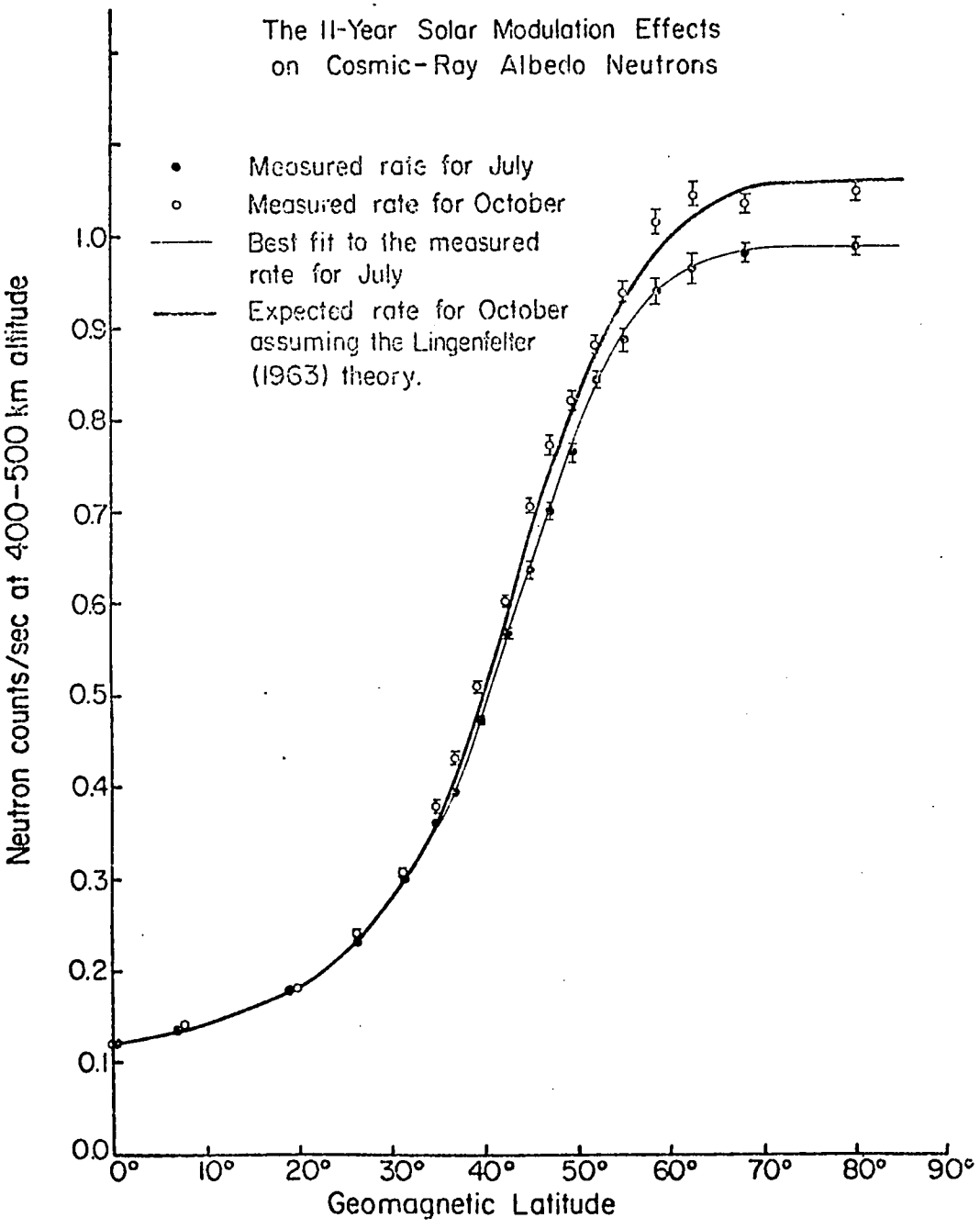
The 11-Year Solar Modulation Effects
on Cosmic-Ray Albedo Neutrons
Measured rate for July
Measured rate for October
Best fit to the measured rate for July
Expected rate for October assuming the Lingenfelter (1963) theory.
Neutron counts/sec at 400-500 km altitude
0.0
0.1
0.2
0.3
0.4
0.5
0.6
0.7
0.8
0.9
1.0
0°
10°
20°
30°
40°
50°
60°
70°
80°
90°
Geomagnetic Latitude

Figure 44

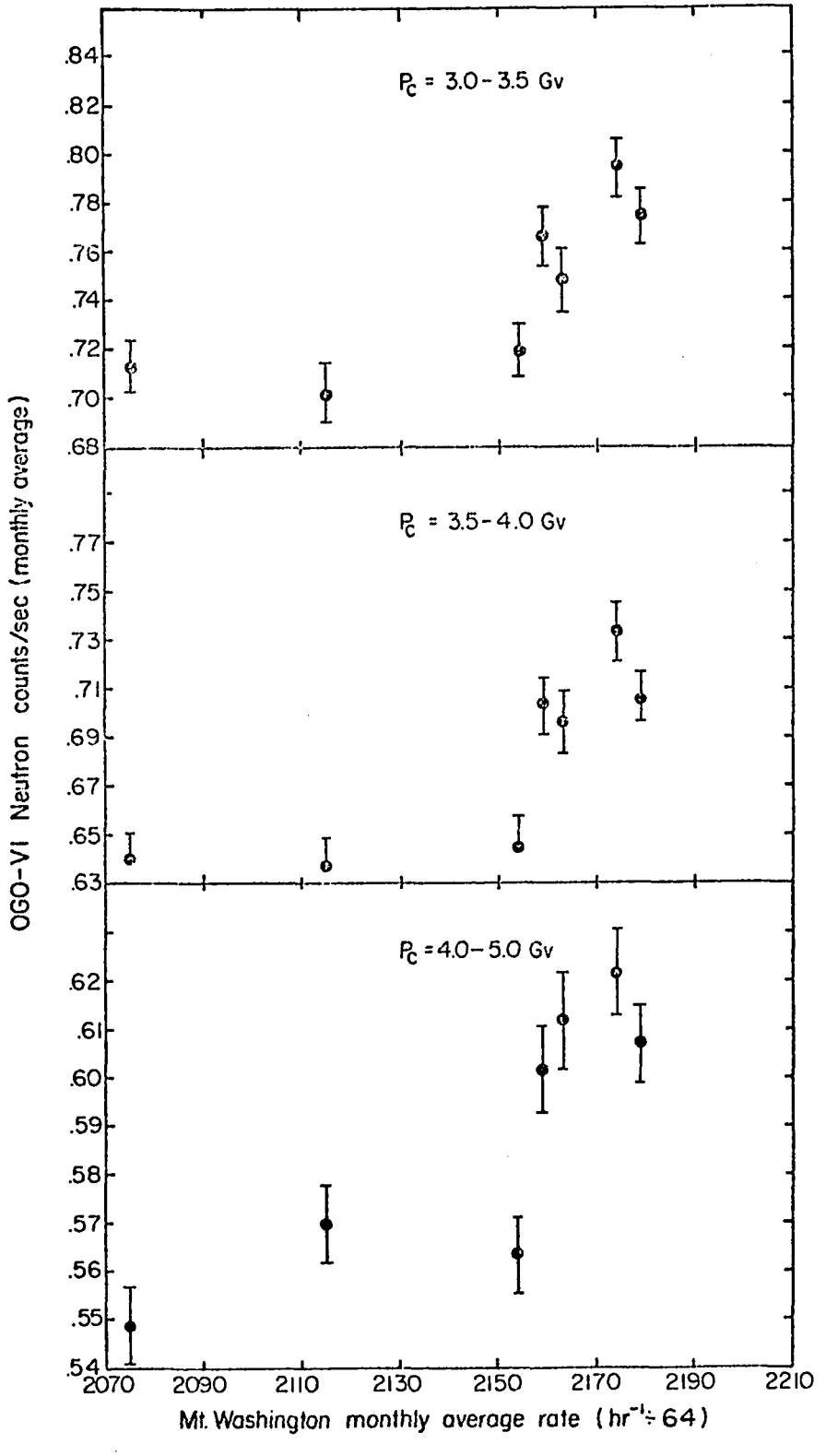
P_c = 3.0-3.5 Gv
P_c = 3.5-4.0 Gv
P_c = 4.0-5.0 Gv
OGO-VI Neutron counts/sec (monthly average)
Mt. Washington monthly average rate ($hr^{-1} \div 64$)
.84
.82
.80
.78
.76
.74
.72
.70
.68
.77
.75
.73
.71
.69
.67
.65
.63
.62
.61
.60
.59
.58
.57
.56
.55
.54
2070
2090
2110
2130
2150
2170
2190
2210

Figure 45

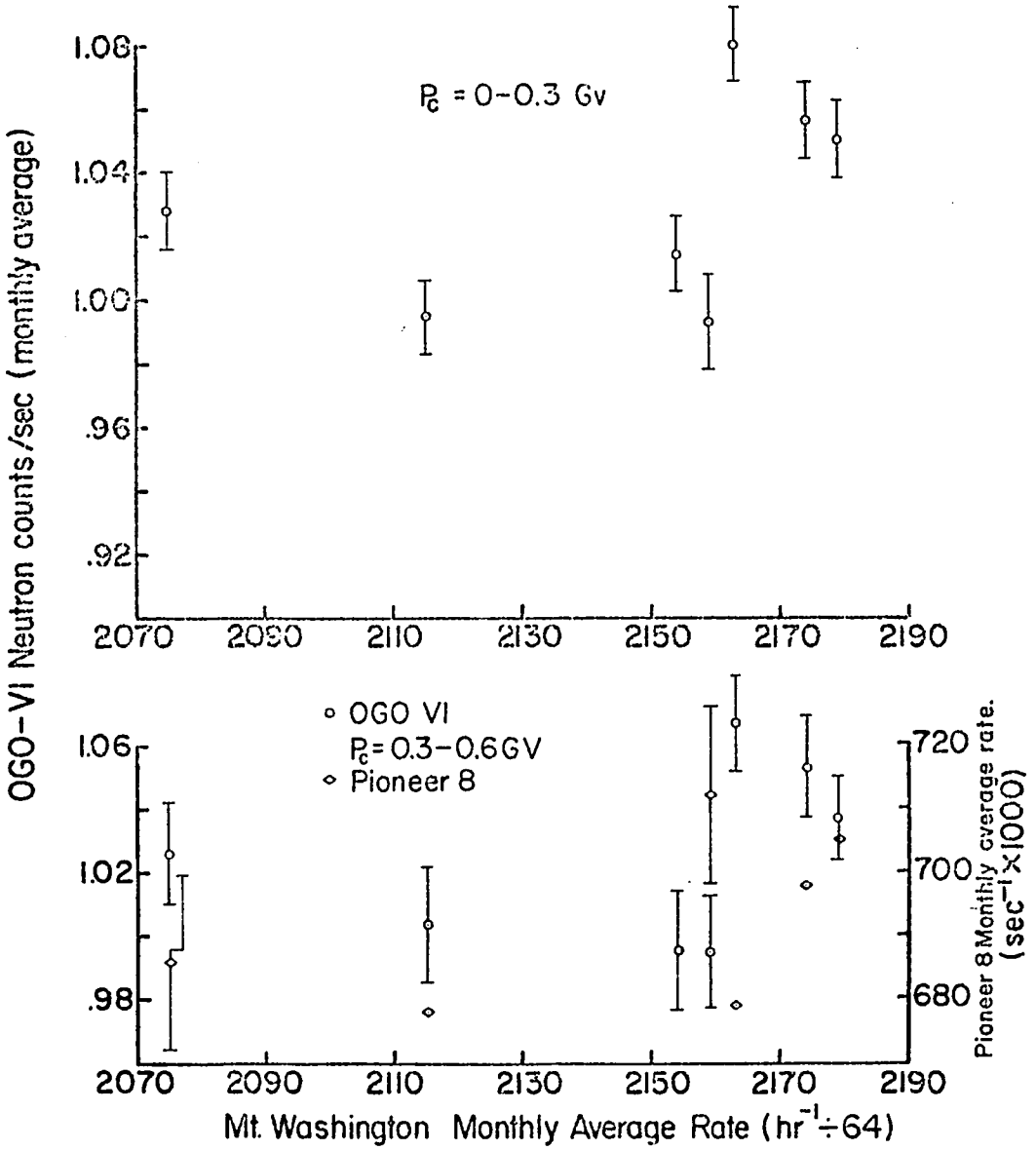
OGO-VI Neutron counts/sec (monthly average)
1.08
1.04
1.00
.96
.92
P_c = 0-0.3 Gv
2070
2090
2110
2130
2150
2170
2190
o OGO VI
P_c= 0.3-0.6GV
◇ Pioneer 8
1.06
1.02
.98
720
700
680
Pioneer 8 Monthly average rate. (sec^{-1}×1000)
Mt. Washington Monthly Average Rate (hr^{-1}÷64)

Figure 46

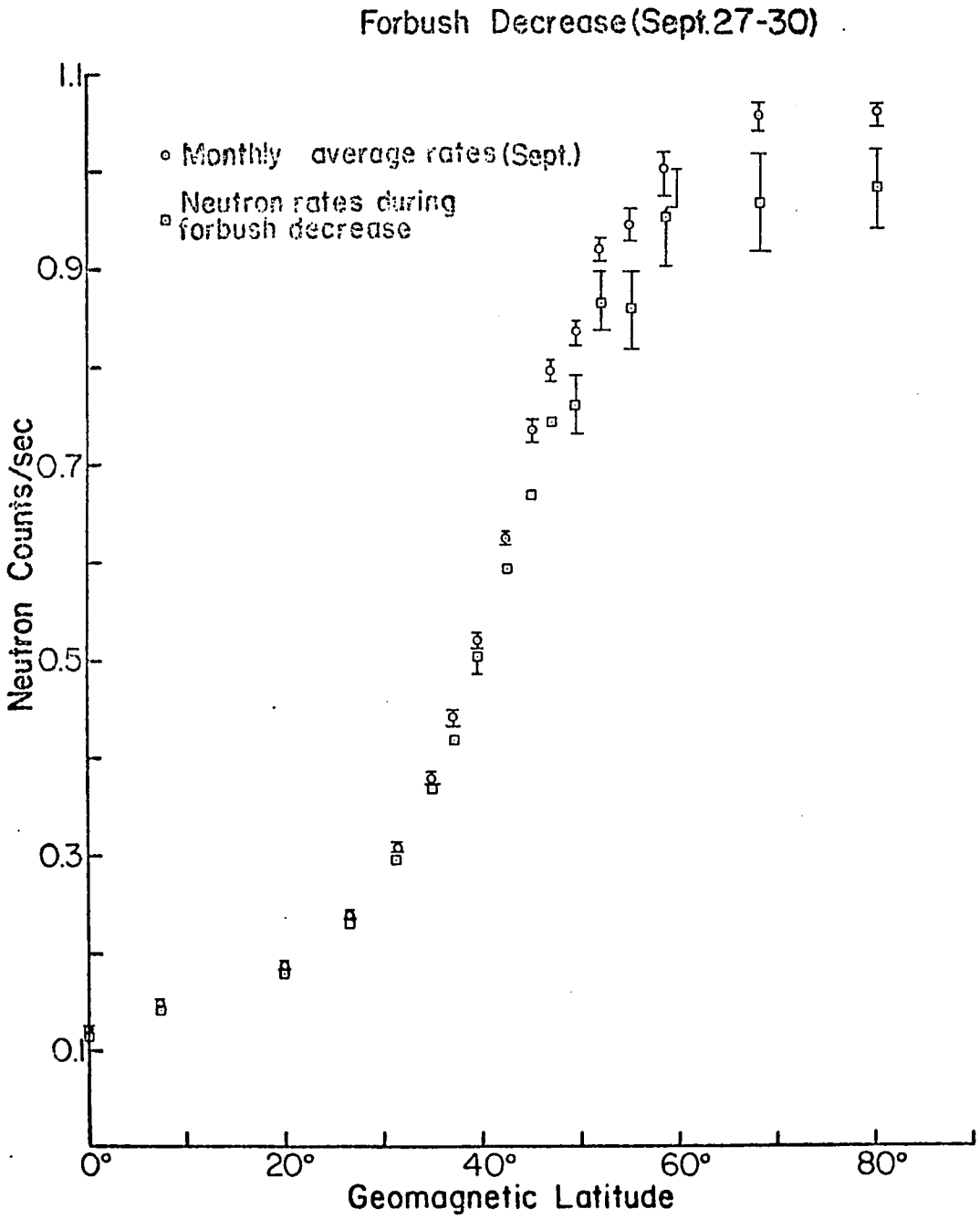
Forbush Decrease (Sept. 27-30)
Monthly average rates (Sept.)
Neutron rates during forbush decrease
Neutron Counts/sec
1.1
0.9
0.7
0.5
0.3
0.1
0°
20°
40°
60°
80°
Geomagnetic Latitude

Figure 47

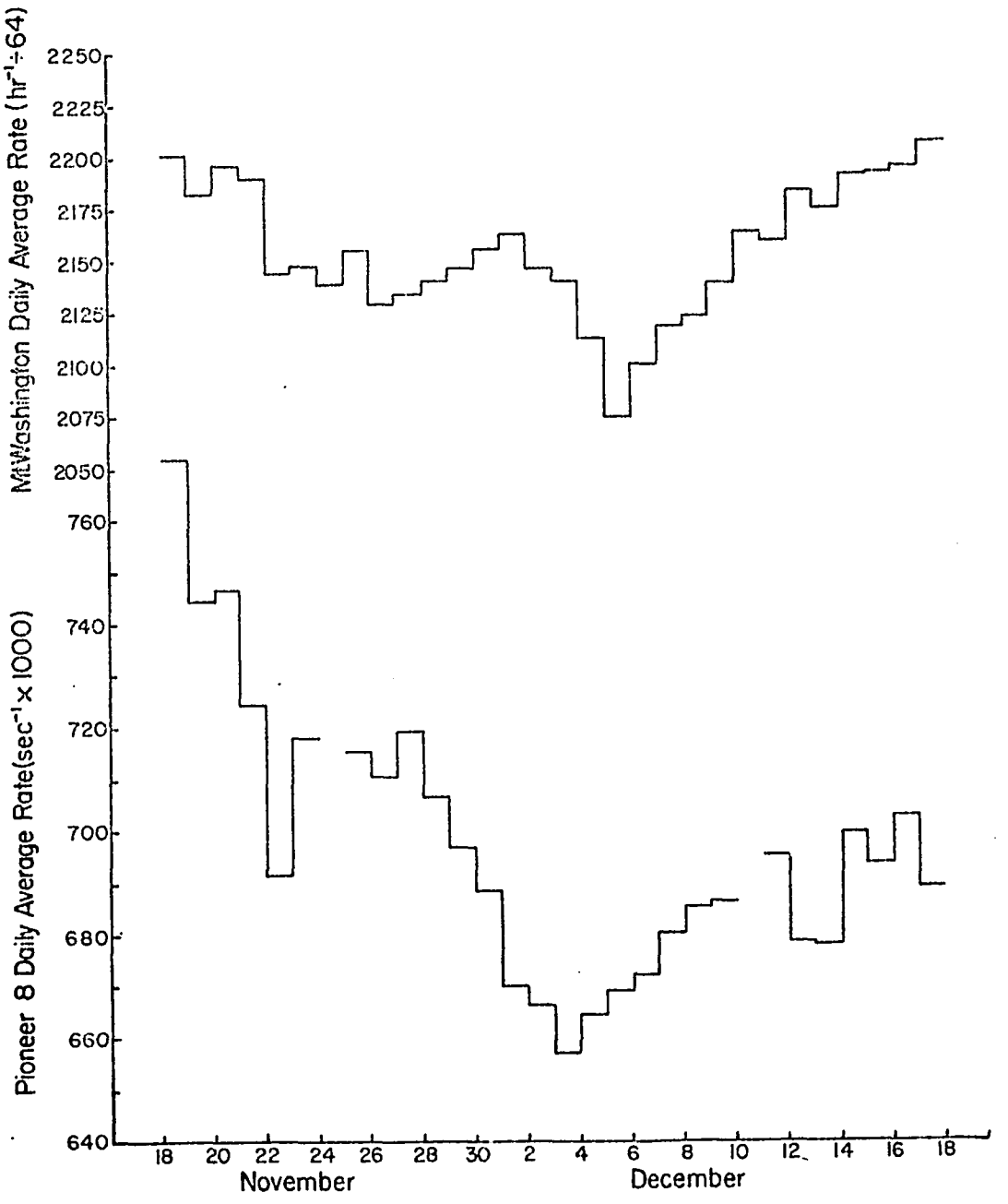
Mt.Washington Daily Average Rate (hr⁻¹÷64)
2250
2225
2200
2175
2150
2125
2100
2075
2050
760
740
720
700
680
660
640
Pioneer 8 Daily Average Rate(sec⁻¹ x 1000)
18 20 22 24 26 28 30 2 4 6 8 10 12 14 16 18
November
December

Figure 48

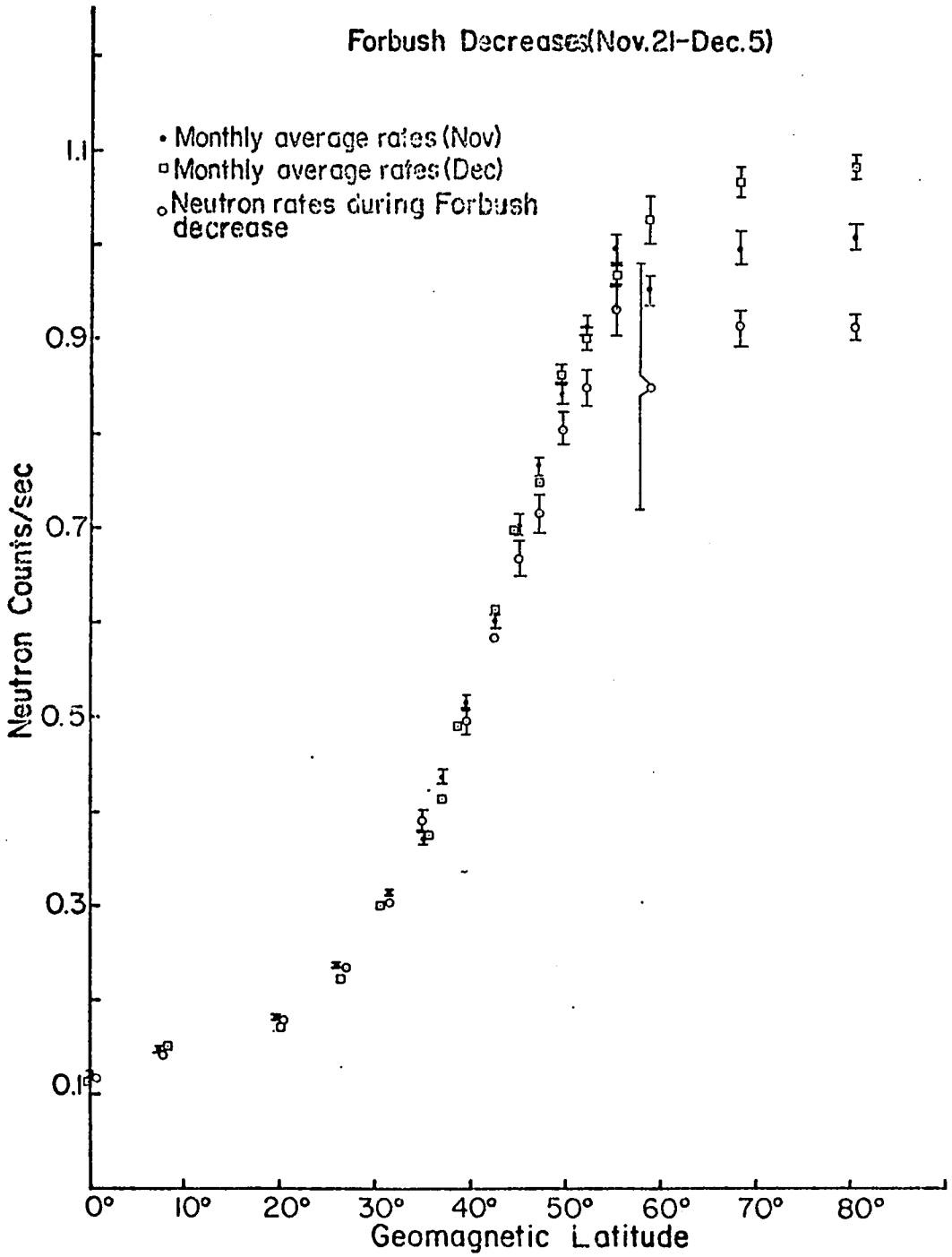
Forbush Decrease(Nov.21-Dec.5)
• Monthly average rates (Nov)
▫ Monthly average rates (Dec)
○ Neutron rates during Forbush decrease
Neutron Counts/sec
1.1
0.9
0.7
0.5
0.3
0.1
0°
10°
20°
30°
40°
50°
60°
70°
80°
Geomagnetic Latitude

Figure 49